Advanced Structured Materials

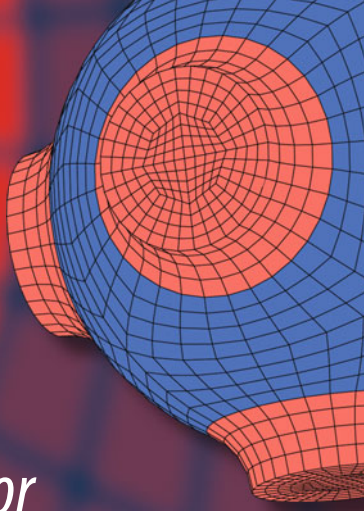

Mezhlum A. Sumbatyan *Editor*

Wave Dynamics, Mechanics and Physics of Microstructured Metamaterials

Theoretical and Experimental Methods

Springer

Advanced Structured Materials

Volume 109

Common engineering materials reach in many applications their limits and new developments are required to fulfil increasing demands on engineering materials. The performance of materials can be increased by combining different materials to achieve better properties than a single constituent or by shaping the material or constituents in a specific structure. The interaction between material and structure may arise on different length scales, such as micro-, meso- or macroscale, and offers possible applications in quite diverse fields.

This book series addresses the fundamental relationship between materials and their structure on the overall properties (e.g. mechanical, thermal, chemical or magnetic etc.) and applications.

The topics of *Advanced Structured Materials* include but are not limited to

- classical fibre-reinforced composites (e.g. glass, carbon or Aramid reinforced plastics)
- metal matrix composites (MMCs)
- micro porous composites
- micro channel materials
- multilayered materials
- cellular materials (e.g., metallic or polymer foams, sponges, hollow sphere structures)
- porous materials
- truss structures
- nanocomposite materials
- biomaterials
- nanoporous metals
- concrete
- coated materials
- smart materials

Advanced Structured Materials is indexed in Google Scholar and Scopus.

More information about this series at http://www.springer.com/series/8611

Mezhlum A. Sumbatyan
Editor

Wave Dynamics, Mechanics and Physics of Microstructured Metamaterials

Theoretical and Experimental Methods

Springer

Editor
Mezhlum A. Sumbatyan
Institute for Mathematics, Mechanics
and Computer Science
Southern Federal University
Rostov-on-Don, Russia

ISSN 1869-8433 ISSN 1869-8441 (electronic)
Advanced Structured Materials
ISBN 978-3-030-17469-9 ISBN 978-3-030-17470-5 (eBook)
https://doi.org/10.1007/978-3-030-17470-5

This Springer imprint is published by the registered company Springer Nature Switzerland AG
The registered company address is: Gewerbestrasse 11, 6330 Cham, Switzerland

Foreword

There is a growing current interest in the production, design, and analysis of structural elements made from metamaterials. Metamaterials are called new, mostly artificial materials, the properties of which are determined mainly by their structure, and not by the properties of the constituent material components. Examples of such a metamaterial are acoustic materials with internal resonators; see [Liu, Z., Zhang, X., Mao, Y., Zhu, Y. Y., Yang, Z., Chan, C. T., & Sheng, P. (2000). Locally resonant sonic materials. Science, 289 (5485), 1734–1736]. The material considered is a matrix with embedded rubber spheres and is an acoustic insulator. Unusual properties with the presence of specific frequency intervals, "cutoff" and "transmission," occur both for regular and for stochastic internal structures.

The papers presented in this book are devoted to the study of the following aspects in the dynamics of metamaterials:

- Analysis of wave propagation and wave processes in general in materials with internal resonators, both three-dimensional and thin-walled.
- Analysis of the intrinsic instabilities inherent in such materials, in any case, to some, based both on the applied theories of plates and shells, and on the three-dimensional nonlinear theory of elasticity.
- Development of "effective" models of metamaterials based on one or another method of averaging and solution to the corresponding initial-boundary value problems for homogeneous media with effective properties.
- Development of new methods and technologies for modeling the behavior of nanostructured materials, taking into account the surface properties and the determination of the effective properties of the material at the macrolevel.

The developed models are focused on their practical use. That is why the authors of the contributions use semi-analytical, numerical, and experimental methods in solving dynamic problems for metamaterials. The papers are characterized by the following features relevant to the study of acoustically and electrically active deformable metamaterials and devices made from these materials at the macro-, micro-, and nano-levels:

- Modern and actual related problems of the theory of elasticity (piezoelectricity or electroelasticity, thermoelectroelasticity, flexoelectricity, models for environments with low porosity); coupled problems of interaction of deformable bodies made of electrically active materials with acoustic media; models of the mechanics of composite electrically active metamaterials with a periodic and quasi-periodic structure.
- Development of the models for description of the behavior of electrically active materials and devices at the macro-, micro-, and nano-levels.
- Development of basic approaches for the modeling at the micro- and nano-levels: a multiscale analysis with the study of micro- and nanostructures; taking into account the surface effects (based on various models of surface elasticity) and the dimensional factors.
- An important algorithmic and software component of the project is in the use of finite element methods for discretization of continual problems for electrically active materials at different scale levels. The finite element algorithms are applied with the symmetric quasi-defined matrices; development of specific software for ANSYS, ABAQUS, COMSOL, and FlexPDE software systems.
- Focusing on computer simulation models and methods for the practical applications: the study of effective and important metamaterials and devices with the elements from electrically active materials (helicoidal objects, layered spiral piezoelectric shells, tubular piezotransducers with spiral electrodes, micro- and nano-sensors, actuators, composite piezogenerators, tunable terahertz metamaterials, and piezoelectric metamaterials having periodic and quasi-periodic structure) at different scale levels.
- The development of analytical methods of wave dynamics is applied for the problems of propagation of the acoustic waves through the internal structures of metamaterials. It includes obtaining explicit approximate solutions and qualitative analysis of the mechanisms of "suppression" and transmission from explicit analytical solutions.
- Continuous and discrete models of solids are developed (including multi-particle models of low and highly molecular systems with complicated strain interactions) as well as the structures taking into account surface elasticity and real properties of materials at the macrolevel.
- Theoretical and experimental approaches are obtained for the problems of acoustic control of active metamaterials of complex internal structure (doubly and threefold systems of internal inclusions, periodic epoxy-based structures, and others).

This book is a logical continuation and further development of the ideas and methods presented in the monograph: *Wave Dynamics and Composite Mechanics for Microstructured Materials and Metamaterials* (ed. by M. A. Sumbatyan). Springer Series: Advanced Structured Materials. Springer Nature: Singapore, 2017.

Saint Petersburg, Russia
January 2019

Alexey Porubov
Institute of Problems in Mechanical Engineering

Contents

Contributors

K. L. Aghayan Institute of Mechanics, National Academy of Sciences, Yerevan, Armenia

Ara S. Avetisyan Institute of Mechanics, National Academy of Sciences, Yerevan, Armenia

Alexandr R. Baidganov Cherepovets State University, Cherepovets, Russian Federation

Emilio Barchiesi International Center M&MOCS Mathematics and Mechanics of Complex Systems, DICEAA, Universitá degli Studi dell'Aquila, L'Aquila, Italy
Dipartimento di Ingegneria Strutturale e Geotecnica, Università degli Studi di Roma "La Sapienza" Rome, Rome, Italy

Olga S. Baruzdina Cherepovets State University, Cherepovets, Russian Federation

Mels V. Belubekyan Institute of Mechanics, National Academy of Sciences, Yerevan, Armenia

Vagharshak M. Belubekyan Institute of Mechanics, National Academy of Sciences, Yerevan, Armenia

Nikolay V. Boyev Southern Federal University, Rostov-on-Don, Russian Federation

Michele Brigante University of Naples—Federico II, Naples, Italy

Vladislav I. Egorov Cherepovets State University, Cherepovets, Russian Federation

Victor A. Eremeyev Faculty of Civil and Environmental Engineering, Gdańsk University of Technology, Gdańsk, Poland;
Southern Federal University, Rostov-on-Don, Russia;
Southern Scientific Center of RASci, Rostov-on-Don, Russia

T. E. Gerasimenko Institute of Mathematics, Mechanics and Computer Science, Southern Federal University, Rostov-on-Don, Russia

Roman A. Gerasimov Southern Federal University, Rostov-on-Don, Russia

Karen B. Ghazaryan Institute of Mechanics, National Academy of Sciences, Yerevan, Armenia

V. N. Hakobyan Institute of Mechanics, National Academy of Sciences, Yerevan, Armenia

G. Iovane Department of Computer Science, University of Salerno, Fisciano, SA, Italy

A. S. Kornievsky Institute of Mathematics, Mechanics and Computer Science, Southern Federal University, Rostov-on-Don, Russia

N. V. Kurbatova Institute of Mathematics, Mechanics and Computer Science, Southern Federal University, Rostov-on-Don, Russia

Marco Laudato Dipartimento di Ingegneria e Scienze dell'Informazione e Matematica, Università degli Studi dell'Aquila, L'Aquila, Coppito, Italy

Andrei V. Maksimov Cherepovets State University, Cherepovets, Russian Federation

Olga G. Maksimova Cherepovets State University, Cherepovets, Russian Federation

Andrei V. Maximov Cherepovets State University, Cherepovets, Russia

Olga G. Maximova Cherepovets State University, Cherepovets, Russia

D. K. Nadolin Institute of Mathematics, Mechanics and Computer Science, Southern Federal University, Rostov-on-Don, Russia

A. V. Nasedkin Institute of Mathematics, Mechanics and Computer Science, Southern Federal University, Rostov-on-Don, Russia

A. A. Nasedkina Institute of Mathematics, Mechanics and Computer Science, Southern Federal University, Rostov-on-Don, Russia

P. A. Oganesyan Institute of Mathematics, Mechanics and Computer Science, Southern Federal University, Rostov-on-Don, Russia

Tatiana O. Petrova Southern Federal University, Rostov-on-Don, Russia

Gayane T. Piliposian Department of Mathematical Sciences, The University of Liverpool, Liverpool, UK

Davit G. Piliposyan Institute of Mechanics, National Academy of Sciences, Yerevan, Armenia

Vitaly V. Popuzin Southern Federal University, Rostov-on-Don, Russian Federation

M. Y. Remizov Institute of Mathematics, Mechanics and Computer Science, Southern Federal University, Rostov-on-Don, Russia

A. V. Sahakyan Institute of Mechanics, National Academy of Sciences, Yerevan, Armenia

A. S. Skaliukh Institute of Mathematics, Mechanics and Computer Science, Southern Federal University, Rostov-on-Don, Russia

A. N. Soloviev Department of Theoretical and Applied Mechanics, Don State Technical University, Rostov-on-Don, Russia

Mezhlum A. Sumbatyan Southern Federal University, Rostov-on-Don, Russian Federation

Alexander E. Tarasov Southern Federal University, Rostov-on-Don, Russian Federation

Vittorio Zampoli University of Salerno, Fisciano (Salerno), Italy

Vladimir M. Zotov Southern Federal University, Rostov-on-Don, Russian Federation

On Anti-Plane Surface Waves Considering Highly Anisotropic Surface Elasticity Constitutive Relations

Victor A. Eremeyev

Abstract Within the framework of highly anisotropic surface elasticity model we discuss the propagation of new type of surface waves that are anti-plane surface waves. By the highly anisotropic surface elasticity model we mean the model with a surface strain energy density which depends on incomplete set of second derivatives of displacements. From the physical point of view this model corresponds to a coating made of a family of parallel long fibers which posses bending and extensional stiffness in one direction only. As for other models with surface energy there exist anti-plane surface waves. In the paper the dispersion relation is derived and dependence on the material parameters is analyzed.

1 Introduction

Surface waves constitute a well-known and rather developed branch of the mechanics. They play an important role in the both solid and fluid mechanics, see, e.g., Achenbach [2], Whitham [35], Goldstein and Maugin [21]. For example, such waves are used in acoustoelectronics as they may bring information on the material structure and its properties in the vicinity of the free surface, see Ewing et al. [17], Überall [32]. Thank to recent advances in nanotechnologies the interest to modelling of materials and structures at the nanoscale is growing. Among various extensions of the standard continuum mechanics the surface elasticity models by Gurtin and Murdoch [23, 24] and by Steigmann and Ogden [28, 29] found many applications, see, e.g., Duan et al. [8], Wang et al. [34], Eremeyev [9], Han et al. [25], Zemlyanova and

V. A. Eremeyev (✉)
Faculty of Civil and Environmental Engineering, Gdańsk University of Technology, ul. Gabriela Narutowicza 11/12, 80-233 Gdańsk, Poland
e-mail: victor.eremeev@pg.edu.pl; eremeyev.victor@gmail.com

Southern Federal University, Milchakova str. 8a, 344090 Rostov on Don, Russia

Southern Scientific Center of RASci, Chekhova str. 41, 344006 Rostov on Don, Russia

M. A. Sumbatyan (ed.), *Wave Dynamics, Mechanics and Physics of Microstructured Metamaterials*, Advanced Structured Materials 109,
https://doi.org/10.1007/978-3-030-17470-5_1

Mogilevskaya [37]. Within these models the surface stresses are introduced which generalize the surface tension for solids. As for many generalized media models, the surface stresses may significantly change the mathematical properties of solutions of corresponding boundary-value problems, see Eremeyev and Lebedev [13].

The paper is organized as follows. First, motivating by discrete model of polymeric brushes consisted of rigid chains, see the seminal paper by Stockmayer [30] and recent works by Gerasimov et al. [18–20], we propose the so-called reduced surface elasticity model. Then we recall the solution form for anti-plane deformations of a half-space. It is well-known that within the classic linear elasticity anti-plane surface waves in an elastic halfspace do not exist, see, e.g., Achenbach [2]. For extended models of continua such waves may exist, see Eremeyev et al. [14, 16] for the surface elasticity and Vardoulakis and Georgiadis [33], Yerofeyev and Sheshenina [36], Gourgiotis and Georgiadis [22] for the strain gradient elasticity. Using the least action principle, we derive the corresponding boundary conditions. Finally, we present the dispersion relations.

2 Constitutive Relations

Let us consider an elastic solid occupying volume V with the boundary $S = \partial V$. In what follows we consider infinitesimal deformations, so the kinematics is based on the displacement field

$$\mathbf{u} = \mathbf{u}(\mathbf{x}, t), \tag{1}$$

where $\mathbf{x}$ is the position vector and t is time. In Cartesian coordinates x_k, $k = 1, 2, 3$, (1) takes the form

$$u_k = u(x_1, x_2, x_3, t)$$

with $\mathbf{u} = \mathbf{u}_k \mathbf{i}_k$. Here $\mathbf{i}_k$ are Cartesian base vectors and the Einstein summation rule is utilized. In what follows we use the direct (coordinate-free) tensor analysis as described in Lebedev et al. [26], Eremeyev et al. [15].

For simplicity we consider an isotropic material in the bulk. So we have the following constitutive equations

$$\mathscr{W} = \mu \mathbf{e} : \mathbf{e} + \frac{1}{2}\lambda (\operatorname{tr} \mathbf{e})^2, \tag{2}$$

$$\mathscr{K} = \frac{1}{2}\rho \dot{\mathbf{u}} \cdot \dot{\mathbf{u}}, \tag{3}$$

$$\boldsymbol{\sigma} \equiv \frac{\partial \mathscr{W}}{\partial \mathbf{e}} = 2\mu \mathbf{e} + \lambda \mathbf{I} \operatorname{tr} \mathbf{e}, \tag{4}$$

where $\mathscr{W}$ and $\mathscr{K}$ are the strain energy and kinetic energy densities, λ and μ are Lamé elastic moduli, $\boldsymbol{\sigma}$ is the stress tensor, $\mathbf{e}$ is the linear strain tensor,

$$\mathbf{e} = \frac{1}{2}\left(\nabla\mathbf{u} + (\nabla\mathbf{u})^T\right), \quad \nabla\mathbf{u} = \frac{\partial u_j}{\partial x_i}\mathbf{i}_i \otimes \mathbf{i}_j,$$

"tr" is the trace operator, and ρ is the mass density. The overdot stands for the derivative with respect to t, the superscript "T" means the transpose operation,":" denotes the scalar product of second-order tensors, ∇ is the 3D nabla operator, and "$\otimes$" stands for dyadic product. In what follows for brevity we use the notation $\frac{\partial}{\partial x_j} = \partial_j$, so, for example, $\nabla\mathbf{u} = \partial_j u_i \mathbf{i}_j \otimes \mathbf{i}_i$.

Within the surface elasticity in addition to the constitutive equations in the bulk, we introduce the surface strain energy and the surface kinetic energy. For example, within the Gurtin–Murdoch linear isotropic model the strain energy is given by

$$\mathscr{W}_s = \mu_s\boldsymbol{\varepsilon} : \boldsymbol{\varepsilon} + \frac{1}{2}\lambda_s(\operatorname{tr}\boldsymbol{\varepsilon})^2, \tag{5}$$

$$\mathbf{s} \equiv \frac{\partial \mathscr{W}_s}{\partial \boldsymbol{\varepsilon}} = \mu_s\boldsymbol{\varepsilon} + \lambda_s(\operatorname{tr}\boldsymbol{\varepsilon})\mathbf{P}, \tag{6}$$

$$\boldsymbol{\varepsilon} = \frac{1}{2}\left(\mathbf{P}\cdot(\nabla_s\mathbf{u}) + (\nabla_s\mathbf{u})^T\cdot\mathbf{P}\right), \tag{7}$$

where λ_s and μ_s are the surface elastic moduli called also surface Lamé moduli, $\nabla_s \equiv \mathbf{P}\cdot\nabla$ is the surface nabla operator, $\mathbf{P} \equiv \mathbf{I} - \mathbf{n}\otimes\mathbf{n}$ is the surface unit second-order tensor, $\mathbf{n}$ is the unit vector of outer normal to S, and $\boldsymbol{\varepsilon}$ is the infinitesimal surface strain tensor, see Gurtin and Murdoch [23].

The linear isotropic model by Steigmann–Ogden is based on the following constitutive equation

$$\mathscr{W}_s = \mu_s\boldsymbol{\varepsilon} : \boldsymbol{\varepsilon} + \frac{1}{2}\lambda_s(\operatorname{tr}\boldsymbol{\varepsilon})^2 + \kappa_s\boldsymbol{\varkappa} : \boldsymbol{\varkappa} + \frac{1}{2}\zeta_s(\operatorname{tr}\boldsymbol{\varkappa})^2, \tag{8}$$

$$\mathbf{s} \equiv \frac{\partial \mathscr{W}_s}{\partial \boldsymbol{\varepsilon}} = \mu_s\boldsymbol{\varepsilon} + \lambda_s(\operatorname{tr}\boldsymbol{\varepsilon})\mathbf{P}, \quad \mathbf{m} \equiv \frac{\partial \mathscr{W}_s}{\partial \boldsymbol{\varkappa}} = \kappa_s\boldsymbol{\varkappa} + \zeta_s(\operatorname{tr}\boldsymbol{\varkappa})\mathbf{P}, \tag{9}$$

$$\boldsymbol{\varkappa} = \frac{1}{2}(\nabla_s\boldsymbol{\vartheta}\cdot\mathbf{A} + \mathbf{A}\cdot\nabla_s\boldsymbol{\vartheta}^T), \quad \boldsymbol{\vartheta} = \nabla_s w + \mathbf{B}\cdot\mathbf{u}, \tag{10}$$

where κ_s and ζ_s are additional surface stiffness parameters related to the surface bending stiffness, $\mathbf{s}$ and $\mathbf{m}$ are the surface stress and surface couple stress tensors, respectively, $w = \mathbf{u}\cdot\mathbf{n}$ and $\mathbf{B} = -\nabla_s\mathbf{n}$ is the tensor of curvature, see, e.g., Eremeyev and Lebedev [13], Zemlyanova and Mogilevskaya [37], Han et al. [25].

In this paper we use another model of surface elasticity. We consider an elastic coating made of ordered polymeric chains attached along the surface. Chains interact each other and with the substrate according to the Stockmayer potential introduced by Stockmayer [30]. For the theory of polymeric brushes we refer to the recent works by Gerasimov et al. [18–20] and the reference therein. From the mechanical point

of view such coating can be represented as a discrete system of parallel long chains connected through elastic hinges or long flexible fibers. For simplicity let us assume that the fibers are oriented along x_1-axis. Using the same argumentation as presented by Boutin et al. [5], dell'Isola et al. [6], Placidi et al. [27], Turco [31], dell'Isola et al. [7] we obtain the surface strain energy density in the form

$$\mathscr{W}_s = \frac{1}{2}\boldsymbol{\varkappa} : \mathbf{K}_s : \boldsymbol{\varkappa} + \frac{1}{2}\nabla_s\nabla_s\mathbf{u} \therefore \mathbf{K}_s \therefore \nabla_s\nabla_s\mathbf{u}, \tag{11}$$

where "$\therefore$" is the triple contraction operation, $\mathbf{K}_s$ and $\mathbf{K}_b$ are the stiffness tensors of fourth- and six-order, respectively. $\mathbf{K}_s$ and $\mathbf{K}_b$ relate to the extension/compression and bending stiffness properties, respectively. Here these tensors are singular and the surface energy density is degenerated as in the 3D reduced strain gradient elasticity, see Eremeyev and dell'Isola [12]. So we may call the proposed model the reduced surface strain gradient elasticity.

In order to describe surface dynamics, we take into account the mass density associated with the surface where surface stresses are defined, as in Gurtin and Murdoch [24]. So the dynamic properties are described through the surface kinetic energy density given by

$$\mathscr{K}_s = \frac{1}{2}m\dot{\mathbf{u}} \cdot \dot{\mathbf{u}}\big|_{\mathbf{x}\in S}, \tag{12}$$

where m is the surface mass density of S. Equation (12) means that we neglect here the rotatory inertia related to the surface elasticity.

The motion equations and natural boundary equations can be derived using the Hamilton variational principle

$$\delta\mathscr{H} = 0 \tag{13}$$

with the functional

$$\mathscr{H} = \int_0^T \int_V (\mathscr{K} - \mathscr{W})\, dV\, dt + \int_0^T \int_{\partial V} (\mathscr{K}_s - \mathscr{W}_s)\, da\, dt, \tag{14}$$

see Berdichevsky [4] for the general statements, and Abali et al. [1], Auffray et al. [3], Eremeyev et al. [14, 16] for generalized continua with surface energy. In what follows we consider the boundary-value problems for the anti-plane deformations.

3 Anti-plane Motions of an Elastic Half-Space

In order to demonstrate some peculiarities of the model let us consider the propagation of the surface anti-plane waves. Earlier such analysis was performed within the Gurtin–Murdoch model by Eremeyev et al. [14] and it was compared with the

Toupin–Mindlin strain gradient elasticity by Eremeyev et al. [16]. Following these works, let us consider an elastic half-space $x_3 \leq 0$. The anti-plane motions have one of the forms, see Achenbach [2],

$$\mathbf{u} = u_1(x_2, x_3, t)\mathbf{i}_1, \quad \text{or} \quad \mathbf{u} = u_2(x_1, x_3, t)\mathbf{i}_2, \tag{15}$$

which correspond two different direction of wave propagation.

With (15) the general motion equations reduce into two wave equations with respect to u_1 and u_2, respectively,

$$\mu(\partial_2^2 + \partial_3^2)u_1 = \rho\partial_t^2 u_1, \tag{16}$$
$$\mu(\partial_1^2 + \partial_3^2)u_2 = \rho\partial_t^2 u_2. \tag{17}$$

Here ∂_t stands for the derivative with respect to t.

Making standard assumption on steady-state behaviour, we are looking for solution of (16) and (17) in the form

$$u_\alpha = U_\alpha(x_\beta, x_3)\exp(i\omega t), \quad \alpha = 1, 2, \beta = 2, 1, \tag{18}$$

where ω is a circular frequency, i is the imaginary unit, and U_α is a amplitude. As a result, (16) and (17) transform into

$$\mu(\partial_2^2 + \partial_3^2)U_1 = -\rho\omega_t^2 U_1, \tag{19}$$
$$\mu(\partial_1^2 + \partial_3^2)U_2 = -\rho\omega^2 U_2. \tag{20}$$

Decaying with the depth solutions of (19) and (20) are given by the following formulae

$$U_1 = U_{01}\exp(\varkappa x_3)\exp(ikx_2), \quad U_2 = U_{02}\exp(\varkappa x_3)\exp(ikx_1), \tag{21}$$

where

$$\varkappa = \varkappa(k, \omega) \equiv \left(k^2 - \frac{\rho}{\mu}\omega^2\right)^{1/2},$$

k is a wavenumber and $U_{0\alpha}$ are constants. Nontrivial solutions (21) exist if they verify the corresponding boundary conditions at $x_3 = 0$. The latter will lead to a dispersion relation that is a certain relation between k and ω. For example, for the classic linear elasticity we have the boundary condition

$$\mu\partial_3 u_\alpha = 0, \tag{22}$$

from which it follows that $U_{0\alpha}$ vanish and so anti-plane surface waves do not exist, see Achenbach [2].

The situation with the surface anti-plane waves is completely different for the media with surface energy, see Vardoulakis and Georgiadis [33], Gourgiotis and Georgiadis [22], Eremeyev et al. [14, 16]. Under the anti-plane deformations $\mathscr{W}_s$ takes the simpler form

$$\mathscr{W}_s = \frac{1}{2}\mathbb{K}_s[(\partial_2 u_1)^2 + (\partial_1 u_2)^2] + \frac{1}{2}\mathbb{K}_b(\partial_1^2 u_2)^2, \tag{23}$$

whereas the kinetic energy is given by

$$\mathscr{K}_s = \frac{m}{2}\left[(\partial_t u_1)^2 + (\partial_t u_2)^2\right]. \tag{24}$$

In (23) we chosen x_1-axis as the direction of chains. So the highly anisotropic properties of the medium is obvious.

Using the least action principle in the form (13) and (14) with constitutive functions (23) and (24) we get the following natural boundary conditions for anti-plane motions

$$\mu\partial_3 u_1 = -m\partial_t^2 u_1 + \mathbb{K}_s\partial_2^2 u_1, \tag{25}$$
$$\mu\partial_3 u_2 = -m\partial_t^2 u_2 + \mathbb{K}_s\partial_2^2 u_2 - \mathbb{K}_b\partial_2^4 u_2, \tag{26}$$

which correspond to (16) and (17), respectively. Note that with $\mathbb{K}_s = \mu_s$ Eq. (25) corresponds to the Gurtin-Murdoch model in the case of of anti-plane deformations, see Eremeyev et al. [14], whereas with $\mathbb{K}_b = \zeta_s$ Eq. (26) includes additional term describing the bending energy as in the linear Steigmann–Ogden model, cmp. Steigmann and Ogden [28]. Equation (26) is a special case of the weakly nonlocal models of surface elasticity introduced in Eremeyev [10]. So we have different boundary conditions at the free surface depending on the direction of the surface wave propagation.

In order to derive the dispersion relations we substitute (21) into (25) and (26) and get

$$\mu\varkappa(k,\omega) = m\omega^2 - \mathbb{K}_s k^2, \tag{27}$$
$$\mu\varkappa(k,\omega) = m\omega^2 - \mathbb{K}_s k^2 + \mathbb{K}_b k^4. \tag{28}$$

Introducing the phase velocity $c = \omega/k$ we transform (27) and (28) into

$$c^2 = c_s^2 + \frac{\mu}{m}\frac{1}{|k|}\sqrt{1 - \frac{c^2}{c_T^2}}, \tag{29}$$

$$c^2 = c_s^2 + \frac{\mathbb{K}_b}{m}k^2 + \frac{\mu}{m}\frac{1}{|k|}\sqrt{1 - \frac{c^2}{c_T^2}}, \tag{30}$$

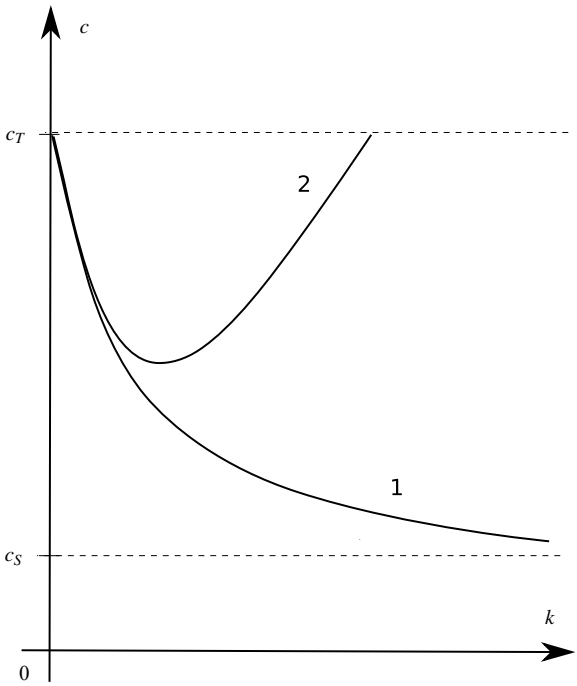

Fig. 1 Dispersion curves. Curves 1 and 2 correspond to Eqs. (29) and (30), respectively

where $c_T = \sqrt{\mu/\rho}$ is the phase velocity of transverse waves and $c_s = \sqrt{\mathbb{K}_s/m}$ is the shear wave velocity in the thin film associated with the Gurtin–Murdoch model. Dispersion relations (29) and (28) were analyzed in details by Eremeyev et al. [14] and by Eremeyev [10], respectively. Let us note that the presence of the term $\mathbb{K}_b k^4$ in (28) changes dramatically the behaviour of dispersion curves, see Fig. 1 for details. Here $\overline{\mathbb{K}}_b$ is normalized dimensionless value of the bending stiffness. In Fig. 1 $\overline{\mathbb{K}}_b = 0.0001$.

4 Conclusions

Here we discuss the propagation of anti-plane surface waves in media with highly anisotropic surface energy. Unlike the models by Gurtin and Murdoch [23, 24] and by Steigmann and Ogden [28, 29] the considered model constitute an intermediate class of surface elasticity constitutive equations. It can be treated as as one-dimensional extension of the Gurtin-Murdoch model towards Steigmann-Ogden model of surface elasticity. Indeed, here the surface strain energy is similar to one-dimensional version of the Steigmann-Ogden model but applied to two-dimensional structure. Following Eremeyev and dell'Isola [12] it could be called the two-dimensional reduced strain gradient model. Such model was applied to modeling of pantographic beam lattices, see, e.g., Boutin et al. [5], dell'Isola et al. [6], and current reviews by Placidi et al.

[27], dell'Isola et al. [7]. Considering anti-plane motions within the proposed model the dispersion relations are derived. In particular, it was shown that the dispersion properties depend on the direction of the wave propagation. Some preliminary results were discussed by Eremeyev [11].

Acknowledgements The author acknowledges financial support from the Russian Science Foundation under the grant "*Methods of microstructural nonlinear analysis, wave dynamics and mechanics of composites for research and design of modern metamaterials and elements of structures made on its base*" (No. 15-19-10008-P).

References

1. Abali, B.E., Müller, W.H., dell'Isola, F.: Theory and computation of higher gradient elasticity theories based on action principles. Arch. Appl. Mech. **87**(9), 1495–1510 (2017)
2. Achenbach, J.: Wave Propagation in Elastic Solids. North Holland, Amsterdam (1973)
3. Auffray, N., dell'Isola, F., Eremeyev, V.A., Madeo, A., Rosi, G.: Analytical continuum mechanics à la Hamilton-Piola least action principle for second gradient continua and capillary fluids. Math. Mech. Solids **20**(4), 375–417 (2015)
4. Berdichevsky, V.: Variational Principles of Continuum Mechanics: I. Fundamentals. Springer, Heidelberg (2009)
5. Boutin, C., dell'Isola, F., Giorgio, I., Placidi, L.: Linear pantographic sheets: asymptotic micro-macro models identification. Math. Mech. Complex Syst. **5**(2), 127–162 (2017)
6. dell'Isola, F., Giorgio, I., Pawlikowski, M., Rizzi, N.: Large deformations of planar extensible beams and pantographic lattices: heuristic homogenisation, experimental and numerical examples of equilibrium. Proc. R. Soc. Lond. Ser. A **472**(2185), 20150,790 (2016)
7. dell'Isola, F., Seppecher, P., Alibert, J.J., Lekszycki, T., Grygoruk, R., Pawlikowski, M., Steigmann, D., Giorgio, I., Andreaus, U., Turco, E., Gołaszewski, M., Rizzi, N., Boutin, C., Eremeyev, V.A., Misra, A., Placidi, L., Barchiesi, E., Greco, L., Cuomo, M., Cazzani, A., Corte, A.D., Battista, A., Scerrato, D., Eremeeva, I.Z., Rahali, Y., Ganghoffer, J.F., Müller, W., Ganzosch, G., Spagnuolo, M., Pfaff, A., Barcz, K., Hoschke, K., Neggers, J., Hild, F.: Pantographic metamaterials: an example of mathematically driven design and of its technological challenges. Continuum Mech. Thermodyn. 1–34 (2018). https://doi.org/10.1007/s00161-018-0689-8
8. Duan, H.L., Wang, J., Karihaloo, B.L.: Theory of elasticity at the nanoscale. In: Advances in Applied Mechanics, vol. 42, pp. 1–68. Elsevier (2008)
9. Eremeyev, V.A.: On effective properties of materials at the nano-and microscales considering surface effects. Acta Mech. **227**(1), 29–42 (2016)
10. Eremeyev, V.A.: On nonlocal surface elasticity and propagation of surface anti-plane waves. In: Altenbach, H., Goldstein, R.V., Murashkin, E. (eds.) Mechanics for Materials and Technologies, pp. 153–162. Springer International Publishing, Cham (2017)
11. Eremeyev, V.A.: On the peculiarities of anti-plane surface waves propagation for media with microstructured coating. In: MATEC Web of Conferences, EDP Sciences, vol. 226, p. 03020 (2018)
12. Eremeyev, V.A., dell'Isola, F.: A note on reduced strain gradient elasticity. In: Altenbach, H., Pouget, J., Rousseau, M., Collet, B., Michelitsch, T. (eds.) Generalized Models and Non-classical Approaches in Complex Materials 1, pp. 301–310. Springer International Publishing, Cham (2018)
13. Eremeyev, V.A., Lebedev, L.P.: Mathematical study of boundary-value problems within the framework of Steigmann-Ogden model of surface elasticity. Continuum Mech. Thermodyn. **28**(1–2), 407–422 (2016)

14. Eremeyev, V.A., Rosi, G., Naili, S.: Surface/interfacial anti-plane waves in solids with surface energy. Mech. Res. Commun. **74**, 8–13 (2016)
15. Eremeyev, V.A., Cloud, M.J., Lebedev, L.P.: Applications of Tensor Analysis in Continuum Mechanics. World Scientific, New Jersey (2018a)
16. Eremeyev, V.A., Rosi, G., Naili, S.: Comparison of anti-plane surface waves in strain-gradient materials and materials with surface stresses. Math. Mech. Solids (2018b). https://doi.org/10.1177/1081286518769960
17. Ewing, W.M., Jardetzky, W.S., Press, F.: Elastic Waves in Layered Media. McGraw-Hill Book Company, New York (1957)
18. Gerasimov, R.A., Eremeyev, V.A., Petrova, T.O., Egorov, V.I., Maksimova, O.G., Maksimov, A.V.: Computer simulation of the mechanical properties of metamaterials. J. Phys. Conf. Ser. **738**(1), 012,100 (2016)
19. Gerasimov, R.A., Eremeyev, V.A., Petrova, T.O., Egorov, V.I., Maksimova, O.G., Maksimov, A.V.: Study of mechanical properties of ferroelectrics metamaterials using computer simulation. Ferroelectrics **508**(1), 151–160 (2017a)
20. Gerasimov, R.A., Maksimova, O.G., Petrova, T.O., Eremeyev, V.A., Maksimov, A.V.: Analytical and computer methods to evaluate mechanical properties of the metamaterials based on various models of polymeric chains. In: Wave Dynamics and Composite Mechanics for Microstructured Materials and Metamaterials, pp. 35–69. Springer, Singapore (2017b)
21. Goldstein, R.V., Maugin, G.A.: Surface Waves in Anisotropic and Laminated Bodies and Defects Detection, NATO ASI. Springer (2004)
22. Gourgiotis, P., Georgiadis, H.: Torsional and SH surface waves in an isotropic and homogenous elastic half-space characterized by the Toupin-Mindlin gradient theory. Int. J. Solids Struct. **62**, 217–228 (2015)
23. Gurtin, M.E., Murdoch, A.I.: A continuum theory of elastic material surfaces. Arch. Ration Mech. Anal. **57**(4), 291–323 (1975)
24. Gurtin, M.E., Murdoch, A.I.: Surface stress in solids. Int. J. Sol. Struct. **14**(6), 431–440 (1978)
25. Han, Z., Mogilevskaya, S.G., Schillinger, D.: Local fields and overall transverse properties of unidirectional composite materials with multiple nanofibers and Steigmann-Ogden interfaces. Int. J. Solids Struct. **147**, 166–182 (2018)
26. Lebedev, L.P., Cloud, M.J., Eremeyev, V.A.: Tensor Analysis with Applications in Mechanics. World Scientific, New Jersey (2010)
27. Placidi, L., Barchiesi, E., Turco, E., Rizzi, N.L.: A review on 2D models for the description of pantographic fabrics. Z. Angew. Math. Phys. **67**(5), 121 (2016)
28. Steigmann, D.J., Ogden, R.W.: Plane deformations of elastic solids with intrinsic boundary elasticity. Proc. R. Soc. A **453**(1959), 853–877 (1997)
29. Steigmann, D.J., Ogden, R.W.: Elastic surface-substrate interactions. Proc. R. Soc. A **455**(1982), 437–474 (1999)
30. Stockmayer, W.H.: Theory of molecular size distribution and gel formation in branched-chain polymers. J. Chem. Phys. **11**(2), 45–55 (1943)
31. Turco, E.: Discrete is it enough? The revival of Piola-Hencky keynotes to analyze three-dimensional Elastica. Continuum Mech. Thermodyn. **30**(5), 1039–1057 (2018)
32. Überall, H.: Surface waves in acoustics. In: Mason, W.P., Thurston, R.N. (eds.) Physical Acoustics, vol. X. Academic Press, New York (1973)
33. Vardoulakis, I., Georgiadis, H.G.: SH surface waves in a homogeneous gradient-elastic half-space with surface energy. J. Elast. **47**(2), 147–165 (1997)
34. Wang, J., Huang, Z., Duan, H., Yu, S., Feng, X., Wang, G., Zhang, W., Wang, T.: Surface stress effect in mechanics of nanostructured materials. Acta. Mech. Solida Sin. **24**, 52–82 (2011)
35. Whitham, G.B.: Linear and Nonlinear Waves. Wiley, New York (1999)
36. Yerofeyev, V.I., Sheshenina, O.A.: Waves in a gradient-elastic medium with surface energy. J. Appl. Math. Mech. **69**(1), 57–69 (2005)
37. Zemlyanova, A.Y., Mogilevskaya, S.G.: Circular inhomogeneity with Steigmann-Ogden interface: local fields, neutrality, and Maxwell's type approximation formula. Int. J. Solids Struct. **135**, 85–98 (2018)

Periodic Problem for a Plane Composed of Two-Layer Strips with a System of Longitudinal Internal Inclusions and Cracks

V. N. Hakobyan, A. V. Sahakyan and K. L. Aghayan

Abstract The paper considers plane deformation state of a piecewise homogeneous uniformly layered plane of two dissimilar materials, when there is a system of cracks on the midlines of layers made of one material, and layers made of the other material are reinforced by a system of elastic inclusions also located on the midlines. A system of governing equations of the problem is obtained in the form of a system of singular integral and integro-differential equations for the dislocation function of the points of the cracks faces and tangential contact stresses acting on the long sides of the inclusions. The solutions of the obtained systems are constructed by the method of mechanical quadrature. A numerical calculation was carried out and the laws of change in the coefficients of concentration of destructive stresses at the end points of cracks and contact stresses were studied depending on the mechanical and geometric parameters of the problem.

1 Introduction

The study of the plane deformation state of an elastic homogeneous plane with periodic and doubly periodic defects of the type of cracks, fully or partially linked to the matrix of elastic or absolutely rigid inclusions, has been the subject of many works. This direction in the field of mixed and contact problems of the theory of elasticity began to develop in the second half of the twentieth century. On the basis of powerful methods of the mathematical theory of elasticity and mathematical physics, closed or effective solutions were obtained for a number of important periodic and

V. N. Hakobyan · A. V. Sahakyan (✉) · K. L. Aghayan
Institute of Mechanics, National Academy of Sciences, Yerevan, Armenia
e-mail: avsahakyan@gmail.com

V. N. Hakobyan
e-mail: vhakobyan@sci.am

K. L. Aghayan
e-mail: karo.aghayan@gmail.com

M. A. Sumbatyan (ed.), *Wave Dynamics, Mechanics and Physics of Microstructured Metamaterials*, Advanced Structured Materials 109,
https://doi.org/10.1007/978-3-030-17470-5_2

doubly periodic problems. The main results in this direction are summarized in monographs [1–3].

As for the study of periodic and doubly periodic problems for piecewise-homogeneous, uniformly layered bodies with interfacial or internal defects, which, in our opinion, are currently very relevant from the point of view of layered composites, as we know, not so much work is devoted. Of these, we point out the works [4–8], which are closely related to the studies conducted here. In [4] constructed discontinuous solutions of the equations of the plane theory of elasticity for a piecewise homogeneous layered plane containing interface doubly periodic defects, on the basis of which the plane deformation state was considered to be piecewise homogeneous layered plane with a doubly periodic system of interface cracks. A similar problem in the case of a doubly periodic system of absolutely rigid inclusions was studied in [5]. In [6], the plane deformation state of a piecewise-homogeneous layered plane with a periodic system of parallel internal cracks was investigated. The interaction of stringers with an infinite plate weakened by a doubly periodic system of cracks was investigated in [8].

2 Problem Statement and Derivation of the Governing Equations

Suppose we have a piecewise-uniform elastic plane, made by alternately connecting layers of thickness $2h$ from two dissimilar materials. The abscissa axis of the Cartesian coordinate system Oxy is directed along the dividing line of materials. On median lines of dissimilar layers $y = (4n + 1)h$ and $y = (4n - 1)h (n \in Z)$ on systems of intervals $L_1 = \bigcup_{j=1}^{N} (a_j, b_j)$ and $L_2 = \bigcup_{j=1}^{M} (c_j, d_j)$ are located cracks and elastic thin inclusions of thickness h_j and reduced elastic moduli $E_I^{(j)} = E_j / \left(1 - v_j^2\right) (j = 1, M)$ respectively. We assume that the plane is deformed under the influence of distributed loads $p_j(x)$, applied to the cracks (a_j, b_j) $(j = 1, N)$, concentrated loads $P_0^{(j)} (j = 1, M)$ applied to inclusions at points $x_0^{(j)} \in [c_j, d_j]$ $(j = 1, M)$ and uniformly distributed loads q_1 and q_2, applied to the layers at infinity (Fig. 1).

Obviously, with this formulation of the problem, the lines $y = (2n + 1)h$ $(n \in Z)$ are lines of symmetry. As a result, the stated problem can be formulated as a problem for a piecewise homogeneous layer (base cell) occupying the region $\Omega\{-\infty < x < \infty; |y| \le h\}$, on the boundaries $y = \pm h$ of which outside cracks and inclusions, symmetry conditions are specified, on L_1 normal stresses are specified, and on L_2 contact conditions of inclusion with a base are specified. Here, the inclusions are interpreted as one-dimensional continua, which under the influence of concentrated loads applied to them and tangential contact stresses are in a uniaxial stress state [9]. Also, we assume that due to the smallness of the thickness of inclu-

sions and the symmetry of the problem with respect to the axes of the inclusions, the vertical displacements of the points of the inclusions are zero.

The task is to determine the patterns of change in the tangential contact stresses acting on the long sides of the inclusions, crack opening and intensity factors of the fracture stresses at the end points of the cracks depending on the mechanical and geometric parameters.

Based on this assumptions, we will have the following conditions on L_1 and L_2:

$$\tau_{xy}^{(1)}(x,h)=0;\quad \sigma_y^{(1)}(x,h)=-p_j(x)\quad \left(a_j<x<b_j,\quad j=1,N\right) \tag{1}$$

$$V_2(x,-h)=0;\quad \frac{dU_2(x,-h)}{dx}=\varepsilon_j(x)\quad \left(c_j<x<d_j,\quad j=1,M\right) \tag{2}$$

where $\tau_{xy}^{(1)}(x,y)$ and $\sigma_y^{(1)}(x,y)$—are the stress components in the upper layer, $V_2(x,y)$ and $U_2(x,y)$—are vertical and horizontal displacements of points of the lower layer, $\varepsilon_j(x)$—is the axial deformation jth inclusion.

To derive the system of governing equations of the problem, we introduce into consideration the unknown functions of displacements of the crack edge $V(x)$ and tangential contact stresses acting on the long sides of inclusions $\tau(x)$, and express the normal stresses and horizontal displacements of the points of the upper $(y=h;\,x\in L_1)$ and lower $(y=-h;\,x\in L_2)$ sides of the composite layer using these functions. To this end, using first conditions from (1) and (2), we consider the following auxiliary boundary value problem:

$$\begin{aligned}
&\sigma_y^{(1)}(x,0)=\sigma_y^{(2)}(x,0);\ \tau_{xy}^{(1)}(x,0)=\tau_{xy}^{(2)}(x,0);\quad (-\infty<x<\infty)\\
&U_1(x,0)=U_2(x,0);\ V_1(x,0)=V_2(x,0);\quad (-\infty<x<\infty)\\
&V_1(x,h)=-V(x);\ (x\in L_1);\ V_1(x,h)=0;\quad (x\notin L_1)\\
&\tau_{xy}^{(1)}(x,h)=0;\quad (-\infty<x<\infty)\\
&\tau_{xy}^{(2)}(x,h)=\tau(x)\ (x\in L_2);\quad \tau_{xy}^{(2)}(x,-h)=0\quad (x\notin L_2);\\
&V_2(x,-h)=0\quad (-\infty<x<\infty),
\end{aligned} \tag{3}$$

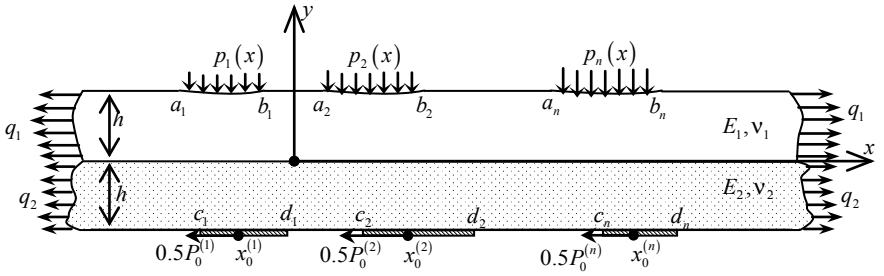

Fig. 1 Schematic representation of the problem

Here, the index $j = 1, 2$ denotes the components of displacements and stresses, respectively, in the upper and lower layers.

To solve the auxiliary boundary-value problem (3), we represent the biharmonic stress functions for each of the heterogeneous layers in the form of Fourier integrals

$$F_j(x, y) = \int_{-\infty}^{\infty} \left[A_j(s)\mathrm{ch}\, sy + B_j(s)\mathrm{sh}\, sy + sy\big(C_j(s)\mathrm{ch}\, sy + D_j(s)\mathrm{sh}\, sy\big)\right]e^{isx}ds + \frac{q_j}{2}y^2; \quad \big(-\infty < x < \infty;\ 0 \le (-1)^{j+1}y \le h;\ j = 1, 2\big), \tag{4}$$

where $A_j, B_j, D_j, C_j (j = 1, 2)$—are unknown coefficients to be determined.

Using the well-known relations connecting the biharmonic functions with stresses and displacements, we satisfy conditions (3) and determine unknown coefficients through the Fourier transforms of the derivative of the crack opening $\bar{V}'(s)$ and tangential contact stresses $\bar{\tau}(s)$, we obtain:

$$A_1(s) = A_2(s) = -\frac{2(1-\nu_1)}{1-\mu_*}D_1(s) + \frac{2\mu_*(1-\nu_2)}{1-\mu_*}D_2(s);$$

$$B_1(s) = \frac{1-2\nu_1+\mu_*}{1-\mu_*}C_1(s) - \frac{2\mu_*(1-\nu_2)}{1-\mu_*}C_2(s);$$

$$B_2(s) = \frac{2(1-\nu_1)}{1-\mu_*}C_1(s) - \frac{1+\mu_*(1-2\nu_2)}{1-\mu_*}C_2(s);$$

$$C_1(s) = -\frac{i\mu_1}{s^2\Delta_1(s)\mathrm{ch}\, hs}\left[\frac{hs(\mu_*-1)\mathrm{cth}\, hs + \mu_* + 1 - 2\nu_1}{1-\nu_1}s\bar{V}'(s) - \mu_*\frac{\bar{\tau}(s)}{\mu_1}\right];$$

$$C_2(s) = \frac{2\mu_1 i}{s^2\Delta_2(s)\mathrm{ch}\, hs}\left\{s\bar{V}'(s) + \frac{\bar{\tau}(s)}{4\mu_1}\left[hs\mathrm{cth}\, hs\,\frac{\mu_*-1}{1-\nu_2} + \frac{1-2\nu_2-\mu_*(3-4\nu_2)}{1-\nu_2}\right]\right\};$$

$$D_1(s) = -\frac{i\mu_1}{s^2\Delta_1(s)\mathrm{sh}\, hs}\left\{2s\bar{V}'(s)\left[1 - \frac{\mu_*-1}{2(1-\nu_1)}hs\,\mathrm{th}\, hs\right] + \mu_*\frac{\bar{\tau}(s)}{\mu_1}\right\};$$

$$D_2(s) = \frac{i\mu_1}{s^2\Delta_2(s)\mathrm{sh}\, hs}\left\{2s\bar{V}'(s) + \frac{\bar{\tau}(s)}{\mu_1}\left[1 - \frac{1-\mu_*}{2(1-\nu_2)}hs\,\mathrm{th}\, hs\right]\right\};$$

where

$$\Delta_1(s) = (\mu_*-1)\frac{2hs}{\mathrm{sh}\, 2hs} + \mu_* + \kappa_1; \quad \mu_* = \frac{\mu_1}{\mu_2};$$

$$\Delta_2(s) = (\mu_*-1)\frac{2hs}{\mathrm{sh}\, 2hs} - 1 - \mu_*\kappa_2; \quad \kappa_j = 3 - 4\nu_j; \quad j = 1, 2;$$

$$\bar{V}'(s) = \frac{1}{2\pi}\int_{-\infty}^{\infty} V'(x)e^{-isx}dx; \quad \bar{\tau}(s) = \frac{1}{2\pi}\int_{-\infty}^{\infty} \tau(x)e^{-isx}dx$$

Note that the loads q_1 and q_2 must also satisfy the compatibility condition for the deformations of heterogeneous layers at infinity. In this case, it can be written in the form:

$$m_1 q_1 = m_2 q_2 \quad \left(m_j = \left(1 - \nu_j^2\right)/E_j;\ j = 1, 2\right). \tag{5}$$

Based on the obtained relations, we write out representations for normal stresses on the line $y = h$ and for the derivative of horizontal displacements on the line $y = -h$, which are necessary to satisfy the boundary conditions on the cracks and the sides of the inclusions:

$$\sigma_y^{(1)}(x, h) = \frac{\lambda_1}{\pi} \int\limits_{L_1} \frac{V'(s)ds}{s - x} + \int\limits_{L_1} R_{11}(x - s)V'(s)ds + \int\limits_{L_2} R_{12}(x - s)\tau(s)ds; \tag{6}$$

$$\frac{dU_2(x, -h)}{dx} = -\frac{\lambda_2}{\pi} \int\limits_{L_2} \frac{\tau(s)ds}{s - x} + \int\limits_{L_1} R_{21}(x - s)V'(s)ds - \int\limits_{L_2} R_{22}(x - s)\tau(s)ds + m_2 q_2 \tag{7}$$

Here the following notations are introduced:

$$R_{ij}(t) = \frac{1}{\pi} \int\limits_0^\infty K_{ij}(\xi) \sin(\xi t)d\xi; \quad \lambda_1 = \frac{\mu_1}{1 - \nu_1}; \quad \lambda_2 = \frac{\mu_* \kappa_2}{4\mu_1(1 - \nu_2)}\ (i, j = 1, 2);$$

$$K_{11}(s) = \frac{\mu_1}{(1 - \nu_1)}\left[\frac{2(hs)^2(\mu_* - 1)}{\operatorname{sh} 2hs\Delta_1(s)} - \frac{16\mu_*(1 - \nu_1)(1 - \nu_2)[1 - \nu_1 + \mu_*(1 - \nu_2)]}{(\mu_* - 1)\Delta_1(s)\Delta_2(s)} \operatorname{th} hs\right.$$
$$+ 4(1 - \nu_1)(1 - \nu_2)\left(\frac{1 - \nu_1}{1 - \nu_2} + \mu_*\right)\frac{\operatorname{sh} 2hs + 2hs}{(\operatorname{ch} 2hs - 1)\Delta_1(s)\Delta_2(s)}$$
$$\left. - \operatorname{th} hs \frac{(\mu_*^2 + (1 - 2\nu_1)^2 + 2\mu_*((1 - 2\nu_1)(2 - \nu_2) + 1 - \nu_2))}{(\mu_* - 1)\Delta_1(s)} + 1\right]$$

$$K_{12}(s) = -\frac{4\mu_*(1 - \nu_2)}{\Delta_1(s)\Delta_2(s)\operatorname{sh} 2hs}\left(\Delta_1(s) - \left(\mu_* + \frac{1 - \nu_1}{1 - \nu_2}\right)(1 + 2hs \operatorname{cth} 2hs)\right)$$

$$K_{21}(s) = -\frac{2\mu_*}{\operatorname{sh} 2hs}\left[\frac{1}{\Delta_1} + \frac{\kappa_2}{\Delta_2} + \left(\frac{\mu_* + \kappa_1}{\Delta_1} + \frac{1 + \mu_* \kappa_2}{\Delta_2}\right)\frac{\operatorname{ch} 2hs}{1 - \mu_*}\right]$$

$$K_{22}(s) = \frac{\mu_*}{\mu_1(\mu_* - 1)}\left[\frac{(hs)^2(\mu_* - 1)^2 + \frac{1}{2}\mu_*^2\kappa_2^2 + 1 - \nu_2 + \frac{1}{2}\kappa_2(1 - 2\nu_2)(1 - 2\mu_*)}{(1 - \nu_2)\Delta_2 \operatorname{sh} 2hs}\right.$$
$$\left. + \frac{4\mu_*(1 - \nu_1)}{\Delta_1 \operatorname{sh} 2hs} - \frac{(\mu_* - 1)\kappa_2(1 + \mu_* \kappa_2)}{2(1 - \nu_2)\Delta_2} \coth 2hs + \frac{(1 - \mu_*)\kappa_2}{2(1 - \nu_2)}\right]$$

We now turn to the derivation of the system of governing equations of the problem. For this, we use relations (6) and (7), and satisfy second parts of conditions on the crack (1) and inclusion (2).

As a result, taking into account that axial deformations of inclusions from loads applied at points $x_0^{(j)}$ are determined by the formula [9]:

$$\varepsilon_j(x) = \frac{1}{h_j E_I^{(j)}} \left[P_0^{(j)} H\left(x - x_0^{(j)}\right) - 2 \int_{c_j}^{x} \tau(s) ds \right] \quad \left(c_j \le x, x_0^{(j)} \le d_j, \ j = 1, M\right), \tag{8}$$

we come to the following system from $N + M$ singular integral and integro-differential equations:

$$\begin{cases} \dfrac{\lambda_1}{\pi} \displaystyle\int_{L_1} \frac{V'(s)ds}{s - x} + \int_{L_1} R_{11}(x - s)V'(s)ds + \int_{L_2} R_{12}(x - s)\tau(s)ds \\ \quad = -p_j(x) \quad \left(a_j < x < b_j, \quad j = 1, N\right) \\ -\dfrac{\lambda_2}{\pi} \displaystyle\int_{L_2} \frac{\tau(s)ds}{s - x} + \int_{L_1} R_{21}(x - s)V'(s)ds + \int_{L_2} R_{22}(x - s)\tau(s)ds + m_2 q_2 \\ \quad = \dfrac{1}{h_j E_I^{(j)}} \left[P_0^{(j)} H\left(x - x_0^{(j)}\right) - 2 \displaystyle\int_{c_j}^{x} \tau(s)ds \right] \quad \left(c_j \le x, x_0^{(j)} \le d_j, \quad j = 1, M\right) \end{cases} \tag{9}$$

Considering that $V'(x)$ and $\tau(x)$ are piecewise unknown functions with N and M components, the resulting system together with the conditions of continuity of displacements at the tips of cracks and the equilibrium conditions of inclusions

$$\int_{a_j}^{b_j} V'(s)ds = 0; \quad (j = 1, N); \quad \int_{c_j}^{d_j} \tau_j(s)ds = P_0^{(j)}/2; \quad (j = 1, M) \tag{10}$$

form a closed system for determining unknown components of functions $V'(x)$ and $\tau(x)$.

3 Solution of the System of Governing Equations

Solution of the system of Eq. (9) under conditions (10) can be constructed using the method of Chebyshev orthogonal polynomials, by reducing it to a quasi-completely regular system of algebraic equations [9]. However, more effective, in our opinion, is the method of mechanical quadratures [10], which we will use. Without loss of generality, we will assume that there is one crack and one inclusion in the base cell, which occupy intervals (a, b) and (c, d).

Turning to dimensionless quantities and introducing the notation

$$a_* = (b-a)/2h; \quad b_* = (b+a)/2h; \quad c_* = (d-c)/2h; \quad d_* = (d+c)/2h;$$

$$\varphi_1(t) = V'(h(a_*t + b_*)); \quad \varphi_2(t) = \frac{c_*\tau(h(c_*t + d_*))}{\mu_1};$$

$$R^*_{11}(t,\xi) = \frac{a_*}{\lambda_1}\int\limits_0^\infty K_{11}(\zeta)\sin(\zeta a_*(t-\xi))d\zeta;$$

$$R^*_{12}(t,\xi) = (1-\nu_1)\int\limits_0^\infty K_{12}(\zeta)\sin(\zeta(a_*t + b_* - c_*\xi - d_*))d\zeta;$$

$$R^*_{21}(t,\xi) = -\frac{4a_*c_*(1-\nu_2)}{\mu_*\kappa_2}\int\limits_0^\infty K_{21}(\zeta)\sin(\zeta(c_*t + d_* - a_*\xi - b_*))d\zeta;$$

$$R^*_{22}(t,\xi) = -\frac{c_*}{\lambda_2}\int\limits_0^\infty K_{22}(\zeta)\sin(\zeta c_*(t-\xi))d\zeta;$$

$$f_1(t) = -\pi p_1[h(a_*t + b_*)]/\lambda_1; \quad f_2(t) = \frac{2\pi c_* q_2\left(1-\nu_2^2\right)}{æ_2\mu_1};$$

$$P_0^* = \frac{P_0^{(1)}}{h\mu_1}; \quad \vartheta_* = \frac{2\pi h(1-\nu_2)c_*E_2}{h_1E_I^{(1)}(1+\nu_2)æ_2},$$

we obtain the following system of defining equations:

$$\begin{cases} \int\limits_{-1}^{1}\frac{\varphi_1(\xi)d\xi}{\xi-t} + \int\limits_{-1}^{1}R^*_{11}(t,\xi)\varphi_1(\xi)d\xi + \int\limits_{-1}^{1}R^*_{12}(t,\xi)\varphi_2(\xi)d\xi = f_1(t) \\ \int\limits_{-1}^{1}\frac{\varphi_2(\xi)d\xi}{\xi-t} + \int\limits_{-1}^{1}R^*_{21}(t,\xi)\varphi_1(\xi)d\xi + \int\limits_{-1}^{1}R^*_{22}(t,\xi)\varphi_2(\xi)d\xi = f_2(t) \\ -\vartheta_*\left[P_0^*H(t-t_0) - 2\int\limits_{-1}^{t}\varphi_2(\tau)d\tau\right] \quad (-1 < t < 1) \end{cases} \tag{11}$$

under conditions

$$\int\limits_{-1}^{1}\varphi_1(s)ds = 0; \quad \int\limits_{-1}^{1}\varphi_2(s)ds = \frac{P_0^*}{2}. \tag{12}$$

It is easy to establish that the desired functions at the end points of the integration interval have a root singularity. Therefore, they can be represented as:

$$\varphi_j(t) = \frac{\varphi_j^*(t)}{\sqrt{1-t^2}} \quad (j = 1, 2), \tag{13}$$

where $\varphi_j^*(t)(j=1,2)$ are continuous smooth functions bounded up to the ends of the interval $[-1,1]$, and can be replaced by interpolation polynomials of order $n-1$

$$\varphi_1^*(t)=\frac{1}{n}\sum_{i=1}^{n}\frac{X_i T_n(t)}{(t-x_i)U_{n-1}(x_i)};\quad \varphi_2^*(t)=\frac{1}{n}\sum_{i=1}^{n}\frac{Y_i T_n(t)}{(t-x_i)U_{n-1}(x_i)} \tag{14}$$

here $X_i, Y_i\left(i=\overline{1,n}\right)$ are unknown coefficients, $x_i=\cos\frac{(2i-1)\pi}{2n}\quad\left(i=\overline{1,n}\right)$ are the roots of Chebyshev polynomial of the first kind $T_n(x)$.

Further, according to the standard procedure from [10], we obtain the following closed system of linear algebraic equations for coefficients X_i and Y_i

$$\begin{cases}\displaystyle\sum_{i=1}^{n}\left[\left(\frac{1}{x_i-y_k}+R_{11}^*(y_k,x_i)\right)X_i+R_{12}^*(y_k,x_i)Y_i\right]=\frac{n}{\pi}f_1(y_k)\\ \displaystyle\sum_{i=1}^{n}\left[\left(\frac{1}{x_i-y_k}+Q_{22}^*(y_k,x_i)\right)Y_i+R_{21}^*(y_k,x_i)X_i\right]=\frac{n}{\pi}\left(f_2(y_k)-\vartheta_* H\left(y_k-t_0\right)\right)\\ \displaystyle\sum_{i=1}^{n}X_i=0\quad\left(k=\overline{1,n-1}\right)\\ \displaystyle\frac{\pi}{n}\sum_{i=1}^{n}Y_i=\frac{1}{2}\end{cases} \tag{15}$$

where $y_k=\cos\frac{k\pi}{n}\quad\left(k=\overline{1,n-1}\right)$ are the roots of Chebyshev polynomial of the second kind $U_{n-1}(x)$,

$$Q_{22}^*(y_k,x_i)=R_{22}^*(y_k,x_i)-\frac{2\vartheta_*}{\pi}\left(\arcsin y_k+\frac{\pi}{2}-2\sqrt{1-y_k^2}\sum_{m=1}^{n-1}\frac{T_m(x_i)U_{m-1}(y_k)}{m}\right).$$

After determining the coefficients $X_i, Y_i\left(i=\overline{1,n}\right)$ from the system (15), it is more convenient to restore the polynomials (14), interpolating functions $\varphi_j^*(t)$, by the formulas

$$\varphi_{\{1,2\}}^*(t)=\frac{1}{n}\sum_{i=1}^{n}\{X_i,Y_i\}\left[1+2\sum_{m=1}^{n-1}T_m(t)T_m(x_i)\right] \tag{16}$$

Further, by means of the obtained analytical representations it is possible to determine all the components of the stress-strain field in the two-component layer. In particular, to determine the dimensionless intensity factor of destructive stresses at the tips of the crack, we obtain the expressions:

$$K_I^*(\pm1)=\frac{K_I(\pm1)}{E_1}=\frac{\sqrt{2\pi}}{E_1}\lim_{\eta\to\pm1\pm0}\sqrt{|t\mp1|}\sigma_y^{(1)}(t,0)=\mp\frac{\sqrt{\pi}}{2\left(1-\nu_1^2\right)}\varphi_1^*(\pm1) \tag{17}$$

3.1 Numerical Analysis

The numerical analysis is conducted based on the formulas of the preceding paragraph. It is assumed that the crack has a constant length equal to a quarter of the half-thickness of the layer h, and is located symmetrically about the axis Oy, i.e. $a_* = 0.25, b_* = 0$. The location of the inclusion, whose length is equal to the length of the crack, can vary and is determined by the parameter l, which is the coordinate of the left end of the inclusion, i.e. $c_* = a_*, d_* = l + a_*$. In order to determine the effect of inclusion on the crack opening and on stress intensity factors (SIF) at its ends, we take the forces acting on the crack faces and the forces at infinity equal to zero ($p_1 = 0, q_2 = 0$). The force applied to the left end of the inclusion ($t_0 = -1$), the ratio of the thickness of the inclusion to the half-thickness of the layer and the ratio of the Young's modulus of the stringer to E_2 will be considered constants with values: $P_0^* = 0.25, h_1/h = 0.01, E_I^{(1)}/E_2 = 5$.

The calculations show that crack opens only when inclusion is located to the right of certain point, in other cases part of the crack is closed and the formulation of the problem is not valid. Note that the crack begins to close from the right end. The location of the above mentioned point can be found by equating the SIF at the right end of the crack to zero and it essentially depends only on the length of the inclusion. So, for example, if the inclusion length is equal to a_*, this point is in the vicinity of the point $-0.8a_*$. If the inclusion length is equal to $2a_*$ the point is around $-2.4a_*$, and if the inclusion length is $0.5a_*$ the point is around $-0.1a_*$. Figure 2 shows the graphs of SIF at the right end of the crack depending on parameter l for different values of the elastic constants of layers.

In Fig. 2, curve 1 corresponds to a homogeneous layer with $\nu_1 = \nu_2 = 0.25$, curves 2, 3, 4—correspond to inhomogeneous layers with parameters $E_1/E_2 = 1$,

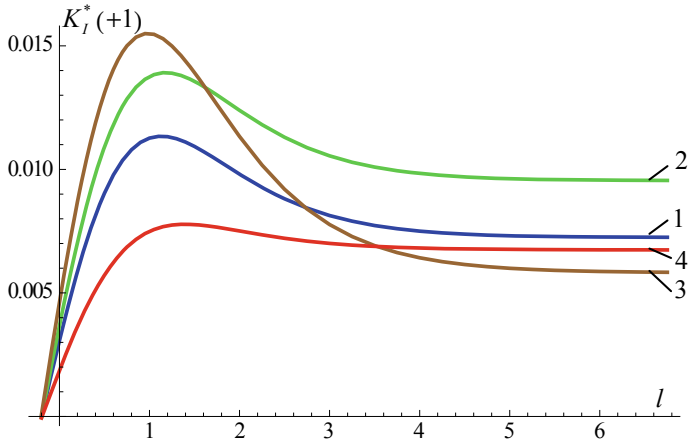

Fig. 2 Dependence of SIF at the right end of the crack on the parameter l

$\nu_1 = 0.25, \nu_2 = 0.35$; $E_1/E_2 = 3, \nu_1 = \nu_2 = 0.25$ and $E_1/E_2 = 1/3, \nu_1 = 0.25, \nu_2 = 0.35$ respectively.

From Fig. 2, we note that SIF acquires the maximum value, when the inclusion is at a distance of about four times the crack half-length. This pattern is also preserved for inclusions longer than a crack, for shorter inclusions this distance increases. The SIF at the left end shows a similar behavior, with the only difference that the initial value differs from zero. It is interesting that the SIF tends to a constant value when the inclusion gets farther away from the crack, and both SIFs tend to the same value. This is explained by the periodicity of the problem, which leads to the restriction of freedom of movement of the boundary points of the base layer in the transverse direction.

After determining the coefficients $X_i\left(i = \overline{1, n}\right)$, crack opening can be calculated by the formula [11]

$$V_*(t) = \frac{V(x)}{(b-a)} = \frac{1}{n}\sum_{k=1}^{n} X_k \left[\arcsin t + \frac{\pi}{2} - 2\sqrt{1-t^2}\sum_{m=1}^{n-1}\frac{T_m(x_k)U_{m-1}(t)}{m}\right] \tag{18}$$

Figure 3 shows the form of crack opening for an inhomogeneous layer with elastic characteristics $E_1/E_2 = 3, \nu_1 = 0.35, \nu_2 = 0.25$ at varying locations of inclusion: $l = -0.8a_*; a_*; 3a_*$. It should be noted that when the values of elastic characteristics change, the presented curves practically experience only a scale change.

Calculations show that the distribution of contact stresses under the inclusion practically depend neither on the elastic characteristics of the inhomogeneous layer, nor on the location of the inclusion relative to the crack. It essentially depends on the length of the inclusion, the ratio of the thickness of the inclusion to the half-thickness of the layer h_1/h and the ratio of Young's modulus of inclusion and the adjacent layer $E_I^{(1)} \Big/ E_2$.

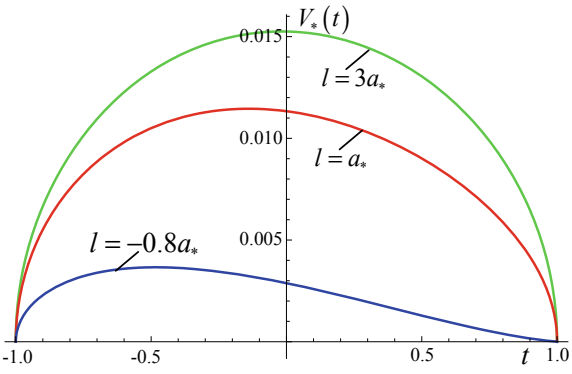

Fig. 3 Form of crack opening

4 Conclusion

The plane deformation state of a piecewise homogeneous uniformly layered plane of two dissimilar materials, when there is a system of cracks on the midlines of layers made of one material, and layers made of the other material are reinforced by a system of elastic inclusions also located on the midlines is studied. For the base cell of the posed periodic problem, a system of governing equations is obtained in the form of a system of singular integral and integro-differential equations for dislocations of the edges of cracks and tangential contact stresses acting on the long sides of the inclusions. The solution of the defining system can be obtained by the method of mechanical quadratures. In the particular case where there is one crack and one inclusion, this solution is presented. A sufficiently detailed numerical analysis of the dependence of the sought functions—crack opening and contact stresses—on the geometric parameters of the problem and the elastic characteristics of the component layers was carried out. In particular, it is shown that, in contrast to the non-periodic problem, when we have only one crack and one inclusion, the influence of even an infinitely remote inclusion does not tend to zero.

Acknowledgements The work is performed within the framework of the Joint Research Project № 18RF-061 of the State Committee on Science of the Ministry of Education and Science of the Republic of Armenia and № 18-51-05012 of the Russian Foundation for Basic Research (RFBR).

References

1. Panasyuk, V.V., Savruk, M.P., Datsyshin, O.P.: Distribution of Stresses near Cracks in Plates and Shells. Naukova Dumka, Kiev (1976). (in Russian)
2. Bardzokas, D.I., Fil'shtinsky, L.A., Fil'shtinsky, M.L.: Actual problems of coupled physical fields in deformable bodies, Vol. 1. Mathematical apparatus of physical and engineering science. Moscow-Izhevsk (2010). (in Russian)
3. Grigolyuk, E.I., Fil'shtinsky, L.A.: Regular Piecewise Homogeneous Structures with Defects. Fizmatlit, Moscow (1994). (in Russian)
4. Hakobyan, V.N., Dashtoyan, L.L.: Discontinuous solutions of a doubly periodic problem for a piecewise homogeneous plate with interphase defects. Mech. Compos. Mater. **53**(5), 601–612 (2017)
5. Hakobyan, V.N., Dashtoyan, L.L.: The stress state of a piecewise uniform layered space with doubly periodic internal cracks. J. Phys. Conf. Ser. **991**(1), 012031 (2018)
6. Hakobyan, V., Dashtoyan, L.: Doubly periodic problem for piecewise homogeneous plane with absolutely rigid inclusions. In: Proceedings of 8th International Conference Contemporary Problems of Architecture and Construction, Yerevan, pp. 125–128 (2016)
7. Hakobyan, V.N., Amirjanyan, A.A.: The stress state of an uniformly piecewise homogeneous layered plane with a system of periodic parallel internal inclusions. In: Proceedings NAS RA, Mechanics, vol. 71(2), pp. 3–17
8. Aghayan, K.L.: Stringers interaction with infinity plate weakened by double-periodic system of cracks. In: Mechanics of Deformable Bodies and Structures. House of Armenian Academy of Sciences, Yerevan, pp. 26–32 (1985). (in Russian)
9. Alexandrov, V.M., Mkhitaryan, S.M.: Contact Problems for Bodies with Thin Coatings and Interlayers. Nauka, Moscow (1983). (in Russian)

10. Sahakyan, A.V., Amirjanyan, H.A.: Method of mechanical quadratures for solving singular integral equations of various types. IOP Conf. Ser. J. Phys. Conf. Ser. **991**, 012070 (2018). https://doi.org/10.1088/1742-6596/991/1/012070
11. Sahakyan, A.V.: Quadrature formulas for computing integrals with a variable upper limit. In: Proceedings of 2nd International Conference "Topical Problems in Continuum Mechanics", Dilijan, Armenia, pp. 107–111 (2010). http://www.mechins.sci.am/publ/avetik_sahakyan/Dilijan2010.doc. (in Russian)

An Experimental Model of the Acoustic Wave Propagation Through a Cascading Triple-Periodic Array of Cylindrical Holes

Vladimir M. Zotov, Vitaly V. Popuzin and M. Y. Remizov

Abstract We study experimental acoustic properties of the meta-materials made as aluminum parallelepipeds with a crossed periodic system of through round holes. The experiments have been made with the use of industrial ultrasonic flaw detectors by the through-transmission technique in a wide interval of the ultrasonic frequencies. There is performed the analysis of the obtained temporary and spectral characteristics of the through-transmitted signal.

1 Introduction

In [1, 2] there is studied a problem on wave propagation of the acoustic signal in bodies with periodic systems of holes; there is performed numerical and experimental analysis of the influence of the structure of the through-transmitted acoustic signal to the filtration properties. The problem there can be reduced to a two-dimensional case since the most part of samples have the same cross-section in a certain direction, among other three ones. To study wave properties in the more complex three-dimensional case we investigate the specimen with a crossed system of cylindrical holes (perforations). For this aim, the direction of the drilling, analogous to those considered in [1, 2], is taken alternate, so that every next row can be obtained from the previous one by a 90° rotation around the axis of propagation of the ultrasonic impulse. Figure 1 demonstrates a photo of the samples produced in this manner.

In this figure at the left we show a sample free of any perforation, we mark it with the number 0. The sample number 1 has been produced with the help of drilling described above, with the diameter of the through hole being equal to 4 mm, the horizontal and the vertical distances between the centers of the two neighbor parallel holes is 8 mm. Such a geometry allows us to put an additional hope between the pair of existing neighbors. The second family of holes possess the same geometry and

V. M. Zotov · V. V. Popuzin (✉) · M. Y. Remizov
Southern Federal University, 105/42 Bolshaya Sadovaya Str., Rostov-on-Don
344006, Russian Federation
e-mail: popuzin@gmail.com

M. A. Sumbatyan (ed.), *Wave Dynamics, Mechanics and Physics of Microstructured Metamaterials*, Advanced Structured Materials 109,
https://doi.org/10.1007/978-3-030-17470-5_3

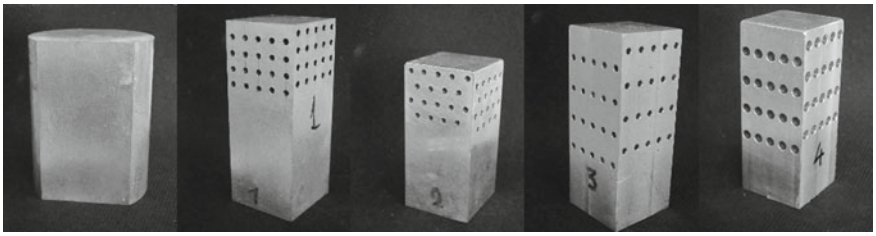

Fig. 1 Experimental samples with respective enumeration

the same structure. The sample number 2 has the holes analogous to the one with number 1, with the only difference that each second unidirectional row is shifted to the distance 4 mm. This guarantees that any vertical ray emitted from the top to the bottom certainly meets a hole over its path, that cannot be guaranteed for the previous sample. Sample number 3 is made to study the influence of the vertical distance between the rows to the through-transmitted signal. The distance in this case is twice greater, being 16 mm between the centers of the neighboring unidirectional holes. The 4th sample is similar to the previous one, with a different diameter of perforation which is 5 mm, and the distance between the rows is 20 mm. It should be noted that with such a geometry the horizontal distance between the neighbor unidirectional holes reduces significantly, spacing for the US beam only very narrow free distance. All samples, except the first one, have the cross-section 40 $\times$ 40 mm, begin made of aluminum, where the wave speed of the longitudinal elastic wave is around 6260–6400 m/s.

2 Applied Instrumentation

We use two industrial US flaw detectors USD60-N and UD9812, shown in Fig. 2. The low-frequency flaw detector USD60-N permits measurements in the frequency range 0.02–2.5 MHz in the two regimes—the through-transmission method and echo-method. There is a possibility to display the full signal, the detected signal, as well as its spectrum. The second flaw detector UD9812 has the working frequency range 0.6–12 МГц, and we use it to perform measurements at frequencies higher than 2.5 MHz. The both flaw detectors permit the transmission of the recorded data to a PC with the help of a special software. In the case of USD60-N for this aim one can use the network interface Ethernet, while the UD9812 can be attached to the PC with a USB 2.0.

As the generator and the receiver of US signals we use available US transducers of various frequencies and diameters.

Let us note that the values reflected in Table 1 are related to the maximum working frequency of the US transducer, while the spectrum generated by the probe contains a set of frequencies around the indicated carrier frequency. The measurements are

Fig. 2 Flaw detectors used for measurements. Left—low-frequency flaw detector USD60-N, right—UD9812

Table 1 Upper line—carrier frequencies (MHz), lower line—diameter (mm) of the US probe

0.04	0.06	0.08	0.1	0.2	0.4	0.6	1.25	1.8	2.5	5	10
20	20	20	20	20	20	14	25	20	14	20	8

carried out by the through-transmitted method, when the radiating probe is placed on the top of the sample and another probe—on its bottom. To provide a good contact, we used a lubricating layer which permits the transition of the mechanical oscillations of the piezo-element inside the specimen at hand (Fig. 3).

A laboratory setup has been equipped to provide the experiments, see Fig. 4, which is a device to fix the US probes and the sample. The device is a rack with three clamps. The first two clamps fix the receiving and radiated US transducers, between them there is a fixed sample for measurements, the third clamp fixes a spring which provides reliable contact between the transducers and the sample.

All experiments were performed without any additional amplifier with a fixed amplitude of 50 V. The following filtration bands was applied to the received signal: at the frequency up to 0.2 MHz we used a filtration over the interval 20–300 kHz; for the frequencies 0.4 and 0.6 MHz we put the filtration for the receiver 200–1250 kHz; the frequencies 1.25, 1.8, 2.5 MHz were measured in the pass band 400–2500 kHz for the frequencies 5 and 10 MHz—the frequency band 0.8–12 MHz.

The goal of the first series of experiments is to analyze the through-transmitted amplitude of the signal on the carrier frequencies of the US transducers. The measured data show that the frequencies lower than 0.4 MHz pass without any change in the amplitude, with minimal variation of the shape of the acoustic signal. Obvi-

Fig. 3 The set of US probes used in experiments

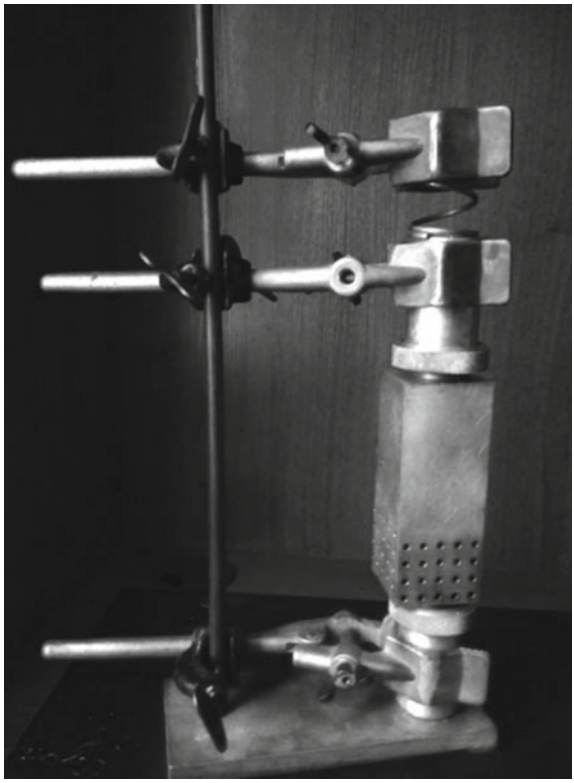

Fig. 4 Laboratory setup with a sample and a pair of US transducers

ously, for such low frequencies the relative size of the obstacles is so small that the propagating wave passes through the cracked medium unchecked, "not feeling" the internal structure of the material.

The filtration property becomes noticeable for frequencies higher than 0.4 MHz. The change of the shape of the through-transmitted signal is demonstrated in Fig. 5, where each line represents a sample corresponding to respective number, and vertical rows correspond to carrier frequencies of the used US probes. To draw the diagrams, there are used the time delay of 6 mks and the sweep of 200 mks. The exception is for the frequencies equal 1.8, 2.5, 5.0 MHz, where for the sake of obviousness the sweep is 70 mks. It is clear from the presented diagrams that re-reflections of the acoustic wave from the system of obstacles has significant effect on the shape of the through-transmitted signal.

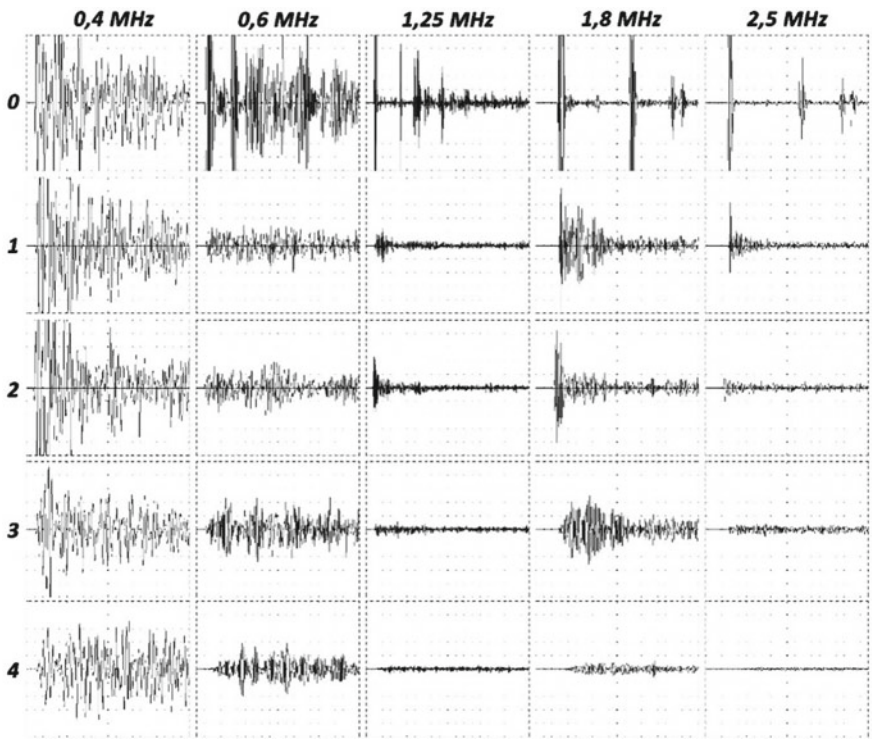

Fig. 5 The shape of the received US signals for samples 0–4 at various frequencies

3 Results of the Measurements

The amplitude characteristics are presented in the Table 2. The analysis of the obtained data shows that obvious filtration properties of first, second and third samples begin after the frequency 0.6 MHz. The increase of the distance between the rows, used in the third sample, has no effect on the through-transmitted amplitude in the latter case; however an obvious change of the impulse shape is quite clear, much more notable than for the first two samples. One may conclude that the increase in the distance between the rows complicated the diffraction field inside the sample. The fourth sample begins to demonstrate its filtration properties just at the frequency of 0.4 MHz, that is obviously connected with smaller ratio of the US wave length above the size of the obstacle.

The preliminary investigations [1, 2] show that after the first filtration strip there is a strip of almost perfect transmission. As can be seen from Fig. 5 and Table 2, for the first three samples such a frequency strip begins from 1.8 MHz. This effect is less pronounced for the fourth sample, though the amplitude of the through-transmitted signal is still higher than at the frequency 1.25 MHz.

Analyzing the table, one may conclude that the increase of the size of the holes (the fourth sample) results in the worst through-transmission in the meta-material, cutting off more than 90% of energy, beginning from the frequency ~1 MHz. The increase of the distance between the rows along the wave propagation also reduces the carrying capacity for higher frequencies, and the passage to the first filtration band becomes smoother (which is obvious for the frequency equal to 0.6 MHz, where the sample 3 demonstrates the best through-transmission). The shift of the rows in the second sample has not so strong effect at low frequencies, and in some

Table 2 Maximal amplitude of the passed signal, measured in dB, in percents with respect the size of the display

f (MHz)	Passed signal amplitude				
	Sample 0	Sample 1	Sample 2	Sample 3	Sample 4
0.4	42.1 dB	42.1 dB	42.1 dB	42.0 dB	37.4 dB
	128%	127%	127%	126%	74%
0.6	42.1 dB	31.8 dB	32 dB	33.4 dB	31.8 dB
	128%	39%	40%	47%	39%
1.25	42.9 dB	28 dB	32 dB	21.6 dB	15.6 dB
	140%	25%	40%	12%	6%
1.8	43.8 dB	39.6 dB	38.8 dB	34 dB	22.3 dB
	154%	95%	87%	50%	13%
2.5	44.3 dB	35.7 dB	26 dB	20 dB	9.5 dB
	164%	61%	20%	10%	3%
5	38 dB	26.8 dB	0 dB	9.5 dB	0 dB
	79%	22%	0%	3%	0%
10	−20 dB	−58 dB	−65 dB	−56 dB	−66 dB

cases even improves the through-transmission of the US signal, as can be seen for example, for the frequency 1.25 MHz. Nevertheless, for higher frequencies one can see a significant suppression of the transmission, which may be connected with a complex structure of the re-reflections inside the meta-material.

For these frequencies the wave radiated by the US probe demonstrates its "ray" nature, hence the obstacles met across its path have significant influence on its trajectory. This is clearly seen at frequencies 5 and 10 MHz for the second and the fourth samples. It should also be noted that at higher frequencies the lower through-transmission of the elastic wave is connected with a higher attenuation, which is typically out of the consideration in numerical or analytical simulation.

As discussed above, the US probes radiate not a single fixed frequency but a spectrum of frequencies located in the band containing the one claimed by the producer. Therefore, for a detailed analysis we studied the spectral characteristics of the received signals.

The flow detector USD60-N permits measurements of the spectral characteristic on the chosen temporary interval, in the frequency range up to 1 MHz, with the characteristics being normalized by maximal amplitude and viewed on display. The obtained diagrams are shown in Fig. 6, where white curve is related to the spectrum of the signal in the standard specimen, and black curves—in the specimen at hand, whose numbers are indicated above the figure. The temporary interval of the spectrum measurement is related to the sweeps discussed above, for each carrier frequency. The three last rows in Fig. 6 are to be analyzed together with Fig. 5 and Table 2, because of the automatic normalization of the amplitude performing by the flaw detector. For other diagrams the amplitude of the passed signal remains unchanged. In common, the spectral characteristic confirm the filtration band on the interval 0.6–1 MHz. The envelope of the measured spectra are demonstrated in Fig. 7.

4 Conclusion

- It is shown that the acoustic meta-materials with a crossed periodic system of through holes demonstrate filtration properties very closed to those inherent in the meta-materials with non-crossed periodic systems, previously studied in [1, 2].
- The increase of the holes diameter decreases the initial frequency of the first filtration interval and significantly decreases the passage of the US impulse for higher frequencies.
- The shift of the rows realized in the sample number 2 has weak influence on filtration characteristics in the low-frequency US interval, and this begins visible only for higher frequencies, when the US wave begins to work like the "ray" propagation.
- The increase of the distance between the crossed rows may shift the initial frequency of the first filtration interval and may strengthen the filtration properties above this frequency. This is connected with the complicated structure of the

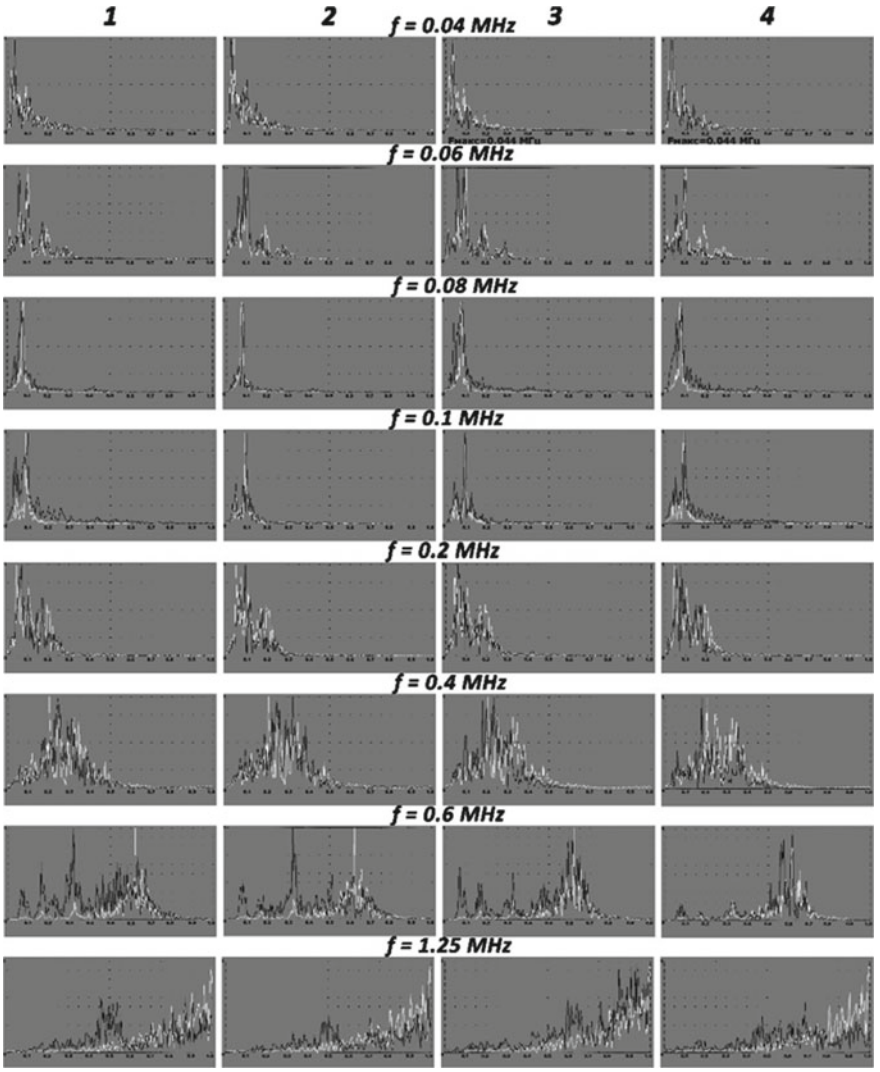

Fig. 6 Comparison of spectra for samples 1–4 (black line) with the standard specimen 0 (white line) at various frequencies

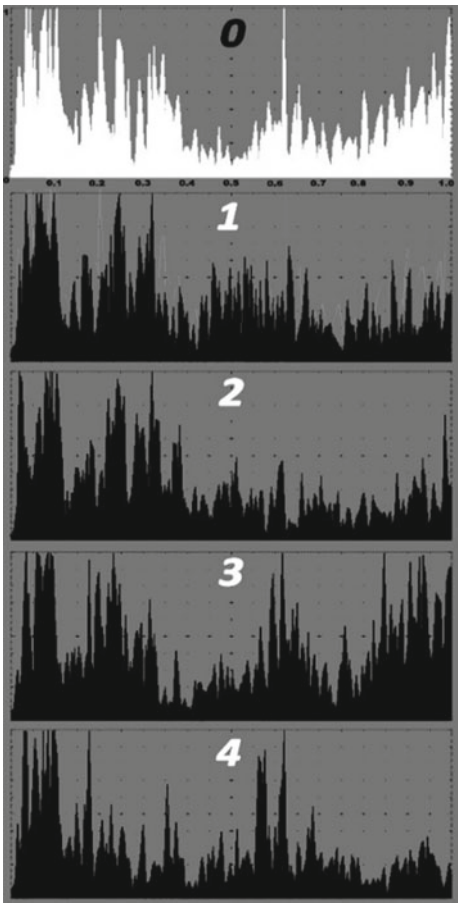

Fig. 7 The envelope lines of the measured spectra

internal diffraction, which is clearly seen from the changed form of the through-transmitted impulse.

Acknowledgements The work is performed under support of the Project № 15-19-10008-P by the Russian Science Foundation (RSCF).

References

1. Popuzin, V.V., Zotov, V.M., Sumbatyan, M.A.: Theoretical and experimental study of an acoustically active material containing a doubly-periodic system of cylindrical holes. In: Advanced Materials—Techniques, Physics, Mechanics and Applications, Springer Proceedings in Physics, Heidelberg, New York, Dordrecht, London, pp. 293–308 (2017)

2. Zotov, V.M., Popuzin, V.V., Tarasov, A.E.: An experimental model of the ultrasonic wave propagation through a doubly-periodic array of defects. In: Wave Dynamics and Composite Mechanics for Microstructured Materials and Metamaterials, Springer: Advanced Structured Materials, pp. 189–204 (2017)

Simulation of the Surface Structure of Ferroelectric Thin Films

Olga G. Maksimova, Tatiana O. Petrova, Victor A. Eremeyev, Vladislav I. Egorov, Alexandr R. Baidganov, Olga S. Baruzdina and Andrei V. Maksimov

Abstract Metropolis and Wang-Landau algorithms are described and illustrated on the base two-dimensional Ising model. The influence of the ferroelectric film thickness and the depolarizing field on the spontaneous polarization and the order parameter of the film has been investigated by means of the Monte-Carlo method. Dependences of the polarization of the thin film on the temperature are calculated at different values of its thickness and the potential well depth of the Lennard-Jones potential. To investigate the geometrical and optical properties of textured coatings the anisotropic three-dimensional model based on the fractal plurality of Julia is used. The developed method allows to determine the values of the model parameters for a number of coating samples of steel sheet obtained under different conditions of their formation. The fractal dimension of the objects obtained on the base of this model is determined.

1 Introduction

The main trend in modern micro- and optoelectronics, optics and a number of other fields of technics is the tendency to reduce the size of electronic devices. The use of thin films in n integral devices and sensors requires the creation of new composite materials, as well as investigation of the film structure s for the rational use and the control of their specific properties.

High efficiency of application of the films and coatings is achieved only by the right choice of design parameters of surface layers, that meet the specified operating conditions, as well as the development of optimal methods for the forming of such layers (in terms of achieving the required properties) [1, 2]. Therefore, the adhe-

O. G. Maksimova · V. I. Egorov · A. R. Baidganov · O. S. Baruzdina · A. V. Maksimov
Cherepovets State University, 5 Lunacharskii Av., Cherepovets 162600, Russian Federation

T. O. Petrova (✉) · V. A. Eremeyev
Southern Federal University, 105/42 Bolshaya Sadovaya Str., Rostov-on-Don 344006, Russian Federation
e-mail: to_87@bk.ru

M. A. Sumbatyan (ed.), *Wave Dynamics, Mechanics and Physics of Microstructured Metamaterials*, Advanced Structured Materials 109,
https://doi.org/10.1007/978-3-030-17470-5_4

sive, strength, optical, deformational, insulating and other surface properties of the polymer coatings of solids are studied at the junction of different fields of science: thermodynamics, physical chemistry and chemistry of high-molecular compounds, solid state physics, metallurgy, classical mechanics, physical and chemical mechanics, mathematical statistics, etc. [3–6].

The study of fundamental properties of thin films and their application are one of the urgent problems of modern research due to a number of reasons. With the decrease in sample size, there comes a moment when any significant size becomes less than a certain characteristic length, and the sample "turns" into a film. It is important that each physical phenomenon is characterized by own characteristic length, when the sample turns into a film, then the phenomenon under study proceeds fundamentally in a different way. There arises an interest to the properties characteristic of bodies in the film form, which may differ significantly from the properties of massive samples. Such research include, for example, the study of optical, electrical, magnetic, and superconducting properties, the study of structural ordering, dislocations, migration phenomena, phase transitions, various surface reactions, and surface phenomena.

Currently, there is great interest in studying the properties of ferroelectrics near the phase transition (PT) region, where a sharp change in the crystal structure of a substance is observed. Near the PT point, the materials significantly change their properties under the influence of electric fields, uniform and non-uniform mechanical stresses, and other external influences. Under the influence of uniaxial pressure and changes, the temperature shift of the first and second order PT in depending on the film thickness is experimentally detected in. Therefore, it is possible to effectively change the structure of a substance by mechanical a action, that is relevant for practical applications. Besides, the introduction of ferroelectric oxide films into modern microelectronic devices, combined with restrictions on reducing the size of the base element, revive the interest to old question of possible existence of the critical film thickness necessary for the emergence of ferroelectricity.

In recent years there has been a considerable interest to polymers with electrical (ferroelectric) and mechanical (ferroelastic) properties [7–9]. These properties are determined by the occurrence of spontaneous polarization or deformation respectively during the phase transitions from an isotropic state to an ordered one. The greatest prospects for the use of polymer ferroelectrics and ferroelastics are associated with the creation of controlled fundamentally new devices for processing acoustoelectric, optical, and other signals.

It is worth to note the predominant number of experimental studies of thin films, in comparison with theoretical studies. Therefore, a sufficiently complete and rigorous theory of accounting surface effects in low-molecular and polymer ferroelectrics currently does not exist. During the last decade, significant progress has been observed in understanding of the mechanisms of phase transitions in different ferroelectric materials, but serious theoretical studies of the surface properties of ferroelectric films and coatings are not sufficient, although this class of problems is the most promising for their practical use.

The main problem of the theories describing the equilibrium properties of monomers or fragments of polymer chains (links, etc.) in extended and finite low-

molecular and polymer systems (domains, layers etc.) is the need to take into account correctly intermolecular boundary conditions (interactions with the substrate, orientational interactions etc.). It is both about the interaction with the environment, for example with a solvent, the surface of the solid phase, that is, with particles in the system, and etc., and about intra- and inter-component interaction.

The strong difference in the properties of bulk materials and bodies under conditions of limited geometry is determined by a significant increase in the proportion of surface atoms and, therefore, the role of the surface becomes defining. The search of the free surface requires needs a special study of two-dimensional (2d) systems. The surface model presented in this paper has a rigorous mathematical description. Herewith, it is taken into account that the equations obtained are deduced depending on the ordering of molecules in the bulk of the film. The surfaces of the membranes, films and coatings of solids are somehow rough; there are big problem in the electrodynamics related with statistical modeling of the geometric properties of the surface.

To describe the ordered state in ferroelectric three-dimensional systems, analytically solvable phenomenological theories have been developed in sufficient detail. For example, in the theory of ferroelectricity, a phenomenological description of phase transitions based on the Landau—Devonshire potential is widely used. This theory is successfully applied, for example, to estimate temperature behavior of $BaTiO_3$ [10], $PbTiO_3$ [11] and other ferroelectrics. However, Landau's theory is a mean field theory; therefore it does not take into account fluctuations of the spontaneous polarization. In the quasi-two-dimensional case, such fluctuations are not small. Therefore, it is'n use for the description of phase transitions in thin ferroelectric films [12]. In this paper, we will considerer a discrete model of the ferroelectric, in which the dimensions of the crystal lattice are not specified, but they are determined in the process of calculation taking into account boundary effects.

The solution of three-dimensional problem seems to be not possible; therefore, it is necessary to apply computer simulation methods. Some authors [13, 14] as well use lattice models and the Monte Carlo (MC) method for the study of low-molecular ferroelectrics. However, when studying the properties of polymers, the Metropolis procedure quickly loses its effectiveness with an increase in the number of intramolecular degrees of freedom. This problem is especially actually for continual models of polymers [15]. Besides, the standard Metropolis algorithm is poorly suited for the study of systems with a complex energy landscape with a large number of local minima. Therefore, currently, the Wang-Landau algorithm is more successful [16], which is an implementation of the entropy modeling method. The main advantage of this algorithm is the ability of direct calculation of the entropy and free energy for a wide temperature range by means of one simulation [17].

2 Simulation Method Using the Wang-Landau Algorithm

Monte-Carlo method use broad class of computational algorithms which are based on random walks. The typical problem in statistical physics that can be solved by these method is calculating mean values of macroscopic variables (energy, order parameter,

etc.) at different temperatures for systems which follows Boltzmann statistics. There are some techniques for Monte-Carlo method: Metropolis [18], Wolff [19], Lee [20], Wang-Landau algorithms [21], parallel tempering [22]. In this section, Metropolis and Wang-Landau algorithms are described and illustrated on the example of two-dimensional Ising model.

The Ising model consists of spins which have two possible orientations. Originally developed for simulation of ferromagnetic materials, now, this model has many applications including the simulation of ferroelectrics [23], spin glasses [24], image data processing [25], neuroscience, etc. In 1944, the two-dimensional Ising model on a square lattice was analytically solved by Onsager [26]. The Hamiltonian of this model is determined by the formula:

$$E = -J \sum_{\langle i,j \rangle} \overrightarrow{S_i}\,\overrightarrow{S_j} - \overrightarrow{H} \sum_i \overrightarrow{S_i}, \tag{1}$$

where $\overrightarrow{S_i}$ is the value of spin located in site i, the symbol $\langle i, j \rangle$ denotes the pairs of nearest-neighbor segments, J is a parameter of spin interactions, $\overrightarrow{H}$ is the external magnetic field strength.

The Metropolis algorithm generates the sequence of states at a predetermined temperature using the probability distribution for the system. For the Ising model, the Metropolis algorithm should be applied as follows:

1. A random spin is chosen and rotated.
2. The new system configuration is accepted with probability:

$$P = \min\left(-\frac{\Delta E}{k_B T},\ 1\right), \tag{2}$$

   where ΔE is energy change due to the spin rotation, k_B is the Boltzmann constant, T is the temperature.
3. Steps 1 and 2 are repeated.

The results of simulation for the two-dimensional Ising model with periodic boundary conditions obtained by means of the Metropolis algorithm are presented in Fig. 1. The heat capacity was determined by the formula:

$$C = \frac{\langle E^2 \rangle - \langle E \rangle^2}{k_B T^2}. \tag{3}$$

The number of Monte-Carlo steps for each temperature was equal to $N^2 \times 10^4$, where N is the linear size of the lattice. It is seen that the temperature of phase transition becomes closer to the theoretically predicted value 2.269 with increasing lattice sizes.

The Metropolis algorithm isn't appropriate for systems with multiple local energy minima like in the Potts model. The sequence of states generated by this technique can be trapped in these minimums at low temperatures. Therefore, other approaches

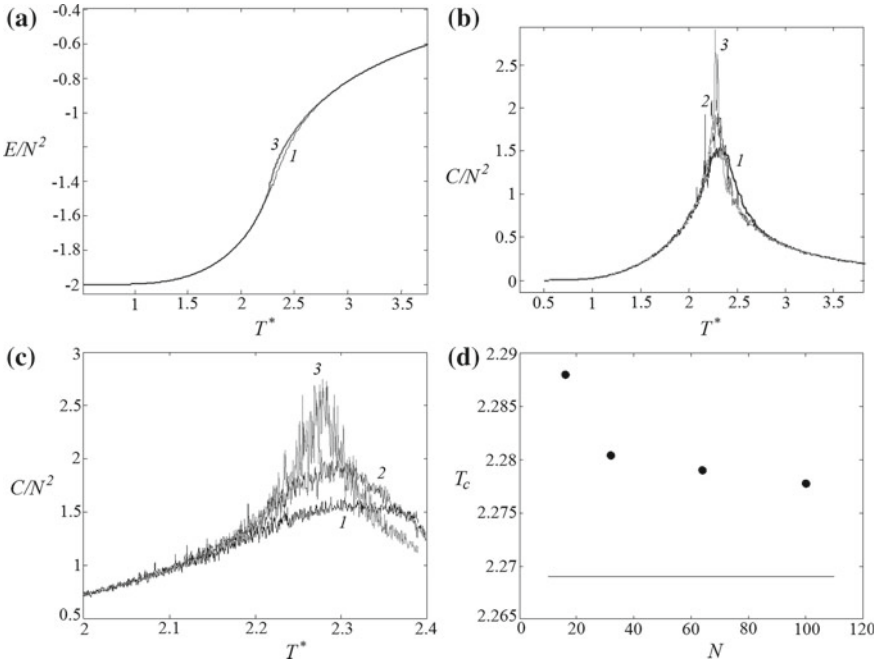

Fig. 1 The Metropolis algorithm. The average energy (**a**) and the heat capacity (**b, c**) versus the renormalized temperature $T^* = k_B T/J$ for the two-dimensional Ising model with lattice sizes 16×16 (*1*), 32×32 (*2*) and 100×100 (*3*) in the absence of external fields. **d** The temperature corresponding the maxima of heat capacity versus the linear size of lattice. The black line is theoretically predicted value of the critical temperature

(Lee or Wang-Landau algorithms) should be used for systems with a rough energy landscape. Lee and Wang-Landau algorithms are used in Monte-Carlo method for estimating the density of states $g(E)$ which is the number of system states with energy E. From the density of states, the canonical distribution may be built for any temperatures:

$$P(E) = \frac{g(E)\exp\left(-\frac{E}{k_B T}\right)}{\sum\limits_i g(E_i)\exp\left(-\frac{E_i}{k_B T}\right)}. \tag{4}$$

The Wang-Landau algorithm for determination the density of states consists of following steps:

1. Firstly, we set initial values of density of states ($g(E) = 1$ for all configurations), a zero histogram $h(E)$ and an initial modification factor $f = e$.
2. A random selected rotator is rotated that changes the ith system state from to jth one. The new configuration is accepted with probability:

$$P = \min\left(\frac{g(E_i)}{g(E_j)},\ 1\right). \tag{5}$$

3. Then, independently from the new configuration was accepted or not, the histogram and the density of states are updated by a rule:
4.

$$\begin{aligned} h(E_k) &\to h(E_k) + 1, \\ g(E_k) &\to g(E_k) f, \end{aligned} \tag{6}$$

where k is the current system configuration.

5. After 10,000 Monte-Carlo steps 2–3, the flatness of the histogram is checked. A flatness criterion in our work means that the histogram for all possible E is not less than 80% of the average histogram. If the criterion is satisfied, the histogram is reset and the modification factor f is updated: $f \to \sqrt{f}$. The simulation continues before the modification factor becomes less than $f_{final} = \exp(10^{-10})$.
6. Then, the density of states should be reweighted taking into account the consideration that the density of states is equal to 2 for the ground state of the Ising model.

The accuracy of results depends on flatness criteria and the final value of the modification factor. The Wang-Landau algorithm for lattices 100×100 and greater requires huge computational time. For accelerating calculations, the random walk may be divided in some energy domains. A more detailed description of this parallelization technique is reported in the work [27]. The results of simulation for the two-dimensional Ising model with periodic boundary conditions obtained by means of the Wang-Landau algorithm are presented in Fig. 2.

To obtain the probability distribution not only for the energy but also for other parameter such as magnetization, a two-dimensional or joint density of states (JDOS) should be estimated by random walk method both in the energy and in this parameter. For the Ising ferromagnetic model, values of the order parameter for the whole temperature range and the external magnetic field may be calculated by means of JDOS $g(E, m)$, where E is the energy in the absence of external field, and m is the order parameter [28]. However, such calculations require much more time than calculations for the ordinary density of states. Dependencies of the order parameter obtained by JDOS are presented in Fig. 3. JDOS was calculated by the Wang-Landau algorithm.

Summarize, the Wang-Landau algorithm gives more accurate results than the Metropolis one and appropriates for systems with the rough energy landscape. In addition, the free energy and the entropy may be calculated directly by this method. However, obtaining JDOS by Wang-Landau algorithm has huge computational cost. Therefore, the Metropolis algorithm is more appropriate for calculating such quantities as the magnetization, the order parameter, the susceptibility, etc.

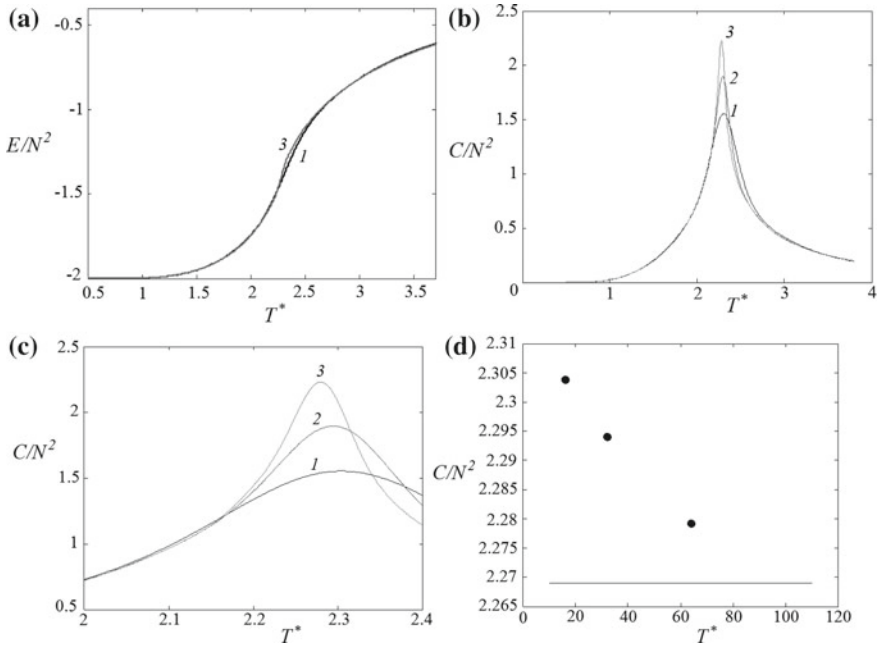

Fig. 2 The Wang-Landau algorithm. The average energy (**a**) and the heat capacity (**b, c**) versus the renormalized temperature $T^* = k_B T/J$ for the two-dimensional Ising model with lattice sizes 16 × 16 (*1*), 32 × 32 (*2*) and 64 × 64 (*3*) in the absence of external fields. **d** The temperature corresponding the maxima of heat capacity versus the linear size of lattice. The black line is theoretically predicted value of critical temperature

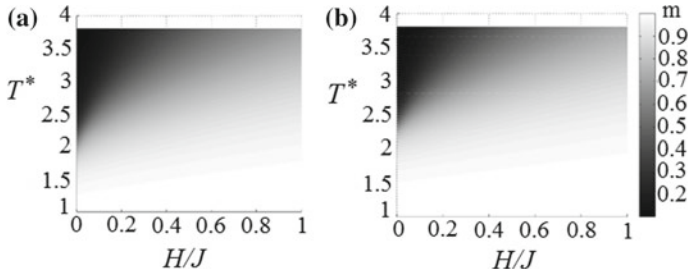

Fig. 3 The Wang-Landau algorithm for the joint state density. The order parameter versus the temperature and the external magnetic field for the Ising model with 10 × 10 (**a**) and 16 × 16 (**b**) lattices

3 Investigation of the Influence of Bulk Properties on the Surface Ones of Ferroelectric Systems

The surface properties of layers are determined not only by chemical composition of the substance, but also by their physical structure and the orientational order of polymer chains [29]. Intermolecular orientation interactions are much weaker than valence interactions; therefore, the self-organization of the system with the given chemical structure is determined by intermolecular interactions. In this chapter, we consider the equilibrium properties and phase transitions on the surface of ferroelectric polymer system, in which orientational interactions both between the surface molecules and molecules located in the bulk are taken into account.

Model. Usually, polymer chains have predominantly planar orientation relatively to the interphase boundary [30]. Therefore, in this paper, to describe the surface of ferroelectric polymer systems, we use a two-dimensional model, which consist of M freely-jointed chains, each of which is a sequence of N connected rigid segments, located in parallel to the surface (Fig. 4).

The main quantitative characteristic of the polymer chain flexibility is the persistent length a, which is related with the energetic constant of intrachain orientation interaction K_1 by the ratio:

$$K_1 = \frac{a \cdot k_B T}{2}. \tag{7}$$

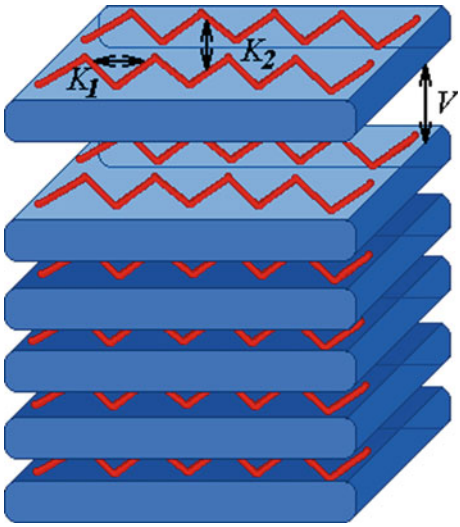

Fig. 4 The layer model of a ferroelectric polymer system

Similar to the persistent length a, we introduce the interchain interaction parameter of b. The orientation interaction of neighboring polymer chain elements is described by the energy constant K_2,

$$K_2 = \frac{b \cdot k_B T}{2}. \tag{8}$$

To take into account the interaction of surface molecules with molecules located in the bulk of the film, we use the mean field constant V and the dimensionless mean field parameter q:

$$q = \frac{V}{k_B T}. \tag{9}$$

The internal energy in the low-temperature approximation can be represented as:

$$H = \frac{1}{2} K_1 \sum_{n,m=1}^{N,M} \left(\varphi_{n,m} - \varphi_{n-1,m}\right)^2 + \frac{1}{2} K_2 \sum_{n,m=1}^{N,M} \left(\varphi_{n,m} - \varphi_{n,m-1}\right)^2 - \mu V \sum_{n,m=1}^{N,M} \cos\left(\varphi_{n,m}\right), \tag{10}$$

where μ is the long-range orientation order parameter, which is defined as the average cosine of the angle between the directions of chain rigid element and the director, i.e. $\mu = \langle \cos \varphi_{\vec{n}} \rangle$.

Free energy and order parameter

To calculate the free energy, the quadratic form (10) by means of variables transformation (Fourier series expansion)

$$\varphi_{\vec{n}} = \sum_{\vec{\psi}} \mathrm{e}^{i\vec{n}\vec{\psi}} Q_{\vec{\psi}}, \tag{11}$$

may be reduced to a diagonal form, that is, to the sum of the squares of normal coordinates $Q_{\vec{\psi}}$. The components of two-dimensional vector $\vec{\psi} = (\vec{\psi}_1, \vec{\psi}_2)$ depend on the size of the system and the type of boundary conditions. For an infinitely extended system, the values ψ_1 and ψ_2 are continuous quantities lying in the interval $(0; \pi)$. For finite system, the values ψ_1 and ψ_2 are discrete ones and they depend on the type of boundary conditions.

Expressions for the free energy have the form,

for infinitely extended system

$$\widetilde{F}(\mu) = \frac{k_B T}{2\pi^2} \int_0^{\pi} \int_0^{\pi} \ln[\mu q + a(1 - \cos x) + b(1 - \cos y)] dx dy$$

$$+\frac{1}{2}k_BTq\mu^2 - k_BTq\mu, \tag{11.1}$$

for free boundary conditions

$$\widetilde{F}(\mu) = \frac{k_BT}{2\pi N}\sum_{y=0}^{N-1}\int_0^{\pi}\ln[\mu q + a(1-\cos x) + b(1-\cos y)]dx$$
$$+\frac{1}{2}k_BTq\mu^2 - k_BTq\mu, \tag{11.2}$$

for fixed boundary conditions

$$\widetilde{F}(\mu) = \frac{k_BT}{2\pi N}\sum_{y=1}^{N}\int_0^{\pi}\ln[\mu q + a(1-\cos x) + b(1-\cos y)]dx$$
$$+\frac{1}{2}k_BTq\mu^2 - k_BTq\mu, \tag{11.3}$$

where the quantities *a, q, b* are determined by the formulas (7)–(9). By the derivation of the formulas, it is assumed that the polymer chains are sufficiently long, so the quantity x is continuous.

The equilibrium value of the orientation order parameter is determined by the condition of minimum of the free energy:

$$f(\mu) = \frac{\partial\widetilde{F}}{\partial\mu} = 0; \quad \frac{\partial^2\widetilde{F}}{\partial\mu^2} > 0. \tag{12}$$

Figure 5 shows the dependence of the free energy derivative $f(\mu) = \frac{\partial\tilde{F}(\mu)}{\partial\mu}$ of an infinitely extended system on the parameter of long-range orientational order μ for different values of the persistent length a and fixed values of the interchain interaction parameters b and mean field values q.

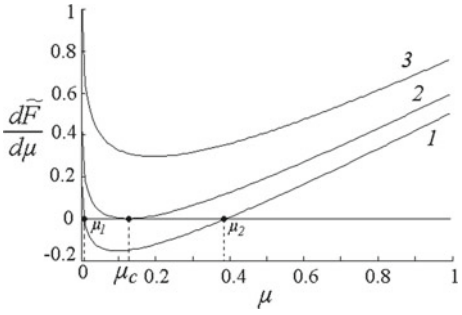

Fig. 5 Dependence of the free energy derivative $\frac{\partial\widetilde{F}(\mu)}{\partial\mu}$ for an infinitely extended system versus the long-range order parameter μ for values of the persistent length $a =$ 0.2 (*1*), 0.4417 (*2*), 0.7 (*3*), $b = 1$, $q = 1$

The curve *1* (at $a = 0.2$) corresponds to the case when Eq. (12) has two roots μ_1 and μ_2. If the value $\mu = \mu_1$ the derivative of the free energy changes the sign from «+» to «−» therefore, this value corresponds to the maximum of the free energy, in contrast to the value μ_2, which is the value of the order parameter of the polymer system. The curve *2* (at $a = 0.4417$) corresponds to the critical value $\mu = \mu_c$, when, Eq. (12) has one root. The value of the persistent length in this case is critical, since the value of the order parameter varies abruptly from μ_c to 0. The curve *3* (at $a = 0.7$) corresponds to the case of increase of the free energy, that is, the minimum value of the order parameter is $\mu = 0$, the system is disordered.

When solving Eq. (12) considering Eqs. (11.1)–(11.3), the equations for calculating the long-range orientational order parameter depending on the energy constants of interactions and temperature are obtained.

For an infinitely extended system, these equations have the form:

$$\frac{1}{\pi}\sqrt{\frac{1}{n+\sqrt{n^2-cd}}}\cdot K\left(\sqrt{\frac{2\sqrt{n^2-cd}}{n+\sqrt{n^2-cd}}}\right)+\mu-1=0, \tag{13.1}$$

for free boundary conditions

$$\frac{1}{\pi}\sqrt{\frac{1}{n+\sqrt{n^2-cd}}}\cdot F\left(arctg\left(\sqrt{\frac{d}{n+\sqrt{n^2-cd}}}tg\left(\frac{\pi(M-1)}{M}\right)\right);\right.$$
$$\left.\sqrt{\frac{2\sqrt{n^2-cd}}{n+\sqrt{n^2-cd}}}\right)+\mu-1=0, \tag{13.2}$$

for fixed boundary conditions

$$\frac{1}{\pi}\sqrt{\frac{1}{n+\sqrt{n^2-cd}}}\cdot F\left(arctg\left(\sqrt{\frac{d}{n+\sqrt{n^2-cd}}}tg\left(\frac{\pi M}{2(M+1)}\right)\right);\right.$$
$$\left.\sqrt{\frac{2\sqrt{n^2-cd}}{n+\sqrt{n^2-cd}}}\right)-\frac{1}{\pi}\sqrt{\frac{1}{n+\sqrt{n^2-cd}}}\cdot F\left(arctg\left(\sqrt{\frac{d}{n+\sqrt{n^2-cd}}}tg\right.\right.$$
$$\left.\left.\left(\frac{\pi}{2(M+1)}\right)\right);\sqrt{\frac{2\sqrt{n^2-cd}}{n+\sqrt{n^2-cd}}}\right)+\mu-1=0, \tag{13.3}$$

where the quantities $n = \mu^2q^2 + 2\mu q(a+b) + 2ab$; $c = \mu^2q^2 + 2a\mu q$; $d = \mu^2q^2 + 4b(a+b) + 2\mu q(a+2b)$. The quantity K is complete elliptic integral of the first kind. The function $F(a; x)$ is incomplete elliptic integral.

When $M \to \infty$, formulas (13.2) and (13.3) convert into Eq. (13.1).

Figures 6 and 7 show the behavior of solutions of Eq. (13.1) for calculating the long-range orientational order parameter on the surface for different values of

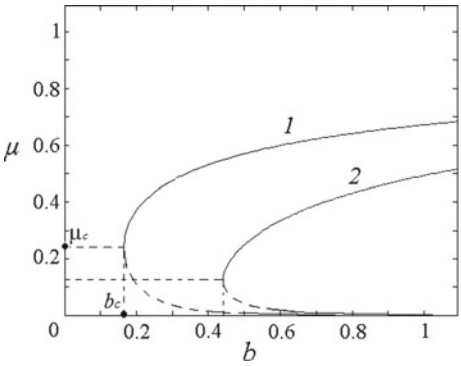

Fig. 6 The long-range orientational order parameter (continuous line) μ of infinitely extended system versus the interchain interaction parameter b for the given value of the persistent length $a = 1$ and different values of the mean-field parameter $q =$ 0.5 (*1*), 0.1 (*2*)

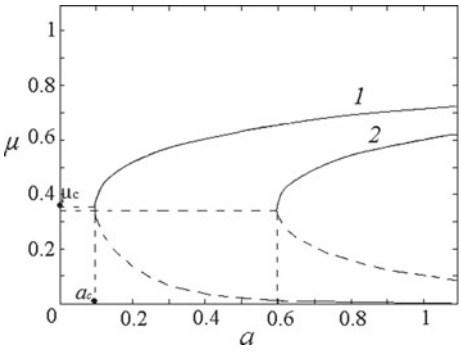

Fig. 7 The order orientational parameter (continuous line) μ of infinitely extended system versus the persistent length a for the given value of the mean-field parameter $q = 1$ and different values of the parameter of interchain interactions $b = 0.5$ (*1*), 0.1 (*2*)

the parameters a, b, q. The long-range orientational order decreases also with the decrease in interchain interactions (parameter b) (the solid line in Fig. 6). The phase transition occurs at a certain value of the parameter b, when the value μ changes abruptly. As the interaction between molecules located on the surface and in the bulk decreases (parameter q), the phase transition occurs at higher values b_c, and the value of the jump for the order parameter decreases. In the absence of the bulk ($q = 0$), the long-range order does not exist in such system, that is in full accordance with the Mermin-Wagner-Hohenberg theorem.

Similar results were obtained for the dependence of the orientational order parameter on the values of the persistent length a (Fig. 7). At certain value of the persistent length a_c, the phase transition occurs and the value μ changes abruptly. When the value of the interchain interaction parameter decreases, the phase transition occurs at higher values a_c, and the value of the jump in the order parameter decreases.

Figure 8 shows the dependence of the long-range orientational order parameter on the mean-field parameter under different boundary conditions. The curve *1* corresponds to the sufficiently extended system, that is, the quantity μ is a solution of Eq. (13.1). The curve *2* is calculated under free boundary conditions [solution of Eq. (13.2)], and the curve *3* is calculated at fixed boundary conditions [Eq. (13.3)]. When introducing free boundary conditions, the order parameter decreases, and the

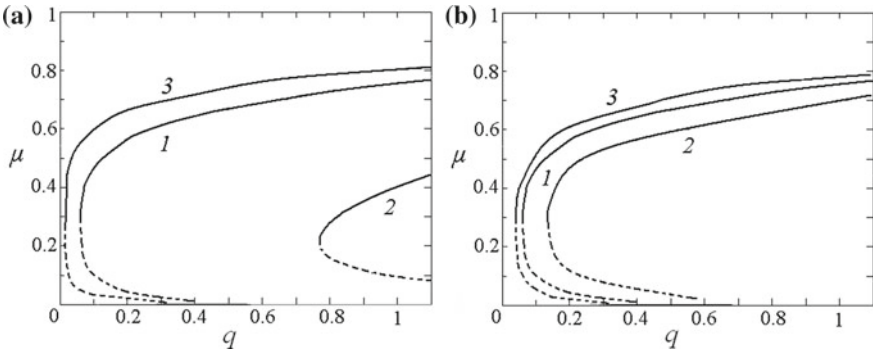

Fig. 8 **a**, **b** The long-range orientational order parameter versus the mean-field parameter for infinitely extended system (*1*), and systems with free (*2*) and fixed (*3*) boundary conditions. The parameters $a = 1$, $b = 1$, the number of chains $M = 20$ (**a**), 100 (**b**)

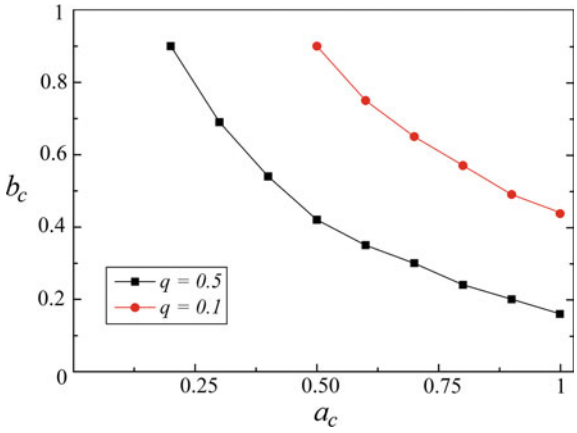

Fig. 9 The interchain interactions parameter b at the phase transition point versus the persistent length a at a constant average field parameter $q = 0.1, 0.5$

critical value of the mean field increases. Conversely, the system with fixed boundary conditions has a larger order and a lower critical value of the mean field.

Figure 9 shows the dependence of the critical value of the parameter of interchain interactions b_c at the phase transition point on the critical value of the persistent length a_c for different values of the mean-field parameter $q = 0.1, 0.5$ for infinitely extended system.

The properties of the surface layers differ from the internal bulk parts of the film. The phase transition point on the surface is determined not only by the persistent length and the interchain interaction parameter, but also by the interaction with the bulk, which is the determining one. The value of the interaction is determined by the distance between the layers of the polymer system. As the distance between layers

decreases, the value of the mean field decreases, leading to the decrease of the phase transition temperature.

4 Effect of Thickness on the Magnitude of Spontaneous Polarization in Thin Ferroelectric Films

To describe properties of the ferroelectric films and to study of ordering effects we use a three-dimensional lattice model (Fig. 10), consisting of N_1, N_2 and N_3 nodes along the respective axes of the Cartesian coordinate system. The position of the lattice node is characterized by the set of three numbers $\vec{n} = (n_1, n_2, n_3)$.

In this paper, the interaction energy of dipoles is described by a potential that takes into account the energy of orientation interactions (as in the classical Ising model) and the additional term representing the Lennard-Jones potential:

$$H = H_{or} + \sum_{\vec{n},\vec{m}} \varepsilon \left(\frac{r_0^{12}}{r_{\vec{n},\vec{m}}^{12}} - \frac{2r_0^6}{r_{\vec{n},\vec{m}}^{6}} \right), \tag{14}$$

where ε is the potential well depth of the Lennard-Jones potential, $r_{\vec{i},\vec{j}}$ is the distance between the dipoles, r_0 is average distance in the absence of orientation interactions.

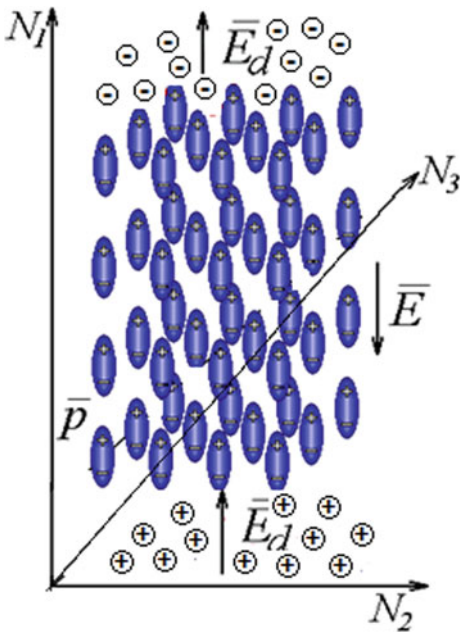

Fig. 10 The three-dimensional lattice model of the thin ferroelectric film

The second term of Eq. (14) does not depend on the temperature and the polarization, in contrast to the first term.

When the polarization decreases, therefore, we must take into account that the distance between the dipoles changes in transverse dimensions N_2 and N_3 of film. The potential of orientation interactions H_{or} is represented by the formula:

$$H_{or} = -\sum_{\vec{n}} K_1 S_{n_1,n_2,n_3} S_{n_1-1,n_2,n_3} - \sum_{\vec{n}} K_2 \frac{r_0^3}{r^3} S_{n_1,n_2,n_3} S_{n_1,n_2-1,n_3}$$
$$- \sum_{\vec{n}} K_2 \frac{r_0^3}{r^3} S_{n_1,n_2,n_3} S_{n_1,n_2,n_3-1} + p \sum_{\vec{n}} S_{\vec{n}} E_d, \tag{15}$$

where the quantity $S_{\vec{n}}$ takes only two values $+1$ and -1, K_1 is the coefficient of exchange interactions in the longitudinal direction, p is the dipole moment, K_2 is the constant of exchange interactions between the dipoles in the transverse direction, E_d is the projection of the vector of the depolarizing field strength on the direction N_1.

The short-range orientation order parameters in the longitudinal and transverse directions $\mu_{||}$ and $\mu_{\perp}$ are determined by the following formulas, correspondingly:

$$\mu_{||} = \frac{1}{N_1 N_2 N_3} \left(\sum_{\vec{n}} S_{n_1,n_2,n_3} S_{n_1-1,n_2,n_3} \right), \tag{16a}$$

$$\mu_{\perp} = \frac{1}{2N_1 N_2 N_3} \left(\sum_{\vec{n}} S_{n_1,n_2,n_3} S_{n_1,n_2-1,n_3} + \sum_{\vec{n}} S_{n_1,n_2,n_3} S_{n_1,n_2,n_3-1} \right). \tag{16b}$$

To simplify the calculations the variable $x^3 = \frac{r_0}{r}$ was introduced. The values $\mu_{||}$ and $\mu_{\perp}$ depend on the variable x. As an example, Fig. 11 shows the dependence of the short-range orientation order parameter $\mu_{\perp}$ on the variable x at different reduced temperatures.

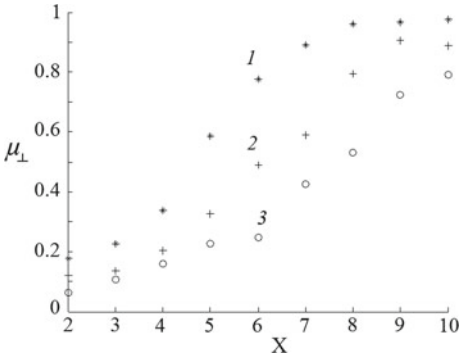

Fig. 11 The short-range orientation order parameter $\mu_{\perp}$ versus the variable x at different the reduced temperature $k_B T/K_1 = 15$ (*1*), 20 (*2*), 25 (*3*) $\varepsilon/K_1 = 0.01$, $K_2/K_1 = 1$

In contrast to the classical Ising model, the interaction between dipoles in the model considered depends on the distance, so for this it was necessary to calculate the mean value of the distance at which the potential energy experiences a minimum.

The mean distance between dipoles has been determined by finding the minimum of the function:

$$h = 4\varepsilon\left(\frac{r_0^{12}}{r^{12}} - \frac{2r_0^6}{r^6}\right) - 2K_1\mu_{||} - 4K_2\mu_{\perp}\frac{r_0^3}{r^3}. \tag{17}$$

The differentiation of Eq. (4) with respect to r leads to the equation:

$$\varepsilon\left(4x^3 - 4x\right) - \frac{1}{2}K_1\frac{\partial\mu_{||}(x)}{\partial x} - K_2\frac{\partial\mu_{\perp}(x)}{\partial x}x - K_2x\mu_{\perp}(x) = 0. \tag{18}$$

To solve Eq. (18) the functions $\mu_{||}(x)$ and $\mu_{\perp}(x)$ were calculated by the Monte Carlo method, these functions were approximated by the function $erf\left(\frac{x-m}{\sigma}\right)$, where m and σ are fitting coefficients.

The change of properties of the system under an external action is described as its response to this action: for example, the dielectric susceptibility:

$$\chi = \frac{1}{k_BT}\left[\left\langle S_{\vec{n}}^2\right\rangle - \left\langle S_{\vec{n}}\right\rangle^2\right], \tag{19}$$

reflects the polarization change upon the application of an electric field.

Figure 12 shows the dependence of the mean distance between the dipoles (a) and the susceptibility of the ferroelectric system (b) on the reduced temperature for different values of the potential well depth in the absence of the depolarizing field.

We see that as the temperature is increased, the mean distance near the phase transition point increases abruptly. At high temperatures, the distance between dipoles $r \to r_0$. With a decrease in the of the potential well depth of the Lennard-Jones potential, the mean distance between the dipoles decreases, which leads to a shift of the phase transition point to higher temperatures.

Influence of depolarizing field

Under the action of an internal electric field caused by the spontaneous polarization, free particles move to the outer surfaces of the film and create an additional depolarizing field which depends on the value of the long-range orientation order:

$$E_d(n_1) = E_0\mu\left(\mathrm{e}^{-\lambda(N_1-n_1)}S_{n_1,n_2,n_3} + \mathrm{e}^{-\lambda(n_1-1)}S_{n_1,n_2,n_3}\right), \tag{20}$$

where E_0 and λ are constants determined by the number of free carriers in the film, μ is the long-range order parameter in the ferroelectric system, which is determined by the following formula:

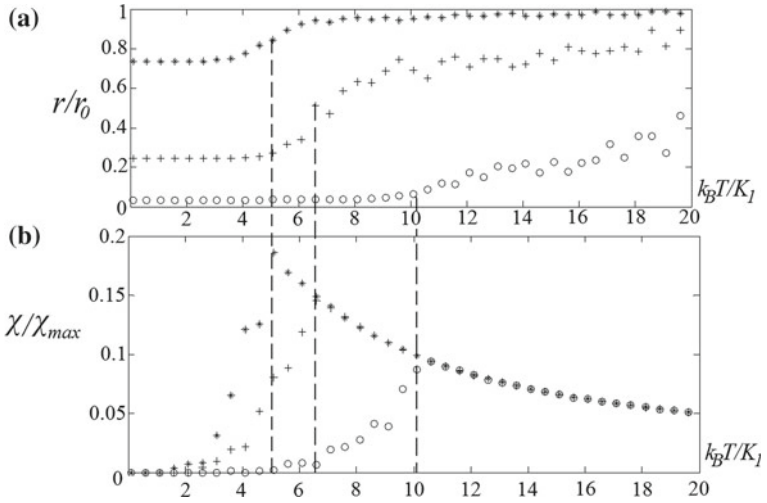

Fig. 12 The mean distance between the dipoles r/r_0 (**a**) and the susceptibility of the ferroelectric system $\chi/\chi\text{max}$(**b**) versus the reduced temperature k_BT/K_1 for values of the potential well depth $\varepsilon/K_1 = 1$ (*), 0.1 (+), 0.01 (o) in the absence of the depolarizing field

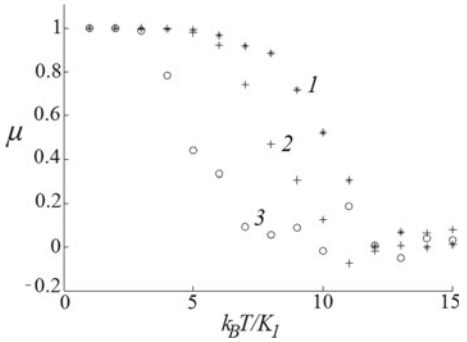

Fig. 13 The long-range orientational order parameter μ versus the reduced temperature k_BT/K_1 without the depolarizing field (*1*), at different values of the reduced field $pE_d/K_1 = 5$ (*2*), 10 (*3*) and the potential well depth $\varepsilon/K_1 = 0.01$

$$\mu = \frac{1}{N_1 N_2 N_3}\left(\sum_{\vec{n}} S_{\vec{n}}\right). \tag{21}$$

Figure 13 shows the dependence of the long-range orientational order parameter μ on the reduced temperature k_BT/K_1 for different values of the depolarizing field. It is shown that the inclusion of a depolarizing field leads to a decrease in the order parameter and to a shift of the phase transition point to the region of lower temperatures.

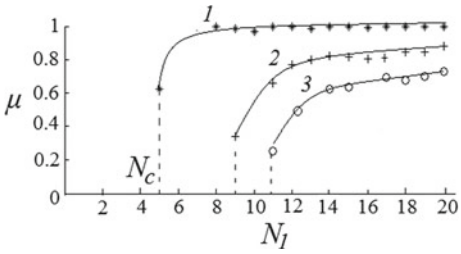

Fig. 14 The long-range order parameter μ versus the thickness of the ferroelectric film N_1 at different the reduced temperatures $k_BT/K_1 = 2$ (*1*), 7 (*2*), 10 (*3*) and the potential well depth $\varepsilon/K_1 = 0.01$

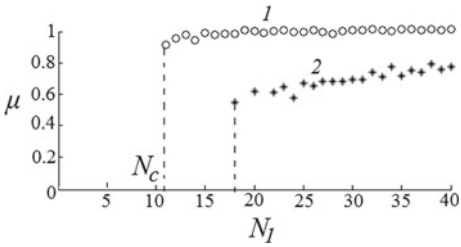

Fig. 15 The long-range order parameter μ versus the thickness of the ferroelectric film N_1 at different the potential well depth $\varepsilon/K_1 =$ 0.01 (*1*), 1 (*2*) and the reduced temperature $k_BT/K_1 = 5$

Figures 14 and 15 show the dependence of the long-range order parameter on the thickness of the ferroelectric film (N_1) at the different t reduced temperatures and the potential well depth. As the thickness of the film decreases, the polarization decreases, and it decreases sharply to zero at a certain thickness. In sufficiently thin films, the polarization is not observed even at low temperatures. This resulted may be explained by the fact that its thickness is less than two values of the thickness of the "dead" layer. The double thickness of the "dead" layer is considered as the critical size of ferroelectric film, at which the ferroelectric loses its ferroelectric properties, and becomes a linear dielectric. As shown in Figs. 14 and 15, the thickness of the "dead" layer is 2–10 unit cells. The critical thickness N_C increases with decrease in the well depth of the potential of Lennard-Jones (Fig. 14) and increasing temperature (Fig. 15). Experimental techniques allowed to investigate the perovskite ferroelectric film with a thickness of 40 Å (ten unit cells) [31]. The authors of ref. [32] identified a critical thickness of about three unit cells, below which there was no ordering at low temperatures. The difference in the experimental results can be explained by the difference of the potential well depth and the concentration of free carriers in the materials considered.

The correlation effect in thin ferroelectric films leads to ordering, which in turn leads to the appearance of a surface charge density, the depolarizing field, and also to the presence of the "dead" layer.

5 Modeling of Geometric and Optical Properties of Textured Coatings of Steel Sheet with Anisotropic Defects

The solution of the problem of creating surfaces with certain properties is necessary both for stable functioning of products and technological control of the surface quality of such products [33]. The use of the fractal approach to describe structural in homogeneities, as well as the justification of general regularities, is one of the modern scientific trends in the surface physics and the chemistry of solids. At present, various mathematical models of fractals (Sierpinski rug, Mandelbrot set), describe well the real imperfections (Brownian) surfaces of metal layers, dielectric layers [34], semiconductor surfaces [35] those have defects of a symmetric type [36, 37]. However, when examining the surface of polymer coatings of metal sheet, the detected defects are anisotropic (Fig. 16a); therefore, these models cannot be used to describe their structure. In this paper, the three-dimensional anisotropic model based on the Julia set will be used to construct a fractal model of the surface.

Algorithm of creating of the fractals

To construct fractal surfaces of the extured polymer coating of sheet metal (Fig. 16a, b), the following algorithm was used:

1. The area in which the fractal is created is divided into 1000 × 1000 rectangles. Each rectangle is characterized by the coordinates $\left(X_{r,s}, Y_{r,s}\right)$ of its center.
2. A sequence is defined by the recurrence formula [38].

$$Z_{r,s}^{(n)} = \left(Z_{r,s}^{(n-1)}\right)^2 + p + iq, \tag{22}$$

where values p and q are parameters of the fractal function (22). The first term of the sequence is defined as

$$Z_{r,s}^{(1)} = X_{r,s} + iY_{r,s}.$$

3. The value of H is select inversely to the rate of increase of the modulus of the sequence term (1). H is equal to the smallest number of the sequence term, when $|z_i| > Q$. In our calculations, we assumed that the value is $Q = 10^6$.

The examples of fractal functions obtained are shown in Fig. 16c, d.

Determining the geometrical parameters of the fractal functions

The type of defects (grooves) in the textured coatings depends on conditions of its formation. The surface relief images of two samples coated by the same polyester material are shown In Fig. 16a, b. The coating of the sample 2 was formed at a higher temperature, which affected the parameters of the grooves. Table 1 presents the mean parameters of the "grooves" on the surface of the samples 1 and 2. To determine

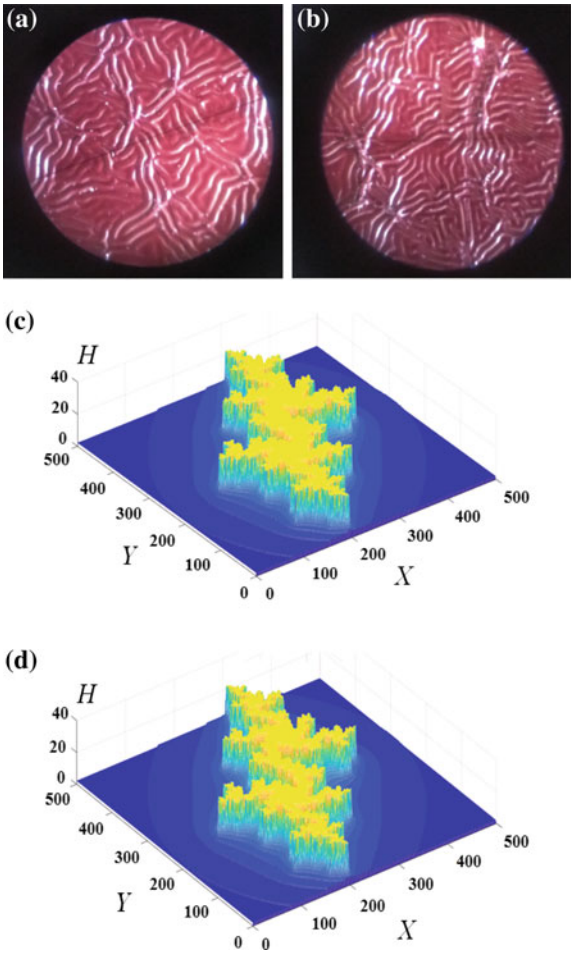

Fig. 16 The pictures of samples surfaces 1 and 2 obtained by then optical microscope method (**a** and **b**) and their fractal models (**c** and **d** correspondingly)

the parameters of the fractal model p and q, the constructed fractal functions were compared with the surface images (Table 1).

To determine the scale ratio $m = L/L_0$, the middle length L_0 of grooves measuring by the optical microscope method (see Fig. 16a, b) and the length of the median line of the fractal function L (see Fig. 17b) were compared. For this purpose, at the construction of fractals, we used the cubic polynomial approximation (Fig. 17a) and calculated its length L.

The width d is defined by dividing the polygon fractal area and the length L. The radius of curvature R is determined as the mean radius of curvature of the median line.

Table 1 The parameters of textured coatings measured with an optical microscope and parameters of their fractal models

No.	Average values of furrows parameters				Model parameters		
	Width d (μm)	Length (μm)	Height (μm)	Radius of curvature (μm)	p	q	Scale $m = L/L_0$ (μm^{-1})
1	34.7	545	36.2	1378	−0.55375	0.55008	0.945
2	28.5	523	31.3	1371	−0.57125	0.55047	0.985

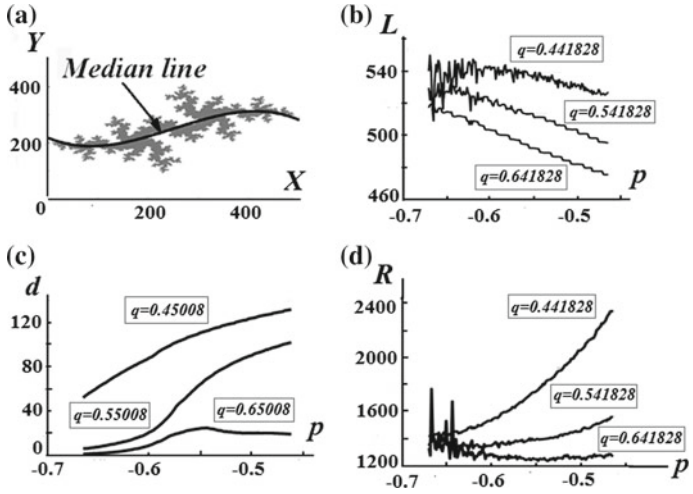

Fig. 17 The construction of the median line (**a**). The length of the median line (**b**), the mean width of the polygon (**c**) and the average curvature (**d**) versus the parameter p for different values of the parameter q

Figure 16c, d show fractal functions for samples 1 and 2, under which the experimental and theoretical parameters coincide. Figure 17c, d show the dependences of the values of d and R on the parameters p and q of the fractal function (1).

The fractal dimension was calculated using the following algorithm:

- A cube is constructed in the three-dimensional $N \times M$ space, where N and M are the numbered points of the fractal surface. The size of the cube edge must be a factor of the smallest unit of the fractal surface.
- It is checked, whether the constructed cube locates particularly or fully in the fractal figure.
- If it locates, then the number of cubes is increased by one.
- The neighboring cube is constructed.
- Firstly, the bottom level of the surface is filled, and then the next level is filled, etc.
- If at some level, no cube enters in the fractal (the empty space), then the cycle is finished.

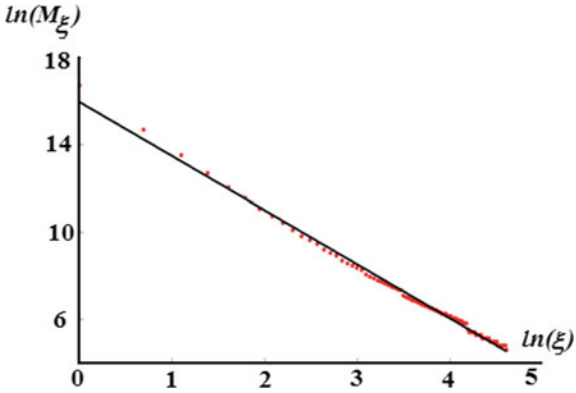

Fig. 18 Determination of the fractal dimension. The points represent the modeling data; the solid line is the corresponding linear regression

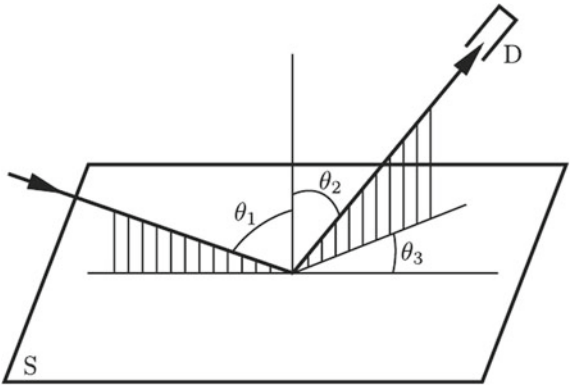

Fig. 19 A schematic representation of the light scattering experiment

The dependence $\ln(M_\xi)$ on $\ln \xi$ is shown in Fig. 18. Here M_ξ is the number of cubes entering in the fractal, and ξ is the cube edge. From the slope of this dependence we obtained the value of fractal dimension $k = 2, 29$.

Study of optical properties of textured surfaces

The scattering of light is associated with a number of structural features of polymers, and it is widely used for their investigation [39–41]. In this paper, it was assumed that light falls on a rough surface S at a given angle of falling light θ_1, and it is scattered in all directions. The scattered wave is characterized by the polar angle θ_2 and the azimuthal angle θ_3 (Fig. 19). The intensity of light scattered in the direction (θ_2, θ_3) is measured by the detector D.

Using the basic formulas of the Kirchhoff method, the strength of scattered field is calculated under the following conditions:

- the incident wave is monochromatic and flat;
- the scattering surface is rough inside the rectangle under consideration and smooth beyond the boundaries;
- the size of the rough surface is much larger than the length of the incident wave;

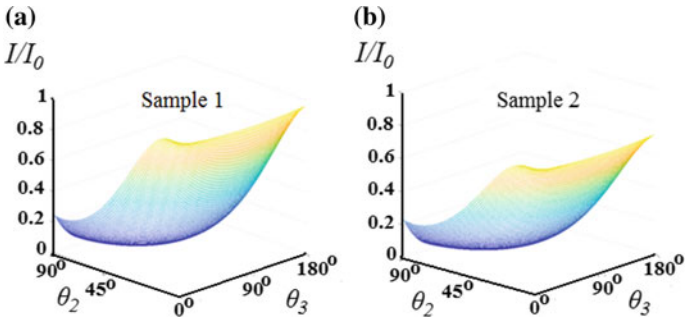

Fig. 20 The reduced intensity of scattered light versus the polar θ_2 and horizontal θ_3 angles for the samples being considered. $\theta_1 = 45°$

- the scattering field is observed in the wave zone, i.e., far enough from the scattering surface.

To study the scattering of light, we used the formulas given in ref. [41]. The dependence of the reduced intensity of scattered of light I/I_0 on the angles θ_2 and θ_3 at $\theta_1 = 45°$ for the red light is shown in Fig. 20. Here I_0 is the maximum calculated value for the sample 1.

The intensity of the light scattered by the surface of sample 2, formed at a higher temperature, is less by 21%. For experimental verification of the results obtained, the gloss of the samples under study was measured. Experimental study has shown that at the same angle of incident light, the gloss of sample 2 is 18% less than for sample 1. The difference between theoretical and experimental results may be explained by the fact that photometric instruments in studying such textured coatings have large errors due to strong scattering of light on them.

6 Conclusion

In this work, by means of analytical methods and computer simulation we have investigated some properties of metamaterials.

Recently, the development of fast algorithms for the JDOS (the joint density of states) calculation is an actual problem. In this work, we employ the modified parallel Wang-Landau algorithm for JDOS, which combines ideas of global updates and two level methods. The algorithm for fast determination of JDOS is proposed. This algorithm combines ideas of global updates consideration and two level methods. The method is analyzed and validated for the two-dimensional ferromagnetic Ising model.

In this work, we considered the equilibrium properties and phase transitions on the surface of ferroelectric polymer system, in which orientational interactions are taken into account both between the surface molecules and molecules located in the bulk.

The properties of the surface layers differ from the internal bulk parts of the bodies. The phase transition point on the surface is determined not only by the persistent length and the interchain interaction parameter, but also by the interaction with the bulk which is the determining one. The value of the interaction is determined by the distance between the layers of the polymer system. As the distance between layers decreases, the value of the mean field decreases, leading to the decrease in the phase transition temperature.

The research results concerning in thin ferroelectric films showed that correlation effects related with the ordering in films lead to the appearance of a surface charge density, the depolarizing field, and also to the presence of the "dead" layer.

It is shown that the depolarizing field decreases the polarization of the film and shifts the phase transition point to the region of lower temperatures. The polarization in sufficiently thin films is not observed even at low temperatures. This result can be explained by the fact that its size is less than double thickness of the "dead" layer that is considered as the critical size of the film, at which its ferroelectric properties disappear, and the film becomes a usual dielectric material. The value of the critical thickness increases with decrease in the well depth of the potential of Lennard-Jones and increasing temperature. In the frame of approach proposed in this paper, such difference in the experimental results can be explained by the difference of the potential well depths and the concentrations of free carriers in the materials considered.

Surfaces of textured polymer coatings of metal sheet are rough and can change their shape under different conditions of their formation. The texture of such rough surfaces of polymer coatings seems chaotic, so a theoretical study of the phenomena occurring on them (for example, the scattering of light, color, and gloss) is difficult. However, applying this technique, we can select the appropriate fractal function and apply standard methods for various kinds of research.

The physical phenomena occurring on these surfaces cannot be described in terms of the standard deviation of the peak height of the correlation function for them. Real surfaces are most adequately described by fractal functions that are confirmed by experimental results on the scattering of light. These results can be used to study other physical phenomena on the surfaces described, such as friction, electrical conductivity, and capacity.

Acknowledgements The work is performed within the framework of the project "Methods of microstructural nonlinear analysis, wave dynamics and mechanics of composites for research and design of modern metamaterials and elements of structures made on its base" (grant No. 15-19-10008-P of by the Russian Science Foundation).

References

1. Wolff, A.: New system for automatic control of colour-coating lines. Stahl und eisen **8**, 11 (2003)
2. Gun, G.: Optimization of Technological and Operational Deformation of Products with Coatings. Magnitogorsk, p. 323 (2006)
3. Oura, K.: Introduction to surface physics, M. In: Science, p. 496 (2006)
4. Pratton, M.: Introduction to Surface Physics. Izhevsk, p. 256 (2000)
5. Roldugin, V.: Physical Chemistry of the Surface. Intellect, Dolgoprudny, p. 586 (2008)
6. Vaz, C.: Magnetism in ultrathin film structures. Rep. Prog. Phys. **71**, 056501 (2008)
7. Shilov, S.: Segmental orientation and mobility of ferroelectric liquid crystal polymers. Liq. Cryst. **22**(2), 203–210 (1997)
8. Zentel, R.: Ferroelectric liquid-crystalline elastomers. Adv. Mater. **6**(7/6), 598–599 (1994)
9. Warner, M.: Nematic elastomers—a new state of matter. Prog. Pol. Sci. **21**(5), 853–891 (1996)
10. Saiko, D., Darinskii, B., Yavlyanskaya, I., Budanov, A.: Numerical study of the minima of the thermodynamic potential of a ferroelectric barium titanate. Bull. Voronezh State Univ. Eng. Technol. **2**, 125–130 (2016)
11. Rossetti, G., Maffei Jr., N.: Specific heat study and Landau analysis of the phase transition in $PbTiO_3$ single crystals. J. Phys. Condens. Matter **7**(25), 3953–3963 (2005)
12. Ginsburg, V.: Phase transitions in ferroelectrics. Phys. Usp. **171**(10), 1091–1097 (2001)
13. Dubrovskii, S., Vasil'ev, V.: Computer simulation of the influence of the functionality of nodes on the elasticity of polyacromonomer grids. Polym. Sci. A **53**(6), 925 (2011)
14. Osari, K., Koibuchi, H.: Finsler geometry modeling and Monte Carlo study of 3D liquid crystal elastomer polymer. Polymer **114**, 355–369 (2017)
15. Tepluchin, A.: Simplified accounting of deformations of valence bonds and angles in full-atom modeling of polymers by the Monte-Carlo method. Polym. Sci. C **55**(7), 911–919 (2013)
16. Wang, F., Landau, D.: Efficient, multiple-range random walk algorithm to calculate the density of states. Phys. Rev. Lett. Am. Phys. Soc. **86**(10), 20-50–20-53 (2001)
17. Wust, T., Landau, D.: Optimized Wang-Landau sampling of lattice polymers: ground state search and folding thermodynamics of HP model proteins. J. Chem. Phys. **137**(6), 064903 (2012)
18. Metropolis, N., et al.: Equation of state calculations by fast computing machines. J. Chem. Phys. **21**(6), 1087–1092 (1953)
19. Wolff, U.: Collective Monte Carlo updating for spin systems. Phys. Rev. Lett. **62**(4), 361 (1989)
20. Lee, J.: New Monte Carlo algorithm: entropic sampling. Phys. Rev. Lett. **71**(2), 211 (1993)
21. Wang, F., Landau, D.: Efficient, multiple-range random walk algorithm to calculate the density of states. Phys. Rev. Lett. **86**(10), 2050 (2001)
22. Swendsen, R., Wang, J.-S.: Replica Monte Carlo simulation of spin-glasses. Phys. Rev. Lett. **57**(21), 2607 (1986)
23. Suzuki, S., et al.: Quantum Ising Phases and Transitions in Transverse Ising Models, vol. 862. Springer, Berlin (2012)
24. Sherrington, D., Kirkpatrick, S.: Solvable model of a spin-glass. Phys. Rev. Lett. **35**(26), 1792 (1975)
25. Cohen, E., Heiman, R., Hadar, O.: Image and video restoration via Ising-like models. In: Image Processing: Algorithms and Systems X; and Parallel Processing for Imaging Applications II, vol. 8295 (2012)
26. Onsager, L.: Crystal statistics. I. A two-dimensional model with an order-disorder transition. Phys. Rev. **65**(3–4), 117 (1944)
27. Vogel, T., et al.: Scalable replica-exchange framework for Wang-Landau sampling. Phys. Rev. E **90**(2), 023302 (2014)
28. Chan, C.-H., Brown, G., Rikvold, P.: Macroscopically constrained Wang-Landau method for systems with multiple order parameters and its application to drawing complex phase diagrams. Phys. Rev. E. **95**(5), 053302 (2017)

29. Grischenko, A., et al.: Self-organization of polymer molecules at interphase boundaries. SPBU, St. Petersburg (2010)
30. Grischenko, A., Cherkasov, A.: Orientational order in surface layers. Adv. Phys. Sci. **40**, 257 (1997)
31. Junquera, J., Ghosez, P.: Critical thickness for ferroelectricity in perovskite ultrathin films. Nature **422**(3), 506–509 (2003)
32. Jaita, P., Takeshi, N., Kawazoe, Y., Waghmare, U.: Ferroelectric phase transitions in ultrathin films of $BaTiO_3$. Phys. Rev. Lett. **99**, 077601 (2007)
33. Potapov, A., Bulavkin, V., German, V., Vyacheslavova, O.: The researching of micro structure surfaces with methods of fractal signatures. Tech. Phys. **50**(5), 560–575 (2005)
34. Wang, M., Li, J., Ren, L.: Characteristics of EM scattering on dielectric fractal surface. Chin. Sci. Bull. **42**(6), 523 (1997)
35. Torkhov, N., Bozhkov, V.: Fractal character of the distribution of surface potential irregularities in epitaxial n-GaAs (100). Semiconductors **43**(5), 551 (2009)
36. Kuzmin, O., Malakichev, A.: Geometric fractals modeling through infinite graphs. Mod. Technol. Syst. Anal. Model. **35**(3), 79 (2012)
37. Gehani, A., Agnihotri, P., Pujara, D.: Analysis and synthesis of multiband Sierpinski carpet fractal antenna using hybrid neuro-fuzzy model. Prog. Electromagnet. Res. Lett. **68**, 59 (2017)
38. Otto, H., Peter, R.: The Beauty of Fractals. Springer, Heidelberg (1986)
39. Zamani, M., Shafiei, F., Fazeli, S., Downer, M., Jafari, G.: Analytic height correlation function of rough surfaces derived from light scattering. Phys. Rev. E. **94**, 042809 (2016)
40. Gozhenko, V., Pinchuk, A., Semchuk, O.: Electromagnetic wave scattering by fractal surface. Ukr. J. Phys. **45**(9), 1129 (2000)
41. Semchuk, O., Grechko, L., Vodopianov, D., Kunitska, L.: Features of light scattering by surface fractal structures. Task Q. **13**(3), 199 (2009)

Diffraction of the High-Frequency Waves by Arrays of Obstacles in the Two-Dimensional Elastic Medium, with Multiple Reflections and Transformations

Nikolay V. Boyev

Abstract Within the geometric theory of diffraction, the problem of the propagation of ultrasonic waves through array of obstacles in an infinite two-dimensional elastic medium is investigated. A tonal impulse of a time-harmonic longitudinal or transverse plane elastic high-frequency wave of several wave-lengths is introduced through the array of obstacles, and in a certain domain inside the elastic medium the through-transmitted wave with arbitrary reflections and transformations is received. Some integral representations for displacement in the reflected waves are written out on the basis of the Kirchhoff physical diffraction theory. With the use of an asymptotic estimate of multiple diffraction integrals by the multidimensional stationary phase method we have written out explicitly the geometric-theory approximation for displacements in the multiply reflected and transformed waves.

1 Introduction

Metamaterials, which are solid inclusions, usually located in the nodes of the periodic lattice and rigidly adhered to the elastic matrix, have important acoustic properties, including filtration ones. The latter are confirmed experimentally [1] and in the acoustic approximation theoretically [2]. The theoretical basis for studying the acoustic properties of such materials is the solution of the problem of the short-wave diffraction of longitudinal and transverse elastic waves on the array of obstacles in an elastic medium, taking into account their various reflections and transformations at mirror reflection points. Single and double reflections and transformations of short acoustic and elastic waves were investigated in [3–6]. An explicit form of the geometric-optical approximation of displacements is obtained for multiple reflections of longitudinal waves from the triple-periodic system of solid round inclusions in the elastic matrix of the metamaterial [2]. The present paper is devoted to the development of the

N. V. Boyev (✉)
Southern Federal University, 105/42 Bolshaya Sadovaya Str.,
Rostov-on-Don 344006, Russian Federation
e-mail: boyev@math.rsu.ru

M. A. Sumbatyan (ed.), *Wave Dynamics, Mechanics and Physics of Microstructured Metamaterials*, Advanced Structured Materials 109,
https://doi.org/10.1007/978-3-030-17470-5_5

ray diffraction theory with respect to arbitrary (nonconvex) smooth two-dimensional obstacles in an elastic medium. Within the geometric theory of diffraction, high-frequency waves are scattered on array of obstacles in a two-dimensional elastic medium, taking into account all possible multiple reflections and transformations.

2 Problem Formulation

In an infinite two-dimensional elastic medium there is an array of obstacles. The obstacles can be of two types: absolutely solid and voids. In the array of obstacles, a pulse is introduced with a tonal filling by several periods of a planar high-frequency, monochromatic longitudinal or transverse elastic wave, and in a certain region of the elastic medium, a transmitted wave with any possible reflections (longitudinal wave to longitudinal one, transverse wave to transverse one) and transformations (longitudinal wave to transverse one, transverse wave to longitudinal one).

The aim of the study is to obtain analytical expressions for displacements in the transmitted longitudinal or transverse wave.

3 Method of Solution

The structure of the input pulse makes it possible to investigate the problem in the regime of harmonic oscillations. The incident plane elastic wave is replaced by a set of point sources of cylindrical waves. Each cylindrical wave propagating in an angle with a vertex in the source directed toward the obstacles and a contracted semi-circle is replaced by a system of corresponding radial propagation rays of the elastic wave. Thus, the problem is reduced to a problem of short-wave diffraction of elastic waves in a local formulation. The total field in the region of reception of propagating elastic waves is composed of rays transmitted through a system of obstacles, which can be of the three types: rays transmitted through the obstacle system without diffraction; rays reflected from the system once or a finite number of times.

4 The Study of the Problem in the Local Formulation

Let a circular monochromatic high-frequency wave fall from the point x_0 of the infinite elastic plane to the boundary contour l of an obstacle or a system of obstacles in it. The wave is generated by the force $\mathbf{Q}e^{i\omega t}$ located at point x_0, where ω is the oscillation frequency. In this case, the displacements at the point y of the elastic plane are determined by the Kupradze matrix [7].

The aim is to study the amplitude characteristics of the scattered field by the contours of obstacles in the through-transmitted elastic wave.

In the directions $\mathbf{q}_1$ and $\mathbf{q}_2$ we have asymptotic representations of the amplitudes of displacements in the incident wave

$$\mathbf{u}_{\mathbf{q}}^{(p)}(y) = \frac{Q_{\mathbf{q}}}{4\mu}\mathbf{q}\, i\frac{k_p^2}{k_s^2}\sqrt{\frac{2}{\pi k_p}}\mathrm{e}^{-i\frac{\pi}{4}}\frac{\mathrm{e}^{ik_pR_0}}{\sqrt{R_0}}\left[1+\mathrm{O}\left(\left(\frac{1}{k_pR_0}\right)\right)\right], \quad Q_{\mathbf{q}} = (\mathrm{Q},\mathrm{q}), \quad (1)$$

$$\mathbf{u}_{\mathbf{q}_1}^{(s)}(y) = \frac{Q_{\mathbf{q}_1}}{4\mu}\mathbf{q}_1\, i\sqrt{\frac{2}{\pi k_s}}\mathrm{e}^{-i\frac{\pi}{4}}\frac{\mathrm{e}^{ik_sR_0}}{\sqrt{R_0}}\left[1+\mathrm{O}\left(\frac{1}{k_sR_0}\right)\right], \quad Q_{\mathbf{q}_1} = \big(\mathrm{Q},\mathrm{q}_1\big). \quad (2)$$

Here the tangential direction $\mathbf{q}_1$ is perpendicular to $\mathbf{q}$. $Q_{\mathbf{q}}$ and $Q_{\mathbf{q}_1}$ are the projections of the force $\mathbf{Q}$ on the directions $\mathbf{q}$ and $\mathbf{q}_1$. Here ρ is the mass density, λ, μ are the Lamè coefficients, $k_p = \omega/c_p$, $k_s = \omega/c_s$, c_p and c_S are the wave numbers and the velocities of the longitudinal and transverse waves. The components of the displacement vector in the reflected wave from the free boundary contour at the point x of the elastic plane are determined by the following integral [8]

$$u_k(x) = \int_l \mathbf{T}_y\big[\mathbf{U}^{(k)}(y,x)\big]\cdot\mathbf{u}(y)\,dl, \quad k = 1,2, \quad (3)$$

$$\mathbf{T}_y\big[\mathbf{U}^{(k)}(y,x)\big] = 2\mu\frac{\partial\mathbf{U}^{(k)}}{\partial n} + \lambda\mathbf{n}\,\mathrm{div}\big(\mathbf{U}^{(k)}\big) + \mu\big(\mathbf{n}\times\mathrm{rot}\big(\mathbf{U}^{(k)}\big)\big), \quad (4)$$

where the Kupradze matrix $\mathbf{U}^{(k)}(y,x)$ is obtained from the matrix $\mathbf{U}^{(k)}(y,x_0)$ by replacing x_0 by x and R_0 by $R = \mid y - x \mid$. $\mathbf{T}_y$ is the force vector at the point y, $\mathbf{u}(y)$ is the vector of the total displacement field on the boundary surface, $\mathbf{n}$ is the outer unit normal to the contour l, directed toward the elastic medium.

In the vector of total displacement on the boundary contour and in the vector $\mathbf{T}_y$ at the point y we select the terms determined by the longitudinal (p-wave) and transverse (s-wave) waves.

$$u_k(x) = \int_l \left\{\mathbf{T}_y\big[\mathbf{U}_p^{(k)}(y,x)\big] + \mathbf{T}_y\big[\mathbf{U}_s^{(k)}(y,x)\big]\right\}\cdot[\mathbf{u}(y;p)+\mathbf{u}(y;s)]\,dl_y \quad (5)$$

$$u_k(x) = \int_l \mathbf{T}_y\big[\mathbf{U}_p^{(k)}(y,x)\big]\cdot\mathbf{u}(y;p)\,dl_y + \int_l \mathbf{T}_y\big[\mathbf{U}_s^{(k)}(y,x)\big]\cdot\mathbf{u}(y;p)\,dl_y$$
$$+ \int_l \mathbf{T}_y\big[\mathbf{U}_p^{(k)}(y,x)\big]\cdot\mathbf{u}(y;s)\,dl_y + \int_l \mathbf{T}_y\big[\mathbf{U}_s^{(k)}(y,x)\big]\cdot\mathbf{u}(y;s)\,dl_y \quad (6)$$

The first and last terms describe p–p and s–s reflections, and the second and the third ones p–s and s–p transformations.

As in the classical geometric theory of diffraction developed in scalar acoustics [9] and developed in the dynamic theory of elasticity [10], it is necessary to distinguish the asymptotics in the local and global sense. In the global formulation, the problem is to calculate the total field at the point x of the elastic plane. In this case, on the basis

of the representation (6), the total field at the point x of the elastic medium is made up of four integral terms and an incident circular wave, as represented in (6). The asymptotic solution constructed below has a local character and gives the leading asymptotic term of the amplitude of the diffracted field in a small neighborhood of any ray emerging from the point x_0, reflected from the boundary contour of the obstacle at the point y^*, and arriving at the point x. Obviously, such rays can exist only if both points y^* and x lie in the illuminated region.

5 Two-Fold Reflection of Elastic Waves on the Plane Contours of Obstacles Taking into Account Possible Transformations

This section is devoted to the development of the ray diffraction theory with respect to arbitrary (nonconvex) smooth two-dimensional obstacles in an elastic medium. Double re-reflection of the high-frequency wave, taking into account possible transformations, can be formed both within the contour of one obstacle (Fig. 1) and two different obstacles (Fig. 2). Numerical investigation of the problems of high-frequency scattering of elastic waves is considerably complex if the wavelength is much smaller than the average size of the scatterer. There are some known numerical methods—the finite element method, the method of boundary elements, all require in this case a large number of nodes on the grid. This leads to instability of the calculation. To calculate the displacement amplitude in a multiply re-reflected wave, it is possible to use the Keller geometric theory of diffraction (GTD) [11], based on the use of divergence coefficients, which is rather cumbersome. If we investigate the problem of the reflection of a high-frequency wave from an obstacle contour in an elastic medium with various possible wave transformations of an arbitrary finite number of times N, then it is more convenient to start from the estimate of the N-fold multiple diffraction integral by the multidimensional stationary phase method. The basis for the investigation of the general case of an arbitrary number of re-reflections is the solution of the problem of double reflection (Figs. 1 and 2), to which we turn.

The direct usage of the integral representation (3) over the entire "light" zone for reflected waves is impossible [9], since it does not describe multiply reflected waves. If one substitutes to the Green's formula (3) the solution of [12] for local problems (8) and (10) and as the primary field takes the total field $u(y)$, then the integral formula (3) gives only a single-reflected wave. A doubly reflected wave is obtained only when the values of $u(y)$ include both the primary field and its single reflection. To solve the problem of double re-reflection, we start from the modification [9] of the integral formula (3). Following this modification, the doubly reflected waves will be found by integrating along the neighborhood l_2^* of the second mirror reflection point y_2^* the rays obtained upon single reflection from the neighborhood l_1^* of the first mirror reflection point y_1^*. Such a modification means that when finding the leading term of the asymptotics of the double diffraction integral, we stay within the

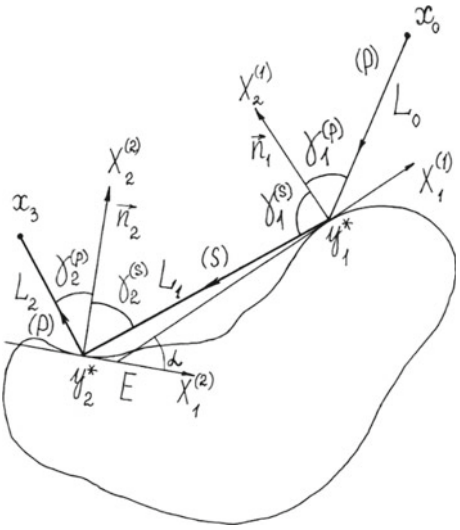

Fig. 1 Two-fold *p–s–p* transformation of a high-frequency longitudinal wave along the ray $x_0 - y_1^* - y_2^* - x_3$ on the boundary contour of one obstacle in an elastic medium

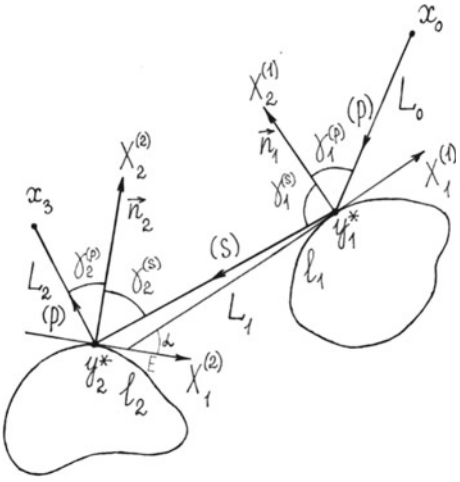

Fig. 2 Two-fold *p–s–p* transformation of a high-frequency longitudinal wave along the ray $x_0 - y_1^* - y_2^* - x_3$ on the boundary contours of two obstacles in an elastic medium

framework of the calculation of the displacement amplitude in a doubly reflected wave in accordance with the GTD.

We consider the reflection of a high-frequency wave using the example of the repeated reflection of a ray $x_0 - y_1^* - y_2^* - x_3$ emitted from a point x_0 [p-wave (1)] and received at a point x_3 with a possible transformation p–s–p (Figs. 1 and 2).

The components of the displacement vector of the p-wave at the point x_3 are given by the following formula

$$u_k^{(p)}(x_3) = \int\limits_{l_2^*} \mathbf{T}_{y_2}\left[\mathbf{U}_p^{(k)}(y_2, x_3)\right] \cdot \mathbf{u}(y_2; s)\, dl_2. \tag{7}$$

Here, $\mathbf{u}(y_2; s)$ is the vector of the complete displacement at the point $y_2 \in l_2^*$ of the neighborhood of the specular reflection point y_2^*, which is determined after the first p–s transformation at the neighborhood of l_1^* of the specular reflection point y_1^*.

In the asymptotic estimate of the Kirchhoff integral in (7), the components of the displacement vector $u_k(y_2; s)$, $k = 1,\ 2$, under the integral sign should be chosen as the solution of the local diffraction problem for the reflection of a plane incident s-wave [12] formed when p–s transforms at a neighborhood l_1^* of the mirror reflection point y_1^*.

$$\begin{aligned} u_1(y_2; s) &= \left(V_{ss}(y_2) - 1 - tg\gamma_1 V_{sp}(y_2)\right) u_1^{(s)}(y_2), \\ u_2(y_2; s) &= \left(V_{ss}(y_2) + 1 + \frac{k_p}{k_s \sin\gamma_1}\sqrt{1 - \frac{k_s^2}{k_p^2}\sin^2\gamma_1}\ V_{sp}(y_2)\right)\ u_2^{(s)}(y_2), \end{aligned} \tag{8}$$

where $V_{ss}(y_2)$ and $V_{sp}(y_2)$ are the reflection coefficients s–s and s–p are the transformation coefficients [12, 13].

At the same time, the components of the displacement vector $u_k^{(s)}(y_2)$, $k = 1,\ 2$ themselves are expressed by a similar formula

$$u_k^{(s)}(y_2) = \int\limits_{l_1^*} \mathbf{T}_{y_1}\left[\mathbf{U}_s^{(k)}(y_1, y_2)\right] \cdot \mathbf{u}(y_1; p)\, dl_1, \tag{9}$$

where the vector of the total displacement field $\mathbf{u}(y_1;\ p)$ at points $y_1 \in l_1^*$ of the neighborhood of y_1^*, should be chosen as the solution of the local diffraction problem on the reflection of a plane incident wave (1) [12]

$$\begin{aligned} u_1(y; p) &= \left(1 + V_{pp}(y) - \frac{k_s}{k_p \sin\gamma}\sqrt{1 - \frac{k_p^2}{k_s^2}\sin^2\gamma}\, V_{ps}(y)\right) u_{1q}^{(p)}(y), \\ u_2(y; p) &= \left(1 - V_{pp}(y) - tg\ \gamma\ V_{ps}(y)\right) u_{2q}^{(p)}(y), \end{aligned} \tag{10}$$

where V_{pp} and V_{ps} are the coefficients of p–p reflection and p–s transformations [12, 13], $u_{1q}^{(p)}(y)$ and $u_{2q}^{(p)}(y)$ are the components of the displacement vector $\mathbf{u}_q^{(p)}(y)$ in the incident p-wave (1).

After substituting (10) into (9), (9) into (8), and (8) into (7) and passing to the local polar coordinate system r, θ at the point y_2^*, we obtain the displacement components at the point x_3:

$$u_r^{(p)}(x_3) = -\frac{Q_{\mathbf{q}}}{4\pi\mu}\left(\frac{k_p}{k_s}\right)^2 2k_s\sqrt{\frac{2}{\pi k_s}}\frac{k_p}{2k_s}\left(-\frac{k_p}{2k_s}\right)e^{-i\frac{\pi}{4}}\frac{\cos\gamma_1\cos\gamma_3}{\sqrt{L_0L_1L_2}} \times V_{ps}\left(y_1^*\right)V_{sp}\left(y_2^*\right)\int\limits_{l_2^*}\int\limits_{l_1^*} e^{ik_p\phi_{psp}}\,dl_1dl_2, \tag{11}$$

$$u_\theta^{(p)}(x_3) = 0,$$

$$\phi_{psp} = |x_0 - y_1| + \frac{k_s}{k_p}|y_1 - y_2| + |y_2 - x_3|,$$

$$L_0 = \left|x_0 - y_1^*\right|, \quad L_1 = \left|y_1^* - y_2^*\right|, \quad L_2 = \left|y_2^* - x_3\right|. \tag{12}$$

At the points of direct mirror reflection $y_1^* \in l_1^*$ and $y_2^* \in l_2^*$, the neighborhoods of these points are related to the Cartesian coordinate systems $O_1X_1^{(1)}X_2^{(1)}$ and $O_2X_1^{(2)}X_2^{(2)}$, determined by the normals $\mathbf{n}_1 = O_1X_2^{(1)}$ and $\mathbf{n}_2 = O_2X_2^{(2)}$ and tangent to the contour of the obstacle, as indicated in Figs. 1 and 2. Along these contours, let us count the length of the arc Δs_1 from the mirror-reflection point y_1^* over a neighborhood of l_1^*, and the length of the arc Δs_2 from the mirror-reflection y_2^* over the neighborhood of l_2^*. For small Δs_1 and Δs_2, let us write out the expressions for the first and the third term of the phase ϕ_{psp}, up to small quantities of the second order, inclusively:

$$|x_0 - y_1| = L_0 + \Delta s_1 \sin\gamma_1^{(p)} + 0.5\left(L_0^{-1}\cos^2\gamma_1^{(p)} + \frac{\cos\gamma_1^{(p)}}{\rho_1}\right)(\Delta s_1)^2, \tag{13}$$

$$|y_2 - x_3| = L_2 - \Delta s_2 \sin\gamma_2^{(p)} + 0.5\left(L_2^{-1}\cos^2\gamma_2^{(p)} + \frac{\cos\gamma_2^{(p)}}{\rho_2}\right)(\Delta s_2)^2. \tag{14}$$

For p–s–p transformation, $\left\{-\sin\gamma_1^{(p)},\ -\cos\gamma_1^{(p)}\right\}$ is the vector which determines the direction of the p-wave (1), and $\left\{-\sin\gamma_1^{(s)},\ \cos\gamma_1^{(s)}\right\}$ is the direction of the reflected wave relatively the coordinate system $O_1X_1^{(1)}X_2^{(1)}$ at the point y_1^*, and $\left\{-\sin\gamma_2^{(s)},\ -\cos\gamma_2^{(s)}\right\}$ is the vector determining the direction of incidence of the s-wave reflected at point y_1^* with respect to the coordinate system $O_2X_1^{(2)}X_2^{(2)}$ at the point y_2^*; while $\left\{-\sin\gamma_2^{(p)},\ \cos\gamma_2^{(p)}\right\}$ is the direction of the reflected p-wave at the point y_2^*.

Let us find the term $|y_1 - y_2| = |\mathbf{y}_2\mathbf{y}_1|$ in the phase ϕ_{psp} (12). The points $y_1 \in l_1^*$ and $y_2 \in l_2^*$ in the local Cartesian coordinate systems $O_1X_1^{(1)}X_2^{(1)}$ and $O_2X_1^{(2)}X_2^{(2)}$ have the coordinates $y_1\left(-\Delta s_1, -\frac{(\Delta s_1)^2}{2\rho_1}\right)$ and $y_2\left(-\Delta s_2, -\frac{(\Delta s_2)^2}{2\rho_2}\right)$, where ρ_i are the radii of curvature of the boundary contours l_1 and l_2 of the two obstacles, respectively, at points y_1^* and y_2^*. The distance $|y_1 - y_2|$ is considered in the coordinate system $O_2X_1^{(2)}X_2^{(2)}$. In this coordinate system we denote the coordinates of the points $y_1(\xi_1, \eta_1)$, $y_2(\xi_2, \eta_2)$, $y_1^*(\ \xi_1^0,\ \eta_1^0\ )$. Taking this into account, we represent the vector $\mathbf{y}_2\mathbf{y}_1$ in the form:

$$\begin{aligned}
&\mathbf{y}_2\mathbf{y}_1 = \mathbf{y}_2^*\mathbf{y}_1^* + \mathrm{A}\mathbf{y}_1^*\mathbf{y}_1 - \mathbf{y}_2^*\mathbf{y}_2,\\
&\mathbf{y}_2\mathbf{y}_1 = \{\xi_1 - \xi_2, \eta_1 - \eta_2\},\ \mathbf{y}_2^*\mathbf{y}_1^* = \left\{\xi_1^0, \eta_1^0\right\}.
\end{aligned} \tag{15}$$

Here $\mathbf{A} = \left(a_{i\,j}\right), i, j = 1, 2$ is the orthogonal transition matrix from the basis of the Cartesian coordinate system $O_2X_1^{(2)}X_2^{(2)}$ at the point y_2^* to the basis of the Cartesian coordinate system $O_1X_1^{(1)}X_2^{(1)}$ at the point y_1^*. The matrix $\mathbf{A}$ has the form (see Figs. 1 and 2)

$$\mathbf{A} = \begin{pmatrix} \cos\alpha & -\sin\alpha \\ \sin\alpha & \cos\alpha \end{pmatrix}.$$

In the local coordinate systems, the vectors $\mathbf{y}_1^*\mathbf{y}_1$ and $\mathbf{y}_2^*\mathbf{y}_2$ have coordinates $\mathbf{y}_i^*\mathbf{y}_i\left(-\Delta s_i, -\frac{(\Delta s_i)^2}{2\rho_i}\right)$. Substituting the coordinates of all the vectors in relation (15), one obtains:

$$\begin{aligned}
|y_1 - y_2| &= \left[(\xi_1 - \xi_2)^2 + (\eta_1 - \eta_2)^2\right]^{1/2}\\
&= \left[\left(\xi_1^0 - \Delta s_1\cos\alpha + \frac{(\Delta s_1)^2}{2\rho_1}\sin\alpha + \Delta s_2\right)^2\right.\\
&\quad \left.+\left(\eta_1^0 - \Delta s_1\sin\alpha - \frac{(\Delta s_1)^2}{2\rho_1}\cos\alpha + \frac{(\Delta s_2)^2}{2\rho_2}\right)\right]^{1/2}.
\end{aligned}$$

By successively squaring each of the brackets in the sum, we obtain the relation up to small quantities of the second order inclusively

$$\begin{aligned}
|y_1 - y_2| = \Big[&L_1^2 - 2\Delta s_1\left(\xi_1^0\cos\alpha + \eta_1^0\sin\alpha\right) + (\Delta s_1)^2 + (\Delta s_2)^2\\
&- 2\Delta s_1\Delta s_2\cos\alpha + \frac{(\Delta s_1)^2}{\rho_1}\left(\xi_1^0\sin\alpha - \eta_1^0\cos\alpha\right)\\
&+2\xi_1^0\Delta s_2 + \eta_1^0\frac{(\Delta s_2)^2}{\rho_2}\Big]^{1/2}
\end{aligned} \tag{16}$$

Let us prove the relation

$$\alpha = \pi - \gamma_1^{(s)} - \gamma_2^{(s)} \tag{17}$$

In the triangle $y_1^* E y_2^*$: $\angle y_2^* y_1^* E = \frac{\pi}{2} - \gamma_1^{(s)}$, $\angle y_1^* y_2^* E = \frac{\pi}{2} - \gamma_2^{(s)}$ and hence $\angle y_1^* E y_2^* = \pi - \left(\frac{\pi}{2} - \gamma_1^{(s)}\right) - \left(\frac{\pi}{2} - \gamma_2^{(s)}\right) = \gamma_1^{(s)} + \gamma_2^{(s)}$. On the other hand, $\alpha + \angle\, y_1^* E\, y_2^* = \pi$. Hence $\pi - \alpha = \gamma_1^{(s)} + \gamma_2^{(s)}$, $\alpha = \pi - \gamma_1^{(s)} - \gamma_2^{(s)}$. Taking into account relation (16), we perform the transformations

$$\begin{aligned}
\xi_1^0 \cos\alpha + \eta_1^0 \sin\alpha &= L_1 \sin\left(\alpha + \gamma_2^{(s)}\right) = L_1 \sin\gamma_1^{(s)},\\
\xi_1^0 \sin\alpha - \eta_1^0 \cos\alpha &= -L_1 \cos\left(\alpha + \gamma_2^{(s)}\right) = L_1 \cos\gamma_1^{(s)},\\
\cos\alpha &= -\cos\left(\gamma_1^{(s)} + \gamma_2^{(s)}\right),
\end{aligned}$$

which permit expression (16) to be rewritten in the form

$$\begin{aligned}
|y_1 - y_2| = L_1 \Bigg[& 1 - 2\frac{\Delta s_1}{L_1}\sin\gamma_1^{(s)} + 2\frac{\Delta s_2}{L_1}\sin\gamma_2^{(s)}\\
& + \frac{(\Delta s_1)^2}{L_1^2}\left(1 + \frac{L_1}{\rho_1}\cos\gamma_1^{(s)}\right) + \frac{(\Delta s_2)^2}{L_1^2}\left(1 + \frac{L_1}{\rho_2}\cos\gamma_2^{(s)}\right)\\
& + 2\frac{\Delta s_1 \Delta s_2}{L_1^2}\cos\left(\gamma_1^{(s)} + \gamma_2^{(s)}\right)\Bigg]^{1/2}.
\end{aligned}$$

Expanding the square root of the right-hand sides in powers of Δs_1 and Δs_2, one obtains the following asymptotic representation for the distance to within small quantities of the second order inclusively:

$$\begin{aligned}
|y_1 - y_2| = L_1 & - \Delta s_1 \sin\gamma_1^{(s)} + \Delta s_2 \sin\gamma_2^{(s)}\\
& + 0.5\left(L_1^{-1}\cos^2\gamma_1^{(s)} + \frac{\cos\gamma_1^{(s)}}{\rho_1}\right)(\Delta s_1)^2\\
& + 0.5\left(L_1^{-1}\cos^2\gamma_2^{(s)} + \frac{\cos\gamma_2^{(s)}}{\rho_2}\right)(\Delta s_2)^2\\
& + L_1^{-1}\Delta s_1 \Delta s_2 \cos\gamma_1^{(s)}\cos\gamma_2^{(s)}
\end{aligned} \tag{18}$$

By summation of the expressions for $|\, x_0 - y_1\,|$, $\frac{k_s}{k_p}\,|\, y_1 - y_2\,|$, $|\, y_2 - x_3\,|$ and using Snell's law $k_p \sin\, \gamma_1^{(p)} = k_s \sin\, \gamma_1^{(s)}$, $k_s \sin\, \gamma_2^{(s)} = k_p \sin\, \gamma_2^{(p)}$, we write out the relation for the phase ϕ_{psp}:

$$\phi_{psp} = L_0 + \frac{k_s}{k_p} L_1 + L_2 + \frac{1}{2}\left(\frac{\cos^{2\cdot} \gamma_1^{(p)}}{L_0} + \frac{k_s \cos^{2\cdot} \gamma_1^{(s)}}{k_p L_1} + \frac{\cos \gamma_1^{(p)}}{\rho_1} + \frac{k_s \cos \gamma_1^{(s)}}{k_p \rho_1} \right) (\Delta s_1)^2$$
$$+ \frac{\cos \gamma_1^{(s)} \cos \gamma_2^{(p)}}{L_1} + \frac{1}{2}\left(\frac{k_s \cos^2 \gamma_2^{(s)}}{k_p L_1} + \frac{\cos^2 \gamma_2^{(p)}}{L_2} + \frac{k_s \cos \gamma_2^{(s)}}{k_p \rho_2} + \frac{\cos \gamma_2^{(p)}}{\rho_2} \right) (\Delta s_2)^2$$

The phase ϕ_{psp} does not contain terms with the first powers of Δs_1 and Δs_2. This indicates that the mirror reflection points are stationary for ϕ_{psp} indeed.

The leading asymptotic term of the double integral (11) can be obtained by applying the method of the two-dimensional stationary phase [14]:

$$u_r^{(p)}(x_3) = -\frac{Q_{\mathbf{q}}}{\mu} \frac{k_p}{k_s} \sqrt{\frac{2}{\pi k_s}} e^{-i\frac{\pi}{4}} \frac{\cos \gamma_1 \cos \gamma_3}{\sqrt{L_0 L_1 L_2}} \times V_{ps}(y^*) V_{sp}(y^*)$$
$$\times \frac{\exp\left\{ i\left[k_p L_0 + k_s L_1 + k_p L_2 + \frac{\pi}{4}\left(\delta_2^{(psp)} - 2 \right) \right] \right\}}{\sqrt{\left| \det D_2^{(psp)} \right|}}. \tag{19}$$

Here $D_2^{(psp)}$ is the Hessian matrix

$$D_2^{(psp)} = \begin{pmatrix} \frac{\cos^2 \gamma_1^{(p)}}{L_0} + \frac{k_s \cos^2 \gamma_1^{(s)}}{k_p L_1} + \frac{\cos \gamma_1^{(p)}}{\rho_1} + \frac{k_s \cos \gamma_1^{(s)}}{k_p \rho_1} & \frac{\cos \gamma_1^{(s)} \cos \gamma_2^{(p)}}{L_1} \\ \frac{\cos \gamma_1^{(s)} \cos \gamma_2^{(p)}}{L_1} & \frac{k_s \cos^2 \gamma_2^{(s)}}{k_p L_1} + \frac{\cos^2 \gamma_2^{(p)}}{L_2} + \frac{k_s \cos \gamma_2^{(s)}}{k_p \rho_2} + \frac{\cos \gamma_2^{(p)}}{\rho_2} \end{pmatrix},$$

and $\delta_2^{(psp)} = sign\ D_2^{(psp)} = \nu^+ - \nu^-$ is the difference between the number of positive ν^+ and negative ν^- eigenvalues of the Hessian matrix $D_2^{(psp)}$.

Thus, in this section we have developed the leading asymptotic term (19) for the amplitude of the displacement $u_r^{(p)}(x_3)$ in the reflected high-frequency longitudinal wave for *p–s–p* transformation from the surfaces of one (Fig. 1) or two (Fig. 2) obstacles in the elastic medium in the two-dimensional case.

The explicit expressions for the principal terms of displacements in the doubly re-reflected waves along the ray $x_0 - y_1^* - y_2^* - x_3$ in the remaining seven cases of various possible reflections and transformations of elastic waves, namely: *p–p–p*, *p–p–s*, *p–s–s*, *s–s–s*, *s–s–p*, *s–p–s*, *s–p–p*, can be obtained by the method described in this section.

6 Multiple Reflections with All Possible Transformations of Elastic Waves

The geometry of the boundary contours of the obstacles in the elastic medium and their arrangement can form such trajectories of the rays $x_0 - y_1^* - y_2^* - \cdots - y_N^* - x_{N+1}$ which lead to any possible sequence of reflections and wave transformations at the points of specular reflection. Suppose that for any N times re-reflected ray, in a certain order, p–p and s–s reflections have been realized at the mirror reflection points $y_1^*, y_2^*, \ldots, y_{N-1}^*, y_N^*$, respectively N_1 and N_3 times, and p–s, and s–p, transformations—respectively N_2 and N_4 times. At the receiving point x_{N+1}, both the longitudinal wave $u(x_{N+1}) = u_r^{(p)}(x_{N+1})$ and the transverse one $u(x_{N+1}) = u_\theta^{(s)}(x_{N+1})$ may be received. In this case, the amplitude of the radial or tangential displacement of the N times reflected ray at the point x_{N+1} relatively the local polar coordinate system r, θ at the point y_N^* of the boundary contour of the obstacle is represented by the multiple Kirchhoff integral, which is formed according to the same laws as the diffraction integral (11), by taking into account reflections and transformations of the propagating ray at the points of mirror reflection:

$$u_r^{(p)}(x_{N+1}) = B(-1)^N \mathrm{e}^{-i\frac{\pi}{4}} \left(\frac{k_p}{2\pi}\right)^{\frac{N_1+N_2}{2}} \left(\frac{k_s}{2\pi}\right)^{\frac{N_3+N_4}{2}} \frac{1}{\sqrt{L_0}} \prod_{n=1}^{N} \frac{\cos\gamma_n^{(2)}}{\sqrt{L_n}} V\left(y_n^*\right) \times \int_{l_N^*} \int_{l_{N-1}^*} \cdots \int_{l_2^*} \int_{l_1^*} \mathrm{e}^{ik_p\varphi} dl_N dl_{N-1} \ldots dl_2 dl_1 \tag{20}$$

$$\varphi = k_p^{-1}\left(k_1|x_0 - y_1| + \sum_{n=1}^{N-1} k_n|y_n - y_{n+1}| + k_N|y_N - x_{N+1}|\right)$$

$$L_0 = \left|x_0 - y_1^*\right|, L_n = \left|y_n^* - y_{n+1}^*\right|, L_N = \left|y_N^* - x_{N+1}\right|, \quad n = 1, 2, \ldots, N-1. \tag{21}$$

Here $B = \frac{Q_{\mathbf{q}}}{4\mu}\left(\frac{k_p}{k_s}\right)^2\sqrt{\frac{2}{\pi k_p}}\left(B = \frac{Q_{\mathbf{q}_1}}{4\mu}\sqrt{\frac{2}{\pi k_s}}\right)$ if the first reflection is either p–p or p–s (respectively, either s–s or s–p). In the expressions (20) and (22), $\gamma_n^{(1)}$, $\gamma_n^{(2)}$ are the angles of incidence and reflection of the corresponding wave at the mirror reflection point y_n^*. Let us select four possible pairs of angles $\gamma_n^{(1)}$, $\gamma_n^{(2)}$

1. $\gamma_n^{(1)} = \gamma_n^{(p)}$, $\gamma_n^{(2)} = \gamma_n^{(p)}$, $V(y_n^*) = V_{pp}(y_n^*)$, (p–p);
2. $\gamma_n^{(1)} = \gamma_n^{(p)}$, $\gamma_n^{(2)} = \gamma_n^{(s)}$, $V(y_n^*) = V_{ps}(y_n^*)$, (p–s);
3. $\gamma_n^{(1)} = \gamma_n^{(s)}$, $\gamma_n^{(2)} = \gamma_n^{(s)}$, $V(y_n^*) = V_{ss}(y_n^*)$, (s–s);
4. $\gamma_n^{(1)} = \gamma_n^{(s)}$, $\gamma_n^{(2)} = \gamma_n^{(p)}$, $V(y_n^*) = V_{sp}(y_n^*)$, (s–p).

if the reflection or transformation indicated in parentheses occurs at the point y_n^*, respectively. $V(y_n^*)$ is the reflection or transformation coefficient [12, 13] at the point y_n^* of the corresponding wave. In the phase φ (21), parameter $k_n = k_p$ (p–p, p–s) and $k_n = k_s$ (s–s, s–p), if the corresponding reflections or transformations of the

wave at point y_n^* are indicated in parentheses. Applying the asymptotic estimate of the diffraction integral (20) in the method of N-dimensional stationary phase [14], we obtain a geometrical-optic approximation of the displacements in the transmitted elastic wave

$$u(x_{N+1}) = B_2 \frac{\exp\left\{i\left[\sum_{n=0}^{N} k_n L_n + \frac{\pi}{4}(\delta_N - (N-1))\right]\right\}}{\left(\prod_{n=0}^{N}\sqrt{L_n}\right)\sqrt{|\det(D_N)|}},$$

$$B_2 = (-1)^{N+N_T} B \prod_{n=1}^{N} \cos\gamma_n^{(2)} V\left(y_n^*\right), \tag{22}$$

where $\delta_N = sign\ D_N$, and $D_N = (d_{nm}), n, m = 1, 2, 3, \ldots, N$ is the Hessian matrix, which is band-like and symmetric $d_{n\,m} = d_{m\,n}$, with the following nonzero elements $d_{n\,m}, n < m$:

$$\begin{aligned} d_{nn} &= \frac{k_{1n}\cos^2\gamma_n^{(1)}}{k_p L_{n-1}} + \frac{k_{2n}\cos^2\gamma_n^{(2)}}{k_p L_n} + \frac{k_{1n}\cos\gamma_n^{(1)}}{k_p \rho_n} + \frac{k_{2n}\cos\gamma_n^{(2)}}{k_p \rho_n}, \quad n = \overline{1, N}, \\ d_{n,n+1} &= L_n \cos\gamma_n^{(1)} \cos\gamma_{n+1}^{(1)}, \quad n = \overline{1, N-1}, \\ d_{nm} &= 0; \quad n \neq m, \quad n \neq m+1. \end{aligned} \tag{23}$$

Here $\gamma_n^{(1)}$ is the angle between the direction of incidence of the wave and $\gamma_n^{(2)}$ is the angle between the direction of reflection of the wave and the external normal to the contour at point y_n^* directed toward the elastic medium, ρ_n is the radius of curvature of the contour at point y_n^*, $V\left(y_n^*\right)$ is the reflection or transformation coefficient at the point y_n^*, N_T is the number of points of specular reflection on the contours of solid obstacles.

In the diagonal elements of the Hesse matrix, the parameters k_{1n} and k_{2n} have four possible pairs of values:

1. $k_{1n} = k_p$, $k_{2n} = k_p$ (p–p);
2. $k_{1n} = k_p$, $k_{2n} = k_s$ (p–s);
3. $k_{1n} = k_s$, $k_{2n} = k_s$ (s–s);
4. $k_{1n} = k_s$, $k_{2n} = k_p$ (s–p);

depending on what kind of reflection or transformation of waves is realized at the point y_n^*.

7 Conclusion

Thus, the leading term of the asymptotics (22) is obtained in the amplitude of the displacement $u(x_{2N+1})$ in the high-frequency longitudinal or transverse wave reflected along the ray $x_0 - y_1^* - y_2^* - \cdots - y_N^* - x_{N+1}$ for an arbitrary sequence of reflections

and transformations from N obstacles in an elastic medium in the two-dimensional case. The amplitude of the displacement in the reflected elastic wave (22) and (23) is determined by the distances from the wave source to the first point y_1^* of mirror reflection L_0, from the last reflecting point y_N^* to the receiving point L_N, the distances L_n, $n = 1, 2, \ldots, N-1$ between the points y_n^* and y_{n+1}^*. The points $y_1^*, y_2^*, \ldots, y_{N-1}^*, y_N^*$ can belong both to the boundaries $l_1, l_2, \ldots, l_{N-1}, l_N N$ of isolated obstacles, and to the boundary l of one obstacle of a complex nonconvex form. There may be cases when single points of specular reflection belong to different obstacles, and simultaneously the cases when several reflecting points belong to different parts of the same obstacle of a complex non-convex form. The leading asymptotic term of the displacement explicitly contains the radii of curvature $\rho_1, \rho_2, \ldots, \rho_{N-1}, \rho_N$ at the points $y_1^*, y_2^*, \ldots, y_{N-1}^*, y_N^*$, the directions of $\gamma_n^{(1)}, \gamma_n^{(2)}$ of the incident and reflected waves at the points of specular reflection, and also the reflection and transformation coefficients $V(y_n^*)$. The phase of the reflected wave $u(x_{N+1})$ (22) is determined by the distances $L_0, L_1, L_2, \ldots, L_{N-1}, L_N$ the wave numbers k_p and k_s, the sign δ_N of the Hessian matrix D_N, and the number of mirror reflection points N.

Acknowledgements The present work is performed within the framework of the Project no. 15-19-10008-P of the Russian Science Foundation (RSCF).

References

1. Liu, Z., Zhang, X., Mao, Y., et al.: Locally resonant sonic materials. Science **289**, 1734–1736 (2000)
2. Boyev, N.V., Sumbatyan, M.A.: Ray tracing method for a high-frequency propagation of the ultrasonic wave through a triple-periodic array of spheres. In: Wave Dynamics and Composite Mechanics for Microstructured Materials and Metamaterials, Advanced Structured Materials, vol. 59. Springer Series, pp. 173–187 (2017)
3. Babich, V.M., Buldyrev, V.S.: Asymptotic methods in short-wavelength diffraction theory. Alpha Sci. Int. (2009)
4. McNamara, D.A., Pistotius, C.W.I.: Introduction to the Uniform Geometrical Theory of Diffraction. Artech House, Microwave Library (1990)
5. Boyev, N.V.: Short-wave diffraction of elastic waves by voids in an elastic medium with double reflections and transformations. In: Wave Dynamics and Composite Mechanics for Microstructured Materials and Metamaterials, Advanced Structured Materials, vol. 59. Springer Series, pp. 91–106 (2017)
6. Sumbatyan, M.A., Boyev, N.V.: High-frequency diffraction by nonconvex obstacles (Part 1). J. Acoust. Soc. Am. **95**(5), 2347–2353 (1994)
7. Kupradze, V.D.: Potential methods in the theory of elasticity. In: Israel Program for Scientific Translations. (1965)
8. Novatsky, V.: Theory of Elasticity. Mir, Moscow (1975). (in Russian)
9. Borovikov, V.A., Borovikov, V.A., Kinber, B.Y., Kinber, B.E.: Geometrical Theory of Diffraction. The Institution of Electrical Engineers, London (1994)
10. Achenbach, J.D., Gautesen, A.K., McMaken, H.: Ray Methods for Waves in elastic solids: with applications to scattering by cracks. Pittman, New York (1982)
11. Hoenl, H., Maue, A., Westpfahl, K.: Diffraction Theory. Mir, Moscow (1964). (in Russian)

12. Brekhovskikh, L.: Waves in Layered Media. Academic Press, New York (2012)
13. Grinchenko, V.T., Meleshko, V.V.: Harmonic Oscillations and Waves in Elastic Bodies. Naukova Dumka, Kiev (1981). (in Russian)
14. Fedorjuk, M.V.: Saddle Point Method. Nauka, Moscow (1977). (in Russian)

The Mixed Boundary Conditions Problem of Layered Composites with Meta-Surfaces in Electro Elasticity

Ara S. Avetisyan

Abstract The influence of taking into account the presence of roughness of both the external mechanically free surfaces, and the internal surfaces connecting various media, on the propagation of a high-frequency wave signal in a multilayer waveguide is investigated. In order to solve the quasistatic problem of the coupled electroelastic (magnetoelastic, thermoelastic) fields, the joints of the rough surfaces at the composites are simulated as meta-surfaces. In different models of the connection of thick piezoelectric layers, in the zone of the connection of their surfaces, the thin geometrically and physically inhomogeneous multilayer zone, which is equivalent to the meta surface with the dynamic loads, virtually arises. Taking into account the known principles of wave formation and propagation of high-frequency (short-wave) wave signals, as well as the magnitude of the surface roughness, hypotheses of magneto (electro, thermo) elastic layered systems are introduced (hypothesis **MELS**—Magneto Elastic Layered Systems). Proper selection of the surface exponential functions (**SEF**) in hypotheses, in equations and in thermodynamic relationships of the problem ensures that the surface roughness is taken into account. The introduction of hypothesis **MELS** allows modeling of the mathematical boundary-value problem of the contact of rough surfaces of continuous media with related physical and mechanical fields. This approach also makes it easy to calculate the equivalent dynamic electromechanical loads on the simulated meta-surface at the interface of the media. The following examples have been analyzed: (i) the propagation of the signal of an elastic shear wave in the case of the connection of rough surfaces of two piezoelectric layers with another thin piezoelectric layer, (ii) the propagation of an electroelastic wav(e in a single-shaped piezoelectric layer, the surfaces roughness of which is filled with an isotropic dielectric or ideal conductor, (iii) the propagation of high-frequency shear elastic waves on interface of isotropic elastic half-spaces with canonical surface protrusions.

A. S. Avetisyan (✉)
Institute of Mechanics, National Academy of Sciences, Yerevan, Armenia
e-mail: ara.serg.avetisyan@gmail.com

M. A. Sumbatyan (ed.), *Wave Dynamics, Mechanics and Physics of Microstructured Metamaterials*, Advanced Structured Materials 109,
https://doi.org/10.1007/978-3-030-17470-5_6

1 Introduction

After electromagnetics, meta materials principles more often became the subject of research in acoustics, which leads to its applications in various areas, such as ultrasound for non-destructive testing Miniaci et al. [1], reducing noise Krushynska et al. [2] and seismic protection Miniaci et al. [3]. They were used to manipulate the elastic and acoustic waves of Deymier [4], Laude [5]. Many exciting effects, such as masking, negative refraction, focus formation or forbidden zones were reproduced with a particularly large range of sizes and proportions of frequencies at which they can occur Hussein et al. [6]. About the achievements of recent years in the field of mechanical metamaterials and metasurfaces one can find in the editorial article Bosia et al. [7]. In peper Moleron et al. [8], the authors theoretically and experimentally investigate visco–thermal effects on the acoustic propagation through metamaterials consisting of rigid slabs with subwavelength slits embedded in air. It was demonstrated that this unavoidable loss mechanism is not merely a refinement. It plays a dominant role in the actual acoustic response of the structure. In [9], the authors extend the concept of metasurfaces to anti-plane surface waves existing in semi-infinite layered media. By means of an effective medium approach, they derive an original closed-form dispersion relation for the metasurface. This relation reveals the possibility to control the Love waves dispersive properties by varying the resonators mechanical parameters. In work [10] Fabro et al., the wave attenuation from a metamaterial beam assembly is investigated considering uncertain connections. In article [11] Fomenko et al., the time-harmonic wave motion in a layered phononic crystal with internal inhomogeneities such as piezoelectric functionally graded interlayers and periodic arrays of cracks is considered. The complete band-gaps in layered piezoelectric functionally graded phononic crystal are revealed and analyzed. It is demonstrated that introduction of periodic cracks leads to the formation of extra band-gaps. Acoustic metasurfaces derive their characteristics from the interaction between acoustic waves and specifically designed materials. Acoustic metasurfaces have added value and unusual functionalities compared with their predecessor in materials science, namely, acoustic metamaterials. These rationally designed 2D materials of sub wavelength thickness provide a new route for sound wave manipulation. In Review [12] by Assouar et al. (where about 130 different studies are cited), the authors delineate the fundamental physics of metasurfaces, describe their different concepts and design strategies, and discuss their functionalities for controllable reflection, transmission and extraordinary absorption. In particular, they outline the main designs of acoustic metasurfaces, including those based on coiling-up space, Helmholtz-resonator-like and membrane-type structures. In the article [13] Miranda Jr. et al., the band structure of flexural waves propagating in an elastic metamaterial thin plate are theoretically investigated. The influence of periodic arrays of multiple degrees of freedom local resonators in square and triangular lattices is studied. The plane wave expansion and extended plane wave expansion methods are used, respectively to solve the governing equation of motion for a thin plate. Thin layers of meta materials are formed during the manufacture of structural elements of high-precision

measuring devices. Even modern technology surface treatment of bodies still keeps the surface roughness. The existence of these irregularities significantly affect the dynamic processes in the body, if the step length of high-frequency oscillations or the length of short waves is comparable with the geometric dimensions of the surface irregularities. When the uneven surfaces of two bodies are joined with glue, a near-surface thin non-uniform three-layer with mixed physicomechanical properties is formed [14, 15]. Taking into account the thinness of the near-surface zone, the piecewise-homogeneous three-layer is modeled as an internal meta-surface of a two-layer waveguide, with unique physical and geometric characteristics. Smoothing the roughness of the surfaces of the piezoelectric layer by pouring different materials, in the near-surface zones, pairs of thin non-uniform layers with mixed physical and mechanical properties are formed [16]. The different fills lead to the formation of different heterogeneous electro mechanical meta-surfaces on the piezoelectric base layer. When connecting two elastic half-spaces with canonical surface pins, a transversely inhomogeneous three-layer is formed [17]. The formed, periodically inhomogeneous three-layer waveguide is modeled as a two-layer waveguide with the internal meta surface. The mixed physicomechanical properties of the newly formed thin layers will naturally depend on the linear characteristics of the surfaces irregularities, the method of chemo thermal treatment and surface bonding, as well as the physicomechanical properties of the materials involved in the compound. The surface roughness of an elastic deformable medium is small-scale geometric heterogeneity in the composite.

Therefore, in the calculations of the mode and dynamic characteristics of high-frequency oscillations of structural elements, and also in the process of determining the propagation dynamics of short (high-frequency) waves in a composite waveguide, the accounting of the surface roughness is especially important when the wavelength of the wave signal is comparable to the average pitch of the surface irregularities. Taking into account the surface inhomogeneities of a layered waveguide certainly complicates the mathematical boundary-value problem. But it gives a chance to identify near-surface wave effects and more accurately calculate the quantitative characteristics of the formed wave field in the near-surface zone of the junction of the composite elements. And naturally, the various contacts of rough surfaces are important for a technical modeling of objects, as well as for the mathematical modeling on their basis. Taking into account the small scale of the surface roughness of the element, in works [14, 15], a combination approach for modeling the joints of the rough surfaces of piezoelectric media is proposed. Depending on the method of joining rough surfaces, it is proposed to virtually select a near-surface homogeneous thin layer of variable thickness (or a near-surface non-uniform thin layer of constant thickness) at the junctions of piezoelectric half-spaces. With the help of the introduced hypotheses MELS, on the distribution of physical and mechanical fields across the thickness of the layers, the obtained meta-surfaces completely describe the physics of the corresponding butt-joints, greatly simplifying the solution of the mathematical boundary value problem [18, 19].

2 Basic Linear Relations of Electro Elasticity for Piezoelectric Materials

In the future, we will consider only electroacoustic interaction in piezoelectric media, where the complete system of quasistatic equations can be conveniently represented as

$$c_{ijkm}\frac{\partial^2 u_k^{(n)}}{\partial x_i \partial x_m} + e_{ijm}\frac{\partial^2 \varphi_n}{\partial x_i \partial x_m} = \rho_n \frac{\partial^2 u_j^{(n)}}{\partial t^2};\ e_{ijm}\frac{\partial^2 u_j^{(n)}}{\partial x_i \partial x_m} - \varepsilon_{im}\frac{\partial^2 \varphi_n}{\partial x_i \partial x_m} = 0. \quad (2.1)$$

in which the physicomechanical characteristics of the material form the tensors describing a specific anisotropy of the piezoelectric material $\left\{\left(\hat{c}_{ijnk}\right)_{6\times 6};\ \left(\hat{e}_{ijm}\right)_{3\times 6};\ \left(\hat{e}_{mij}\right)_{6\times 3};\ \left(\hat{\varepsilon}_{nk}\right)_{3\times 3}\right\}_{9\times 9}$, and determine the structural composition of the coupled electroelastic wave field $\{u_i(x_k, t); \varphi(x_k, t)\}$.

Formally, the role of the conjugation conditions of mechanical fields in the adjoining electro- (magneto-thermo-) elastic media is played by the conditions of continuity of mechanical stresses $\sigma_{ij}^{(m)}$ and elastic displacements $u_k^{(m)}$ at the media interface $\Sigma_m(x_i)$

$$\left(\sigma_{ij}^{(1)} - \sigma_{ij}^{(2)}\right)\cdot n_j\Big|_{\Sigma_m(x_i)} = 0; \quad u_k^{(1)}\Big|_{\Sigma_m(x_i)} = u_k^{(2)}\Big|_{\Sigma_m(x_i)}. \quad (2.2)$$

In electro-elastic media, the conjugacy conditions at the interface of the media are represented as continuity of the tangential components of the electric field strength and normal components of the electric displacements in the adjacent media. In the media interface $\Sigma_m(x_i)$, these conditions are written as

$$\left(D_j^{(1)} - D_j^{(2)}\right)\cdot n_j\Big|_{\Sigma_m(x_i)} = 0; \quad \varphi^{(1)}\Big|_{\Sigma_m(x_i)} = \varphi^{(2)}\Big|_{\Sigma_m(x_i)}. \quad (2.3)$$

In the problems of electro elasticity (magneto elasticity), the vacuum is also considered as an interacting "medium", on the outer surfaces of the waveguide. In these cases, the conditions of mechanically open borders are written as

$$\sigma_{ij}^{(1)}\cdot n_j\Big|_{\Sigma_0(x_i)} = 0. \quad (2.4)$$

In the case of a rigidly clamped outer surface of the waveguide, we will have the fixing conditions for elastic displacements

$$u_k^{(1)}\Big|_{\Sigma_0(x_i)} = 0. \quad (2.5)$$

In the case of the metallized (shielded) surface of a dielectric material, the condition of an "electrically closed" boundary is satisfied on the surface

$$\varphi^{(1)}\big|_{\Sigma_0(x_i)} = 0. \tag{2.6}$$

When the contiguous dielectric (not piezoelectric) medium has a very small value of the dielectric constant, instead of the surface conditions (2.6), we simply have an "electrically open" boundary condition

$$D_j^{(1)} \cdot n_j \Big|_{\Sigma_0(x_i)} = 0. \tag{2.7}$$

A unit normal with varying components will no longer change along the direction of the axis ox_γ and therefore, in two-dimensional problems in accordance with the statement of the problem we can take

$$n_j^{(*)}(x_\alpha, h(x_\alpha)) = \left\{ h_{,\alpha}(x_\alpha)/\sqrt{1+\left[h_{,\alpha}(x_\alpha)\right]^2};\ 1/\sqrt{1+\left[h_{,\alpha}(x_\alpha)\right]^2};\ 0 \right\} \tag{2.8}$$

Taking into account the changes of the normal in the surface (2.8), the conditions of complete conjugacy of electromechanical fields (2.2) and (2.3), on the interface between the media $x_\beta = h(x_\alpha)$, in the problem of a plane electroactive deformation $\left\{u_\alpha\left(x_\alpha, x_\beta, t\right);\ u_\beta\left(x_\alpha, x_\beta, t\right);\ 0;\ \varphi\left(x_\alpha, x_\beta, t\right)\right\}$, will be written as

$$\begin{aligned}&\left[\sigma_{\alpha\alpha}^{(1)}(x_\alpha, h(x_\alpha), t) - \sigma_{\alpha\alpha}^{(2)}(x_1, h(x_\alpha), t)\right] \cdot h_{,\alpha}(x_\alpha)\\ &\quad + \left[\sigma_{\beta\alpha}^{(1)}(x_\alpha, h(x_\alpha), t) - \sigma_{\beta\alpha}^{(2)}(x_\alpha, h(x_\alpha), t)\right] = 0;\end{aligned} \tag{2.9}$$

$$\begin{aligned}&\left[\sigma_{\beta\alpha}^{(1)}(x_\alpha, h(x_\alpha), t) - \sigma_{\beta\alpha}^{(2)}(x_\alpha, h(x_\alpha), t)\right] \cdot h_{,\alpha}(x_\alpha)\\ &\quad + \left[\sigma_{\beta\beta}^{(1)}(x_\alpha, h(x_\alpha), t) - \sigma_{\beta\beta}^{(2)}(x_\alpha, h(x_\alpha), t)\right] = 0;\end{aligned} \tag{2.10}$$

$$\begin{aligned}&\left[D_\alpha^{(1)}(x_\alpha, h(x_\alpha), t) - D_\alpha^{(2)}(x_\alpha, h(x_\alpha), t)\right] \cdot h_{,\alpha}(x_\alpha)\\ &\quad + \left[D_\beta^{(1)}(x_\alpha, h(x_\alpha), t) - D_\beta^{(2)}(x_\alpha, h(x_\alpha), t)\right] = 0;\end{aligned} \tag{2.11}$$

$$\begin{aligned}u_\alpha^{(1)}(x_\alpha, h(x_\alpha), t) &= u_\alpha^{(2)}(x_\alpha, h(x_\alpha), t);\\ u_\beta^{(1)}(x_\alpha, h(x_\alpha), t) &= u_\beta^{(2)}(x_\alpha, h(x_\alpha), t);\end{aligned} \tag{2.12}$$

$$\varphi^{(1)}(x_\alpha, h(x_\alpha), t) = \varphi^{(2)}(x_\alpha, h(x_\alpha), t). \tag{2.13}$$

Similarly, on the interface of the media $x_\beta = h(x_\alpha)$, the conjugacy conditions of the electromechanical fields (2.2) and (2.3), in the problem of an electroactive antiplane deformation $\left\{0;\ 0;\ u_\gamma\left(x_\alpha, x_\beta, t\right);\ \varphi\left(x_\alpha, x_\beta, t\right)\right\}$, will be written as

$$\begin{aligned}&\left[\sigma_{\gamma\alpha}^{(1)}(x_\alpha, h(x_\alpha), t) - \sigma_{\gamma\alpha}^{(2)}(x_\alpha, h(x_\alpha), t)\right] \cdot h_{,\alpha}(x_\alpha)\\ &\quad + \left[\sigma_{\gamma\beta}^{(1)}(x_\alpha, h(x_\alpha), t) - \sigma_{\gamma\beta}^{(2)}(x_\alpha, h(x_\alpha), t)\right] = 0;\end{aligned} \tag{2.14}$$

$$\left[D_{\alpha}^{(1)}(x_{\alpha}, h(x_{\alpha}), t) - D_{\alpha}^{(2)}(x_{\alpha}, h(x_{\alpha}), t)\right] \cdot h_{,\alpha}(x_{\alpha}) + \left[D_{\beta}^{(1)}(x_{\alpha}, h(x_{\alpha}), t) - D_{\beta}^{(2)}(x_{\alpha}, h(x_{\alpha}), t)\right] = 0; \tag{2.15}$$

$$u_{\gamma}^{(1)}(x_{\alpha}, h(x_{\alpha}), t) = u_{\gamma}^{(2)}(x_{\alpha}, h(x_{\alpha}), t); \tag{2.16}$$

$$\varphi^{(1)}(x_{\alpha}, h(x_{\alpha}), t) = \varphi^{(2)}(x_{\alpha}, h(x_{\alpha}), t). \tag{2.17}$$

The continuity conditions of mechanical stresses (2.9), (2.10), (2.14) and elastic displacements (2.12), (2.16), as well as the continuity conditions for the tangential components of the electric field strength (2.13), (2.17) and the normal components of electrical displacements (2.11), (2.15) in the case of a mechanically free surface of the body (on the section of the medium with a vacuum) are naturally simplified. The mechanical components of the second medium disappear from the relations

$$\sigma_{ij}^{(2)}(x_{\alpha}, h(x_{\alpha}), t) \equiv 0, u_{k}^{(2)}(x_{\alpha}, h(x_{\alpha}), t) \equiv 0, \quad \text{where } i; j; k \in \{\alpha; \beta; \gamma\} \tag{2.18}$$

and the characteristics of the electric field of the second medium describe the vacuum

$$D_{k}^{(2)}(x_{\alpha}, h(x_{\alpha}), t) = -\varepsilon_0 \varphi_{,k}^{(e)}(x_{\alpha}, h(x_{\alpha}), t); \quad \varphi^{(2)}(x_{\alpha}, h(x_{\alpha}), t) = \varphi^{(e)}(x_{\alpha}, h(x_{\alpha}), t) \tag{2.19}$$

In the vacuum region, the Laplace equation $\nabla^2 \varphi^{(e)}(x_{\alpha}, x_{\beta}, t) = 0$, for the electric potential is solved.

In the considered problems, we will assume that the material of the main piezoelectric layer belongs to the class 6 mm of hexagonal symmetry, for which the electroactive shear deformation $\{0;\ 0;\ w(x, y, t);\ \varphi(x, y, t)\}$ is separated from the non-electroactive plane strain.

3 Mathematical Modeling of the Metasurfaces by the Introduction of Magneto Elastic Layered Systems Hypotheses (Hypothesis MELS)

3.1 The Connection of Two Piezoelectric Layers with Rough Surfaces with the Other Piezoelectric Thin Layer (Model–1)

When the roughness surfaces of two bodies are joined with the piezoelectric glue (Fig. 1), a near-surface thin non-uniform three-layer with mixed physico mechanical properties is formed [14, 15]. Take into account a thinness of the near-surface zone,

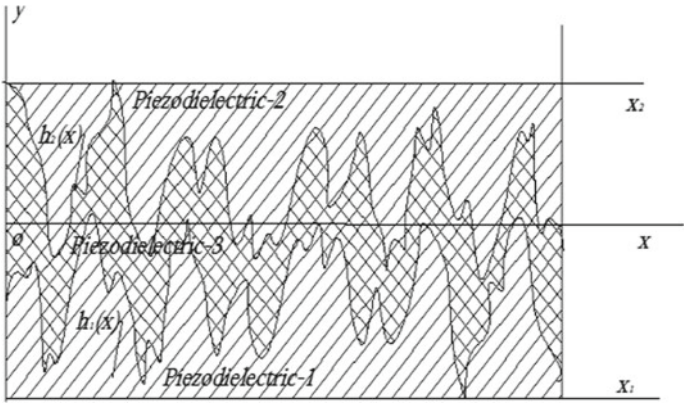

Fig. 1 The cross section of the interface between two glued homogeneous piezoelectric materials

the piecewise-homogeneous three-layer is modeled as an internal meta-surface of a two-layer waveguide, with unique physical and geometric characteristics (Fig. 1).

The thickness of the adhesive layer is also small compared to the effective thickness of the adjacent layers. In studies of the propagation of the wave signal electroactive antiplane deformation, in the internal adhesive gap of variable width $\Omega_3 = \{|x| < \infty, h_2(x) \le y \le h_1(x), |z| < \infty\}$, as well as in each half space $\Omega_1 = \{|x| < \infty, h_1(x) \le y < \infty, |z| < \infty\}$ and $\Omega_2 = \{|x| < \infty, -\infty < y \le h_2(x), |z| < \infty\}$ quasistatic equations of electroactive antiplane deformation are solved

$$c_{44}^{(m)} \frac{\partial^2 \mathrm{w}_m}{\partial x^2} + e_{15}^{(m)} \frac{\partial^2 \varphi_m}{\partial x^2} + \frac{\partial \sigma_{yz}^{(m)}}{\partial y} = \rho_m \frac{\partial^2 \mathrm{w}_m}{\partial t^2}; \tag{3.1}$$

$$e_{15}^{(m)} \frac{\partial^2 \mathrm{w}_m}{\partial x^2} - \varepsilon_{11}^{(m)} \frac{\partial^2 \varphi_m}{\partial x^2} + \frac{\partial D_y^{(m)}}{\partial y} = 0 \tag{3.2}$$

Taking into account the effective thickness of the adjacent layers, the solutions of Eqs. (3.1) and (3.2) in each half space have the following form

$$\mathrm{w}_n(x, y, t) = W_{0n} \exp[(-1)^n \alpha_n k y] \cdot \exp[i(kx - \omega t)] \tag{3.3}$$

$$\varphi_n(x, y, t) = \left\{ \begin{array}{l} \Phi_{0n} \exp[(-1)^n k y] \\ +(e_n \backslash \varepsilon_n) \cdot W_{0n} \exp[(-1)^n \alpha_n k y] \end{array} \right\} \cdot \exp[i(kx - \omega t)] \tag{3.4}$$

The function of the distribution of the wave field is chosen so that it simply and completely (without loss of physical phenomena) describes the nature of the change of the desired quantities on surfaces and along the thickness of the adhesive layer.

i. The choice of this function should ensure the conjugacy of the physicomechanical fields on the surfaces $h_m(x)$ (when $m = 1; 2$) of media sections (2.14)–(2.17)

$$\begin{aligned} \mathrm{w}_3^*(x, h_m(x), t) &= \mathrm{w}_m(x, h_m(x), t); \\ \varphi_3^*(x, h_m(x), t) &= \varphi_m(x, h_m(x), t) \end{aligned} \tag{3.5}$$

$$\begin{aligned} &\left[\sigma_{yz}^{(m)}(x, h_m(x), t) - \sigma_{yz}^{(3)}(x, h_m(x), t)\right] \\ &\quad + \left[\sigma_{zx}^{(m)}(x, h_m(x), t) - \sigma_{zx}^{(3)}(x, h_m(x), t)\right] \cdot h_{m,x}(x) = 0 \end{aligned} \tag{3.6}$$

$$\begin{aligned} &\left[D_2^{(m)}(x, h_m(x), t) - D_2^{(3)}(x, h_m(x), t)\right] \\ &\quad + \left[D_1^{(m)}(x, h_m(x), t) - D_1^{(3)}(x, h_m(x), t)\right] \cdot h_{m,x}(x) = 0 \end{aligned} \tag{3.7}$$

ii. The distribution function also includes the wave characteristic of the adhesive layer $\alpha_3 k = \sqrt{k^2 - \omega^2 \cdot (\tilde{G}_3/\rho_3)}$, as well as superficial functions $h_m(x)$.

iii. The waves in all three areas are connected, and they have one propagation function: $\exp[i(kx - \omega t)]$.

Thus, the constructed hypothetical solutions in a thin adhesive layer will be written in the form

$$\begin{aligned} \mathrm{w}_3(x, y, t) = f_3(h_m(x), y) \cdot [\mathrm{w}_2(x, h_2(x), t) - \mathrm{w}_1(x, h_1(x), t)] \\ + \mathrm{w}_1(x, h_1(x), t) \end{aligned} \tag{3.8}$$

$$\begin{aligned} \varphi_3(x, y, t) = f_3(h_m(x), y) \cdot [\varphi_2(x, h_2(x), t) - \varphi_1(x, h_1(x), t)] \\ + \varphi_1(x, h_1(x), t) \end{aligned} \tag{3.9}$$

where the resulting distribution function is quite good in character and is represented as a surface exponential function

$$f_3(h_m(x), y) = sh[\alpha_3 k(y - h_1(x))]/sh[\alpha_3 k(h_2(x) - h_1(x))] \tag{3.10}$$

Compared to the case of smooth contact surfaces $y = const$, from the boundary conditions (3.6) it can be seen that differential dynamic mechanical forces appear on the corresponding joint surfaces

$$\sigma_{yz}^{(2)}(x,(R_1+R_2),t)-\sigma_{yz}^{(1)}(x,0,t)=-\int_0^{h_1(x)}\left[\frac{\partial\sigma_{zx}^{(1)}}{\partial x}-\rho_1\frac{\partial^2 w_1}{\partial t^2}\right]\cdot dy$$
$$-\int_{h_1(x)}^{h_2(x)}\left[\frac{\partial\sigma_{zx}^{(3)}}{\partial x}-\rho_1\frac{\partial^2 w_3}{\partial t^2}\right]\cdot dy$$
$$-\int_{h_2(x)}^{R_1+R_2}\left[\frac{\partial\sigma_{zx}^{(2)}}{\partial x}-\rho_2\frac{\partial^2 w_2}{\partial t^2}\right]\cdot dy \quad (3.11)$$

Similarly, from the boundary conditions (3.7) it can be seen that with non-smooth surfaces of the contact of media, in comparison with the case of smooth contact surfaces $y = const$, differential dynamic displacements of the electric field also appear

$$D_y^{(2)}(x,(R_1+R_2),t)-D_y^{(1)}(x,0,t)=-\int_0^{h_1(x)}\frac{\partial D_x^{(1)}}{\partial x}\cdot dy$$
$$-\int_{h_1(x)}^{h_2(x)}\frac{\partial D_x^{(3)}}{\partial x}\cdot dy-\int_{h_2(x)}^{R_1+R_2}\frac{\partial D_x^{(2)}}{\partial x}\cdot dy. \quad (3.12)$$

The introduced hypotheses make it possible to determine not only the distribution of the elastic displacement and the electric potential across the thickness of the formed near-surface zone of the junction of rough surfaces, but it also determines the influence of the roughness on the wave propagation function. Taking into account the fact that the hypothetical representations (3.8) and (3.9) must also satisfy Eqs. (3.1) and (3.2), for the amplitude functions of the inner layer we find

$$A_{31}=\frac{W_{01}\cdot\exp[-\alpha_1 kh_1(x)]\cdot ch(\alpha_3 kh_2(x))-W_{02}\cdot\exp[\alpha_2 kh_2(x)]\cdot ch(\alpha_3 kh_1(x))}{sh[\alpha_3 k(h_1(x)-h_2(x))]}$$
$$A_{32}=\frac{W_{02}\cdot\exp[\alpha_2 kh_2(x)]\cdot sh(\alpha_3 kh_1(x))-W_{01}\cdot\exp[-\alpha_1 kh_1(x)]\cdot sh(\alpha_3 kh_2(x))}{sh[\alpha_3 k(h_1(x)-h_2(x))]}$$

From the obtained expressions it follows that inside the junction of rough surfaces, at all points of contact, when $h_1(x) = h_2(x)$, internal resonance may occur.

3.2 *Smoothing the Roughness of the Surfaces of the Piezoelectric Layer by Pouring Different Materials (Model–2)*

Smoothing the roughness of the surfaces of the piezoelectric layer by pouring different materials (Fig. 2), in the near-surface zones, thin non-uniform double layers with mixed physical and mechanical properties are formed [16,18, 19]. Different fills lead to the formation of heterogeneous electromechanical meta-surfaces of the piezoelectric base layer.

Let us assume that the waveguide surface irregularities $y = h_+(x)$ are filled to the level $y = h_0(1+\gamma_+)$ with a good dielectric, and the waveguide's surface irregularities $y = h_-(x)$ are filled to the level $y = -h_0(1+\gamma_-)$ with a good electrical conductor.

Here $\gamma_\pm \ll 1$ are the heights of the profiles of irregularities and h_0 is a half of the base thickness of the homogeneous piezoelectric layer. So we have a composite waveguide, which consists of five layers:

- the base layer $\Omega_0\{x, y\}$ of a constant thickness $-h_0(1-\gamma_-) \le y \le h_0(1-\gamma_+)$
- an electrically conductive layer $\Omega_-^c\{x, y\}$ of thickness $\xi_c(x) = |h_0(1+\gamma_-) + h_-(x)|$,
- nonhomogeneous piezoelectric thin layer $\Omega_-^p\{x, y\}$ of thickness $\xi_{p-}(x) = |-h_0(1-\gamma_-) - h_-(x)|$,
- nonhomogeneous piezoelectric thin layer $\Omega_+^p\{x, y\}$ of thickness $\xi_{p+}(x) = |h_+(x) - h_0(1-\gamma_+)|$,
- a dielectric thin layer $\Omega_+^d\{x, y\}$ of thickness $\xi_d(x) = h_0(1+\gamma_+) - h_+(x)$.

Thus, near the surface area $y = h_-(x)$ we have a composite layer, which consists of transversely inhomogeneous piezoelectric and homogeneous, perfectly conducting materials. The same way, near the surface area $y = h_+(x)$ we have a composite layer, which consists of homogeneous dielectric and transversely inhomogeneous

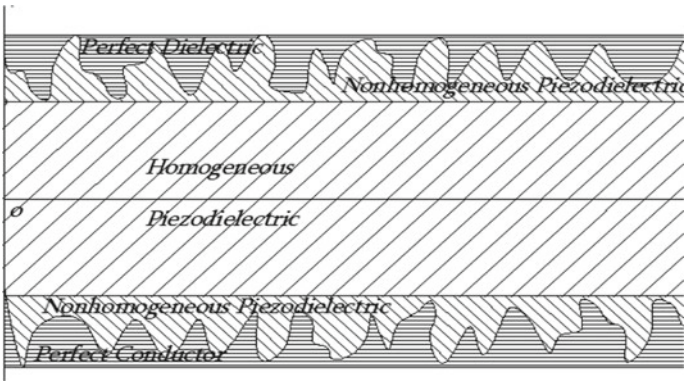

Fig. 2 The model of smoothing roughness surfaces of the piezoelectric layer by pouring different materials

piezoelectric materials. The homogeneous piezoelectric waveguide with filled surface irregularities is modeled as a multilayer waveguide made of different materials.

In each separated layer, we must solve the quasi-static equations of electro magneto elasticity (2.1). The conjugacy conditions (2.14)–(2.17) of the electromagnetic and mechanical fields on the six interface surfaces of body are satisfied.

The localization of elastic shear waves energy in the formed near-surface inhomogeneous thin interlayers is investigated in the case, when the high frequency shear elasticity wave (SH) signal (short wave: the length of which is much smaller than the base layer thickness) is propagating in a composite waveguide.

A mixed boundary mathematical problem is cumbersome, and its analytical solution is not always possible. Applying the hypothesis **MELS** (3.5)–(3.10) to the thin layers $\Omega_-^c\{x, y\}$, $\Omega_-^p\{x, y\}$, $\Omega_+^p\{x, y\}$ and $\Omega_+^d\{x, y\}$ of the composite, we obtain a homogenous piezoelectric waveguide of constant thickness $h_0(2 - \gamma_+ - \gamma_-)$, with two meta-surfaces $y_- = -h_0(1 - \gamma_-)$ and $y_+ = h_0(1 - \gamma_+)$, which are equivalents to the electromechanical loads of thin layers, respectively.

The wave solution of the equations system (2.1) in the base homogeneous piezoelectric layer can be written in the form of a normal wave

$$\mathrm{w}_0(x, y, t) = \left[A_0 \exp(-\alpha_0 k y) + B_0 \exp(\alpha_0 k y)\right] \cdot \exp[i(kx - \omega t)] \tag{4.1}$$

$$\begin{aligned}\varphi_0(x, y, t) = {} & \{C_0 \exp(-ky) + D_0 \exp(ky)\} \cdot \exp[i(kx - \omega t)] \\ & + (e_{15}/\varepsilon_{11})\mathrm{w}_0(x, y, t)\end{aligned} \tag{4.2}$$

Here $\alpha_0(k) = \sqrt{1 - \left(\omega_0^2/k^2\right) \cdot \left(\rho_0/\tilde{G}_0\right)}$ is the coefficient of elastic waves formation across the thickness of the base layer.

The elastic shear and the electric field potential in the virtually cut inhomogeneous piezoelectric layer $\Omega_+^p\{x, y\}$ are represented as follows:

$$\begin{aligned}\mathrm{w}_+^p(x, y, t) = {} & f_+^p(kh_0, h_+(x)) \cdot \left[\mathrm{w}_+^p(x, h_+(x), t) - \mathrm{w}_0(x, h_0(1 - \gamma_+), t)\right] \\ & + \mathrm{w}_0(x, h_0(1 - \gamma_+), t)\end{aligned} \tag{4.3}$$

$$\begin{aligned}\varphi_+^p(x, y, t) = {} & f_+^p(kh_0, h_+(x)) \cdot \left[\varphi_+^p(x, h_+(x), t) - \varphi_0(x, h_0(1 - \gamma_+), t)\right] \\ & + \varphi_0(x, h_0(1 - \gamma_+), t)\end{aligned} \tag{4.4}$$

where $f_+^p(kh_0, h_+(x)) = sh[\alpha_{p+}k(y - h_0(1 - \gamma_+))]/sh[\alpha_{p+}k(h_+(x) - h_0(1 - \gamma_+))]$ is the distribution function of an electromechanical field in the inhomogeneous piezoelectric layer. Obviously, the unknown characteristics formation function $f_+^p(kh_0, h_+(x))$ is represented by the formation coefficient $\alpha_+^p(k) = \left[(\omega_0^2/k^2)(\rho_+/\tilde{G}_+) - 1\right]^{1/2}$ and the variable thickness $\xi_{p+}(x) = |h_+(x) - h_0(1 - \gamma_+)|$.

Similarly, in the homogeneous dielectric smoothing layer Ω_+^d the elastic shear and the electric field potential are represented as follows:

$$\mathrm{w}_+^d(x,y,t) = f_+^d(kh_0, h_+(x)) \cdot \left[\mathrm{w}_+^d(x, h_0(1+\gamma_+), t) - \mathrm{w}_+^p(x, h_+(x), t)\right] + \mathrm{w}_+^p(x, h_+(x), t) \tag{4.5}$$

$$\varphi_+^d(x,y,t) = f_+^d(kh_0, h_+(x)) \cdot \left[\varphi_+^d(x, h_0+\gamma_+, t) - \varphi_+^p(x, h_+(x), t)\right] + \varphi_+^p(x, h_+(x), t) \tag{4.6}$$

where the formation function $f_d(kh_0; h_+(x)/h_0) = sh\left[\alpha_d k(y - h_+(x))\right]/sh\left[\alpha_d k(h_0(1+\gamma_+) - h_+(x))\right]$ in a homogeneous dielectric layer is already represented by the corresponding homogeneous layer parameters $\alpha_+^d(k) = \left[(\rho_d\omega_0^2/k^2 G_d) - 1\right]^{1/2}$ and $\xi_d(x) = h_0(1+\gamma_+) - h_+(x)$.

Analogous to relations (4.3) and (4.4), the elastic shear and the electric field potential in the virtually cut inhomogeneous piezoelectric layer $\Omega_-^p\{x, y\}$ are represented as follows:

$$\mathrm{w}_-^p(x,y,t) = f_-^p(kh_0, h_-(x)) \cdot \left[\mathrm{w}_-^c(x, h_-(x), t) - \mathrm{w}_0(x, -h_0(1-\gamma_-), t)\right] + \mathrm{w}_0(x, -h_0(1-\gamma_-), t) \tag{4.7}$$

$$\varphi_-(x,y,t) = \{1 - f_-(kh_0, h_-(x))\}\varphi_0(x, -h_0(1-\gamma_-), t) \tag{4.8}$$

where the formation function $f_-^p(kh_0, h_+(x)) = sh\left[\alpha_-^p k(y + h_0(1-\gamma_-)\right]/sh\left[\alpha_-^p k(h_-(x) + h_0(1-\gamma_-))\right]$ in the inhomogeneous piezoelectric layer $\Omega_-^p\{x, y\}$ is represented by a new formation coefficient $\alpha_-^p(k) = \left[(\rho_-\omega_0^2/k^2\tilde{G}_-) - 1\right]^{1/2}$ and by the variable thickness $\xi_-^p(x) = h_0(1-\gamma_-) - h_-(x)$.

Since there is no electric field potential in the perfectly conductive smoothing layer Ω_-^c, only the elastic shear is represented as follows:

$$\mathrm{w}_-^c(x,y,t) = f_-^c(kh_0, h_+(x)) \cdot \left[\mathrm{w}_-^c(x, -h_0(1-\gamma_-), t) - \mathrm{w}_-^p(x, h_-(x), t)\right] + \mathrm{w}_-^p(x, h_-(x), t) \tag{4.9}$$

where the formation function $f_-^c(kh_0, h_+(x)) = sh\left[\alpha_-^c k(y - h_-(x))\right]/sh\left[\alpha_-^c k(-h_0(1+\gamma_-) - h_-(x))\right]$ in the homogeneous perfectly conductive layer is represented by the corresponding homogeneous conductive layer parameters $\alpha_-^c(k) = \left[(\rho_c\omega_0^2/k^2 G_c) - 1\right]^{1/2}$ and $\xi_-^c(x) = h_-(x) - h_0(1+\gamma_-)$.

It is important to note, that by choosing the corresponding formation functions $f_+^d(kh_0, h_+(x))$, $f_+^p(kh_0, h_+(x))$, $f_-^p(kh_0, h_-(x))$ and $f_-^c(kh_0, h_+(x))$ in hypothetical representation (4.3)–(4.9), the boundary conditions on the interface surfaces of layers, are automatically satisfied for the elastic shear and the electric field potential of thin layers. Moreover, each of the represented distributions of the unknown quantities (4.3)–(4.9) includes a formation coefficient for the dielectric interlayer, the conductive interlayer, the virtually isolated interlayers of inhomogeneous piezo-

electric and surface values of the electromechanical field of the base homogeneous piezoelectric layers.

Using the obtained surface values of the unknown quantities of distributions (4.1)–(4.9), we can represent the elastic shear and the electric field potential in each layer in expanded form [16]. By integrating the electro-magnetic-elasticity equations over the depth of flooded roughness $y = h_-(x)$ and $y = h_+(x)$, taking into account the surface conjugacy conditions in internal surfaces, we obtain electromechanical loads on the meta-surfaces $y = h_0(1 - \gamma_+)$ and $y = -h_0(1 - \gamma_-)$ of the base layer, respectively.

By satisfying the surface conditions for smooth media interface boundaries $y = h_0(1 - \gamma_+)$ and $y = -h_0(1 - \gamma_-)$, we get the system of algebraic linear equations, relatively independent amplitudes $\{A_0; B_0; C_0; D_0; E_0\}$ of possible electroelastic wave signal in the piezoelectric base layer and in the vacuum half-space, respectively. From the condition for the existence of nontrivial solutions, the dispersion equation for the formed wave field is obtained in the following form:

$$\det \left\| g_{ij}(G_k;\ \rho_k;\ e_k;\ \varepsilon_k;\ h_\pm(x);\ \omega;\ k(\omega_0) \right\|_{4\times 4} = 0 \tag{4.10}$$

The variable coefficients $\left\{ g_{ij}(G_k; \rho_k; e_k; \varepsilon_k; h_\pm(x); \omega; k(\omega) \right\}_{4\times 4}$ of the tensor-dispersion equation are cumbersome. The coefficients of the fifth column of tensor $g_{15} = g_{25} = g_{45} = g_{55} \equiv 0$, and $g_{35}(\alpha_d; \varepsilon^{(e)}/\varepsilon^d; h_+(x); kh_0) \geq 0$ is positive-definite and describes the oscillations of electric field in vacuum.

It is also shown in [20] that during propagation of long wave signals there is almost no interaction between the propagating wave and slight irregularities. As a basis of numerical calculations, test numerical data for material constants of adjacent materials of layers, given in Table 1, were taken, as well as geometric linear dimensions of the base layer and the surface irregularities

$$\begin{aligned} h_-(x) &= -h_0[1 + \varepsilon_- \sin(k_- x) + \delta_- \cos(k_- x)], \\ h_+(x) &= h_0[1 + \varepsilon_+ \sin(k_+ x) + \delta_+ \cos(k_+ x)] \end{aligned} \tag{4.11}$$

Investigation of propagation of high frequency (short wave) wave signal in waveguides considering the surface irregularities is caused by the fact that the linear dimensions of these irregularities are small compared to the base layer thickness $\gamma_\pm = \sqrt{\varepsilon_\pm + \delta_\pm}$.

Figures 3 and 4 are showing the wave number as a function of the wave signal frequency for normal waves.

Calculations show that for low-frequency (long-wave) signals, up to a certain value $k_n \sim 0.058$, there is a pair of periodically repeating frequencies (Fig. 3), which are determined by the physical-mechanical constants of the materials, relations of geometric linear dimensions of the base layer and surface irregularities of the waveguide.

The cycle period of wave formation in the given calculations $T = 200\pi$ is determined by the ratio of the linear dimensions of base layer and the surface irregularities.

Table 1 Numerical test data of constants of composite waveguide materials

	$G_i = C_{44}^{(i)}$	ρ_i	$\varepsilon_i = \varepsilon_{11}^{(i)}$	$e_i = e_{15}^{(i)}$
Homogeneous Piezo crystal of class 6 mm	1.49×10^{10} N/m^2	4.82×10^3 kg/m^3	7.99×10^{-11} F/m	-0.21 C/m^2
Nonhomogeneous Piezo crystal of class 6 mm ($\pm 10\%$)	1.639×10^{10} N/m^2 1.341×10^{10} N/m^2	5.302×10^3 kg/m^3 4.338×10^3 kg/m^3	8.789×10^{-11} F/m 7.191×10^{-11} F/m	-0.23 C/m^2 -0.19 C/m^2
Dielectric	1.788×10^{10} N/m^2 1.192×10^{10} N/m^2	5.784×10^3 kg/m^3 3.856×10^3 kg/m^3	9.588×10^{-11} F/m 6.392×10^{-11} F/m	
Conductor Gold Au Silver Ag	2.7×10^{10} N/m^2 3.03×10^{10} N/m^2	19.32×10^3 kg/m^3 10.49×10^3 kg/m^3		
Vacuum			0.885×10^{-11} F/m	

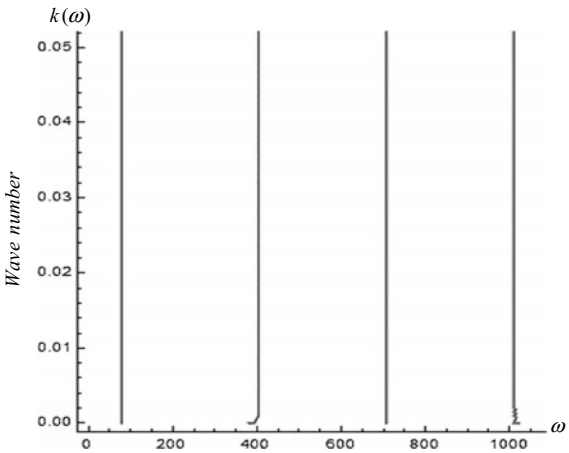

Fig. 3 The dependence of wave number on the frequency of long wave signal

Frequency of long wave signal.

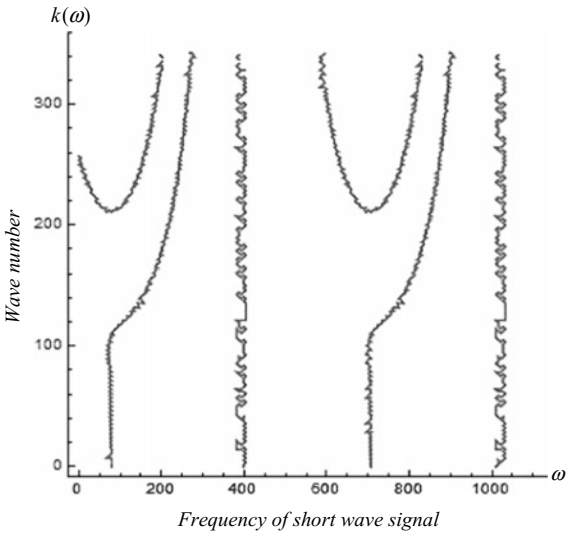

Fig. 4 The dependence of wave number on the frequency of short wave signal

This means that a low frequency electro-elastic wave signal during its propagation does not identify the existence of slight surface irregularities and very thin material interlayers on the waveguide surface of layer.

From Fig. 4 we see that the dispersion surface for high-frequency (short wave) signal changes greatly. This leads to a small quantitative change of the second wave with wavenumber $k_{02}(\omega)$.

But the first wavenumber $k_{01}(\omega)$ of wave changes qualitatively for quite short wave signals $k_{01}(\omega) \sim 100\ \mathrm{m}^{-1}$ (i.e.$\lambda_{01}(\omega) \sim 0.0628$ mm), giving a space for a new wave mode emergence. It's interesting that ultra-short wave solutions do not exist somewhere about $k_n(\omega) \geq 350\ \mathrm{m}^{-1}$.

The investigation of the arising frequency pattern in the problem of propagation of an electro-elastic shear wave signal in a piezoelectric homogeneous waveguide with irregular surfaces, where the irregularities on one surface are filled with perfect conductor, and on the other surface—with a good dielectric, gives some interesting results. For the fast waves, when the phase velocity is greater than the values of shear spatial waves in the adjacent materials—$V_\phi(k;\omega) \geq c_{nt}$, the dispersion of the long waves when $k \in [0; 1.6]$ occurs in the interval $\omega(k) \in [0; 5000]$ (Fig. 5).

In the case of slow wave signals, when the phase velocity is less than the values of shear spatial waves in the adjacent materials—$V_\phi(k;\omega) < c_{nt}$—we obtain an interesting phase pattern again (Fig. 6).

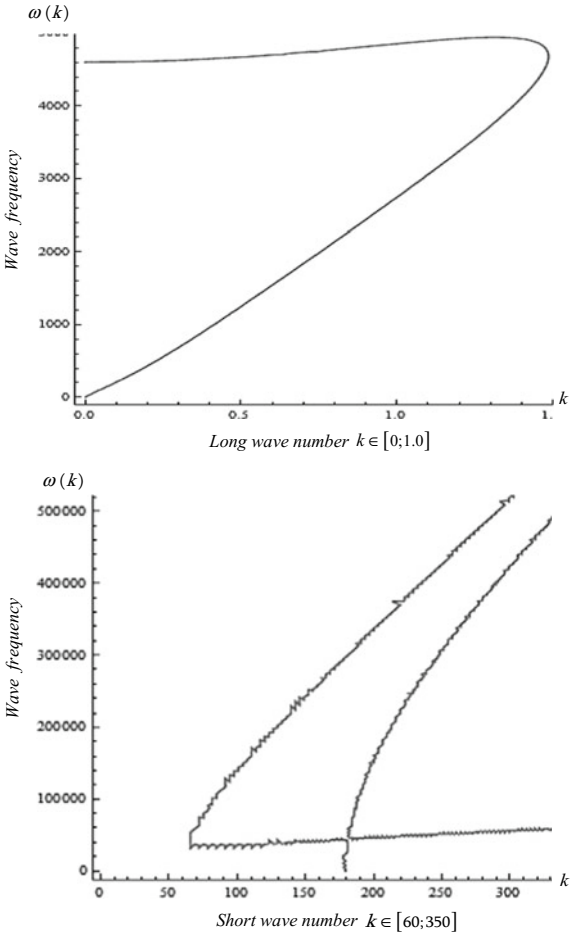

Fig. 5 The frequency versus of wave number for slow shear waves

3.3 The Propagation of High-Frequency Shear Elastic Waves on Interface of Isotropic Elastic Half-Spaces with Canonical Surface Protrusions (Model–3)

The features of the formation and propagation of forms of an elastic shear wave, concatenated with a canonical (rectangular, periodic in section) protrusions of surfaces each with the other one in elastic isotropic half-spaces (Fig. 7) is investigated [17]. The connection of two half-spaces with surface canonical protrusions is modeled as a composite waveguide consisting of periodically, longitudinally inhomogeneous embedded inner layer in two homogeneous half-spaces.

It is shown from the formation of half-spaces with protrusions, that for the convenience of the mathematical boundary value problem, the coordinate plane *yoz*

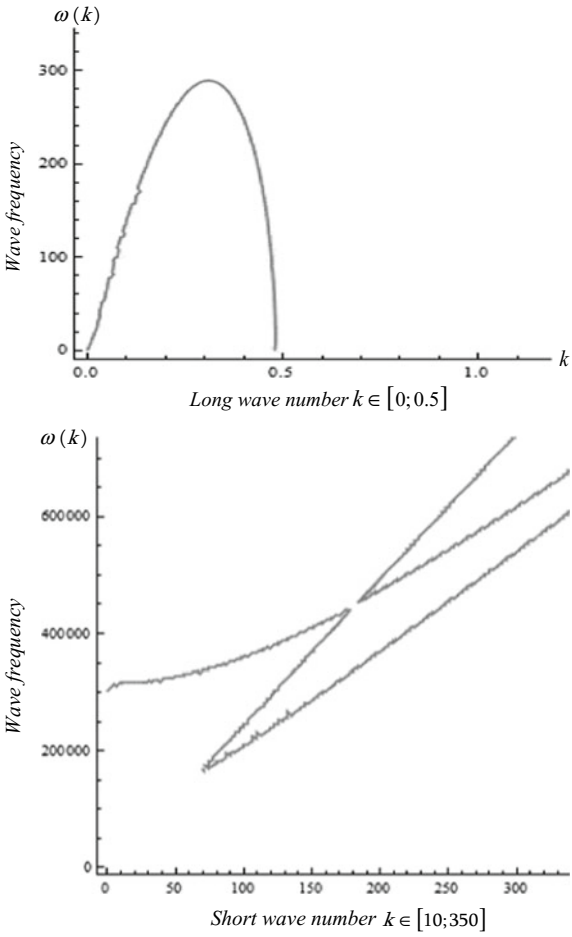

Fig. 6 The frequency versus of wave number for fast shear waves

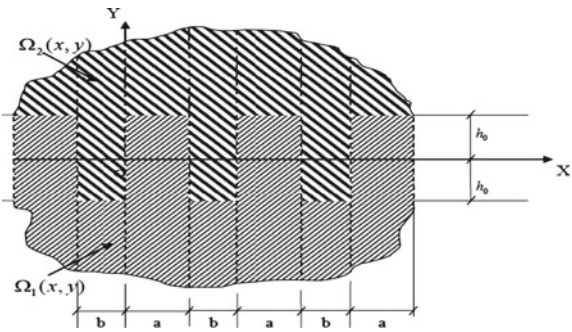

Fig. 7 Connection diagram of two elastic half-spaces with canonical surface pins, as a three-layer waveguide with a periodically inhomogeneous inner layer

(coordinate plane $x = 0$) is allocated on one of lateral surfaces of the protrusion contact of the half-spaces $\Omega_1\{x; y\}$ and $\Omega_2\{x; y\}$, and the coordinate axis oz is parallel to the forming of these projections. The canonicity of projections (the forms of pins and their linear dimensions) allows us to provide the full mechanical contact along the entire line of contact of half-spaces.

By input of virtual cross-sections, in fact a three-layer waveguide is formed from two homogeneous half-spaces and virtually separated longitudinally inhomogeneous (piecewise-homogeneous) layer of periodically distributed cells of protrusions pairs $\Omega_{1n}\{x; y\}$ and $\Omega_{2n}\{x; y\}$.The mathematical boundary problem on the propagation of normal wave signal (***SH***) of elastic shear is formulated from the equations of the corresponding homogeneous half-spaces and their respective protrusions:

– in $\Omega_1\{x; y\}$ and $\Omega_{1n}\{x; y\}$

$$\partial^2 \mathrm{w}_1(x; y)/\partial x^2 + \partial^2 \mathrm{w}_1(x; y)/\partial y^2 = -\omega^2/c_{1t}^2 \cdot \mathrm{w}_1(x; y), \tag{5.1}$$

– in $\Omega_2\{x; y\}$ and $\Omega_{2n}\{x; y\}$

$$\partial^2 \mathrm{w}_2(x; y)/\partial x^2 + \partial^2 \mathrm{w}_2(x; y)/\partial y^2 = -\omega^2/c_{2t}^2 \cdot \mathrm{w}_2(x; y), \tag{5.2}$$

One group of boundary conditions of full mechanical contact is satisfied on the virtual cross-sections $y = h_0$ and $y = -h_0$ along the widths of surface protrusions, respectively. Along the width of each protrusion $\Omega_{1n}\{x; y\}$, the continuity surface conditions of mechanical fields will be

$$\begin{aligned} &\mathrm{w}_1(x; -h_0; t) \equiv \mathrm{w}_1(x; -h_0; t), \\ &G_1 \cdot \partial \mathrm{w}_1(x; y; t)/\partial y|_{y=-h_0} \equiv G_1 \cdot \partial \mathrm{w}_1(x; y; t)/\partial y|_{y=-h_0} \end{aligned} \tag{5.3}$$

$$\begin{aligned} &\mathrm{w}_1(x; h_0; t) = \mathrm{w}_2(x; h_0; t), \\ &G_1 \cdot \partial \mathrm{w}_1(x; y; t)/\partial y|_{y=h_0} = G_2 \cdot \partial \mathrm{w}_2(x; y; t)/\partial y|_{y=h_0} \end{aligned} \tag{5.4}$$

Along the width of each protrusion $\Omega_{2n}\{x; y\}$, the continuity surface conditions of mechanical fields will be

$$\begin{aligned} &\mathrm{w}_2(x; -h_0; t) = \mathrm{w}_1(x; -h_0; t), \\ &G_2 \cdot \partial y/\partial \mathrm{w}_2(x; y; t)|_{y=-h_0} = G_1 \cdot \partial \mathrm{w}_1(x; y; t)/\partial y|_{y=-h_0} \end{aligned} \tag{5.5}$$

$$\begin{aligned} &\mathrm{w}_2(x; h_0; t) \equiv \mathrm{w}_2(x; h_0; t), \\ &G_2 \cdot \partial \mathrm{w}_2(x; y; t)/\partial y|_{y=h_0} \equiv G_2 \cdot \partial \mathrm{w}_2(x; y; t)/\partial y|_{y=h_0} \end{aligned} \tag{5.6}$$

In addition to the given boundary conditions on virtual selected sections, surface conditions of full mechanical contact are satisfied on the entire lateral surfaces of protrusions.

Taking into account the periodicity of the structure of internal virtual layer, theory of Lyapunov-Floquet is used and the boundary value problem is solved for the repeated cell with the number zero.

Satisfying the conditions of full mechanical contact on the lateral surface of the protrusions $x = 0$,

$$\begin{aligned} &\mathrm{w}_1(0; y; t) = \mathrm{w}_2(0; y; t), \\ &G_1 \cdot \partial \mathrm{w}_1(x; y; t)/\partial x|_{x=0} = G_2 \cdot \partial \mathrm{w}_2(x; y; t)/\partial x|_{x=0} \end{aligned} \tag{5.7}$$

as well as the conditions on lateral surfaces of protrusions $x = -b$ and $x = a$, taking into account the periodicity of solutions by x coordinate

$$\begin{aligned} &\mathrm{w}_1(x; y; t)|_{x=a} = \mu^{-1}\, \mathrm{w}_2(x; y; t)|_{x=-b}, \\ &\mu \cdot G_1 \cdot \partial \mathrm{w}_1(x; y; t)/\partial x|_{x=a} = G_2 \cdot \partial \mathrm{w}_2(x; y; t)/\partial x|_{x=-b} \end{aligned} \tag{5.8}$$

damping through the depth of homogeneous half-spaces $\Omega_1\{x; y\}$ and $\Omega_2\{x; y\}$, as well as in canonical (rectangular, periodic in section) protrusions of surfaces for $y \to \pm\infty$, respectively, normal waves are presented in the form

$$\mathrm{w}_1(x; y; t) = A_1 \cdot X_{01}(x) \cdot \exp(\alpha_{1t} k_1 y) \cdot \exp(-i\omega t) \text{ in } \Omega_1\{x; y\} \tag{5.9}$$

$$\mathrm{w}_2(x; y; t) = A_2 \cdot X_{02}(x) \cdot \exp(-\alpha_{2t} k_2 y) \cdot \exp(-i\omega t) \text{ in } \Omega_2\{x; y\} \tag{5.10}$$

$$\mathrm{w}_1^*(x; y; t) = X_{01}(x) \cdot \left[A_1^* \cdot sh(k_1\alpha_{1t} y) + B_1^* \cdot ch(k_1\alpha_{1t} y)\right] \cdot \exp(-i\omega t) \tag{5.11}$$

$$\mathrm{w}_2^*(x; y; t) = X_{02}(x) \cdot \left[A_2^* \cdot sh(k_2\alpha_{2t} y) + B_2^* \cdot ch(k_2\alpha_{2t} y)\right] \cdot \exp(-i\omega t) \tag{5.12}$$

For the corresponding homogeneous half-spaces, $\alpha_{nt} \triangleq \sqrt{1 - \omega^2/[k_n^2(\omega) \cdot c_{nt}^2]}$ are the wave formation coefficients (in the case of slow waves—coefficients of attenuation into the corresponding half-spaces).

As follows from the Eqs. (5.1) and (5.2), the solutions providing synchronicity of propagation waves in homogeneous half-spaces and their rectangular protrusions, match and are written by harmonic functions in periodic, laterally inhomogeneous layer

$$X_{0n}^*(x) = X_{0n}(x) = C_n \sin(k_n x) + D_n \cos(k_n x), \quad \text{for } n = 1; 2 \tag{5.13}$$

After satisfying the boundary conditions of continuity of mechanical fields (5.3)–(5.6) we obtain the dispersion relations.

$$th(2\alpha_{1t} k_1 h_0) = G_1\alpha_{1t} \cdot (G_1\alpha_{1t} + G_2\alpha_{2t})/\left(G_1\alpha_{1t} G_2\alpha_{2t} + G_{01}^2\alpha_{1t}^2\right) \tag{5.14}$$

$$th(2\alpha_{2t} k_2 h_0) = G_2\alpha_{2t} \cdot (G_1\alpha_{1t} + G_2\alpha_{2t})/\left(G_1\alpha_{1t} G_2\alpha_{2t} + G_0^2\alpha_{2t}^2\right) \tag{5.15}$$

The system of dispersion relations (5.14) and (5.15) represents itself the dispersion equation of wave formation through the thickness of composite waveguide. Their joint solution provides synchronized values of wave numbers in composite vertical components of waveguide.

The localization of wave energy near the junction of surfaces is possible only in the case of propagation of slow shear waves, for which $V_\phi(\omega/k) < \min\{c_{1t}; c_{2t}\}$. In this case the system of dispersion relations (5.14) and (5.15) takes a rather simple form

$$th(2h_0\alpha_{1t}(\omega)\cdot k_1(\omega)) = 1 \quad and \quad th(2h_0\alpha_{2t}(\omega)k_2(\omega)) = 1 \tag{5.16}$$

Since the hyperbolic tangents are quickly descending in Eq. (5.16) and allowed wave lengths for periodic inhomogeneity are always of order of the composite layer widths $\lambda(\omega) \sim \min\{a;\ b\}$, from (5.16) the approximation of the solution with great precision for arguments $2\alpha_{nt}k_nh_0 = 4\pi$ is received

$$k_n(\omega) = (\omega/c_{nt})\cdot\sqrt{1+(2\pi c_{nt}/\omega h_0)^2}, \quad n = 1; 2 \tag{5.17}$$

Here the found wave numbers in both half-spaces provide lower phase velocity than bulk shear wave in each medium. Corresponding to the slow wave, phase velocity in each composite layer can be written as

$$\begin{aligned} V_{a\phi}(\omega/k) &= c_{1t}/\sqrt{1+\left(2\pi c_{1t}/\omega h_0\right)^2} \\ V_{b\phi}(\omega/k) &= c_{2t}/\sqrt{1+\left(2\pi c_{2t}/\omega h_0\right)^2} \end{aligned} \tag{5.18}$$

The obtained value of phase velocity $V_{a\phi}(\omega/k)$ in the first layer satisfies the condition of slow waves $V_{1\phi}(\omega/k) < c_{2t}$ in the frequency range

$$0 < \omega \le (2\pi/h_0)\cdot(c_{1t}c_{2t}/\sqrt{c_{1t}^2 - c_{2t}^2}) \tag{5.19}$$

Therefore, the connection of isotropic, elastic half-spaces with canonical surface protrusions, for some ratios of the linear dimensions of protrusions leads to the localization of wave energy of elastic shear signal with certain frequency ω, near the virtual surfaces of homogeneous half-spaces.

By depth of a three-layer composite waveguide wave field will have the following description

$$Y_{0a}(y) = \begin{cases} A_1\cdot\exp[k_a(\omega)\alpha_{1t}(\omega)y] & -\infty < y \le -h_0 \\ A_1^*\cdot sh[k_a(\omega)\alpha_{1t}(\omega)y] & \\ +B_1^*\cdot ch[k_a(\omega)\alpha_{1t}(\omega)y] & -h_0 \le y \le h_0 \\ A_2\cdot\exp[-k_a(\omega)\alpha_{2t}(\omega)y] & h_0 \le y < \infty \end{cases} \tag{5.20}$$

$$Y_{0b}(y) = \begin{cases} A_1 \cdot \exp[k_b(\omega)\alpha_{1t}(\omega)y] & -\infty < y \le -h_0 \\ A_2^* \cdot sh[k_b(\omega)\alpha_{2t}(\omega)y] & \\ +B_2^* \cdot ch[k_b(\omega)\alpha_{2t}(\omega)y] & -h_0 \le y \le h_0 \\ A_2 \cdot \exp[-k_b(\omega)\alpha_{2t}(\omega)y] & h_0 \le y < \infty \end{cases} \tag{5.21}$$

To construct the obtained localized forms of wave distributions over the thickness of a layered waveguide (5.19) and (5.20), it is necessary to match the wave numbers determined by (5.17) to the dispersion equation for wave propagation in a periodically longitudinally non-uniform structure

$$\cos[L \cdot k_f(\omega)] = \cos[k_1(\omega) \cdot a] \cdot \cos[k_2(\omega) \cdot b] - \frac{G_2^2 k_2^2(\omega) + G_1^2 k_1^2(\omega)}{2G_2 k_2(\omega) \cdot G_1 k_1(\omega)} \sin[k_1(\omega) \cdot a] \cdot \sin[k_2(\omega) \cdot b] \tag{5.22}$$

In dispersion relation (5.21) $\lambda(\omega) = \exp(Lk_f(\omega))$ is a multiplier, and $L = a + b$ is the period of wave numbers $k_1(\omega)$ and $k_2(\omega)$ in the surface protrusions $\Omega_{1n}\{x; y\}$ and $\Omega_{2n}\{x; y\}$, respectively. $k_f(\omega) = 2\pi/\lambda_f(\omega)$ is the wave number of formed wave (Floquet wave number) corresponding to allowed wave length $\lambda_f(\omega)$.

Synchronization of shear wave propagation in general assumes the same allowed wave number

$$k_f(\omega) = \frac{\arccos\left\{ \begin{array}{l} \dfrac{(G_2k_2 + G_1k_1)^2 \cos(k_1a + k_2b)}{4G_2k_2G_1k_1} \\ -\dfrac{(G_2k_2 - G_1k_1)^2 \cos(k_1a - k_2b)}{4G_2k_2G_1k_1} \end{array} \right\}}{L} \tag{5.23}$$

Considering the received relations as an area of definition for the allowed lengths of the wave signal in the periodic structure, from (5.22) we get

$$\lambda_f(\omega) = \frac{2\pi L}{\arccos\left\{ \frac{(G_2k_2+G_1k_1)^2}{4G_2k_2G_1k_1} \left[\cos(k_1a + k_2b) - \frac{(G_2k_2-G_1k_1)^2}{(G_2k_2+G_1k_1)^2} \cos(k_1a - k_2b) \right] \right\}} \tag{5.24}$$

It should be noted, that the allowed wave lengths for the known inhomogeneity are always of order of the composite layer widths $\lambda_f(\omega) \sim \min\{a; b\}$.

Numerical calculations are carried out for cases when the conductor and the piezoelectric are bounded, without considering their electromagnetic properties (Table 1).

The formation of zones of forbidden and/or the allowed frequencies is shown on Fig. 8 for slow high-frequency shear waves with phase speed less than the minimum bulk wave of adjacent materials $V_\phi(\omega/k) \le \min\{c_{1t}; c_{2t}\}$, in a composite waveguide of ZnO and Au. It is shown analytically, that slow waves are formed at relatively low frequencies (5.19), in this case up to $\approx 0.85 \times 10^{10}$ Hz. The zones of allowed

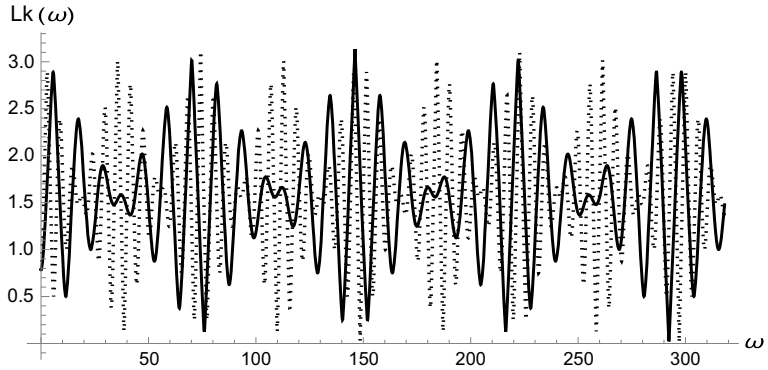

Fig. 8 The dispersion curves of localized shear nanometer waves $\lambda \sim 10^{-9}$ m at the mechanically free surface of half-space of piezoelectric crystal (PZT-4) or Gold (Au), for micrometer height $h_0 = 10^{-6}$ m and micrometer widths of protrusions and cavities of surface protrusions $a = 10^{-8}$ m and $b = 5 \times 10^{-7}$ m

frequencies of these localized waves are already determined from the system (5.23) taking into account (5.17), in the definition range (5.19).

It follows from the calculations, that the formation of localized slow waves with the wave numbers (5.17) in the composite waveguide, in contrast to the case of propagation of shear bulk wave in periodically longitudinally inhomogeneous waveguide of homogeneous layers with wave numbers $k_n(\omega) = \omega/c_{nt}$ [20], have an almost continuous range of frequencies with one thin frequency slit. Their joint solution provides synchronized values of wave numbers in composite vertical components of waveguide.

From more visual graphs of high-frequency propagation (Fig. 8), it follows that forbidden frequency zones do not form in this task, in which wave numbers $k(\omega)$ do not exist. In this case, the dispersion lines have clearly outlined envelopes at the top and bottom. It is also obvious, that the different stiffness of the materials of half-spaces lead to frequency shear of the dispersion curves between each other.

It is interesting, that in all these cases the nature of changes of phase speeds are the same in the virtually selected layers Fig. 8, while the phase speed in the cavity layer ($a \le x \le a + b$) is less than the phase speed in the protrusion layer ($0 \le x \le a$).

4 Conclusion

The boundary joints of rough surfaces are virtually modeled as a laminate of thin, geometrically or physically inhomogeneous media. Taking into account the randomness of the inhomogeneities of the surface band, the hypothesis MELS is introduced.

By the introduction of the hypothesis MELS, according to surfaces inhomogeneities, the near-surface inhomogeneity zone is mathematically simulated as a

meta-surface with the equivalent electromechanical loades. The piezoelectric layer with a smoothed roughness of both surfaces by casting different materials is mathematically modeled as an inner base waveguide with electromechanical loads on the meta-surfaces.

The connection of two half-spaces with surface canonical protrusions is modeled as a composite waveguide consisting of periodically, laterally inhomogeneous embedded inner layer in two homogeneous half-spaces. In neighboring cells of periodically inhomogeneous layered composite waveguide, the conditions of shear elastic wave propagation are obtained.

From the dispersion equations for the formation of a waveform across the layer thickness, nature of change of the phase speeds and amplitude distribution through the thickness of the waveguide in the virtually sectioned vertical layers are investigated.

From the dispersion equation describing the propagation of the formed wave, the zones of allowed and forbidden frequencies for wave propagation are determined.

References

1. Miniaci, M., Gliozzi, A.S., Morvan, B., Krushynska, A., Bosia, F., Scalerandi, M., et al.: Proof of concept for an ultrasensitive technique to detect and localize sources of elastic nonlinearity using phononic crystals. Phys. Rev. Lett. **118**, 214301 (2017). https://doi.org/10.1103/PhysRevLett.118.214301
2. Krushynska, A.O., Bosia, F., Miniaci, M., Pugno, N.M.: Spider web-structured labyrinthine acoustic metamaterials for low-frequency sound control. New J. Phys. **19**, 105001 (2017). https://doi.org/10.1088/1367-2630/aa83f3
3. Miniaci, M., Krushynska, A., Bosia, F., Pugno, N.: New J. Phys. **18**, 083041 (2016). https://doi.org/10.1088/1367-2630/18/8/083041
4. Deymier, P.A. (ed.): Acoustic Metamaterials and Phononic Crystals, Springer Series in Solid-State Sciences. Springer, Berlin, Heidelberg (2013). https://doi.org/10.1007/978-3-642-31232-8
5. Laude, V.: Phononic Crystals: Artificial Crystals for Sonic, Acoustic, and Elastic Waves. Walter de Gruyter GmbH , Berlin, Boston, MA (2015)
6. Hussein, M.I., Leamy, M.J., Ruzzene, M.: Dynamics of phononic materials and structures: historical origins, recent progress, and future outlook. Appl. Mech. Rev. **66**, 040802 (2014). https://doi.org/10.1115/1.4026911
7. Bosia F., Krushynska A.O., Miniaci M., Morvan B. and Pugno N.M. (eds.): Advances in Mechanical Metamaterials, 19 Sept 2018. https://doi.org/10.3389/fmats.2018.00056
8. Moleron, M., Serra-Garcia, M., Daraio, C.: Visco-thermal effects in acoustic metamaterials: from total transmission to total reflection and high absorption. New J. Phys. **18**(3), 03303 (2016). https://doi.org/10.1088/1367-2630/18/3/033003
9. Palermo, A., Marzani, A.: Control of love waves by resonant metasurfaces. Sci. Rep. **8**(1), 7234 (2018). https://doi.org/10.1038/s41598-018-25503-8
10. Fabro, A.T., Sampaio, R., de Cursi, E.S.: Wave attenuation from a metamaterial beam assembly with uncertainties. Preprint July 2018. https://doi.org/10.13140/RG.2.2.16674.73921
11. Fomenko, S.I., Golub, M.V., Zhang, C.: Wave phenomena and band-gap formation in layered phononic crystals with functionally graded interlayers and periodic arrays of cracks. J. Physics: Conf. Series **1092**, 012035 (2018). https://doi.org/10.1088/1742-6596/1092/1/012035
12. Assouar, B., Liang, B., Wu, Y., Li, Y., Cheng, J.-C., Jing, Y.: Acoustic metasurfaces. Nat. Rev. Mater. Article (2018). https://doi.org/10.1038/s41578-018-0061-4

13. Miranda Jr., E.J.P., Nobrega, E.D., Ferreira, A.H.R., Dos Santos, J.M.C.: Flexural wave band gaps in a multi-resonator elastic metamaterial plate using Kirchhoff-Love theory. Mech. Syst. Sign. Process. **116**, 480–504 (2019). https://doi.org/10.1016/j.ymssp.2018.06.059
14. Avetisyan, A.S.: The boundary problem modeling of rough surfaces continuous media with coupled physical-mechanical fields. Rep. NAS Armenia **115**(2), 119–131 (2015)
15. Avetisyan, A.S.: On the formulation of the electro-elasticity theory boundary value problems for electro-magneto-elastic composites with interface roughness. Proc. NAS Armenia Mech. **68**(2), 29–42 (2015)
16. Avetisyan, A.S., Kamalyan, A.A., Hunanyan, A.A.: Features of localization of wave energy at rough surfaces of piezodielectric waveguide. Proc. NAS Armenia Mech. **70**(1), 40–63 (2017)
17. Avetisyan, A.S., Belubekyan, M.V., Ghazaryan, K.B.: The propagation of high-frequency shear elastic waves on interface of isotropic elastic half-spaces with canonical surface protrusions. Am. J. Earth Sci. Eng. **1**(2), 114–128 (2018)
18. Avetisyan, A.S., Hunanyan, A.A.: The efficiency of application of virtual cross-sections method and hypotheses MELS in problems of wave signal propagation in elastic waveguides with rough surfaces. J. Adv. Phys. 11(7), 3564–3574 (2016). https://doi.org/10.13140/RG.2.1.4348.5049
19. Avetisyan, A.S., Hunanyan, A.A.: Amplitude-phase distortion of the normal high-frequency shear waves in homogeneous elastic waveguide with weakly rough surfaces. Proc. NAS Armenia Mech. **70**(2), 28–42 (2017)
20. Piliposyan, G.T., Avetisyan, A.S., Ghazaryan, K.B.: Shear wave propagation in periodic phononic/photonic piezoelectric medium. Wave Motion **49**(1), 125–134 (2012). https://doi.org/10.1016/j.wavemoti.2011.08.001

A Comparative Analysis of Wave Properties of Finite and Infinite Cascading Arrays of Cracks

Vitaly V. Popuzin, M. Y. Remizov, Mezhlum A. Sumbatyan and Michele Brigante

Abstract Reflection and transmission coefficients in the problems of the normal plane wave incidence on the system of finite and infinite periodic arrays of cracks in an elastic body are determined. We propose a method permitting to solve the scalar diffraction problem for both single crack and any finite number of cracks with arbitrary lattice geometry. Under the condition of one-mode frequency regime the problem is reduced to a discretization of the basic integral equation holding on the boundary of the scatterers located in one horizontal waveguide. A semi-analytical method developed earlier for diffraction problems on infinite periodic crack arrays permits a comparative analysis of the properties of the main external parameters for a finite periodic system of cracks, where the solution of the boundary integral equations is numerically constructed, and we obtain explicit analytical representations for the wave field at the boundary of the obstacles. The analysis of the properties of the scattering coefficients depending on the physical parameters is carried out for three diffraction problems: a finite periodic system in a scalar formulation, an infinite periodic system in a scalar formulation, an infinite periodic system in a plane problem of the elasticity theory.

1 Introduction

In the present paper we continue to study the properties of metamaterials with application to mechanical, electromagnetic and acoustic problems possessing some specific periodic internal structure [1, 2]. The most part of the theoretical methods are based on numerical treatment such as Finite element method or Boundary element method. In recent years, the experimental base devoted to this topic is being actively devel-

V. V. Popuzin · M. Y. Remizov · M. A. Sumbatyan (✉)
Southern Federal University, 105/42 Bolshaya Sadovaya Str.,
Rostov-on-Don 344006, Russian Federation
e-mail: sumbat@math.rsu.ru

M. Brigante
University of Naples—Federico II, Via Claudio 21, 84125 Naples, Italy

M. A. Sumbatyan (ed.), *Wave Dynamics, Mechanics and Physics of Microstructured Metamaterials*, Advanced Structured Materials 109,
https://doi.org/10.1007/978-3-030-17470-5_7

oped. There are also some semi-analytical methods used for infinite or semi-infinite periodic structures, which are based on some asymptotic (low-frequency or high-frequency) estimates, being valid only in the far zone of the wave field [3–8]. In [5, 9–11], the analytical formulas for the coefficients of reflection and transmission in the low frequency range of the acoustic, electromagnetic and elastic waves, penetrating through the periodic system of holes of arbitrary shape and three-dimensional obstacles, are presented. Two-dimensional problems of wave propagation through a periodic screen lattice in elastic bodies with a single—periodic system of cracks are studied in [7, 12], and in [13–17] there is considered a doubly-periodic system. In [18–20] the problems of diffraction by a plane lattice of cylindrical cavities are solved. It should be noted that the wave properties of elastic media containing periodic structures of more complex physical nature—pores, inclusions, et al., have been analyzed in [21–24].

The problems discussed in this paper are related to the theory of the so-called "acoustic metamaterials", which, due to their specific internal structure, have the properties of acoustic filters. This means that such a material is able to pass the passing wave over certain frequency intervals and lock the wave channel for other frequencies. The property was experimentally discovered and presented in [25]. Some fundamental aspects related to the acoustic metamaterials are discussed in [26–28] and some other publications.

It should be noted that a semi-analytical method in wave dynamics of periodic structures has also been proposed in [29].

2 Problem Formulation

To study the filtration properties of the metamaterials, let us consider the normal incidence of a plane longitudinal wave, propagating in an unbounded medium $p^{inc} = e^{ikx_1}$, on a doubly-periodic system of finite number $M(>2)$ of identical vertical arrays, which are finite or infinite along x_2 and infinite in the direction x_3. Each of them is an ordinary periodic system of coplanar linear cracks located at $x = 0, d, 2d, \ldots, (M-1)d$. In the infinite case, under the natural symmetry, the problem is reduced to the consideration of a plane waveguide of the width $2a$, which includes M cracks (Fig. 1). For the finite case it is necessary to solve the corresponding boundary integral equation over all available contours of the crack system.

It is assumed that with the normal wave incidence $e^{i(k_1x_1-\omega t)}$ there is a regime of one-mode propagation at $k_1a < \pi$, where k_1—the wave number of the longitudinal wave, $2a$—the period of the system in the vertical direction, d—in the horizontal one. The semi-analytical method is used when the distance between the adjacent parallel arrays d and the incident wave length $\lambda = 2\pi/k_1$ are such that the condition $\lambda/d \gg 1$ is satisfied. A comparative analysis of the properties of the scattering parameters is carried out for the three diffraction problems for a finite and infinite periodic system in a scalar formulation, as well as for an infinite periodic system under the conditions of the plane problem of the elasticity theory.

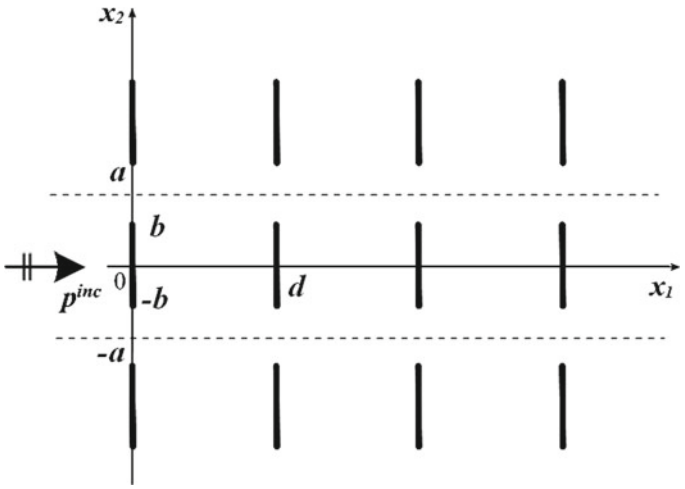

Fig. 1 Incidence of a plane wave on a periodic array of linear obstacles

3 Infinite Periodic System. Anti-plane Problem

The solution for elastic problems with infinite periodic arrays of cracks, in the anti-plane formulation is presented in [5, 7, 15]. Omitting some routine transformations, the problem can be reduced to the following system of M integral equations regarding the unknown functions $g^s(y)$; $|y| < b$; $s = 1, \ldots, M$, [8]:

$$\begin{gathered}
\frac{1}{2a}\int_{-b}^{b} g^1(t)\left\{\frac{1}{2}-\frac{K(y-t)}{ik_2}\right\}dt+\frac{e^{ik_2 d}}{4a}\int_{-b}^{b} g^2(t)dt+\frac{e^{2ik_2 d}}{4a}\int_{-b}^{b} g^3(t)dt+\ldots+\frac{e^{ik_2(M-1)d}}{4a}\int_{-b}^{b} g^M(t)dt=1;\\
\frac{e^{ik_2 d}}{4a}\int_{-b}^{b} g^1(t)dt+\frac{1}{2a}\int_{-b}^{b} g^2(t)\left\{\frac{1}{2}-\frac{K(y-t)}{ik_2}\right\}dt+\frac{e^{ik_2 d}}{4a}\int_{-b}^{b} g^3(t)dt+\ldots+\frac{e^{ik_2(M-2)d}}{4a}\int_{-b}^{b} g^M(t)dt=e^{ik_2 d};\\
\frac{e^{ik_2 2d}}{4a}\int_{-b}^{b} g^1(t)dt+\frac{e^{ik_2 d}}{4a}\int_{-b}^{b} g^2(t)dt+\frac{1}{2a}\int_{-b}^{b} g^3(t)\left\{\frac{1}{2}-\frac{K(y-t)}{ik_2}\right\}dt+\ldots+\frac{e^{ik_2(M-3)d}}{4a}\int_{-b}^{b} g^M(t)dt=e^{ik_2 2d};\\
\ldots \qquad (1)\\
\frac{e^{ik_2(M-1)d}}{4a}\int_{-b}^{b} g^1(t)dt+\frac{e^{ik_2(M-2)d}}{4a}\int_{-b}^{b} g^2(t)dt+\ldots+\frac{e^{ik_2 d}}{4a}\int_{-b}^{b} g^{M-1}(t)dt+\frac{1}{2a}\int_{-b}^{b} g^M(t)\left\{\frac{1}{2}-\frac{K(y-t)}{ik_2}\right\}dt=e^{ik_2(M-1)d},
\end{gathered}$$

where the kernel has the following form: $K(y) = \sum_{n=1}^{\infty} r_n \cos(a_n y)$, $r_n = \sqrt{(\pi n/a)^2 - k_2^2}$, $a_n = \pi n/a$, k_2—the wave number of the incident transverse wave. As mentioned for some aspects of the proposed semi-analytical method [16, 17], it is necessary to consider the auxiliary integral equation, whose kernel $K(y)$ requires a special treatment:

$$\frac{1}{2a}\int_{-b}^{b} h(\eta)K(y-\eta)d\eta = 1,\ K(y) = \sum_{n=1}^{\infty} r_n \cos(a_n y),\quad |y| < b. \tag{2}$$

Since $r_n \sim a_n, n \to \infty$, the expression for the kernel (2) can be transformed to the following form

$$K(y) = \sum_{n=1}^{\infty} a_n \cos(a_n y) + \sum_{n=1}^{\infty}[r_n - a_n]a_n \cos(a_n y),\ K(y) = I(y) + K_r(y). \tag{3}$$

Here the second part of the kernel is a certain regular function. The first part contains both regular and singular parts: $I(y) = [I_r(y) + I_s(y)]$. Obviously,

$$\frac{a}{\pi} I(y) = \sum_{n=1}^{\infty} n \cos(\pi n y/a) \tag{4}$$

The representation for the sum (4) can be calculated in a generalized sense, as follows

$$\sum_{n=1}^{\infty} n \cos(\pi n y/a) = \lim_{\varepsilon \to +0} \sum_{n=1}^{\infty} \mathrm{e}^{-\varepsilon n} n \cos(\pi n y/a)$$
$$= -\frac{1}{4\sin^2(\pi y/2a)}, \left(\sim -\frac{a^2}{\pi^2 y^2}, y \to 0\right),$$

then the kernel of the integral Eq. (3) is $K(y) = I_r(y) + I_s(y) + K_r(y)$, where the singular and the regular parts of function $I(y)$ are, respectively

$$\frac{a}{\pi} I_s(y) = -\frac{a^2}{\pi^2 y^2},\ \frac{a}{\pi} I_r(y) = \frac{a^2}{\pi^2 y^2} - \frac{1}{4\sin^2(\pi y/2a)}. \tag{5}$$

In can be seen that the behavior of the kernel for small argument is hyper-singular, which is in a good agreement with the classical theory of cracks in the elasticity theory for unbounded media [30]. To provide a stable numerical method, we apply here a discrete quadrature formula for the hyper-singular kernels, known as "the method of discrete vortices" [31]. By applying the new expression for the kernel of the basic integral Eqs. (3), (5), let us rewrite it in the following form:

$$\frac{1}{2a}\int_{-b}^{b} h(\eta)\left[\Phi_r(y-\eta) - \frac{a}{\pi(y-\eta)^2}\right]d\eta = 1,\ \Phi_r(y) = I_r(y) + K_r(y) \tag{6}$$

The discretization of the integral operator in the left-hand side (6) leads to the following formula

$$\frac{1}{2a}\sum_{k=1}^{N}\int_{\eta_{k-1}}^{\eta_k} h(\eta)\left[\Phi_r(y_l-\eta)-\frac{a}{\pi(y_l-\eta)^2}\right]d\eta$$
$$=\frac{1}{2a}\sum_{k=1}^{N}h(\eta_k)\left[\Phi_r(y_l-\eta_k)\varepsilon-\frac{a}{\pi}\int_{\eta_{k-1}}^{\eta_k}\frac{d(\eta-y_l)}{\pi(y_l-\eta)^2}\right]$$
$$=\frac{1}{2a}\sum_{k=1}^{N}h(\eta_k)\left[\Phi_r(y_l-\eta_k)\varepsilon-\frac{a}{\pi}\left(\frac{1}{y_l-\eta_k}-\frac{1}{y_l-\eta_{k-1}}\right)\right],$$

where $\eta_k=-b+k\varepsilon$, $y_l=-b+(l-0.5)\varepsilon$, $l=1,\ldots,N$, $\varepsilon=2b/N$. As a result, we obtain the following algebraic system of linear equations:

$$\frac{1}{2a}\sum_{k=1}^{N}h(\eta_k)\left[\Phi_r(y_l-\eta_k)\varepsilon-\frac{a}{\pi}\left(\frac{1}{y_l-\eta_k}-\frac{1}{y_l-\eta_{k-1}}\right)\right]=1 \tag{7}$$

By using the auxiliary Eq. (2), for which we introduce the integral characteristics

$$H=\int_{-b}^{b}h(t)dt,\quad J_j=\int_{-b}^{b}g_x^j(t)dt,\quad j=1,2,\ldots,M, \tag{8}$$

one deduces from (1) and (2), in terms of function $h(y)$:

$$\begin{aligned}
&ik_2^{-1}g^1(\eta)=-h(\eta)[(1/4a)J_1+(e^{ik_2d}/4a)J_2+(e^{ik_2 2d}/4a)J_3+\ldots+(e^{ik_2(M-1)d}/4a)J_M-1];\\
&ik_2^{-1}g^2(\eta)=-h(\eta)[(e^{ik_2d}/4a)J_1+(1/4a)J_2+(e^{ik_2d}/4a)J_3+\ldots+(e^{ik_2(M-2)d}/4a)J_M-e^{ik_2d}];\\
&ik_2^{-1}g^3(\eta)=-h(\eta)[(e^{ik_2 2d}/4a)J_1+(e^{ik_2d}/4a)J_2+(1/4a)J_3+\ldots+(e^{ik_2(M-3)d}/4a)J_M-e^{ik_2 2d}];\\
&\qquad\qquad\ldots\\
&ik_2^{-1}g^M(\eta)=-h(\eta)[(e^{ik_2(M-1)d}/4a)J_1+(e^{ik_2(M-2)d}/4a)J_2+\ldots+(e^{ik_2d}/4a)J_{M-1}+(1/4a)J_M-e^{ik_2(M-1)d}].
\end{aligned} \tag{9}$$

By integrating (9) over the interval $|y|<b$, we obtain the following system of linear algebraic equations regarding $\tilde{J}_j=J_j/4a,\ j=1,2,\ldots,M$

$$\begin{aligned}
&\left(1+\tfrac{4ai}{k_2H}\right)\tilde{J}_1+e^{ik_2d}\tilde{J}_2+e^{ik_2 2d}\tilde{J}_3+\ldots+e^{ik_2(M-1)d}\tilde{J}_M=1;\\
&e^{ik_2d}\tilde{J}_1+\left(1+\tfrac{4ai}{k_2H}\right)\tilde{J}_2+e^{ik_2d}\tilde{J}_3+e^{ik_2 2d}\tilde{J}_4+\ldots+e^{ik_2(M-2)d}\tilde{J}_M=e^{ik_2d};\\
&e^{ik_2 2d}\tilde{J}_1+e^{ik_2d}\tilde{J}_2+\left(1+\tfrac{4ai}{k_2H}\right)\tilde{J}_3+e^{ik_2d}\tilde{J}_4+e^{ik_2 2d}\tilde{J}_5+\ldots+e^{ik_2(M-3)d}\tilde{J}_M=e^{ik_2 2d};\\
&\qquad\qquad\ldots\\
&e^{ik_2(M-1)d}\tilde{J}_1+e^{ik_2(M-2)d}\tilde{J}_2+\ldots+e^{ik_2d}\tilde{J}_{M-1}+\left(1+\tfrac{4ai}{k_2H}\right)\tilde{J}_M=e^{ik_2(M-1)d}.
\end{aligned} \tag{10}$$

The matrix of system (10) takes the following form, with $\alpha=1+4ai/k_2H;\ \beta=e^{ik_2d}$:

$$\left[\begin{array}{ccccc|c} \alpha & \beta & \beta^2 & \dots & \beta^{m-1} & 1 \\ \beta & \alpha & \beta & \dots & \beta^{m-2} & \beta \\ \beta^2 & \beta & \alpha & \dots & \beta^{m-3} & \beta^2 \\ \dots & \dots & \dots & \dots & \dots & \dots \\ \beta^{m-1} & \beta^{m-2} & \beta^{m-3} & \dots & \alpha & \beta^{m-1} \end{array}\right]; \; Q_m = \begin{vmatrix} \alpha & \beta & \beta^2 & \dots & \beta^{m-1} \\ \beta & \alpha & \beta & \dots & \beta^{m-2} \\ \beta^2 & \beta & \alpha & \dots & \beta^{m-3} \\ \dots & \dots & \dots & \dots & \dots \\ \beta^{m-1} & \beta^{m-2} & \beta^{m-3} & \dots & \alpha \end{vmatrix} \tag{11}$$

To solve the system (11) by Cramer's rule, let us apply the recurrent relations for its main determinant Q_m and for determinants in (10), which are obtained by changing the columns of the main matrix by the column of the right-hand side, $j = 1, 2, \dots, M$, [17].

As a result, we obtain an explicit form for the quantities J_j, $j = 1, 2, \dots, M$ $(m = M)$, as follows:

$$J_j = 4a \frac{Q_M^j}{Q_M}, \quad j = 1, 2, \dots, M \tag{12}$$

Defining solution (12) with the known value of parameter H, we determine all required wave characteristics. In particular, the reflection and transmission coefficients are expressed in the following form:

$$R = \frac{1}{4a} \sum_{j=1}^{M} \mathrm{e}^{ik_2(j-1)d} J_j; \quad T = -\frac{1}{4a} \sum_{j=1}^{M} \mathrm{e}^{ik_2(M-j)d} J_j + \mathrm{e}^{ik_2(M-1)d}. \tag{13}$$

Since the present theory allows us to find coefficients (13) explicitly, and the only point which is solved numerically is the solution to the auxiliary Eq. (7), the proposed method may be called as "semi-analytical method".

4 Infinite Periodic System. Plane Problem

The solution to the plane elasticity theory for the infinite periodic systems by the developed semi-analytical method is presented in [16, 17]. Let us cite here only the properties of the kernel for respective integral equations and the discretization scheme.

As indicated above, it is necessary to consider the auxiliary integral equation, for which we should study the properties of its kernel [16, 17]:

$$\frac{1}{2a} \int_{-b}^{b} h(\eta) K(y - \eta) d\eta = 1; \; K(y) = \sum_{n=1}^{\infty} L_n \cos(a_n y); \; L_n = \frac{R_n}{k_2^2 q_n}, \; |y| < b$$

$$q_n = \left[(\pi n/a)^2 - k_1^2\right]^{1/2}, \; r_n = \left[(\pi n/a)^2 - k_2^2\right]^{1/2},$$

$$R_n = [2a_n^2 - k_2^2]^2 - 4r_n q_n a_n^2, \quad a_n = \pi n/a. \tag{14}$$

Here k_1, k_2—wave numbers for the longitudinal and the transverse waves. Let us notice that $L_n \sim -2(1 - c_2^2/c_1^2)a_n, \ n \to \infty$, where c_1, c_2—the speed of the longitudinal and the transverse wave, respectively. Then the expression for the kernel is transformed to the following form

$$\begin{aligned} K(y) &= -2\left(1 - \frac{c_2^2}{c_1^2}\right)\sum_{n=1}^{\infty} a_n \cos(a_n y) + \sum_{n=1}^{\infty}\left[L_n + 2\left(1 - \frac{c_2^2}{c_1^2}\right)a_n\right]\cos(a_n y) \\ &= -2\left(1 - \frac{c_2^2}{c_1^2}\right)I(y) + K_r(y). \end{aligned} \tag{15}$$

Here the second sum is a certain regular function. The first one has both regular and singular parts: $I(y) = [I_r(y) + I_s(y)]$. After some transformations of the kernel (15) of the auxiliary integral Eq. (14) the regular and the singular parts become, respectively

$$I_r(y) = \frac{a}{\pi y^2} - \frac{\pi}{4a\sin^2(\pi y/2a)}; \ I_s(y) = -\frac{a}{\pi y^2}. \tag{16}$$

The singularity of the kernel for small arguments contains a hyper-singularity arising in the classical crack theory [30]. To provide the stability of the numerical method, here we again apply the method "of discrete vortices" [31]. By using the new representation for the kernel of the basic integral Eq. (14), let us rewrite the latter in the following form:

$$\begin{aligned} &\frac{1}{2a}\int_{-b}^{b} h(\eta)\left[\Phi_r(y-\eta) + \frac{2a\left[1 - \frac{c_2^2}{c_1^2}\right]}{\pi(y-\eta)^2}\right]d\eta = 1, \\ &\Phi_r(y) = -2\left[1 - \frac{c_2^2}{c_1^2}\right]I_r(y) + K_r(y). \end{aligned} \tag{17}$$

The discretization of the relation (17) leads to the formula

$$\begin{aligned} &\frac{1}{2a}\sum_{k=1}^{N}\int_{\eta_{k-1}}^{\eta_k} h(\eta)\left[\Phi_r(y_l - \eta) + \frac{2a\left[1 - \frac{c_2^2}{c_1^2}\right]}{\pi(y_l - \eta)^2}\right]d\eta \\ &= \frac{1}{2a}\sum_{k=1}^{N} h(\eta_k)\int_{\eta_{k-1}}^{\eta_k}\left[\Phi_r(y_l - \eta_k) + \frac{2a\left[1 - \frac{c_2^2}{c_1^2}\right]}{\pi(y_l - \eta)^2}\right]d(\eta - y_l) \\ &= \frac{1}{2a}\sum_{k=1}^{N} h(\eta_k)\left[\Phi_r(y_l - \eta_k)\varepsilon_1 + \frac{2a\left[1 - \frac{c_2^2}{c_1^2}\right]}{\pi(y_l - \eta_k)} - \frac{2a\left[1 - \frac{c_2^2}{c_1^2}\right]}{\pi(y_l - \eta_{k-1})}\right], \end{aligned}$$

where $\eta_k = -b + k\varepsilon_1$, $y_l = -b + (l - 0.5)\varepsilon_1$, $l = 1, \ldots, N$, $\varepsilon_1 = 2b/N$, and as a result, we obtain the linear algebraic system of equations:

$$\frac{1}{2a}\sum_{k=1}^{N} h(\eta_k)\left[\Phi_r(y_l - \eta_k)\varepsilon_1 + \frac{2a[1 - \frac{c_2^2}{c_1^2}]}{\pi}\left(\frac{1}{(y_l - \eta_k)} - \frac{1}{(y_l - \eta_{k-1})}\right)\right] = 1. \tag{18}$$

Further, by using the auxiliary equation in (14), we determine all wave characteristics. In particular, for three vertical periodic systems [16], the reflection and transmission coefficients are expressed in the explicit form:

$$R = -\frac{1}{4aik_1}\int_{-b}^{b} g_x^1(t)dt - \frac{e^{ik_1 d}}{4aik_1}\int_{-b}^{b} g_x^2(t)dt - \frac{e^{ik_1 2d}}{4aik_1}\int_{-b}^{b} g_x^3(t)dt;$$

$$T = -\frac{e^{ik_1 2d}}{4aik_1}\int_{-b}^{b} g_x^1(t)d - \frac{e^{ik_1 d}}{4aik_1}\int_{-b}^{b} g_x^2(t)dt - \frac{1}{4aik_1}\int_{-b}^{b} g_x^3(t)dt + e^{ik_1 2d}. \tag{19}$$

The present theory also allows us to determine coefficients (19) in explicit form, as soon as the numerical solution of the auxiliary hyper-singular equation is constructed (17) with the help of the linear algebraic system (18).

5 Finite Periodic System. Scalar Formulation

In order to solve the problem in the scalar case, we first consider the incidence of a plane wave upon a doubly-periodic system of rigid screens, which is finite in the both directions. In frames of the scalar acoustics, the wave equation for full acoustic pressure $\mathbf{p}$ is reduced to the Helmholtz equation

$$\left(\Delta + k^2\right)\mathbf{p} = 0, \tag{20}$$

where k—the wave number of the acoustic wave, Δ denotes the two-dimensional Laplace operator, and the full wave pressure is a linear sum of the incident and the scattered field: $\mathbf{p} = \mathbf{p}^{inc} + \mathbf{p}^{sc}$. To be more specific, let us restrict the consideration by the normal incidence of a plane wave, hence the incident wave field is $\mathbf{p}^{inc}\left(y^0\right) = e^{iky_1^0}$, where the two-dimensional point is $y^0 = \left(y_1^0, y_2^0\right)$.

The boundary condition, in the case of acoustically hard boundary $\tilde{L}$ has the form

$$\left.\frac{\partial \mathbf{p}}{\partial \mathbf{n}_y}\right|_{\tilde{L}} = 0, \quad (y \in \tilde{L}). \tag{21}$$

Here $\mathbf{n}_y$ is the unit normal vector at the point y, and $\tilde{L} = \sum_{m=1}^{M} \tilde{l}_m$ represents itself the full set of boundary contours.

In order to develop the basic boundary integral equation, let us introduce a respective closed contour l_m around the current screen. Obviously, for the given contours, in the case when the observation point x is outside, the following standard integral representation is valid

$$p^{sc}(y^0) = \int\limits_L \left(p(y) \frac{\partial \Phi}{\partial n_y} - \frac{\partial p(y)}{\partial n_y} \Phi \right) dL_y, \quad (y \in L), \tag{22}$$

where $\Phi = \Phi(r)$ is the Green's function, which in the two-dimensional acoustic case is expressed through the Hankel function of the first kind $\Phi(r) = (i/4) H_0^{(1)}(r)$, $r = \left| y - y^0 \right|$.

If each surrounding closed contour converges to the respective rigid screen located inside, then the second term in (22) is cancelled, due to the boundary condition. The opposite sides of each obstacle are considered separately, being l_m^- и l_m^+, where the sign "plus" is related to the normal $\mathbf{n}_m^+$, directed along the propagation of the incident wave, and the negative sign—oppositely. Then, the integral representation (22) can be reduced to the expression

$$\begin{aligned} \mathbf{p}^{sc}(y^0) &= \sum_{m=1}^{M} \left(\int\limits_{\ell_m^+} \left(\mathbf{p}^+(y) \frac{\partial \Phi}{\partial \mathbf{n}_y^+} \right) d\ell_y^+ + \int\limits_{\ell_m^-} \left(\mathbf{p}^-(y) \frac{\partial \Phi}{\partial \mathbf{n}_y^-} \right) d\ell_y^- \right) \\ &= \sum_{m=1}^{M} \int\limits_{\ell_m^+} \mathbf{g}(y) \frac{\partial \Phi}{\partial \mathbf{n}_y^+} \left(k \left| y - y^0 \right| \right) d\ell_y^+, \mathbf{g}(y) = \mathbf{p}^+(y) - \mathbf{p}^-(y), \quad (y \in l_m) \end{aligned} \tag{23}$$

The introduced quantity $\mathbf{g}(y)$ represents the pressure fall when passing the barrier. The obtained formula allows us to find the scattered pressure field at arbitrary point of the space y^0, however, to use it in practice, it is necessary to know the value of the function $\mathbf{g}(y)$ over the boundary of the obstacles. To find this quantity, by analogy to the classical approach, let us set the point y^0 tending to the boundary of the obstacle: $y^0 \to x \in L$. By expressing the reflected field, taken from the formulas, in terms of the difference of the full and the incident ones, by differentiating the obtained expression along the normal, we come to the following representation

$$\frac{\partial p(x)}{\partial n_x^+} = \frac{\partial p^{inc}(x)}{\partial n_x^+} + \sum_{m=1}^{M} \int\limits_{\ell_m^+} g(y) \frac{\partial^2 \Phi}{\partial n_x^+ \partial n_y^+} (k|y - x|) d\ell_y^+ \tag{24}$$

With the boundary condition, Eq. (24) is reduced to the system of BIEs, to find function $\mathbf{g}(y)$

$$\sum_{m=1}^{M} \int_{\ell_m^+} \mathbf{g}(y) \frac{\partial^2 \Phi}{\partial \mathbf{n}_x^+ \partial \mathbf{n}_y^+}(kr) d\ell_y = -\frac{\partial \mathbf{p}^{inc}(x)}{\partial \mathbf{n}_x^+}, \quad r = |y - x| \tag{25}$$

Since there are no "minus" signs, let us omit all over below the sign "plus", in the notation of normal and obstacles. Let us write out the quantities explicitly present in the equation. Obviously, all normal vectors are collinear: $\mathbf{n} = (0, 1)$, and the right-hand side is expressed as follows: $\frac{\partial \mathbf{p}^{inc}(x)}{\partial \mathbf{n}_x} = ike^{ikx_1}$. The first derivative of the Green's function can be obtained in the following way:

$$\frac{\partial \Phi}{\partial \mathbf{n}_y} = \frac{\partial \Phi}{\partial r} \frac{\partial r}{\partial \mathbf{n}_y} = -\frac{ik}{4} H_1^{(1)}(kr) \frac{y_2 - x_2}{r}, \tag{26}$$

where we have taken into account that for any function $\frac{\partial f}{\partial \mathbf{n}_x} = (grad_x f \cdot \mathbf{n}_x) = n_1^x \frac{\partial f}{\partial x_1} + n_2^x \frac{\partial f}{\partial x_2}$. The second derivative can be determined by analogy:

$$\begin{aligned}
&\frac{\partial^2 \Phi}{\partial \mathbf{n}_x \partial \mathbf{n}_y} \\
&= -\frac{ik}{4} \left\{ k \frac{\partial H_1^{(1)}(kr)}{\partial (kr)} \frac{\partial r}{\partial \mathbf{n}_x} \frac{y_2 - x_2}{r} + H_1^{(1)}(kr) \left[\frac{\partial}{\partial r} \left(\frac{y_2 - x_2}{r} \right) \cdot \frac{\partial r}{\partial \mathbf{n}_x} - \frac{\partial}{\partial \mathbf{n}_x} \left(\frac{y_2 - x_2}{r} \right) \right] \right\} \\
&= -\frac{ik}{4} \left\{ -k \left[H_0^{(1)}(kr) - \frac{1}{kr} H_1^{(1)}(kr) \right] \frac{(y_2 - x_2)^2}{r^2} + H_1^{(1)}(kr) \left[\frac{(y_2 - x_2)^2}{r^3} - \frac{1}{r} \right] \right\}
\end{aligned} \tag{27}$$

It is clear from the last equation that with $r \to 0$ there is a singularity in the integrand in (25). It is known the behavior of the Hankel function for small arguments: $H_1^{(1)}(x) \overset{x \to 0}{\sim} -2i/(\pi x)$. Then we can extract the hyper-singular part of the integrand explicitly:

$$\begin{aligned}
\frac{\partial^2 \Phi}{\partial \mathbf{n}_x \partial \mathbf{n}_y} = -\frac{ik}{4} \Bigg\{ &-k \left[H_0^{(1)}(kr) - \frac{1}{kr} H_1^{(1)}(kr) \right] \frac{(y_2 - x_2)^2}{r^2} + \Bigg\} \\
&+ H_1^{(1)}(kr) \left[\frac{(y_2 - x_2)^2}{r^3} - \frac{1}{r} \right] - \frac{2i}{\pi} \frac{1}{r^2} + \frac{2i}{\pi} \frac{1}{r^2}.
\end{aligned}$$

For the numerical solution, let us divide each obstacle's contour l_i^+ to n intervals of the same length $h = l_i^+ / n$ and place the grid nodes in the middle of each elementary interval (for simplicity, we consider only equal lengths of all obstacles). Then the integral in the left-hand side (25) can be replaced by a sum over the elementary intervals. In the case when $r \neq 0$ the integrand may be approximated by its value at the current point, but if $r \to 0$ then the integration of the hyper-singular part is performed in the following way:

$$\int_{x_j-\frac{h}{2}}^{x_j+\frac{h}{2}} \frac{dy_j}{(y_1^j - x_1^i)^2 + (y_2^j - x_2^i)^2} = \frac{1}{x_2^j - x_2^i}\left(arctg\left(\frac{x_1^j - x_1^i + \frac{h_j}{2}}{x_2^j - x_2^i}\right)\right.$$
$$\left. - arctg\left(\frac{x_1^j - x_1^i - \frac{h_j}{2}}{x_2^j - x_2^i}\right)\right). \tag{28}$$

Obviously, if the both point are located over the same obstacle, the integration of the hyper-singular part takes the simpler form:

$$\int_{x_j-\frac{h}{2}}^{x_j+\frac{h}{2}} \frac{dy_j}{(y_1^j - x_1^i)^2} = \frac{h_j}{\left(x_2^j - x_2^i\right)^2 - (h/2)^2}$$

As a result of the discretization performed, integral Eq. (25) is reduced to a SLAE (System of linear algebraic equations), which is solved numerically.

6 Numerical Analysis

Let us perform a numerical analysis of the problems considered above, on example of the medium with the longitudinal wave speed $c_1 = 6000$ m/s (steel), and the ratio of the longitudinal and the transverse wave speeds is $c_1/c_2 = 1.87$.

To begin with, let us compare the moduli of reflection and transmission coefficients versus frequency parameter, between the three studied cases, for a single vertical array (see Figs. 2 and 3). With so doing, we assume that the longitudinal wave speed in the problem 2 is equal to the transverse wave speed of the problems 1 and 3. This condition shortens the one-mode frequency interval, whose limit from the right becomes $\pi/1.87 = 1.680$, (see Figs. 2 and 3). In Figs. 4, 5, 6, 7 and 8 the comparative numerical analysis of the scalar problems 1 and 3 has been performed for the transverse incident wave. Let us notice that for all cases the filtration interval can be seen in the upper part of the one-mode frequency range. It is shown that lines 2 and 3 in Figs. 2 and 3, related to the scalar problems, are practically coinciding that takes place even for $N = 10$ cracks in each vertical array. It should also be noted that line 1 related to the elastic problem, shows a significant domination of the filtration property, when compared with both infinite and finite scalar problems. Let us also notice that for two vertical arrays in the elastic problem a perfect filtration takes place for $ak \geq 0.7$, but for one vertical row this property is valid only for $ak \geq 1.5$; this also confirms the evident property that with the growth of the vertical rows the filtration becomes stronger.

Let us pass to the analysis of the grid size to the precision of the obtained results.

It is stated that in the case of a single obstacle it is sufficient to take 10 grid nodes per each wavelength, to provide reliable results. With so doing, for the frequency

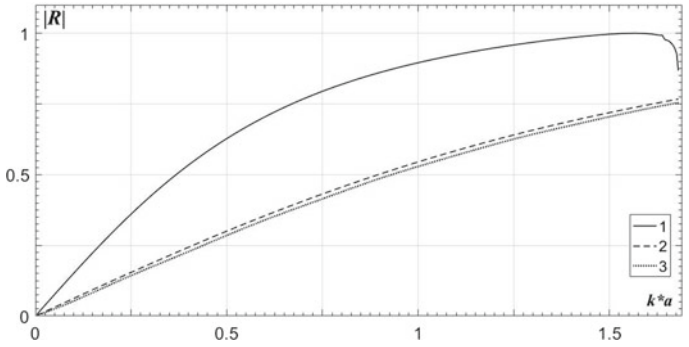

Fig. 2 Comparison of three different periodic models: one vertical row (M = 1), period of the lattice is 0.02 m, size of each crack is 2b = 0.015 m; line 1—infinite array, elastic theory; line2—infinite array, scalar theory; line 3—finite array with $M_1 = 7$ vertical cracks, scalar theory

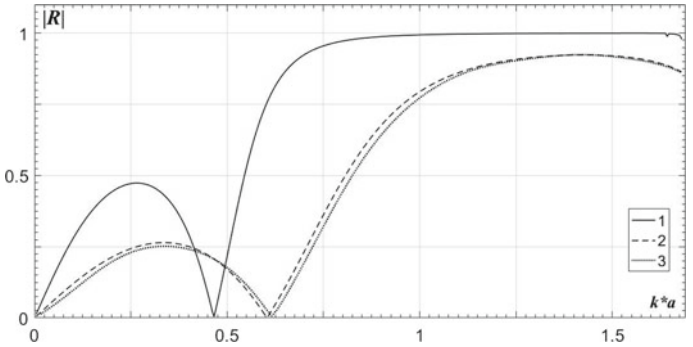

Fig. 3 Comparison of three different periodic models: two vertical rows (M = 2), period of the lattice is 0.02 m, size of each crack is 2b = 0.015 m, distance between the rows is d = 0.02 m; line 1—infinite array, elastic theory; line 2—infinite array, scalar theory; line 3—finite array with $M_1 = 7$ vertical cracks, scalar theory

0.16 MHz in this formulation the wavelength is 3.75 cm, hence on the obstacle of the length 1.5 cm it is sufficient to take only 5 nodes. However, the complex geometry of the diffraction lattice requires greater number of nodes. It can be seen from Fig. 4, which represents the results for the array of 10 vertical rows, each containing 10 obstacles, that with 10 nodes over each obstacle the calculations are correct only in the low-frequency case (for $k^*a < 1$).

The investigation shows that for 5 vertical arrays with the obstacles of the length 1.8 cm, 10 obstacles in each vertical row ($M_1 = 10$) are sufficient, to get finite case quite close to the infinite one (see Fig. 5). It is stated that with the growing number of obstacles in a single vertical row, so with the growth of parameter M_1, keeping all other parameters unchanged, the interval of the frequency cutoff varies insignificantly. The reflection inside this frequency interval is almost constant, being

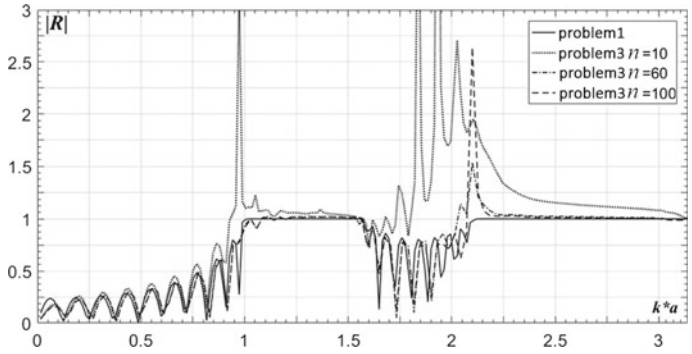

Fig. 4 Comparison of two scalar models: ten vertical rows (M = 10), period of the lattice is 0.02 m, size of each crack is 2b = 0.015 m, distance between the rows is d = 0.02 m; problem 1—infinite array; problem 3—finite array with $M_1 = 10$ vertical cracks; n is the number of the numerical grid nodes on each crack

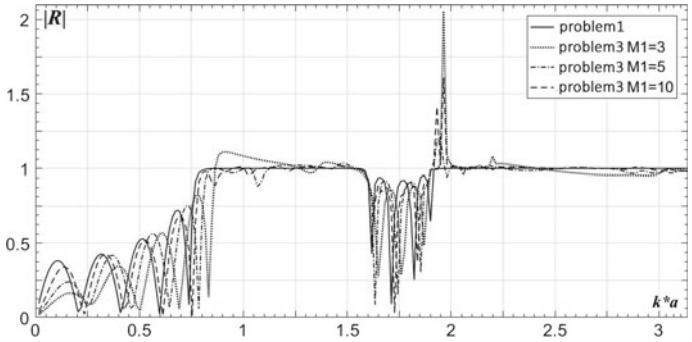

Fig. 5 Comparison of two scalar models: five vertical rows (M = 5), period of the lattice is 0.02 m, size of each crack is 2b = 0.018 m, distance between the rows is d = 0.02 m; problem 1—infinite array; problem 3—finite array with various number M_1 of vertical cracks

equal to unit value, and the respective line on the diagram is almost horizontal. This property takes place also for infinite arrays, where M is a number of such arrays.

Figure 6 characterizes the influence of the number of vertical rows, parameter M, to the reflection coefficient (the length of each obstacle is 1.5 cm, the width of the strip is 2 cm). With the growth of parameter M the filtration for middle frequencies becomes perfect, and for higher frequencies this is observed for all M.

Figure 7 demonstrates the influence of the strip width to the reflection coefficient in the case $M = 2$, and the length of the obstacle $2b = 1.5$ cm. For small d the perfect filter at high frequencies is characterized by a poor cutoff at low frequencies. For large d the cutoff intervals arise more often and the horizontal filtration line at higher frequencies is divided to several intervals.

The dependence of obstacles' size on the reflection coefficient in the array of 5 vertical rows with the width of the layer 2 cm can be extracted from Fig. 8. With

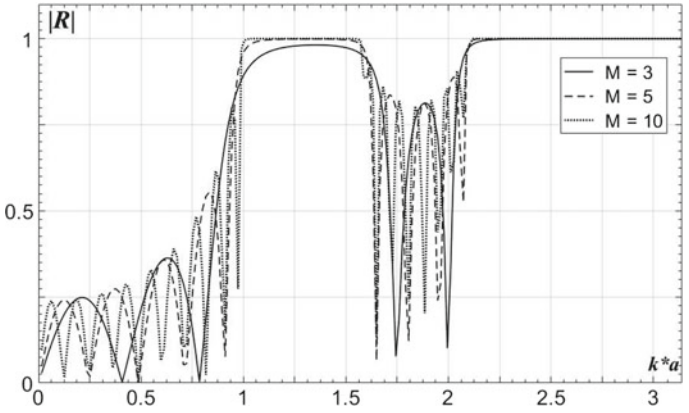

Fig. 6 The scalar model for various number M of infinite vertical arrays: period of the lattice is 0.02 m, size of each crack is 2b = 0.015 m, distance between the rows is d = 0.02 m

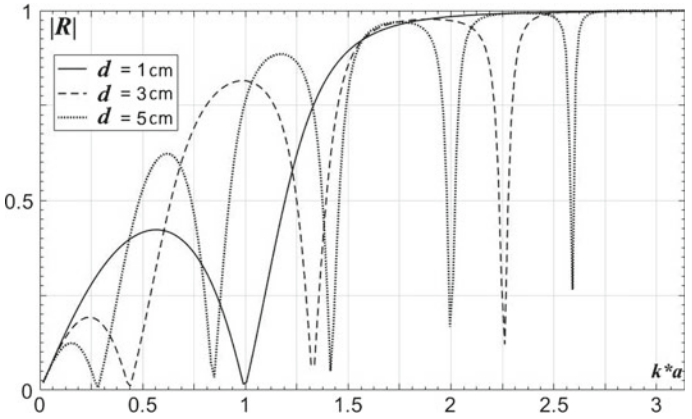

Fig. 7 The scalar model for M = 2 infinite vertical arrays: period of the lattice is 0.02 m, size of each crack is 2b = 0.015 m, for various distance d between the rows

the growing size of the screens the cutoff intervals at middle and high frequencies become longer, and the filtration property strengthens over the full one-mode interval.

7 Conclusions

1. Virtually any frequency interval with the wave channel locking can be created by controlling the relative crack size, the number of vertical arrays, and the lattice period in the horizontal direction.

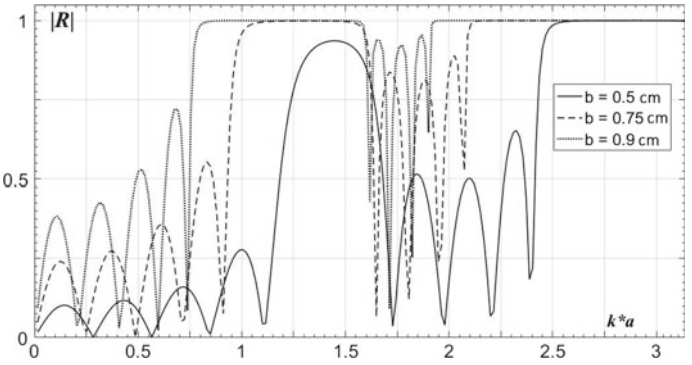

Fig. 8 The scalar model for M = 5 infinite vertical arrays: period of the lattice is 0.02 m, distance between the rows is d = 0.02 m, for various half-length b of each crack

2. When the number of cracks in one row increases, the locking interval changes slightly. And the analysis shows that even 10 cracks sufficiently well approximate the case of the infinite system.
3. The properties of the problems in the scalar formulation (1, 3) demonstrate the possible replacement of infinite crack arrays by the finite periodic systems while maintaining the filtration properties.
4. The enhancement of the locking property of the wave channel occurs when considering infinite doubly-periodic systems in the context of the elastic model in comparison with the infinite and finite scalar analogue.

Acknowledgements The present work is performed within the framework of the Project no. 15-19-10008-P of the Russian Science Foundation (RSCF).

References

1. Guenneau, S., Craster, R.V.: Acoustic Metamaterials Negative Refraction, Imaging, Lensing and Cloaking. Springer, Dordrecht, Heidelberg, New York, London (2013)
2. Deymier, P.A.: Acoustic Metamaterials and Phononic Crystals. Springer-Verlag, Berlin, Heidelberg (2013)
3. Twersky, V.: Multiple scattering of sound by a periodic line of obstacles. J. Acoust. Soc. Am. **53**(1), 329–338 (1973)
4. Shenderov, E.L.: Transmission of sound through a perforated screen of finite thickness. Acoust. Phys. **16**(2), 295–304 (1970)
5. Achenbach, J.D., Li, Z.L.: Reflection and transmission of scalar waves by a periodic array of screens. Wave Motion **1986**(8), 225–234 (1986)
6. Miles, J.W.: On Rayleigh scattering by a grating. Wave Motion **4**, 285–292 (1982)
7. Scarpetta, E.: In-plane problem for wave propagation through elastic solids with a periodic array of cracks. Acta Mech. **154**, 179–187 (2002)
8. Sumbatyan, M.A., Remizov, MYu.: On the theory of acoustic metamaterials with a triple-periodic system of interior obstacles. Adv. Struct. Mater. **41**, 19–33 (2017)

9. Zarrillo, G., Aguiar, K.: Closed-form low frequency solutions for electro-magnetic waves through a frequency selective surface. IEEE Trans. Antennas Prop. **AP-35**(12), 1406–1417 (1988)
10. Sumbatyan, M.A., Chupahin, A.A.: Plane wave propagation through an elastic medium with a periodic system of volumetric defects. Russian Izvestiya. North-Caucas. Region. Nat. Sci. **4**, 37–38 (1999). (in Russian)
11. Scarpetta, E., Sumbatyan, M.A.: Wave propagation through elastic solids with a periodic array of arbitrarily shaped defects. Math. Comp. Model. **37**(1, 2), 19–28 (2003)
12. Angel, Y.C., Bolshakov, A.: In-plane waves in an elastic solid containing a cracked slab region. Wave Motion **31**, 297–315 (2000)
13. Angel, Y.C., Achenbach, J.D.: Harmonic waves in an elastic solid containing a doubly periodic array of cracks. Wave Motion **9**, 377–385 (1987)
14. Mykhaskiv, V.V., Zhbadynskyi, I.Y., Zhang, C.: Dynamic stresses due to time-harmonic elastic wave incidence on doubly periodic array of penny-shaped cracks. J. Math. Sci. **203**, 114–122 (2014)
15. Scarpetta, E., Sumbatyan, M.A.: On wave propagation in elastic solids with a doubly periodic array of cracks. Wave Motion **25**, 61–72 (1997)
16. Remizov, M.Y.: Low-frequency penetration of elastic waves through a periodic array of cracks. Vestn. Don State Tech. Univ. **1**(88), 18–27 (2017). (in Russian)
17. Remizov, M.Y., Sumbatyan, M.A.: 3-D one—mode penetration of elastic waves through a doubly periodic array of cracks. Math. Mech. Solids **23**(4), 636–650 (2018)
18. Glazanov, V.E.: Diffraction of a plane longitudinal wave by a lattice of cylindrical cavities in an elastic medium. Acoust. Phys. **13**(3) (1967)
19. Kljukin, I.I., Chabanov, V.E.: Sound diffraction on a plane grating of cylinders. Acoust. Phys. **20**(6) (1974)
20. Popuzin, V.V., Zotov, V.M., Sumbatyan, M.A.: Theoretical and experimental study of an acoustically active material containing a doubly-periodic system of cylindrical holes. Springer Proceedings in Physics, Heidelberg, New York, Dordrecht, London (2017)
21. Datta, S.K.: Diffraction of plane elastic waves by ellipsoidal inclusions. J. Acoust. Soc. Am. **61**, 1432–1437 (1977)
22. Willis, J.R.: A polarization approach to the scattering of elastic waves—II. J. Mech. Phys. Solids **28**, 307–327 (1980)
23. Kuznetsov, S.V.: A direct version of the method of boundary integral equations in the theory of elasticity. J. Appl. Math. Mech. **56**(5), 617–622 (1992)
24. Yang, Ch., Achenbach, J.D.: Time domain scattering of elastic waves by a cavity, represented by radiation from equivalent body forces. Int. J. Eng. Sci. **115**, 43–50 (2017)
25. Liu, Z., Zhang, X., Mao, Y., Zhu, Y.Y., Yang, Z., Chan, C.T., Sheng, P.: Locally resonant sonic material. Science **289**(5485), 1734–1736 (2000)
26. Craster, R.V., Guenneau, S.: Acoustic Metamaterials. Springer Series in Materials Science, vol. 166. Springer, Dordrecht (2013)
27. Huang, H.H., Sun, C.T., Huang, G.L.: On the negative effective mass density in acoustic metamaterials. Int. J. Eng. Sci. **47**, 610–617 (2009)
28. Kriegsmann, G.A.: Scattering matrix analysis of a photonic Fabry-Perot resonator. Wave Motion **37**, 43–61 (2003)
29. Scarpetta, E., Sumbatyan, M.A.: On the oblique wave penetration in elastic solids with a doubly periodic array of cracks. Q. Appl. Math. **58**, 239–250 (2000)
30. Sneddon, I.N., Lowengrub, M.: Crack Problems in the Classical Theory of Elasticity. Wiley, London (1969)
31. Belotserkovsky, S.M., Lifanov, I.K.: Method of Discrete Vortices. CRC Press, Boca Raton (1992)

Homogenization of Piezoelectric Composites with Internal Structure and Inhomogeneous Polarization in ACELAN-COMPOS Finite Element Package

T. E. Gerasimenko, N. V. Kurbatova, D. K. Nadolin, A. V. Nasedkin, A. A. Nasedkina, P. A. Oganesyan, A. S. Skaliukh and A. N. Soloviev

Abstract The paper presents the current version of the finite element package ACELAN-COMPOS with the focus on its capabilities for solving the homogenization problems for piezoelectric composites with inhomogeneous polarization of piezoceramic phase. We describe the basic version of the effective moduli method, as well as the simplified theoretical approaches for taking into account the inhomogeneous polarization in the finite element solution of the homogenization problems. We provide the brief description of the main features of the ACELAN-COMPOS package, which we use for solving the described problems. The results of the numerical solution of the homogenization problems for porous piezoceramic composites demonstrate the importance of taking into account the inhomogeneous polarization field for the effective moduli determination.

T. E. Gerasimenko · N. V. Kurbatova · D. K. Nadolin · A. V. Nasedkin (✉) · A. A. Nasedkina · P. A. Oganesyan · A. S. Skaliukh
Institute of Mathematics, Mechanics and Computer Science, Southern Federal University, Milchakova Street 8a, Rostov-on-Don 344090, Russia
e-mail: nasedkin@math.sfedu.ru

T. E. Gerasimenko
e-mail: tanyapol@inbox.ru

N. V. Kurbatova
e-mail: nvk-ru@yandex.ru

D. K. Nadolin
e-mail: nadolin@yandex.ru

A. A. Nasedkina
e-mail: nasedkina@math.sfedu.ru

P. A. Oganesyan
e-mail: nwolwerine@yandex.ru

A. S. Skaliukh
e-mail: a.s.skaliukh@gmail.com

A. N. Soloviev
Department of Theoretical and Applied Mechanics, Don State Technical University, Gagarin sq., 1, Rostov-on-Don 344000, Russia
e-mail: solovievarc@gmail.com

M. A. Sumbatyan (ed.), *Wave Dynamics, Mechanics and Physics of Microstructured Metamaterials*, Advanced Structured Materials 109,
https://doi.org/10.1007/978-3-030-17470-5_8

1 Introduction

Piezoelectric composite materials are widely used in modern piezoengineering. As it is known, the piezoceramic materials, which are the most effective in practical applications, are obtained with the help of special fabrication stages, which consist of the preparation of initial powders, their pressing, sintering and polarization. It is possible to modify these processes, in order to obtain the composite materials with controlled functional properties, for example, by adding other fractions or pore-forming agents to the initial powders. As a result, piezocomposite materials of various compositions and connectivity can be produced.

The most popular are two-component (two-phase, binary) piezoceramic composites, which include the first active piezoceramic phase and the second phase, which can be represented either by inclusions from another piezoceramic or elastic material or by pores [20, 31, 32, 40]. To denote the connectivity types of the components for such composites, it is convenient to use the classification proposed by R. E. Newnham [28]. According to this classification, the digits indicate the number of axes of the Cartesian coordinate system along which a connected path through the composite can be constructed for the material of this phase. Thus, the connectivity of a two-phase composite can be denoted by the digits from 0 to 3 for each phase. The most important connectivity types for mixed composites are the following: 3–3 (with connected materials in all three directions for both phases), 3–0 (with connected material in three directions for the first phase, and with isolated parts of the second phase), and 0–3 (with inverted connectivity compared to 3–0).

To determine the effective properties of binary piezocomposites, one can solve homogenization problems using various generalizations of the methods adopted in the mechanics of composite materials. The ACELAN-COMPOS package, developed by the authors and their colleagues, is aimed at the finite element solution of the homogenization problems for two-phase piezocomposites by using the effective moduli method and computer simulation of representative volumes, which takes into account their internal structure.

The initial concept of the ACELAN-COMPOS package and the main features of this package were described in the last papers [13, 14, 25]. As shown by numerous investigations [6–8, 29], the internal structure has a significant influence on the effective properties of the composites. In connection to this, special algorithms were implemented in ACELAN-COMPOS, in order to simulate the piezocomposites with 3–3, 3–0, 0–3 and 1–3 connectivity types [10–14].

This paper focuses on some new features of the ACELAN-COMPOS package with an emphasis on the homogenization problems for composites with non-uniform polarization of the piezoceramic phase. The heterogeneity of polarization is also important for determining the functional properties of the composite [16, 21, 33, 39]. In this paper, we describe simplified methods for taking into account inhomogeneities of the polarization. Note that more accurate approaches [13, 34, 35], which are based on solving non-linear polarization problems, require significantly more

computational resources and are not implemented in this version of the ACELAN-COMPOS package.

In order to demonstrate the use of the simplified methods for inhomogeneous polarization, we present some numerical results of the effective properties calculation for porous piezoceramic materials. These results show significant influence of the inhomogeneity of polarization field and the porosity structure on the effective properties of porous piezocomposites.

In this paper, we will not discuss other features of the ACELAN-COMPOS package, related to the computer design of magnetoelectric composites [13, 14] and composites with imperfect interface boundaries that simulate nanoscale inclusions or pores [25, 27]. The interested reader is referred to the above references for more details.

2 Homogenization of Piezoelectric Composites

To determine the effective properties of piezoelectric composites, in ACELAN-COMPOS package we use classical version of the effective moduli method. For piezoelectric composites this method was applied in a large number of papers [5, 9, 22, 24, 30], with its mathematical basis given in [22, 24]. In this section, we describe the formulation of the homogenization problem using the Voigt vector-matrix notation, which is generally accepted in the physical and theoretical literature on piezoelectricity.

The input data for the homogenization problem for two-phase piezoelectric (electroelastic) composite material is its representative volume element Ω together with the parts $\Omega^{(1)}$ and $\Omega^{(2)}$ filled with materials of different phases. In the domains $\Omega^{(j)}$, $j = 1, 2$, the following material moduli are known: the elastic stiffnesses $c^E_{\alpha\beta} = c^{E(j)}_{\alpha\beta}$, measured at constant electric field; the piezoelectric moduli $e_{k\beta} = e^{(j)}_{k\beta}$; and the dielectric permittivity constants $\varepsilon^S_{km} = \varepsilon^{S(j)}_{km}$, measured at constant strain; $\alpha, \beta = 1, 2, \ldots, 6, k, m = 1, 2, 3$; $\mathbf{x} \in \Omega^{(j)}$.

We also introduce the following notation: $\Gamma = \partial\Omega$ is the outer boundary of the volume; $\mathbf{u} = \mathbf{u}(\mathbf{x})$ is the vector function of displacements; $\varphi = \varphi(\mathbf{x})$ is the electric potential function; $\mathbf{T} = \{\sigma_{11}, \sigma_{22}, \sigma_{33}, \sigma_{23}, \sigma_{13}, \sigma_{12}\}$ is the array of stress components σ_{km}; $\mathbf{S} = \{\varepsilon_{11}, \varepsilon_{22}, \varepsilon_{33}, 2\varepsilon_{23}, 2\varepsilon_{13}, 2\varepsilon_{12}\}$ is the array of the strain components ε_{km}; $\mathbf{D}$ is the vector of electric induction or electric displacement; $\mathbf{E}$ is the vector of electric field; $\mathbf{c}^E$ is the 6×6 matrix of elastic stiffness moduli $c^E_{\alpha\beta}$, $\mathbf{e}$ is the 3×6 matrix of piezoelectric modui $e_{k\beta}$; $\boldsymbol{\varepsilon}^S$ is the 3×3 matrix of dielectric permittivity moduli ε^S_{km}.

In the homogenization problem, it is necessary to determine the effective moduli $\tilde{c}^E_{\alpha\beta}, \tilde{e}_{k\beta}, \tilde{\varepsilon}^S_{km}$. In order to do this, we need to solve a set of static boundary piezoelectric problems

$$\mathbf{L}^*(\nabla) \cdot \mathbf{T} = 0, \quad \nabla \cdot \mathbf{D} = 0, \quad \mathbf{x} \in \Omega\,, \tag{1}$$

$$\mathbf{T} = \mathbf{c}^E \cdot \mathbf{S} - \mathbf{e}^* \cdot \mathbf{E} = 0, \quad \mathbf{D} = \mathbf{e} \cdot \mathbf{S} + \boldsymbol{\varepsilon}^S \cdot \mathbf{E} = 0\,, \tag{2}$$

$$\mathbf{S} = \mathbf{L}(\nabla) \cdot \mathbf{u}, \quad \mathbf{E} = -\nabla\varphi\,, \tag{3}$$

$$\mathbf{u} = \mathbf{L}^*(\mathbf{x}) \cdot \mathbf{S}_0, \quad \varphi = -\mathbf{x} \cdot \mathbf{E}_0, \quad \mathbf{x} \in \Gamma\,, \tag{4}$$

where $\mathbf{S}_0$ is the six-dimensional array of constant values, $\mathbf{E}_0$ is the constant vector, $(\ldots)^*$ is the transpose operation, $\mathbf{L}(\nabla)$ is the matrix operator of differentiation, which in transposed form is defined as follows

$$\mathbf{L}^*(\nabla) = \begin{bmatrix} \partial_1 & 0 & 0 & 0 & \partial_3 & \partial_2 \\ 0 & \partial_2 & 0 & \partial_3 & 0 & \partial_1 \\ 0 & 0 & \partial_3 & \partial_2 & \partial_1 & 0 \end{bmatrix}.$$

The set of boundary value problems is determined by specific forms of boundary conditions (4). Let

$$\mathbf{S}_0 = \varepsilon_0 \mathbf{g}_\zeta\,, \quad \mathbf{E}_0 = 0\,, \tag{5}$$

where $\varepsilon_0 = \text{const}$, $\zeta = 1, 2, \ldots, 6$ is the fixed index,

$$\mathbf{g}_1 = \{1, 0, 0, 0, 0, 0\}, \quad \mathbf{g}_2 = \{0, 1, 0, 0, 0, 0\}, \quad \mathbf{g}_3 = \{0, 0, 1, 0, 0, 0\}\,, \tag{6}$$

$$\mathbf{g}_4 = \{0, 0, 0, 1/2, 0, 0\}, \quad \mathbf{g}_5 = \{0, 0, 0, 0, 1/2, 0\}, \quad \mathbf{g}_6 = \{0, 0, 0, 0, 0, 1/2\}\,. \tag{7}$$

Then for each boundary value problem (1)–(5) with $\zeta = 1, 2, \ldots, 6$ and (6), (7) it is necessary to find the solutions and determine the stress fields T_α, $\alpha = 1, 2, \ldots, 6$, $(T_1 = \sigma_{11}, T_2 = \sigma_{22}, T_3 = \sigma_{33}, T_4 = \sigma_{23}, T_5 = \sigma_{13}, T_6 = \sigma_{12})$ and electric inductions D_j, $j = 1, 2, 3$. After this, the stress fields and the electric induction fields, averaged over the volume, will allow us to find the effective stiffness moduli $\tilde{c}^E_{\alpha\zeta}$ and the effective piezomoduli $\tilde{e}_{j\zeta}$:

$$\tilde{c}^E_{\alpha\zeta} = \langle T_\alpha \rangle / \varepsilon_0, \quad \tilde{e}_{j\zeta} = \langle D_j \rangle / \varepsilon_0\,, \tag{8}$$

where

$$\langle (\ldots) \rangle_\Omega = \frac{1}{|\Omega|} \Big(\int_\Omega (\ldots)\, d\Omega \Big)\,. \tag{9}$$

Now we assume in (4)

$$\mathbf{S}_0 = 0, \quad \mathbf{E}_0 = E_0 \mathbf{e}_k\,, \tag{10}$$

where $E_0 = \text{const}$, $\mathbf{e}_k$ are the orts of the Cartesian coordinate system, $k = 1, 2, 3$ is the fixed index.

By solving three ($k = 1, 2, 3$) problems (1)–(4), (10) we calculate the fields T_α, $\alpha = 1, 2, \ldots, 6$, and D_j, $j = 1, 2, 3$, their averaged values by (9) and determine the effective piezoelectric moduli $\tilde{e}_{k\alpha}$, and the effective dielectric permittivity moduli $\tilde{\varepsilon}^S_{jk}$:

$$\tilde{e}_{k\alpha} = -\langle T_\alpha \rangle / E_0, \quad \tilde{\varepsilon}^S_{jk} = \langle D_j \rangle / E_0\,. \tag{11}$$

We emphasize that the values T_α and D_j in (8) with $\zeta = 1, 2, \ldots, 6$ and in (11) with $k = 1, 2, 3$ are different, since they are calculated from the solutions of problems (1)–(4) with different boundary conditions (4), specified by (5)–(7) or by (10), respectively.

Note that up to the calculation accuracy, the following properties should be satisfied:

- the matrix of the effective stiffness moduli $\tilde{c}^E_{\alpha\zeta}$, found by (8) from the solutions of six problems (1)–(5), should be symmetric;
- the effective piezoelectric moduli $\tilde{e}_{j\zeta}$, found by (8) from the of six problems (1)–(5), should coincide with those found by (11) from the solutions of three problems (1)–(4), (10);
- the matrix of the effective dielectric permittivity moduli $\tilde{\varepsilon}^S_{jk}$, found by (11) from the solutions of three problems (1)–(4), (10), should be symmetric.

3 Some Models of Inhomogeneous Polarization for Piezoelectric Composites

When analyzing the composites with the skeleton made of elastic piezoceramic material containing inclusions or pores, we can expect high inhomogeneity of the residual polarization vector $\mathbf{P}$ of piezoceramics. Indeed, even if the piezoceramics are polarized in one direction, the electric field or electric induction vectors inside the composite will not be parallel to this direction but will go around the inhomogeneities of the composite. Then it is logical to assume that the directions of the vector $\mathbf{P} = \mathbf{P}(\mathbf{x})$ at the first approximation can be obtained from the solution of the model problem of the polarization of composite material in linear setting. We will provide the mathematical setting of this problem in relation to the subsequent finite element homogenization problem.

Let Ω be a cubic representative volume of the composite of the size $L \times L \times L$ with the mesh consisting of finite elements Ω^{em}, $\Omega = \cup_m \Omega^{em}$. It is assumed that each element Ω^{em} belongs to the domain of one of the two phases, namely, the unpolarized piezoceramics $\Omega^{(1)}$ or the inclusion $\Omega^{(2)}$. Consequently, each element Ω^{em} has dielectric properties of two phases, which we will consider isotropic materials with dielectric permeabilities $\varepsilon_i = \varepsilon_i^{(j)}$, $\mathbf{x} \in \Omega^{(j)}$, $j = 1, 2$. We assume that the edges $x_3 = 0$ and $x_3 = L$ of the volume Ω are electrodized and are subjected to the potential difference $\Delta V = LE_*$ with the field value E_*, which is enough for the polarization of homogeneous piezoceramic material.

For the representative volume Ω with the help of FEM we solve the problem of electrostatics

$$\nabla \cdot \mathbf{D} = 0, \quad \mathbf{D} = \varepsilon_i \mathbf{E}, \quad \mathbf{E} = -\nabla\varphi, \quad \mathbf{x} \in \Omega\,, \tag{12}$$

$$\varphi = LE_*, \quad x_3 = 0; \quad \varphi = 0, \quad x_3 = L\,. \tag{13}$$

Using the obtained solution of the problem (12), (13) in central points of finite elements $\Omega^{em} \subset \Omega^{(1)}$, we compute the vectors $\mathbf{P}^{em} = \mathbf{D}^{em} - \varepsilon_0 \mathbf{E}^{em}$, where ε_0 is the dielectric permeability of the vacuum, $\varepsilon_0 = 8.85 \times 10^{-12}$ F/m. Let us assume that these vectors with the accuracy up to the normalization are the vectors of the piezoceramic polarization. Thus, here we assume that the direction of the residual polarization vector coincides with the direction of the induced polarization component under the action of the electric field in the composite nonpolarized material.

By virtue of the adopted hypothesis, we can associate with the finite elements $\Omega^{em} \subset \Omega^{(1)}$ the element coordinate systems $Ox_1^{em}x_2^{em}x_3^{em}$ [23, 26] with the axis Ox_3^{em} directed along the vector $\mathbf{P}^{em}$. Let us denote as θ_{31}^{em} the angle, which this vector forms with the axis Ox_3 (Fig. 1).

In order to define the remaining axes, we consider the line of the intersection of the plane Ox_1x_2 with the plane orthogonal to the axis Ox_3^{em}, and denote the angle between this line and the axis Ox_1 as θ_{12}^{em}. Thus, the axes of local coordinate system are obtained with the help of two rotations of the main coordinate system for the given angles. The first rotation is performed around the axis Ox_3 for the angle θ_{12}^{em}, which leads to the coordinate system $O\tilde{x}_1^{em}\tilde{x}_2^{em}x_3$. The second rotation is performed around the axis $O\tilde{x}_2^{em}$ for the angle θ_{31}^{em}, which ultimately gives the necessary element coordinate system $Ox_1^{em}x_2^{em}x_3^{em}$.

In the case when the direction of the polarization vector $\mathbf{P}^{em}$ is close to the direction of the axis Ox_3, in order to ensure greater stability of the algorithm, the choice of the first rotation angle θ_{12}^{em} can be subjected to the following conditions: $\cos\theta_{12}^{em} = P_1^{em}/|\mathbf{P}_{12}^{em}|$, if $|\mathbf{P}_{12}^{em}| \geq l_{12}^{em}$; $\cos\theta_{12}^{em} = 1$, if $|\mathbf{P}_{12}^{em}| < l_{12}^{em}$, where $l_{12}^{em} = 0.001|\mathbf{P}_{12}^{em}|$, $\mathbf{P}_{12}^{em} = \mathbf{P}^{em} - P_3^{em}\mathbf{e}_3$.

Now we can additionally take into account the inhomogeneity of the piezoceramic polarization, when solving the homogenization problems described in Sect. 2. Taking advantage of APDL language of the finite element software ANSYS, we have previously implemented the following computation strategy [23, 24, 26]. In

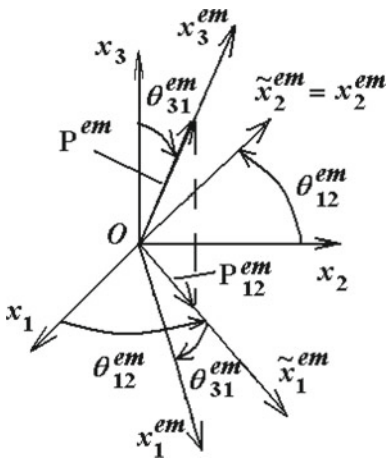

Fig. 1 Element coordinate system for a separate finite element

the existing finite element mesh, we modified all the electrostatic elements into the elements with the possibilities of piezoelectric analysis. New elements were assigned with the material properties of two types: the properties of polarized piezoceramics for the finite elements of the first phase and the properties of inclusions or pores for the elements of the second phase. At the same time, if the second phase consisted of the set of pores, then the pores were considered as piezoceramic material with negligibly small elastic and piezoelectric moduli and with dielectric permittivities equal to the dielectric permittivities of vacuum. The element coordinate systems $Ox_1^{em}x_2^{em}x_3^{em}$, determined from the polarization vectors $\mathbf{P}^{em}$ obtained at the previous stage, were assigned with the finite elements of the piezoceramic material of the first phase. Further, in order to determine the effective moduli, we solved the problems of electroelasticity for the inhomogeneous representative volume, using the methods described in Sect. 1. We note that when taking into account the inhomogeneous polarization, the homogenization problems are solved on the finite element mesh, in which each element of the polarized piezoceramics has, generally speaking, its own moduli $\mathbf{c}^{Eem}$, $\mathbf{e}^{em}$, $\boldsymbol{\varepsilon}^{Sem}$, obtained by the known formulas for the recalculation of the tensor coefficients, when making a transition from the main coordinate system $Ox_1x_2x_3$ to the element coordinate systems $Ox_1^{em}x_2^{em}x_3^{em}$ [15].

If the polarization field is inhomogeneous, then problem (12), (13) is not used, and all finite elements in the homogenization problem have either the properties of the piezoceramic material of the 6 mm class polarized along the axis Ox_3, or the properties of pores. In the described above approach, the material moduli $\mathbf{c}^{Eem}$, $\mathbf{e}^{em}$, $\boldsymbol{\varepsilon}^{Sem}$ of the finite elements of the first phase of piezoceramic composite were obtained from the original moduli $\mathbf{c}^{E(1)}$, $\mathbf{e}^{(1)}$, $\boldsymbol{\varepsilon}^{S(1)}$, where the tensor coefficients were recalculated after the rotation of the element coordinate systems. In the case when the residual polarization vector does not achieve the maximal possible value of the saturation polarization, the material moduli are the functions of this vector and the tensor of residual strain. Not going into details for the determination of such dependence, here we use linear approximation and assume that the material moduli $\mathbf{c}^{Eem}$, $\mathbf{e}^{em}$, $\boldsymbol{\varepsilon}^{Sem}$ of the inhomogeneously polarized piezoceramics are linear functions of the residual polarization. I.e. the material properties of the partially polarized ceramic linearly change from the values at the state when the piezoceramics are thermally depolarized ($\mathbf{c}_i^E$, $\mathbf{e}_i = 0$, $\boldsymbol{\varepsilon}_i^S$), to the values of these moduli at the state of saturation $\mathbf{c}^{E(1)}$, $\mathbf{e}^{(1)}$, $\boldsymbol{\varepsilon}^{S(1)}$. Indeed, following [36, 37], we adopt the following dependences

$$\mathbf{c}^{Eem} = (1 - k_p)\mathbf{c}_i^E + k_p\mathbf{c}_p^{Eem}, \tag{14}$$

$$\mathbf{e}^{em} = k_p\mathbf{e}_p^{em}, \tag{15}$$

$$\boldsymbol{\varepsilon}^{Sem} = (1 - k_p)\boldsymbol{\varepsilon}_i^S + k_p\boldsymbol{\varepsilon}_p^{Sem}, \tag{16}$$

where $\mathbf{c}_p^{Eem}$, $\mathbf{e}_p^{em}$, $\boldsymbol{\varepsilon}_p^{Sem}$ are the moduli obtained with the recalculation of the initial moduli $\mathbf{c}^{E(1)}$, $\mathbf{e}^{(1)}$, $\boldsymbol{\varepsilon}^{S(1)}$ by the rotations of the element coordinate systems; $\mathbf{c}_i^E$, $\boldsymbol{\varepsilon}_i^S$ are the moduli for isotropic material, i.e. for nonpolarized ceramics the transversely

isotropic 6 *mm* class reduces to isotropic class: $c^E_{i11} = c^E_{i33}$, $c^E_{i12} = c^E_{i13}$, $c^E_{i44} = (c^E_{i11} - c^E_{i12})/2$, $\varepsilon^S_{i11} = \varepsilon^S_{i33} = \varepsilon_i$.

The multiplier k_p in (14)–(16) is the ratio of the magnitude of the element vector of polarization $\mathbf{P}^{em}$ to the value of the magnitude of the polarization vector for the homogeneous piezoceramics

$$k_p = |\mathbf{P}^{em}|/p_{sat}\,, \tag{17}$$

where p_{sat} is the polarization value at the state of saturation, which in the frames of the adopted model is determined by the following formula

$$p_{sat} = (\varepsilon_i - \varepsilon_0)E_*\,. \tag{18}$$

When solving the problems of electrostatic for inhomogeneous material with non-smooth interphase boundaries, it is possible to encounter singularities in the electric potential, electric field and electric induction. In such situations, the magnitude of the residual polarization vector can exceed the maximal allowed value for the polarization at the saturation state, which is usually not permitted. In connection to this, we can change the formula (17), thus eliminating the possibility of "superpolarization" for the piezoceramic material:

$$k_p = \begin{cases} |\mathbf{P}^{em}|/p_{sat}, & |\mathbf{P}^{em}| \le p_{sat}\,, \\ 1, & |\mathbf{P}^{em}| > p_{sat}\,. \end{cases} \tag{19}$$

One more alternative approach is connected with the use of other constitutive relations for the piezoceramics and therefore other dependences for the compliance moduli of the inhomogeneously polarized ceramic $\mathbf{s}^{Eem}_p$, measured at constant electric field, the piezomoduli $\mathbf{d}^{em}_p$ and the dielectric permittivities $\boldsymbol{\varepsilon}^{Tem}_p$, measured at constant (zero) mechanical stress [13, 35].

$$\mathbf{s}^{Eem} = (1 - k_p)\mathbf{s}^E_i + k_p\mathbf{s}^{Eem}_p\,, \tag{20}$$

$$\mathbf{d}^{em} = k_p\mathbf{d}^{em}_p\,, \tag{21}$$

$$\boldsymbol{\varepsilon}^{Tem} = (1 - k_p)\boldsymbol{\varepsilon}^T_i + k_p\boldsymbol{\varepsilon}^{Tem}_p\,. \tag{22}$$

Here, similarly to (14)–(16), $\mathbf{s}^{Eem}_p$, $\mathbf{d}^{em}_p$, $\boldsymbol{\varepsilon}^{Tem}_p$ are the moduli obtained by recalculation the original moduli $\mathbf{s}^{E(1)}$, $\mathbf{d}^{(1)}$, $\boldsymbol{\varepsilon}^{T(1)}$ with the rotations of the element coordinate systems.

As the moduli from the sets $\{\mathbf{c}^{E(1)}, \mathbf{e}^{(1)}, \boldsymbol{\varepsilon}^{S(1)}\}$ and $\{\mathbf{s}^{E(1)}, \mathbf{d}^{(1)}, \boldsymbol{\varepsilon}^{T(1)}\}$ and so on are connected with each other by the known relations $\mathbf{s}^{E(1)} = (\mathbf{c}^{E(1)})^{-1}$, $\mathbf{d}^{(1)} = \mathbf{e}^{(1)} \cdot \mathbf{s}^{E(1)}$, $\boldsymbol{\varepsilon}^{T(1)} = \boldsymbol{\varepsilon}^{S(1)} + \mathbf{d}^{(1)} \cdot \mathbf{e}^{(1)*}$), then having determined one of the sets of the material moduli, it is possible to find the values of the moduli for the other set.

Meanwhile, relations (14)–(16) and (20)–(22) are not equivalent, and thus, the question about the best approach for the determination of the moduli for

inhomogeneously polarized piezoceramics in these simplified models remain open. The approach connected with the use of relations (20)–(22) is more difficult for practical implementation, but seems to be more reasonable.

At the same time, both models (14)–(16) and (20)–(22) can be implemented also in ANSYS finite element software with the use of the programs in ANSYS APDL, if we modify the electrostatic elements for piezoelectric analysis, changing their element coordinate systems, as well as the values of their material properties.

4 ACELAN-COMPOSE Package Structure

4.1 Software Package Concept

ACELAN-COMPOS is a client-server GUI application with a modular structure. The user interface is implemented as an application developed using HTML and JavaScript and runs in a web-browser. The client-side application consists of the following moduli:

1. Graphic 3D preprocessor – a component for creating and viewing the source geometry. It is developed using the WebGL Framework. Currently, to start solving the problem the user provides parameters for the new model, including preferred connectivity type. Then the preprocessor allows analyzing generated mesh.
2. Tools for editing physical models – a set of forms for specifying boundary conditions and material properties with the help of the ACELAN command language.
3. Graphic 3D postprocessor – a module for analyzing the solution obtained, which includes the ability to view the solution both in tabular form and in the form of visualizations over the original geometry. Supported viewing modes include heat maps, vector field visualizations, sections and body viewing capabilities, etc. WebGL Framework is also selected as the implementation tool for the graphic postprocessor.

The server-side part of the package is a cross-platform application, developed using the .Net Core Framework and the C# programming language. It is responsible for performing calculations and processing the results of solving the problem. It allows performing computations for different users simultaneously. The interaction between the server and the client application is implemented by means of the REST API. The main components are:

1. A set of mesh generators for composites of supported types. Various plug-in mesh generators allow users to get models of composites that meet the required criteria. Currently only two-component composites are supported.
2. The ALGLIB Library and custom implementation of the Page-Sanders algorithm for solving systems of linear equations.
3. Finite element method solvers.

4. Postprocessor for additional processing of the obtained solution and calculation of derived values.

On the server side a relational database is used to store user problems data.

4.2 Material Editor

ACELAN-COMPOS material library consists of two major parts: the storage system built with relational database and the user interface. The storage system is implemented with object-relational mapping tools from .NET packages. Universal storage format is used for all material types. In this format, each material has its name and a set of basic properties, such as density and anisotropy class, where all non-zero characteristics of material properties are stored. The proposed storage scheme is based on the ideas of sparse matrices storage formats. Due to the client-server architecture of the package with multiple users, the database provides concurrent user access rights. For a desktop version of the package, an embedded database is used. The material database includes the ability to transform the set of material properties for isotropic material to another type, such as, the Young's modulus and Poisson's ratio, the Lame coefficients, or the bulk modulus and the shear modulus. Anisotropic materials can depend on polarization angle and modulus. In this case, the rotation of the local coordinate system is used to define the material properties.

The results of the effective moduli calculation for the composite material are stored in the specially constructed material structures. After the effective moduli calculation, these structures may have almost zero elements that contain negligibly small values compared to the input numerical tolerance. In some cases, due to the material distribution in representative volume, the anisotropy class of the composite material can be different from anisotropy classes of its constituents. Such cases require the analysis of anisotropy class change. However, in most cases the anisotropy class of the composite does not differ from initial anisotropy classes of its constitutive phases, so that the negligibly small values, which appear at the places of initial zero elements of the material properties structures, can be regarded as zeros. According to the specified numerical tolerance, the computation results can be automatically filtered, where almost zero values are replaced with zeros (Fig. 2). This filtration is optional to the user, who can choose either the original or filtered results and therefore control the output values.

The user interface was built with quite simple markup with the following features: individual representations for the most used anisotropy classes, an auto-symmetry tool to facilitate the process of the material properties input, and a tree structure for easy access to the groups of materials.

Evaluated Electric Permittivity, F/m:

6.46E-09	-1.18E-26	1.94E-25
1.01E-27	6.46E-09	-2.39E-25
-1.05E-27	2.86E-25	5.62E-09

Filtered Electric Permittivity, F/m:

6.46E-09	0.00E+00	0.00E+00
0.00E+00	6.46E-09	0.00E+00
0.00E+00	0.00E+00	5.62E-09

Fig. 2 User interface for results viewer

4.3 Representative Volume Element Models

The representative volumes of the composite materials in ACELAN-COMPOS can be constructed using two basic models of 3–3 and 3–0 connectivity types. Since the constitutive materials of the composite are identified in the volume only by numeric labels, both models can be reversed by re-enumerating the bodies inside the volume. The representative volumes are generated as the finite element meshes, with possibility to perform export to the well-known CAE software formats as .inp. The methods of the 3–3 and 3–0 models generation were previously presented in [11] and [12] respectively. These methods are based on the well-known octree algorithm [19].

Brief description of the 3–3 representative volume generation can be given as follows. Each volume consists of clusters (Fig. 3), where each cluster is a cube made of 512 finite elements with eight elements on each edge. All clusters are generated separately, so that the parallel implementation can be used to improve performance. Current version of the package is able to determine the number of the available processors and to use them for simultaneous cluster generation. In each cluster, anchor points for both materials are placed in specific predefined locations on the surface to ensure that the material connectivity will not be broken between the clusters. At the beginning, all other elements are marked as material #1. At the next step, a random element of the cluster is marked as material #2. Then the shortest path is constructed to connect this element with the material #2 anchor points. Afterwards, the constructed material #2 structure is enlarged to achieve the needed percentage of materials. As the connectivity of material #1 can be violated inside the cluster during this process, the algorithm specially checks it at each step by a breadth-first search.

In ACELAN-COMPOS, two variants of the 3–3 algorithm are implemented. In the direct 3–3 connectivity algorithm, the connectivity of material #1 (orange elements in Fig. 3) is ensured by the domain vertices, and the paths to the vertices are constructed starting from the internal element in the domain. The connectivity of material #2 (blue elements in Fig. 3) is ensured by the anchors located approximately in the middle of

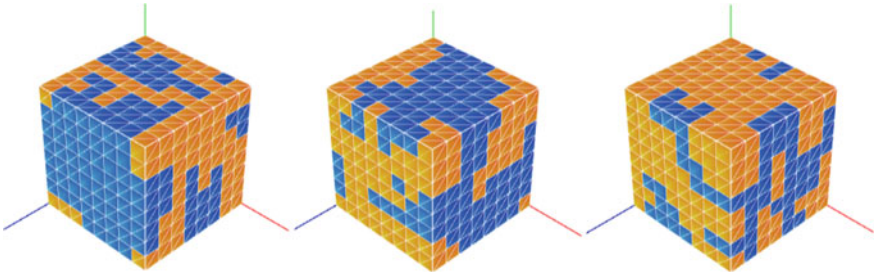

Fig. 3 Clusters for 3–3 representative volume with different input parameters

the domain faces. In the inverted 3–3 connectivity algorithm the phases numbers are swapped. A detailed description of these algorithms can be found in [11, 12].

As it can be seen from Fig. 3, for a small proportion of inclusions the direct algorithm distributes a significant part of the framework elements near the domain edges (orange elements in Fig. 3 in the center and on the right), and, on the contrary, the reverse algorithm collects most of the elements in the central part of the domain (blue elements in Fig. 3 in the center and on the left). With a larger number of domains, these effects are leveled, since in this case a part of the domain boundaries lays inside the representative volume.

For 3–0 models, user can setup not only the needed percentage but also the granule size limits, as well as define whether the granules are allowed to join each other during the representative volume generation process. These parameters are important for setting limitations on the resulting material distribution. Therefore, they must be chosen according to the known information about the studied composite.

The generated finite element meshes can be viewed in ACELAN-COMPOS web application user interface (Fig. 4).

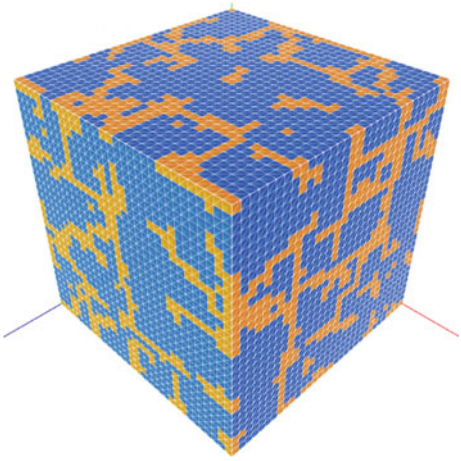

Fig. 4 Example of 3–3 representative volume with 32,768 elements

4.4 Finite Elements, Solvers, and Postprocessing

ACELAN-COMPOS finite element library contains two types of elements: HEX8 and HEX20. These elements are an isoparametric 8-node linear hexahedron and a 20-node quadratic serendipity hexahedron, respectively, with the capabilities of piezoelectric, elastic or electrostatic analyses. Most numerical experiments in current version of the package were performed with HEX8 element. This element is based on the multiplicative cubature formula with 8 integration points.

Class hierarchy and several program interfaces allow us to use the elements with different shape functions and integration schemes. The current version of the finite element library was designed for conventional analysis, but in the case of solving the problems for a representative volume with regular mesh, we can make some simplifications. Note that all finite elements in pre-generated volumes have the same size, form and their faces are parallel to the coordinate axes. Then the brick elements are not actually isoparametric, since the parametric mapping becomes trivial, and the any single element provides linear behavior respect to each variable x_1, x_2 and x_3. Moreover, as there are only two materials, only two different element matrices must be evaluated.

The global finite element matrix is stored in sparse format and can be passed to direct or iterative solvers. Both open-source and custom solvers are included in the current version of the package. Export of matrices is also supported for further research of the most applicable external sparse system solving tools. Normalization technique is applied to global matrix to reduce computational errors in coupled problems.

After solving the boundary value problems (1)–(5) or (1)–(4), (10) by the finite element method, the ACELAN-COMPOS package calculates by (8) or (11) the components of the averaged stress and electric induction. In order to calculate the components $T_\alpha \sim \sigma_{ij}$ and D_j, it is necessary to determine the derivatives of the finite element solutions $\mathbf{u}(\mathbf{x})$ and $\varphi(\mathbf{x})$. As is known, the calculation of derivatives in FEM has some features associated with their smoothing. Moreover, in the case of composite media, it is suggested [3, 4, 38] to carry out such smoothing separately along the subdomains of different phases. However, to find the effective moduli, we need not the values of the stress fields and electric induction at different points of the medium, but rather their integral characteristics. For these integral values, smoothing is not necessary, and we can calculate the integrals of the various components of stresses and electric induction over separate finite elements. These calculations are performed with the same multiplicative 8-point cubature formulas that were used to calculate the element matrices. This approach allows us to use the optimal values of the field gradients [1] and implicitly restore these gradients, at least in the form of full linear polynomials for each variable x_1, x_2 and x_3.

5 Numerical Examples

As an example, we present the results of the effective moduli calculation for a porous piezoceramic material. The main active phase is the PZT-4 solid piezoceramic material, with the following moduli in the crystallographic coordinate system: $c_{11}^{E(1)} = 13.9 \times 10^{10}$ (N/m^2); $c_{12}^{E(1)} = 7.78 \times 10^{10}$ (N/m^2); $c_{13}^{E(1)} = 7.43 \times 10^{10}$ (N/m^2); $c_{33}^{E(1)} = 11.5 \times 10^{10}$ (N/m^2); $c_{44}^{E(1)} = 2.56 \times 10^{10}$ (N/m^2); $e_{31}^{(1)} = -5.2$ (C/m^2); $e_{33}^{(1)} = 15.1$ (C/m^2); $e_{15}^{(1)} = 12.7$ (C/m^2); $\varepsilon_{11}^{S(1)} = 730\varepsilon_0$; $\varepsilon_{33}^{S(1)} = 635\varepsilon_0$, $\varepsilon_0 = 8.85 \times 10^{-12}$ (F/m). The second phase of the composite is the pores, which will be considered as a piezoceramic material with negligibly small moduli: $c_{\alpha\beta}^{E(2)} = \kappa c_{\alpha\beta}^{E(1)}$; $e_{j\beta}^{(2)} = \kappa e_{j\beta}^{(1)}$; $\varepsilon_{jj}^{S(2)} = \varepsilon_0$; $\kappa = 10^{-10}$.

We will investigate three models of porous PZT ceramics:

- model 1 with uniform polarization of the piezoceramic phase;
- model 2 with inhomogeneous polarization based on $c^E e\varepsilon^S$-relations (14)–(16) and (17), (18);
- model 3 with inhomogeneous polarization based on $s^E d\varepsilon^T$-relations (20)–(22) and (17), (18).

In cases 2 and 3, we find the moduli of unpolarized ceramics as Hill-averaged polycrystalline body constants equal to the moduli of dense polarized PZT ceramics $\mathbf{s}^{E(1)} = (\mathbf{c}^{E(1)})^{-1}, \boldsymbol{e}^{T(1)}$. As a result of the calculations, we obtain the following values: $c_{i11}^E = 13.0 \times 10^{10}$ (N/m^2); $c_{i12}^E = 7.52 \times 10^{10}$ (N/m^2); $\varepsilon_{i11}^S = \varepsilon_{i11}^T = 1387\varepsilon_0$.

In numerical calculations, we used an inverted 3–3 connectivity algorithm for the representative volume with 16 elements on each side.

The results of the calculations are presented in Figs. 5, 6, 7 and 8 for porosity $0 \le p \le 60\%$. Here and after $r()$ denotes the relative values of the effective properties, with respect to the corresponding values of the moduli for zero porosity. For example, $r(c_{33}^E) = \tilde{c}_{33}^E / c_{33}^{E(1)}$, where $\tilde{c}_{33}^E$ is the effective stiffness modulus for the porous PZT ceramics, $c_{33}^{E(1)}$ is the value of the stiffness modulus for an ordinary piezoceramic material and so on. The curves 1–3 correspond to the models 1–3, respectively.

As can be seen from Figs. 5, 6, 7 and 8, the dependences on porosity and on polarization models for the effective stiffness moduli, the piezomoduli and the dielectric permittivities are quite different.

The effective stiffness moduli monotonously decrease with increasing porosity, and taking into account inhomogeneous polarization only slightly reduces their values. The $s^E d\varepsilon^T$-model for most porosity values gives slightly smaller stiffness values compared to the $c^E e\varepsilon^S$-model. At the same time, Fig. 5 shows only the graphs for the relative moduli $r(c_{33}^E)$ and $r(c_{13}^E)$. The other stiffness moduli behave similarly to those given. However, for the relative shear modulus $r(c_{44}^E)$ there is a situation, when even for a small porosity the model which takes into account inhomogeneous polarization slightly increases the values of $r(c_{44}^E)$ compared to the homogeneous polarization model.

The effective piezomoduli (Figs. 6 and 7a) also decrease with increasing porosity, but taking into account the inhomogeneity of the polarization field significantly

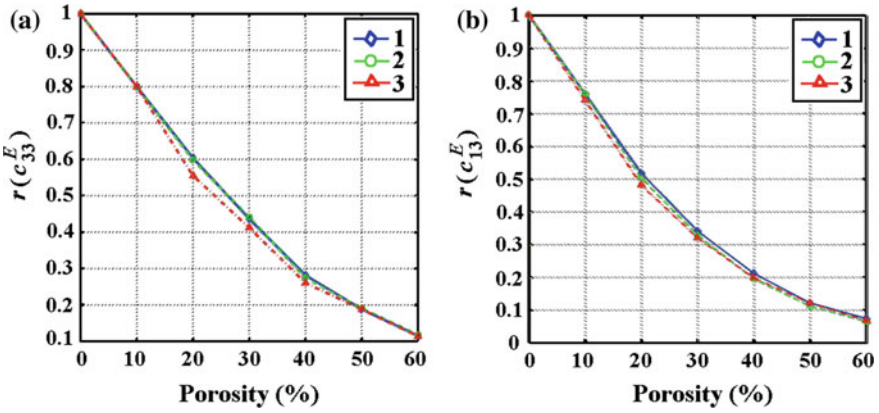

Fig. 5 Dependencies of the relative effective stiffness moduli $r(c_{33}^E)$ and $r(c_{13}^E)$ versus porosity

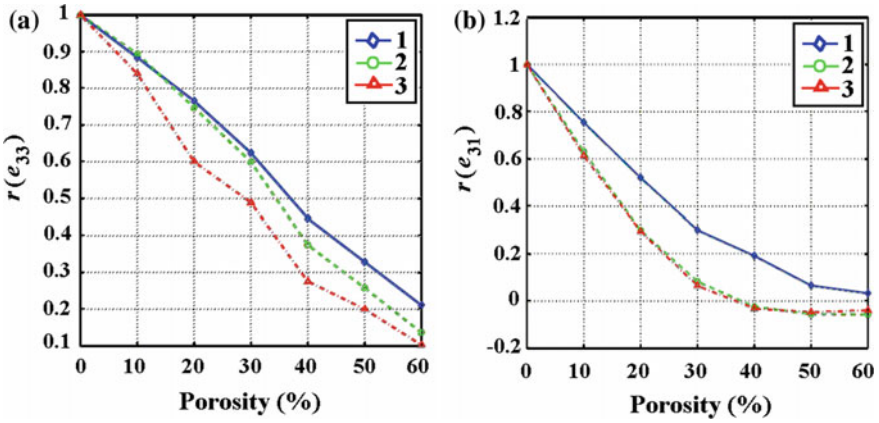

Fig. 6 Dependencies of the relative effective piezomoduli $r(e_{33})$ and $r(e_{31})$ versus porosity

reduces their values, and the most significant decrease takes place for the $s^E d\varepsilon^T$-model. The behavior of the relative piezomodulus $r(e^{31})$ (Fig. 6b) versus porosity $p > 40\%$ is unusual in the sense that it becomes negative and even slightly increases for $p > 50\%$. A similar effect was observed in other computational experiments with 3-3 connectivity algorithms [11]. This effect for other models of the representative volumes does not always occur, and can be explained by the peculiarities of the composite phases generation, as well as by very small values of the effective piezomodulus $\tilde{e}^{31}$.

The effective dielectric constant $\tilde{\varepsilon}_{33}^S$ (Fig. 7b) also decreases with increasing porosity. But, in contrast to the effective stiffness, taking into account inhomogeneous polarization leads to an increase in their values for most porosity values, and the

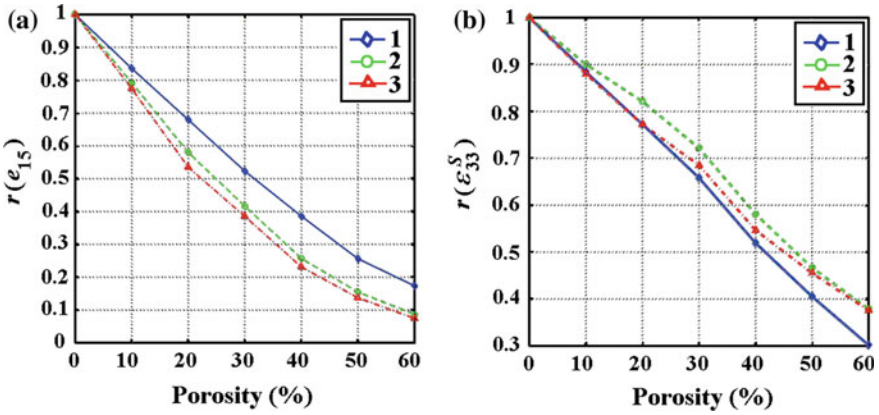

Fig. 7 Dependencies of the relative effective piezomodulus $r(e_{15})$ and dielectric permittivity $r(\varepsilon_{33}^S)$ versus porosity

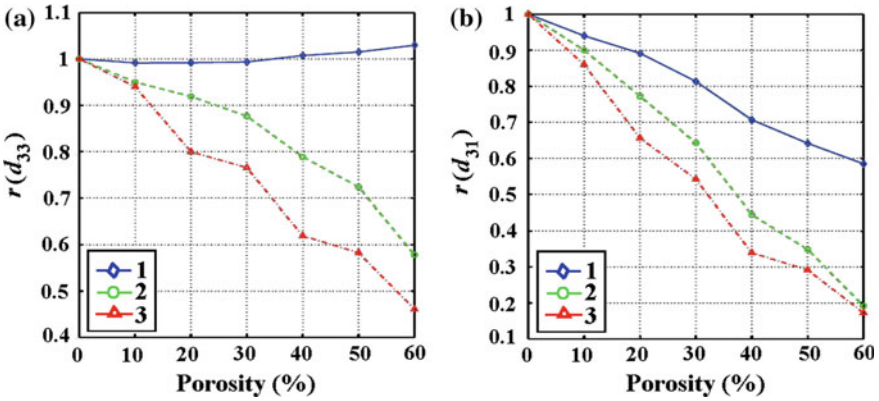

Fig. 8 Dependencies of the relative effective piezomoduli $r(d_{33})$ and $r(d_{31})$ versus porosity

$c^E e\varepsilon^S$-model gives the highest values. The effective dielectric permittivity $\tilde{\varepsilon}_{11}^S$ behave similarly to the $\tilde{\varepsilon}_{33}^S$ modulus.

Note that for practical applications, especially in hydroacoustics, the values of the piezomoduli $\tilde{d}_{i\alpha}$ are very important. In a number of papers [5, 6, 32], it was noted that for a porous piezoceramics, the effective thickness piezomodule $\tilde{d}_{33}$ practically does not decrease with increasing porosity. In other papers [2, 17, 18, 41], a decrease in the effective thickness piezomodule was noted. As we see from Fig. 8a without polarization heterogeneity, the effective thickness piezomodule $\tilde{d}_{33}$ is almost constant, and with a large porosity it even slightly increases. Meanwhile, taking into account the polarization inhomogeneity leads to a decrease in the modulus $\tilde{d}_{33}$, which corresponds to the papers [5, 6, 32]. This effect also depends on the structure of the representative volume. Thus, Fig. 8a confirms that the structure of porosity and the

technology creating of porous piezoceramics significantly affect of the piezomodule $\tilde{d}^{33}$. The relative effective piezomodule $r(d_{31})$ (Fig. 8b) decreases with increasing porosity, and taking into account the polarization inhomogeneity gives its stronger decrease. This behavior is consistent with other known papers.

6 Conclusion

In this paper we have described new features of the ACELAN-COMPOS package. This package is designed to determine the effective moduli of active composites. It solves the homogenization problems based on the effective moduli method, the representative volume simulation and the finite element method. Taking into account inhomogeneous polarization in combination with the simulation of various structures of the representative volumes allows us to detect the main features of the porous piezoceramic effective moduli dependence versus porosity. These features also depend on the values of the moduli c^E_{i11}, c^E_{i12}, ε^S_{i11} for the nonpolarized piezoceramics. In the above numerical example, there was the situation when $c^{E(1)}_{33} \le c^E_{i11} \le c^{E(1)}_{11}$; $c^{E(1)}_{13} \le c^E_{i12} \le c^{E(1)}_{12}$; $\varepsilon^S_{i11} = 1.9\varepsilon^{S(1)}_{11}$. In this case, taking into account the inhomogeneity of the polarization field had a different influence on the stiffness moduli and on the dielectric permittivity constants.

Our models prove, that taking the inhomogeneous polarization into account leads to the fact that a sufficiently large part of PZT ceramics turns out to be less polarized than for the case of uniform polarization. In addition, the directions of the polarization vector in the vicinity of the pores become different from the main polarization direction along the Ox_3 axis. In this case, the polarization vectors in the vicinity of the pores rotate in different directions, going around the pores. Thus we can mark a conclusion that taking into account inhomogeneous polarization significantly reduces the relative values of the effective piezomoduli, especially the piezomoduli $r(e_{31})$ and $r(d_{31})$.

Further research on the influence of nonuniform polarization field on the effective moduli of porous PZT ceramics can be associated with the using more accurate nonlinear polarization models and performing calculations for various structures and connectivities of porous piezoceramics.

Acknowledgements The authors are grateful for the support of the Ministry of Science and Higher Education of the Russian Federation, project No. 9.1001.2017/4.6.

References

1. Barlow, J.: Optimal stress locations in finite element models. Int. J. Numer. Methods Eng. **10**, 243–251 (1976)
2. Bowen, C.R., Perry, A., Lewis, A.C.F., Kara, H.: Processing and properties of porous piezoelectric materials with high hydrostatic figures of merit. J. Eur. Ceram. Soc. **24**, 541–545 (2004)

3. Choudhary, S.K., Grosse, I.R.: Effective stress-based finite element error estimation for composite bodies. Eng. Fract. Mech. **50**, 687–701 (1995)
4. Feng, Z., Rowlands, R.E.: Smoothing finite-element and experimental hybrid technique for stress analyzing composites. Comput. Struct. **39**, 631–639 (1991)
5. Getman, I., Lopatin, S.: Theoretical and experimental investigation of the porous PZT ceramics. Ferroelectrics **186**, 301–304 (1996)
6. Hikita, K., Yamada, K., Nishioka, M., Ono, M.: Effect of porous structure to piezoelectric properties of PZT ceramics. Jpn. J. Appl. Phys. **22**, 64–66 (1983)
7. Iyer, S., Venkatesh, T.A.: Electromechanical response of porous piezoelectric materials: effects of porosity connectivity. Appl. Phys. Lett. **97**, 072904 (2010)
8. Iyer, S., Venkatesh, T.A.: Electromechanical response of (3–0) porous piezoelectric materials: effects of porosity shape. J. Appl. Phys. **110**, 034109 (2011)
9. Khoroshun, L.P., Maslov, B.P., Leshchenko, P.V.: Prediction of Effective Pproperties of Piezoactive Composite Materials. Naukova Dumka, Kiev (1989). (in Russian)
10. Kudimova, A.B., Mikhayluts, I.V., Nadolin, D.K., Nasedkin, A.V., Nasedkina, A.A., Oganesyan, P.A., Soloviev, A.N.: Computer design of porous and ceramic piezocomposites in the finite element package ACELAN. Procedia Struct. Integr. **6**, 301–308 (2017)
11. Kudimova, A.B., Nadolin, D.K., Nasedkin, A.V., Nasedkina, A.A., Oganesyan, P.A., Soloviev, A.N.: Models of porous piezocomposites with 3–3 connectivity type in ACELAN finite element package. Mater. Phys. Mech. **37**(1), 16–24 (2018)
12. Kudimova, A.B., Nadolin, D.K., Nasedkin, A.V., Oganesyan, P.A., Soloviev, A.N.: Finite element homogenization models of bulk mixed piezocomposites with granular elastic inclusions in ACELAN package. Mater. Phys. Mech. **37**(1), 25–33 (2018)
13. Kurbatova, N.V., Nadolin, D.K., Nasedkin, A.V., Nasedkina, A.A., Oganesyan, P.A., Skaliukh, A.S., Soloviev, A.N.: Models of active bulk composites and new opportunities of ACELAN finite element package. In: Sumbatyan, M.A. (ed.) Wave Dynamics and Composite Mechanics for Microstructured Materials and Metamaterials. Ser. Advanced Structured Materials, vol. 59, pp. 133–158. Springer, Singapore (2017)
14. Kurbatova, N.V., Nadolin, D.K., Nasedkin, A.V., Oganesyan, P.A., Soloviev, A.N.: Finite element approach for composite magneto-piezoelectric materials modeling in ACELAN-COMPOS package. In: Altenbach, H., Carrera, E., Kulikov, G. (eds.) Analysis and Modelling of Advanced Structures and Smart Systems. Ser. Advanced Structured Materials, vol. 81, pp. 69–88. Springer, Singapore (2018)
15. Lekhnitskii, S.G.: Theory of Elasticity of an Anisotropic Elastic Body. Holden-Day, San Francisco, CA (1963)
16. Lewis, R.W.C., Dent, A.C.E., Stevens, R., Bowen, C.R.: Microstructural modelling of the polarization and properties of porous ferroelectrics. Smart Mater. Struct. **20**, 085002 (2011)
17. Li, J.F., Takagi, K., Ono, M., Pan, W., Watanabe, R., Almajid, A., Taya, M.: Fabrication and evaluation of porous piezoelectric ceramics and porosity-graded piezoelectric actuators. J. Am. Ceram. Soc. **86**, 1094–1098 (2003)
18. Liu, W., Du, L., Wang, Y., Yang, J., Xu, H.: Effects of foam composition on the microstructure and piezoelectric properties of macroporous PZT ceramics from ultrastable particle-stabilized foams. Ceram. Int. **39**, 8781–8787 (2013)
19. Meagher, D.: Octree Encoding: A New Technique for the Representation, Manipulation and Display of Arbitrary 3-D Objects by Computer. (Technical Report IPL-TR-80-111). Rensselaer Polytechnic Institute (1980)
20. Mercadelli, E., Sanson, A., Galassi, C.: Porous piezoelectric ceramics. In: Suaste-Gomez, E. (ed.) Piezoelectric Ceramics, pp. 111–128. InTechOpen (2010)
21. Nan, C.W., Weng, G.J.: Influence of polarization orientation on the effective properties of piezoelectric composites. J. Appl. Phys. **88**(1), 416–423 (2000)
22. Nasedkin, A.V., Shevtsova, M.S.: Improved finite element approaches for modeling of porous piezocomposite materials with different connectivity. In: Parinov, I.A. (ed.) Ferroelectrics and Superconductors: Properties and Applications, pp. 231–254. Nova Science Publications, New York, NY (2011)

23. Nasedkin, A.V., Shevtsova, M.S.: Effective moduli simulation for various types of porous piezoceramic materials. Vestnik DSTU **72–73**(3–4), 16–26 (2013). (In Russian)
24. Nasedkin, A.V., Shevtsova, M.S.: Multiscale computer simulation of piezoelectric devices with elements from porous piezoceramics. In: Parinov, I.A., Chang, S.-H. (eds.) Physics and Mechanics of New Materials and their Applications, pp. 185–202. Nova Science Publications, New York, NY (2013)
25. Nasedkin, A., Skaliukh, A., Soloviev, A.: New models of coupled active materials for finite element package ACELAN. AIP Conf. Proc. **1637**, 714–723 (2014)
26. Nasedkin, A.V., Nasedkina, A.A., Rybyanets, A.N.: Numerical analysis of effective properties of heterogeneously polarized porous piezoceramic materials with local alloying pore surfaces. Mater. Phys. Mech. **40**(1), 12–21 (2018)
27. Nasedkin, A.V., Kornievsky, A.S.: Finite element homogenization of elastic materials with open porosity at different scale levels. AIP Conf. Proc. **2046**, 020064 (2018)
28. Newnham, R.E., Skinner, D., Cross, L.E.: Connectivity and piezoelectric - pyroelectric composites. Mat. Res. Bull. **13**(5), 525–536 (1978)
29. Nguyen, B.V., Challagulla, K.S., Venkatesh, T.A., Hadjiloizi, D.A., Georgiades, A.V.: Effects of porosity distribution and porosity volume fraction on the electromechanical properties of 3–3 piezoelectric foams. Smart Mater. Struct. **25**(12), 125028 (2016)
30. Odegard, G.M.: Constitutive modeling of piezoelectric polymer composites. Acta Mater. **52**(18), 5315–5330 (2004)
31. Ringgaard, E., Lautzenhiser, F., Bierregaard, L.M., Zawada, T., Molz, E.: Development of porous piezoceramics for medical and sensor applications. Materials. **8**(12), 8877–8889 (2015)
32. Rybyanets, A.N.: Porous ceramic and piezocomposites: modeling, technology, and characterization. In: Newton, A. (ed.) Advances in Porous Ceramics, pp. 53–109. Nova Science Publications, New York, NY (2016)
33. Schwaab, H., Grunbichler, H., Supancic, P., Kamlah, M.: Macroscopical non-linear material model for ferroelectric materials inside a hybrid finite element formulation. Int. J. Solids Struct. **49**, 457–469 (2012)
34. Skaliukh, A.: About mathematical models of irreversible polarization processes of a ferroelectric and ferroelastic polycrystals. In: Irzaman, H. (ed.) Ferroelectrics and Their Applications, pp. 39–70. IntechOpen (2018)
35. Skaliukh, A., Nasedkin, A., Oganesyan, P., Soloviev, A.: Linear and nonlinear models of electroelasticity in the software package ACELAN. In: 2015 Joint IEEE International Symposium on Applications of Ferroelectric (ISAF), International Symposium on Integrated Functionalities (ISIF), and Piezoresponse Force Microscopy Workshop (PFM) (ISAF-ISIF-PFM 2015), 24–27 May, 2015, Singapore. IEEE Conference Publications, pp. 36–39 (2015)
36. Skaliukh, A.S., Soloviev, A.N., Oganesyan, P.A.: Modeling of piezoelectric elements with inhomogeneous polarization in ACELAN. Ferroelectrics **483**(1), 95–101 (2015)
37. Soloviev, A.N., Oganesyan, P.A., Skaliukh, A.S.: Modeling of piezoelectric elements with inhomogeneous polarization by using ACELAN. In: Parinov, I.A., Chang, S.-H., Theerakulpisut, S. (eds.) Advanced Materials - Studies and Applications, pp. 169–192. Nova Science Publications, New York, NY (2015)
38. Song, K.N.: A procedure for the improved continuous stress field of composite media. KSME Int. J. **12**, 871–880 (1998)
39. Stark, S., Neumeister, P., Balke, H.: A hybrid phenomenological model for ferroelectroelastic ceramics. Part I: single phased materials. J. Mech. Phys. Solids. **95**, 774–804 (2016)
40. Topolov, V.Y., Bowen, C.R., Bisegna, P.: Piezo-Active Composites: Microgeometry-Sensitivity Relations. Springer, Berlin (2018)
41. Yang, A.K., Wang, C.A., Guo, R., Huang, Y.: Microstructure and electrical properties of porous PZT ceramics fabricated by different methods. J. Am. Ceram. Soc. **93**, 1984–1990 (2010)

Three-Dimensional Problems of Harmonic Wave Propagation in an Elastic Layer

Mels V. Belubekyan and Vagharshak M. Belubekyan

Abstract In the present paper three-dimensional problem of propagation of elastic waves in a waveguide is considered, when several different boundary conditions are realized on the surfaces of the waveguide. We then establish the conditions where surface waves are permissible.

1 Introduction

Problems of dynamics of theory of elasticity of isotropic solids allow decou-pling of solutions for plane and anti-plane deformation. Fundamental results in investigation of elastic waves in layers are obtained for decoupled problems, e. g. Rayleigh waves and Love waves [1, 2]. On other hand, while three-dimensional problems are more natural to formulate, the investigation of such problems is more complex, than problems for decoupled plane or anti-plane waves.

A beginning to investigations in area of three-dimensional waves was set by the work of J. K. Knowles, where a generalization of Rayleigh surface wave is provided. Later the waves of Rayleigh type with mixed boundary conditions of a surface on a semi-plane in the three-dimensional formulation were studied in [3–5]. Similar problems for anisotropic media were considered in [6, 7], and waves of the Stoneley type in [8].

2 Problem Statement

Let the elastic layer in the Cartesian coordinate system (x, y, z) occupy the domain: $-\infty < x < \infty, 0 \leq y \leq h, -\infty < z < \infty$. The equation of wave propagation in isotropic elastic media is taken in the form following the notations of Nowacki [9]:

M. V. Belubekyan · V. M. Belubekyan (✉)
Institute of Mechanics, National Academy of Sciences, Yerevan, Armenia
e-mail: vbelub@googlemail.com

M. A. Sumbatyan (ed.), *Wave Dynamics, Mechanics and Physics of Microstructured Metamaterials*, Advanced Structured Materials 109,
https://doi.org/10.1007/978-3-030-17470-5_9

$$c_t^2 \Delta \overline{u} + \left(c_e^2 - c_t^2\right) grad\, div \overline{u} = \frac{\partial^2 \overline{u}}{\partial t^2} \tag{2.1}$$

where $\overline{u}$ is the vector of elastic displacements, and

$$\overline{u} = u\hat{i} + v\hat{j} + w\hat{k}, c_e^2 = \frac{\lambda + 2\mu}{\rho}, c_t^2 = \frac{\mu}{\rho} \tag{2.2}$$

Following [3] we introduce potential functions in Eq. (2.1):

$$u = \frac{\partial \varphi}{\partial x} + \frac{\partial \psi}{\partial z}, w = \frac{\partial \varphi}{\partial z} - \frac{\partial \psi}{\partial x}, \tag{2.3}$$

these are similar to the known Lamé transform for problems of plane deformation. With the help of (2.3) the projections of vector Eq. (2.1) are obtained in the following form:

$$\begin{aligned} &c_e^2 \Delta_2 \varphi + c_t^2 \frac{\partial^2 \varphi}{\partial y^2} - \frac{\partial^2 \varphi}{\partial t^2} + \left(c_e^2 - c_t^2\right) \frac{\partial v}{\partial y} = 0 \\ &c_t^2 \Delta v + \left(c_e^2 - c_t^2\right) \frac{\partial}{\partial y} \Delta_2 \varphi + \left(c_e^2 - c_t^2\right) \frac{\partial^2 v}{\partial y^2} = \frac{\partial^2 v}{\partial t^2} \\ &c_t^2 \Delta \psi = \frac{\partial^2 \psi}{\partial t^2}, \Delta_2 \equiv \frac{\partial^2}{\partial x^2} + \frac{\partial^2}{\partial y^2} \end{aligned} \tag{2.4}$$

Taking derivative on y of the second equation of the system (2.4) and substituting the expression for $\partial v/\partial y$ from the first equation, as in [3] we obtain:

$$\left(\Delta - \frac{1}{c_t^2} \frac{\partial^2}{\partial t^2}\right)\left(\Delta \varphi - \frac{1}{c_t^2} \frac{\partial^2 \varphi}{\partial t^2}\right) = 0 \tag{2.5}$$

Thus we obtained autonomous (decoupled) equations with respect to the unknown function φ, which is Eq. (2.5), and ψ, which is the third equation of the system (2.4). Note that φ and ψ functions yield all components of the elastic displacements: u, w are obtained from definition of φ and ψ (2.3), and v is obtained from the first equation of the system (2.4).

3 Harmonic Waves Representation

Let us represent the solutions of Eq. (2.5) and the third equation of system (2.4) in the form of harmonic waves:

$$\begin{aligned} \varphi &= \phi(y) \exp i(\omega t - k_1 x - k_3 z) \\ \psi &= \psi(y) \exp i(\omega t - k_1 x - k_3 z) \end{aligned} \tag{3.1}$$

The substitution of (3.1) into autonomous equations for $\varphi(x, y, z, t)$, $\psi(x, y, z, t)$ yields ordinary equations with respect to functions $\phi(y)$, $\psi(y)$, and the general solution to those equations would be:

$$\begin{aligned}\phi(y) &= A_1 e^{p_1 ky} + B_1 e^{-p_1 ky} + A_2 e^{p_{2ky}} + B_2 e^{-p_2 ky} \\ \psi(y) &= c_1 e^{p_2 ky} + c_2 e^{-p_2 ky}\end{aligned} \tag{3.2}$$

where

$$\begin{aligned}&p_1 = \sqrt{1-\theta\eta},\ p_2 = \sqrt{1-\eta},\ k = \sqrt{k_1^2 + k_2} \\ &\eta = \frac{\omega^2}{k^2 C_t^2},\ \theta = \frac{C_t^2}{C_e^2}\end{aligned} \tag{3.3}$$

Expressing the component v of displacements as follows:

$$v(x, y, z, t) = V(y)\exp i(\omega t - k_1 x - k_3 z) \tag{3.4}$$

from the second equation of system (2.4), taking into account (3.1) and (3.2) we obtain:

$$V(y) = k\left(p_1 A_1 e^{p_1 ky} - p_1 B_1 e^{-p_1 ky} + \frac{1}{p_2} A_2 e^{p_2 ky} - \frac{1}{p_2} B_2 e^{-p_2 ky}\right) \tag{3.5}$$

Based on the obtained general solutions, in the present paper we aim to study the propagation of elastic waves in the layer, when the surface $y = 0$ is free of stresses, as in the three-dimensional formulation of Rayleigh's problem [10]:

$$\sigma_{yy} = 0, \sigma_{yx} = 0, \sigma_{yz} = 0 y = 0 \tag{3.6}$$

while several types of boundary conditions can be realized on the second surface $y_1 = h$.

Conditions (3.6) expressed in terms of displacements yield:

$$(\lambda + 2\mu)\frac{\partial v}{\partial y} + \lambda\left(\frac{\partial u}{\partial x} + \frac{\partial w}{\partial z}\right) = 0, \frac{\partial v}{\partial x} + \frac{\partial u}{\partial y} = 0, \frac{\partial v}{\partial z} + \frac{\partial w}{\partial y} = 0 \tag{3.7}$$

Applying the transformation (2.3) and representation of the general solutions (3.1), (3.4), from (3.7) we obtain the boundary conditions with respect to the new desired functions:

$$(\lambda + 2\mu)V' - \lambda k^2 \phi = 0, V + \phi' = 0, \psi' = 0 \quad \text{when } y = 0 \tag{3.8}$$

By requiring that the general solution (3.2), (3.5) should satisfy the boundary conditions (3.8), one obtains relations between the arbitrary constants: the constants

$B_{11}B_2$ are expressed through A_1, A_2 and the constant C_2 is expressed through C_1, as follows:

$$B_1 = -\frac{1}{R}[R_1 A_1 + 4(2-\eta)A_2] \tag{3.9}$$

$$B_2 = \frac{1}{R}[4p_1p_2(2-\eta)A_1 + R_1A_2],\ C_2 = C_1 = 2C$$

where

$$R = (2-\eta)^2 - 4p_1p_2,\ R_1 = (2-\eta)^2 + 4p_1p_2 \tag{3.10}$$

And finally for solutions satisfying to free-boundary conditions at the surface $y = 0$, we obtain:

$$\begin{aligned}
\phi &= \frac{2}{R}[(2-\eta)^2 shp_1ky - 4p_1p_2 chp_1ky + 2p_1p_2(2-\eta)e^{-p_2ky}]A_1 \\
&\quad + \frac{2}{R}\left[(2-\eta)^2 chp_2ky - 4p_1p_2 shp_2ky - 2(2-\eta)e^{-p_1ky}\right]A_2 \\
\psi &= C\ chp_2ky \\
v &= \frac{2k}{R} \times \left\{p_1\left[(2-\eta)^2 chp_1ky - 4p_1p_2 shp_1ky - 2(2-\eta)e^{-p_2ky}\right]A_1\right. \\
&\quad \left. + \frac{1}{p_2}[(2-\eta)^2 shp_2ky - 4p_1p_2 chp_2ky + 2p_1p_2(2-\eta)e^{-p_1ky}]A_2\right\}
\end{aligned} \tag{3.11}$$

The expressions (3.11) contain three yet unknown constants A_1, A_2, C, which are to be determined from the boundary conditions at the second surface of the layer, the $y = h$ surface.

4 Navier Conditions at the Second Surface

Let the second surface $y = h$ be subjected to Navier conditions:

$$\sigma_{yy} = 0,\ u = 0,\ v = 0 \text{ when } y = h \tag{4.1}$$

Introducing functions φ, ψ the conditions (4.1) are transformed to the following:

$$\frac{\partial v}{\partial y} = 0,\ \frac{\partial \varphi}{\partial x} + \frac{\partial w}{\partial z} = 0,\ \frac{\partial \varphi}{\partial z} - \frac{\partial w}{\partial x} = 0 \quad \text{when } y = h \tag{4.2}$$

After some transformations, expressions (3.1), (3.4) yield the following simple boundary conditions:

$$\phi = 0, \phi'' = 0, \psi = 0 \quad \text{when } y = h \tag{4.3}$$

According to expansion for ψ taken from (3.10) and the third condition of (4.3), the following equality holds:

$$C\ ch\ p_2 kh = 0 \tag{3.4}$$

From (4.4) it follows that either $C = 0$ and all the phase velocities would be determined solely from equations for A_1, A_2 according to boundary conditions for function $\phi(y)$, or the following conditions should hold $\eta > 1$, $\left(p_2 = i\sqrt{\eta - 1}\right)$, and thus

$$\cos\sqrt{\eta - 1}\, kh = 0, \eta = 1 + \left[\frac{(2n-1)\pi}{2kh}\right]^2, \tag{4.5}$$

The equality (4.5) means that in that case purely shear waves are propagating with phase velocity (η) defined by (4.5). Obviously if (4.5) takes place, then for such phase velocities $A_1 = A_2 = 0$ ($\phi \equiv 0$).

On other hand, the requirement for ϕ from (3.2) to satisfy the boundary conditions (4.3), leads to the following system of linear algebraic equations with respect to constants A_1, A_2:

$$\begin{aligned}
&\left[(2-\eta)^2 sh\ p_1 kh - 4p_1 p_2 ch\ p_1 kh + 2p_1 p_2 (2-\eta) e^{-p_2 kh}\right] A_1 \\
&\quad + \left[(2-\eta)^2 ch\ p_2 kh - 4p_1 p_2 sh\ p_2 kh - 2(2-\eta) e^{-p_1 kh}\right] A_2 = 0 \\
&p_1\left[(2-\eta)^2 p_1 sh\ p_1 kh - 4p_1^2 p_2 ch\ p_1 kh + 2p_2^3 (2-\eta) e^{-p_2 kb}\right] A_1 \\
&\quad + \left[(2-\eta)^2 p_2^2 ch\ p_2 kh - 4p_1 p_2^3 sh\ p_2 kb - 2(2-\eta) p_1^2 e^{-p_1 kh}\right] A_2 = 0
\end{aligned} \tag{4.6}$$

Setting the determinant of system (4.6) to zero, after some transformations we obtain the dispersion equation:

$$K(\eta) \equiv -\left(p_1^2 - p_2^2\right) R_2(\eta) = 0 \tag{4.7}$$

where:

$$\begin{aligned}
R_2(\eta) \equiv\ & (2-\eta)^4 shp_1 kh\, chp_2 kh - 4p_1 p_2 (2-\eta)^2\, shp_1 khshp_2 kh - \\
& - 4p_1 p_2 (2-\eta)^2 chp_1 khchp_2 kh + 16 p_1^2 p_2^2 chp_1 kh \cdot\ shp_2 kh + \\
& + 4p_1 p_2 (2-\eta)^2 e^{-(p_1+p_2)kh}
\end{aligned} \tag{4.8}$$

For short waves (in approximation $kh >> 1$) the equation $R_2(\eta) = 0$ is reduced to the known Rayleigh equation [9]:

$$R_2(\eta) \equiv e^{(p_1+p_2)kh}\left[(2-\eta)^2 - 4p_1 p_2\right]^2 = 0 \tag{4.9}$$

Equation (4.8) has always a root satisfying the condition of localization:

$$0 < \eta < 1 \tag{4.10}$$

This becomes obvious if long waves' approximation $(kh)^2 << 1$ is considered.

In monographs [11, 12] the solutions of spatial problems for elastic layers are provided using asymptotical methods in approximation of thin layer.

5 Boundary Conditions of Sliding Contact and Clamped Edge at the Second Surface

As a second type of boundary conditions on the surface $y = h$ let us consider the conditions of sliding contact:

$$v = 0, \sigma_{yx} = 0, \sigma_{yz} = 0 \quad \text{when} \quad y = h \tag{5.1}$$

By using the Hooke's law, instead of (5.1) one can write:

$$v = 0, \frac{\partial}{\partial y}\left(\frac{\partial \varphi}{\partial x} + \frac{\partial \psi}{\partial z}\right) = 0, \frac{\partial}{\partial y}\left(\frac{\partial \varphi}{\partial z} - \frac{\partial \psi}{\partial x}\right) = 0 \quad \text{when } y = h \tag{5.2}$$

Then by using expressions (5.1), (3.4) the conditions of the sliding contact can be finally represented as follows:

$$\phi' = 0, V = 0, \psi' = 0 \quad \text{when } y = h \tag{5.3}$$

The condition $\psi' = 0$, similarly to the previous case, leads to purely shear waves $(c \neq 0)$ with the following phase velocity:

$$\eta = 1 + \left(\frac{n\pi}{kh}\right)^2 \tag{5.4}$$

Alternatively, in the case $C = 0$ the dispersion equation is obtained by satisfying the first two conditions from (5.3). These leads to the following system of linear algebraic equations with respect to constants A_1, A_2:

$$\begin{aligned}
&p_1\left[(2-\eta)^2 chp_1kh - 4p_1p_2 shkp_1kh - 2p_2^2(2-\eta)e^{-p_2kh}\right]A_1 \\
&\quad + \left[(2-\eta)^2 p_2 shp_2kh - 4p_1p_2^2 chp_2kh + 2p_1(2-\eta)e^{-p_1kh}\right]A_2 = 0 \\
&\quad + p_1\left[(2-\eta)^2 chp_1kh - 4p_1p_2 shp_1kh - 2(2-\eta)e^{-p_2kh}\right]A_1 \\
&\quad + \frac{1}{p_2}\left[(2-\eta)^2 shp_2kh - 4p_1p_2 chp_2kh + 2p_1p_2(2-\eta)e^{-p_1kh}\right]A_2 = 0
\end{aligned} \tag{5.5}$$

By setting the determinant of system (5.5) equal to zero, after some transformations we obtain the dispersion equation:

$$\begin{aligned} M(\eta) \equiv\ & (2-\eta)^4 thp_2 kh - 4p_1 p_2 (2-\eta)^2 (1 + thp_1 khthp_2 kh) \\ & + 16 p_1^2 p_2^2 thp_1 kh \\ & + 4p_1 p_2 (2-\eta)^2 (chp_1 khchp_2 kh)^{-1} e^{-(p_1+p_2)kh} = 0 \end{aligned} \tag{5.6}$$

Equation (5.6) in the short-wave approximation $kh > 1 (thp_2 kh \approx 1, thp_1 kh \approx 1)$ reduces to the squared Rayleigh's equation:

$$\left[(2-\eta)^2 - 4p_1 p_2\right]^2 = 0 \tag{5.7}$$

The value of $\eta = 1 (p_2 = 0)$ satisfies Eq. (5.6). In the phase space the root $\eta = 1$ divides the domain of phase velocities $\eta > 1$ from domain $0 < \eta < 1$ of phase velocities for which localization near the free surface takes place [13]. By eliminating the root $\eta = 1$ from equation dividing it by p_2 and taking the limit $p_2 \to 0$, we obtain the new equation:

$$\left(kh - 4\sqrt{1-\theta}\right) ch\sqrt{1-\theta} kh - 4\sqrt{1-\theta} \exp\left(-\sqrt{1-\theta} kh\right) = 0 \tag{5.8}$$

Denoting the root of Eq. (5.8) as $(kh)_*$, then obviously when $kh > (kh)_*$ and also in the limit case $kh \to \infty$ corresponding to Eq. (5.7), the dispersion equation should have a root within the range $0 < \eta < 1$. From Eq. (5.8) there also follows an approximate formula for the root:

$$(kh)_* \approx 4\sqrt{1-\theta} = \frac{2\sqrt{2}}{\sqrt{1-v}} \tag{5.9}$$

Let us also consider the case of boundary conditions of the clamped edge [14, 15]:

$$u = 0, v = 0, w = 0 \text{ when } y = 0 \tag{5.10}$$

Applying transformation (2.3) and expressions (3.1), (3.4), the boundary conditions for the sought functions are obtained as follows:

$$\Phi = 0, \mathrm{V} = 0, \Psi = 0 \quad \text{when } y = 0 \tag{5.11}$$

Similarly to the above considered cases, from condition $\Psi = 0$ there follows either condition $C = 0$ or a condition for purely shear waves. Requiring that solution (3.8) should satisfy the first two boundary conditions of (5.11), one comes to a system of linear algebraic equations with respect to A_1, A_2. By putting the determinant of this

system equal to zero, we obtain the dispersion equation with respect to dimensionless characteristic η of the phase velocity:

$$\begin{aligned}&\left[(2-\eta)^2 shp_1kh - 4p_1p_2 chp_1kh + 2p_1p_2(2-\eta)e^{-p_2kh}\right]\times\\ &\quad\times\left[(2-\eta)^2 shp_2kh - 4p_1p_2 chp_2kh + 2p_1p_2(2-\eta)e^{-pikh}\right]-\\ &\quad- p_1p_2\left[(2-\eta)^2 chp_2kh - 4p_1p_2 shp_2kh 2(2-\eta)e^{-p_1kh}\right]\times\\ &\quad\times\left[(2-\eta)^2 chp_1kh - 4p_1p_2 shp_1kh - 2(2-\eta)e^{-p_2kh}\right] = 0\end{aligned} \tag{5.12}$$

For the short waves approximation Eq. (5.12) is reduced to the known Rayleigh equation [9, 10, 16]:

$$(1-p_1p_2)\left[(2-\eta)^2 - 4p_1p_2\right]^2 = 0 \tag{5.13}$$

Equation (5.12) has the root $\eta = 1 (p_2 = 0)$. Eliminating this root from the equation, we obtain the equation with respect to the relative wavelength kh, defining the transition localized waves, that is the transition to the range $0 < \eta < 1$ of the allowable waves of the Rayleigh type:

$$\begin{aligned}&\left(kh - 4\sqrt{1-0}\right) sh\sqrt{1-\theta}kh - \sqrt{1-\theta}\, ch\sqrt{1-\theta}kh +\\ &\quad + 2\sqrt{1-\theta}\left(sh\sqrt{1-\theta}kh + ch\sqrt{1-\theta}kh - 1\right)e^{-\sqrt{1-\theta}kh}\\ &\quad + \sqrt{1-\theta} = 0\end{aligned} \tag{5.14}$$

Noticing, that the roots of this equation should be greater than 1, we obtain the approximate expression:

$$(kh)_* > 5\sqrt{1-\theta} \tag{5.15}$$

Thus, for these values of kh, the waves localized in the vicinity of the free surface ($y = 0$) of the layer are permissible.

6 Conclusion

The problems of wave propagation in the elastic layer are studied in the three-dimensional formulation. One of the external surfaces of the layer is considered to be free of stresses. For a second surface a number of different boundary conditions are investigated, namely Navier conditions, sliding contact conditions and clamped boundary conditions. Short- and long-wave approximations of the respective dispersion equations are analyzed. Then we formulate the conditions, under which the localization of waves in the vicinity of the free surface is possible.

References

1. Love, A.: Mathematical theory of elasticity, 676p (Russian translation). Moscow ONTI (1935)
2. Meleshko, V.V., Bondarenko, A.A., Dolgiy, S., van Heist, G.J.F.: Elastic waveguides: history and the state of the art. Pidstryhach Institute of Applied Problems of Mechanics and Mathematics. Math. Methods Phys.-Mech. Fields (L'viv) **51**(2), 86–104 (2008). (In Russian)
3. Belubekyan, V.M., Belubekyan, M.V.: Three-dimensional problem of Rayleight wave propagation. Rep. Armenian NAS **105**(4), 362–369 (2005). (In Russian)
4. Ardazishvili, R.V.: Three-dimensional surface wave for mixed boundary conditions on the surface. In: College of "Mechanics", Yerevan State University publications, pp. 74–78 (2013) (In Russian)
5. Sarkisyan, S.V.: Three-dimensional problem of waves propagation in half-space with an elastically restrained boundary. In: Proceedings of Armenian National Sc. Academy, Mechanics, vol. 70, No. 2, pp. 74–83 (2017) (In Russian)
6. Belubekyan, V.M., Mheryan, D.H.: Three-dimensional problem of the surface waves propagation in transversely isotropic elastic medium. In: Proceedings of Armenian National Sc. Academy, Mechanics, vol. 59, No. 2, pp. 3–9 (2006) (In Russian)
7. Belubekyan, M.V., Mheryan, D.H.: Three dimensional problem of surface wave propagation in elastic half-space with the properties of cube symmetry. In: Proceedings of Armenian National Sc. Academy, Mechanics, vol. 61, No. 1, pp. 23–29 (2008) (In Russian)
8. Sarkisyan, S.V., Melkonyan, A.V.: On the three-dimensional problem of Stoneley wave propagation. In: Problems of Deformable Solid Body, pp. 245–249. Institute of Mechanics of Armenian National Sc., Academy (2012) (In Russian)
9. Nowacki, W.: Theory of Elasticity, 872p (Russian translation). Mir publishers, Moscow (1975)
10. Knowles, L.K.: A note on surface waves. J. Geophys. Res. **21**(22), 5480–5481 (1966)
11. Aghalovyan, L.A., Gevorgyan, R.S.: Non classical boundary-value problems of anisotropic layered beams, Plates and Shells. In: Publishing House of the National Academy of Sciences of Armenia, 468p. Yerevan (2005) (In Russian)
12. Agalovyan, L.A.: Asymptotic Theory of Anisotropic Plates and Shells, 360p. New Jersey, Singapore (2015)
13. Belubekyan, M.V.: On the condition planar localized vibrations appearance in the vicinity of the free edge of a thin rectangular plate. Proc. YSU **51**(1), 42–45 (2017)
14. Vardanov, A.H.: Solution of a problem of natural oscillations of a finite plate with fastened base and method of Levinson. In: Proceedings of Armenian NAS, Mechanics, vol. 63, No. 4, pp. 23–30 (2010)
15. Belubekyan, M.V., Sargsyan, S.V.: Three-dimensional problem of Rayleigh waves in a half-space with restrained boundary. In: ZAMM, pp. 1623–1631 (2018)
16. Sumbatyan, M.A., Scalia, A.: Foundations of Diffraction with Applications to Mechanics and Acoustics, 328p. Fizmatlit publishers, Moscow (2013)

The Experimental Study of a Metamaterial with a Triple-Periodic Microstructure on the Epoxy Base

Vladimir M. Zotov, Vitaly V. Popuzin and Alexander E. Tarasov

Abstract We perform an experimental investigation of the acoustic properties of a metamaterial consisting of triple periodic system of metallic spheres, coated with an epoxy resin. Comparisons are given with the replacement of the wave propagation medium from an epoxy base to water and ice. Then we consider the case of aluminum specimens with holes filled with water and ice. A detailed analysis of the experimental data is performed.

1 Introduction

Many published works are devoted to the study of the filtering properties of acoustic meta-materials. A classical approach is developed in [1], where the passage of an acoustic wave through a cube consisting of steel spheres covered with a thin silicone film and coated with epoxy resin is considered. It was one of the first works in this area, where the study of this phenomenon has been carried from the purely experimental point of view. Many important properties of the metamaterials are discussed in [2–5]. It should also be noted that an efficient mathematical model for US evaluation has been proposed in [6].

Here we continue to perform some experimental research and pay a special attention to some new aspects. We evaluate how critical is the presence of the silicone shell in terms of filtering properties of this meta-material. In addition, we estimate the effect of various media which fill the holes in the meta-material—an epoxy resin, water, and ice. In the second part we use some samples from experimental Chapter "An Experimental Model of the Acoustic Wave Propagation Through a Cascading Triple-Periodic Array of Cylindrical Holes" of this book, in which the orthogonal holes were filled with analogous media.

V. M. Zotov · V. V. Popuzin (✉) · A. E. Tarasov
Southern Federal University, 105/42 Bolshaya Sadovaya Str., Rostov-on-Don
344006, Russian Federation
e-mail: popuzin@gmail.com

M. A. Sumbatyan (ed.), *Wave Dynamics, Mechanics and Physics of Microstructured Metamaterials*, Advanced Structured Materials 109,
https://doi.org/10.1007/978-3-030-17470-5_10

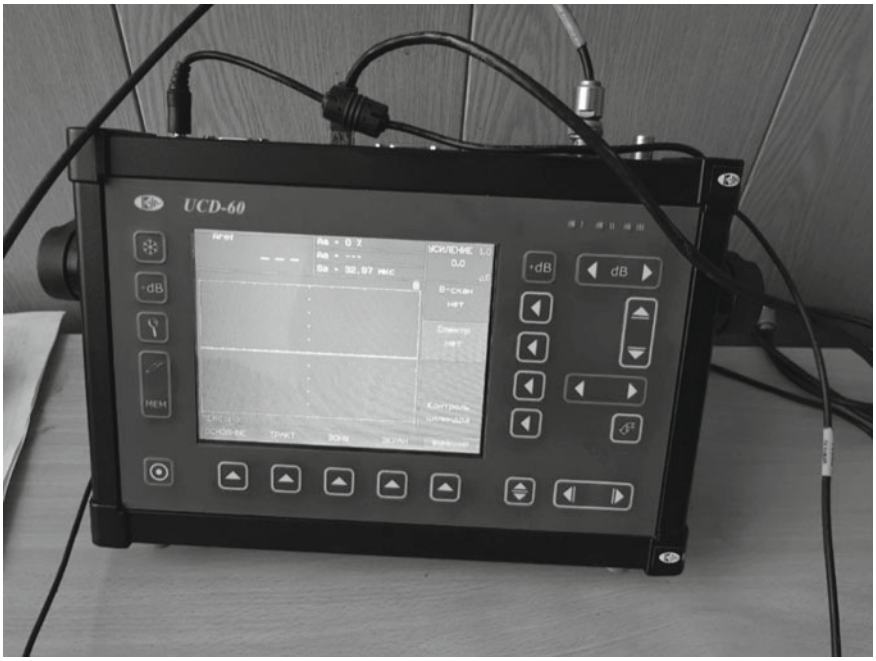

Fig. 1 Industrial ultrasonic flaw detector USD60-N

As the measuring equipment, we use the industrial ultrasonic flaw detector USD60-N (Fig. 1) with a set of sensors listed in Table 1 of Chap. 3 (Fig. 2), where we choose only the with the operating frequency low than 2.5 MHz. All measurements were carried out by the thorough-transmission method, when the radiating and the receiving sensors are located on the opposite sides of the sample.

2 Materials and Samples

A set of samples were prepared for this series of experiments. As a metamaterial with a triple periodic microstructure we use a sample which is made in the form of a cube containing 5 mm diameter metal spheres, coated with epoxy resin. The technology of making such a cube sample consist of several stages. First, we make a plexiglass box with internal dimensions $30 \times 30 \times 30$ mm. Next, we place spheres as horizontal layers of 6×6 rows into the box. Then, the spheres in the box are gradually, so that no air bubbles remain, coated with epoxy resin, after which the box is placed in a

Fig. 2 A set of low-frequency ultrasonic sensors used in the measurements

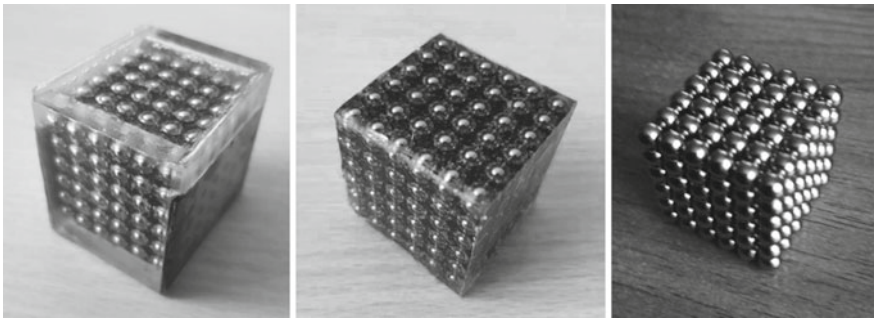

Fig. 3 Experimental samples: on the left—steel spheres coated with epoxy resin inside a Plexiglas box; in the center—the previous sample, extracted from the plastic box; on the right there is a cube of magnetized spheres

heating cabinet heated to 60 °C to polymerize the epoxy resin. After polymerization the cube of the balls in a polymerized epoxy resin is removed from the box (Fig. 3).

As a second sample we use a cube of magnetized spheres, made of an alloy of Nd–Fe–B with a chromium-nickel coating. The measurements with this sample are made in water and in ice. The measurements in water for the described cube are

carried out by an immersion method. The cube is placed in a bath of water. By using the receiving and transmitting ultrasonic sensors with connectors hermetically isolated from the water, we investigate the passage of the ultrasonic waves at different frequencies. The ultrasonic sensors are tightly sealed with a rubber sheath, preventing the liquid from the contact points of the sensor to the flaw detector. Most of the sensor part is placed inside the water tank, and the part connected to the flaw detector is located above the water. For similar measurements with ice, we use a cube frozen at −10 °C in a small bath of water, which was cut out of the bath in accordance with the 30 × 30 × 30 mm size required for measurements, and then the ultrasound studies are carried out. It should be noted that in this case a weak melting of ice creates a good contact medium for the passage of the ultrasonic pulse, and as a consequence, the use of additional lubricants typical in the ultrasonic flaw detection is not required.

For the second series of experiments, to study the acoustic properties of metamaterials with different filling of the buffer space (water, ice), we use aluminum samples with a system of holes described in Chapter "An Experimental Model of the Acoustic Wave Propagation Through a Cascading Triple-Periodic Array of Cylindrical Holes", filling their holes. The measurements of the amplitude of the transmitted ultrasonic pulse through the samples were carried out for three cases of the holes' filling: air, water, and ice. The experiments with air are described in detail in Sect. 3. The measurements in the case of water differ from those for a cubic sample of spheres. In this case, the immersion method is not used. Instead, we use a special preliminary preparation of the sample. The sample is first immersed in the water. Then it is covered with a rubber bandage over the holes, as shown in Fig. 4. After

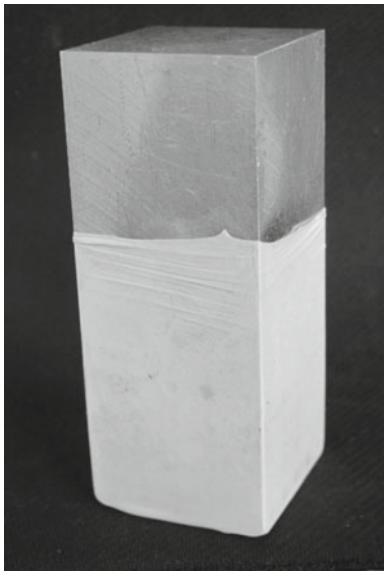

Fig. 4 Aluminum sample with a cross hole system, covered with a bandage, to keep the holes full of water and further freezing

that, the sample is removed from the water, placed on the installation desk, to perform the measurements. The preparation of the Sample, for measurements with ice, is carried out similarly to the preparation of a cubic sample of spheres. The sample with water in the holes held by a rubber bandage is frozen at −10 °C, after which the measurements are performed.

3 Results of the Experiments

Let us consider the experimental data obtained. Figure 5 presents the diagrams for the through-transmitted signal, for the cubic samples consisting of the triple periodic array of spheres with different media filling the space between these spheres. The vertical amplitude in Fig. 5 represents the difference in dB between the peak of the passed signal in the sample and the amplitude of the reference passed signal.

The diagrams demonstrate the filtering properties of the meta-material at a frequency around 1 MHz, where the minimum of the amplitude of the passed signal is clearly visible. It is curious that at a given frequency, the transverse wave length in the spheres, of which the sample is composed, is approximately equal to 5.15 mm, which is very closed to the diameter of the spheres (the velocity of the transverse waves in steel and iron is approximately 5150 m/s.). It is worth noting that in water this minimum shifts towards a higher frequency.

Also, from this graph one can notice some differences in the influence of purely acoustic (water) and elastic media on the filtering properties of the studied meta-

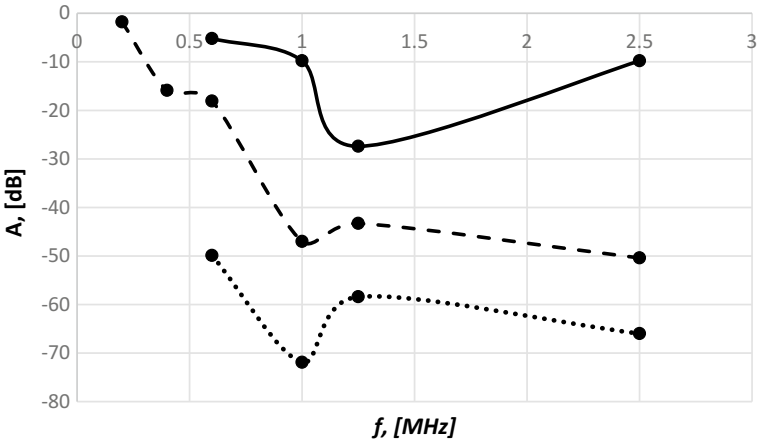

Fig. 5 The amplitude of the through-transmitted signal versus frequency: upper solid line—experiments in water by the immersion method; middle dashed line—experiments for the sample filled with epoxy resin; bottom dotted line—experiments for the sample filled with ice

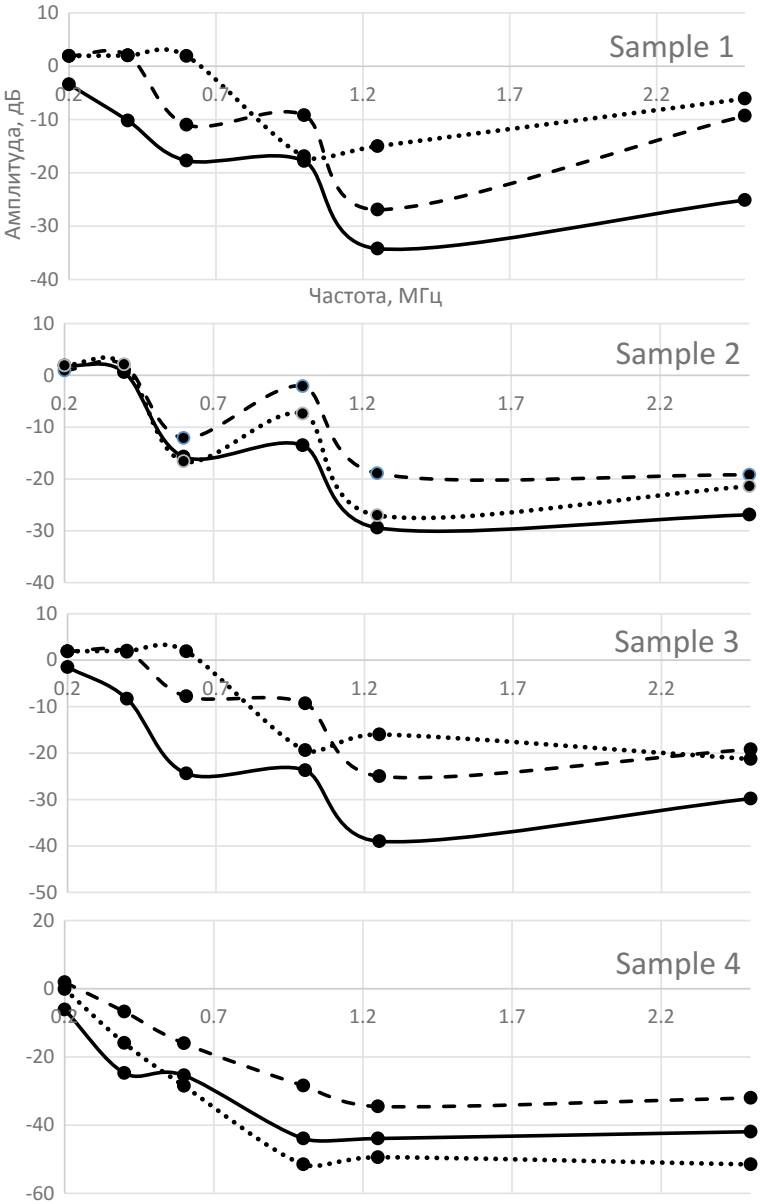

Fig. 6 Comparison of experimental results for aluminum parallelepipeds with different filling of cross holes systems. The solid line is water, the dashed line is air, the dotted line is ice

material. The main distinctive property of elastic media is the possibility of transforming longitudinal waves to transverse one and vice versa, while in purely acoustic media only longitudinal waves can propagate.

In the case of the acoustic medium, the filter band begins with a sharp decline starting from around 1 MHz, and after a minimum value of the of transmission amplitude this again tends to increase. In the case of the considered elastic media, the appearance of the filtering band becomes smoother, without a sharp jump noted in the acoustic case. Moreover, the subsequent maximum occurs rather quickly and is not so high, after which a gradual decrease in the passage of the wave follows again.

Figure 6 shows the measured results for aluminum parallelepipeds with different fillings of cross hole systems, where the vertical amplitude, as in the previous case, means the difference in dB between the peak of the passed signal in the measured sample and the amplitude of the reference passed signal. It can be seen from the diagrams that acoustic media show similar filtering properties in the entire frequency range, with the only difference that filling the holes with water reduces the amplitude of the passed signal. Ice filling behaves differently for different samples. So, in the case of the second sample, the elastic medium is between acoustic water and air,

Table 1 The maximum amplitude of the passed signal, measured in dB, and as a percent with respect to size of the display

f (MHz)	Passed signal amplitude	
	Boxed	Unboxed
2.5	−5.9 dB	−2.1 dB
1.8	12 dB	12 dB
	4%	4%
1.25	−4 dB	9.5 dB
	–	3%
0.6	32.5 dB	31.6 dB
	42%	38%
0.4	22.9 dB	35.4 dB
	14%	59%
0.2	42 dB	34.3 dB
	52%	126%
0.08-0.1	42 dB	42 dB
	126%	126%
0.06	29.2 dB	42 dB
	29%	126%
0.04	41.9 dB	41.7 dB
	125%	122%

representing the average. For the first and third samples, the change in the vertical distance between the horizontal rows of holes leads to a shift in the beginning of the first filter fall to higher frequencies, and in the remaining interval the elastic medium has better transmission characteristics almost everywhere. It is interesting that, for the fourth sample, the behavior is rather opposite, since the filling of the holes with ice leads to the smallest amplitude of the passed signal, starting from the frequency in which, for samples 1 and 3, such filling, on the contrary, improves the permeability when compared with acoustic media.

In addition, we carried out a series of measurements for a cubic sample of spheres coated with epoxy resin, before and after removal from the forming box. The obtained results are shown in Table 1. It is seen that the presence of a layer of Plexiglas affects only at a certain set of frequencies. Thus, a significant damping of the amplitude of the transmitted signal in such a case is noticeable at frequencies of 0.06, 0.2, 0.4 and 1.25 MHz.

Figure 7 represents the spectral analysis taken over a 200 μs interval. The spectral characteristics are automatically normalized by the amplitude of the signal received at the receiver, therefore these graphs should be analyzed together with Table 1. The frequencies of 0.09, 0.6 and 0.85 MHz out, as can also be seen from the envelope of the obtained spectra, shown in Fig. 8.

4 Conclusion

- When used as a component of meta-materials, elastic and acoustic media are distinguished by their influence on filtering properties. Acoustic media generally increase the transmission coefficient, while the elastic ones enhance the filtering properties.
- In the case of elastic media for a cubic experimental sample of metal spheres coated with epoxy resin, strongly expressed filtration at a frequency of 1 MHz appears. This property, in our opinion, is associated with the propagation of transverse elastic waves inside the spheres themselves, whose wavelength at a given frequency is equal to the diameter of the spheres.
- The use of an additional plexiglass interlayer between a sample of spheres coated with epoxy resin has effects only for a discrete set of selective frequencies 0.06, 0.2, 0.4 and 1.25 MHz, suppressing the transmission coefficient, with almost no change in the rest of the spectrum.

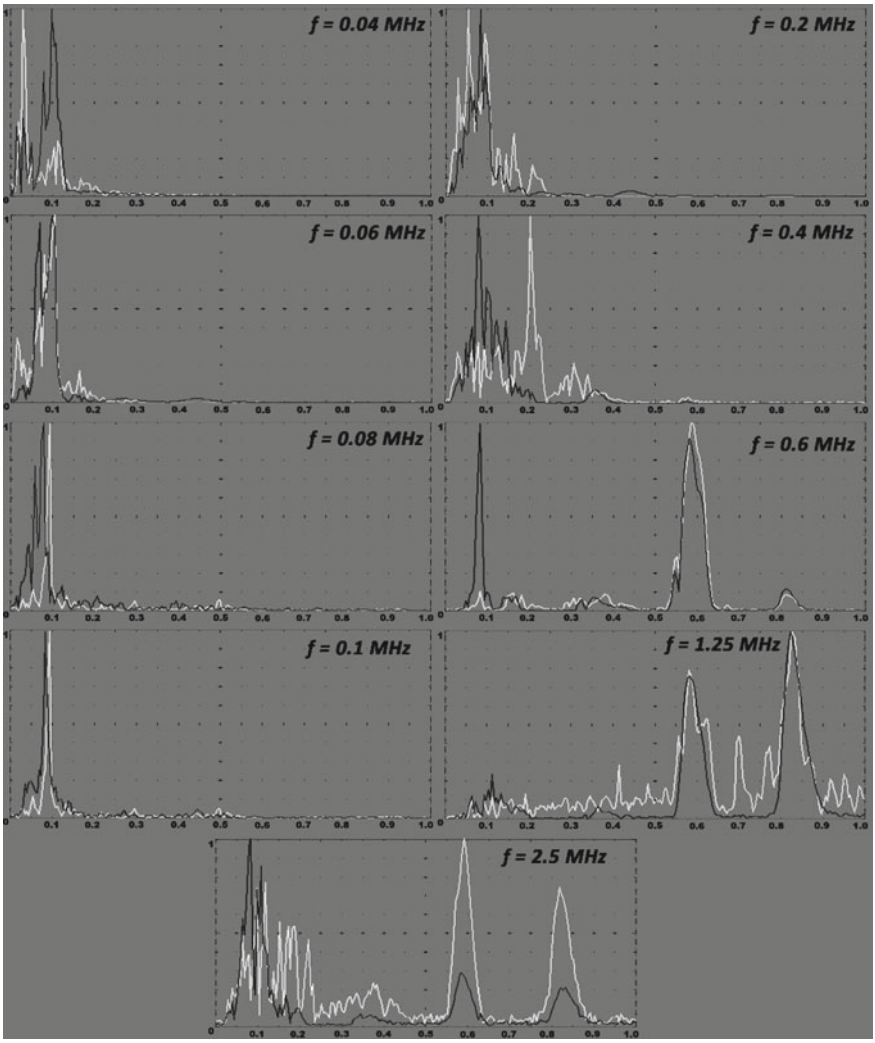

Fig. 7 Comparison of the spectra of a cubic experimental sample of metal spheres coated with epoxy, before and after extraction from a plastic box. White curves—before extraction, black—after extraction

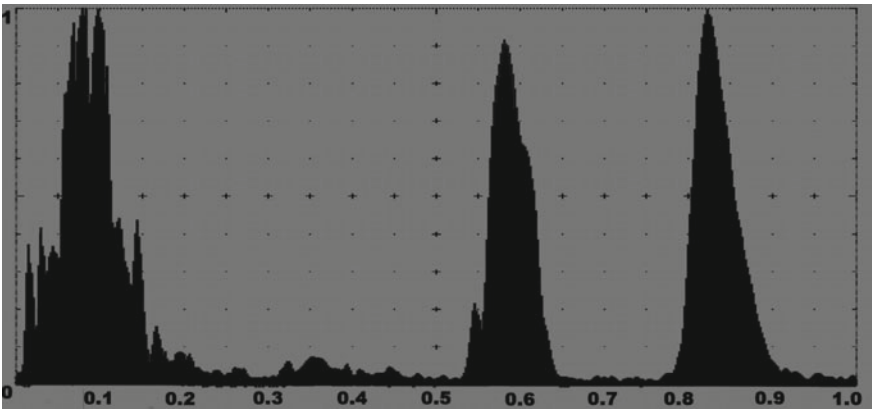

Fig. 8 The envelopes of the measured spectra of a cubic experimental sample of metallic spheres coated with epoxy resin, after being extracted from a plastic box

– Spectral analysis demonstrates obvious dominance of frequencies 0.09, 0.6 and 0.85 MHz, especially in the cases of almost complete signal damping. Most likely, these frequencies coincide with the natural vibration frequencies of the acoustic meta-material at hand.

Acknowledgements The work is performed within the framework of the Project № 15-19-10008-P of the Russian Science Foundation (RSCF).

References

1. Liu, Z., Zhang, X., Mao, Y., et al.: Locally resonant sonic materials. Science **289**, 1734–1736 (2000)
2. Achenbach, J.D., Kitahara, M.: Harmonic waves in a solid with a periodic distribution of spherical cavities. J. Acoust. Soc. Amer. **81**, 595–598 (1987)
3. Deymier, P.A.: Acoustic Metamaterials and Phononic Crystals. Springer, Berlin (2013)
4. Guenneau, S., Craster, R.V.: Acoustic Metamaterials: Negative Refraction, Imaging, Lensing and Cloaking. Springer, The Netherlands (2013)
5. Banerjee, B.: An Introduction to Metamaterials and Waves in Composites. CRC Press, Taylor & Francis Group, Boca Raton, FL (2011)
6. Scalia, A., Sumbatyan, M.A.: On efficient quantitative analysis in real-time ultrasonic detection of cracks. Ultrasonics **37**, 239–245 (1999)

On the Equations of the Surface Elasticity Model Based on the Theory of Polymeric Brushes

Roman A. Gerasimov, Tatiana O. Petrova, Victor A. Eremeyev, Andrei V. Maximov and Olga G. Maximova

Abstract Motivating by theory of polymers, in particular, by the models of polymeric brushes we present here the homogenized (continual) two-dimensional (2D) model of surface elasticity. A polymeric brush consists of an system of almost aligned rigid polymeric chains. The interaction between chain links are described through Stockmayer potential, which take into account also dipole-dipole interactions. The presented 2D model can be treated as an highly anisotropic 2D strain gradient elasticity. The surface strain energy contains both first and second derivatives of the surface field of displacements. So it represents an intermediate class of 2D models of the surface elasticity such as Gurtin-Murdoch and Steigmann-Ogden ones.

R. A. Gerasimov · T. O. Petrova · V. A. Eremeyev
Southern Federal University, Milchakova str. 8a, 344090 Rostov on Don, Russia
e-mail: roman-gerasimoff@yandex.ru

T. O. Petrova
e-mail: to_87@bk.ru

V. A. Eremeyev
Faculty of Civil Environmental Engineering, Gdańsk University of Technology, ul. Gabriela Narutowicza 11/12, 80-233 Gdańsk, Poland

V. A. Eremeyev (✉)
Southern Scientific Center of RASci, Chekhova str. 41, 344006 Rostov on Don, Russia
e-mail: eremeyev.victor@gmail.com; victor.eremeev@pg.edu.pl,

A. V. Maximov · O. G. Maximova
Cherepovets State University, 5 Lunacharskii Av, 162600 Cherepovets, Russia
e-mail: a_v_maximov@mail.ru

O. G. Maximova
e-mail: og62@mail.ru

M. A. Sumbatyan (ed.), *Wave Dynamics, Mechanics and Physics of Microstructured Metamaterials*, Advanced Structured Materials 109,
https://doi.org/10.1007/978-3-030-17470-5_11

1 Introduction

Nowadays the applications of the continuum mechanics and mechanics of structures to modelling of some physical phenomena at the nanoscale became very common, see, e.g., [2, 11, 22, 33]. Among the approaches used for nano-structured materials it is worth to note the surface elasticity and strain gradient elasticity. In particular, the model by Gurtin and Murdoch [26, 27] and by Steigmann and Ogden [37, 38] found various application in the nanomechanics, see, e.g., [11, 12, 28, 30, 31, 35, 45, 46] and the reference therein.

The basic idea of the surface elasticity stands on introduction of two independent systems of constitutive equations for the bulk and for its boundary. From the physical point of view these models correspond to the presence of a solid body an elastic membrane or an elastic shell, which constitutive equations should be introduced in addition to ones in the bulk. Obviously, presence of such kind of boundary reinforcements may results in significant changes of effective properties of materials at the nanoscale.

Here we introduce a model of surface elasticity based on a certain heuristic homogenization of so-called polymeric brush coatings, see, e.g., [6, 7, 9, 21]. These coatings consist of a system long polymeric chains. At the molecular level the interactions between chain links is described by Stockmayer potential, see [39]. Some recent results related to the polymeric brushes modelling are presented by Gerasimov et al. [23–25], Petrova et al. [36].

The interest to modelling of coatings made polymeric brushes relates to recent developments in superhydrophobic and superoleophobic surfaces used for manufacturing of so-called self-cleaning and bactericide coatings, see the references in the reviews by Eremeyev [12, 14].

The paper is organized as follows. In Sect. 2 we briefly recall the basic elements of the polymeric brush discrete structure and used interaction potential. Then in Sect. 3 we introduce the continuum 2D model related to the discrete one. For simplicity here we consider infinitesimal deformations. Finally, with the Lagrange principle we derive the equilibrium equations and the corresponding natural boundary conditions.

2 Polymeric Brush and Its Mechanical Interpretation

We consider a polymeric brush as a system of almost aligned rigid chains. Each chain consists of many links elastically connected to each other, see Fig. 1. There is an interaction between chains. Following [39] the energy of interactions depends on the changes in mean distances between neighbour links and in their relative orientation. We denote $r^j_{i-1,i}$ the mean distance between neighbour jth links in $(i-1)$th and ith chains. In order to describe the orientation we attach to each link a trihedron of unit

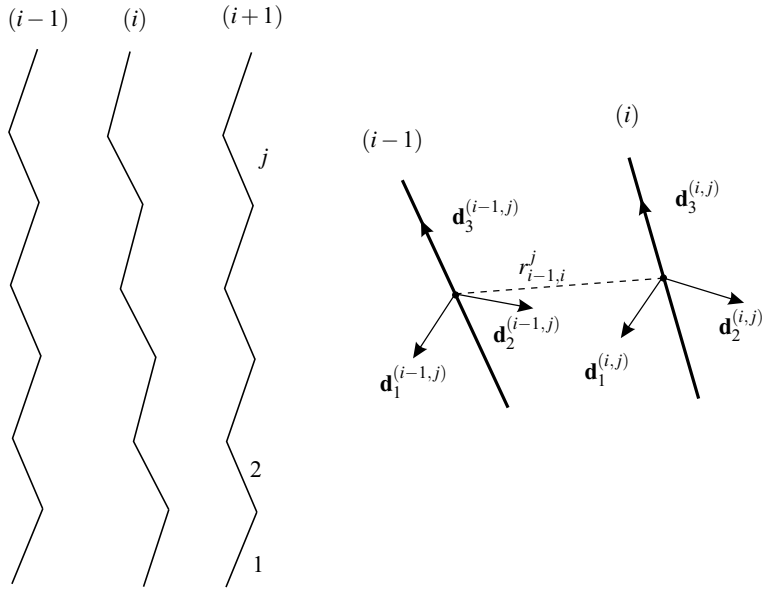

Fig. 1 Schematic structure of a polymeric brush and the kinematics of two links

vectors $\mathbf{d}_k$ called directors. Hereinafter we use the coordinate-free (direct) tensor calculus as described in [19, 32, 34], so for vectors and tensors we use the bold font shape. For jth link of ith chain we introduce three vectors $\mathbf{d}_k^{(i,j)}$, $k = 1, 2, 3$, $\mathbf{d}_k^{(i,j)} \cdot \mathbf{d}_m^{(i,j)} = \delta_{mn}$, δ_{mn} is the Kronecker symbol, and the centered dot denotes the scalar product. For simplicity we assume that $\mathbf{d}_3^{(i,j)}$ is tangent to the corresponding link.

As a result, the energy of the polymeric brush can be introduced as a sum of terms

$$U_{ij} = U_{ij}(r^j_{i-1,i}, \{\mathbf{d}_k^{(i-1,j)}\}, \{\mathbf{d}_k^{(i,j)}\}).$$

For detailed description we refer here to [23–25, 36].

From the mechanical point of view the described above approach is quite similar to so-called Hencky model for an elastic beam, see original work by Hencky [29] and recent papers by Turco et al. [40–43], Wang et al. [44], Zhang et al. [47]. So in what follows we consider continual beam-lattice model for chains.

In this paper we consider coatings made of one layer of ordered chains attached parallel to a surface, as shown in Fig. 2. From the physical point of view this assumption corresponds to highly anisotropic coating with one preferred direction along the chains.

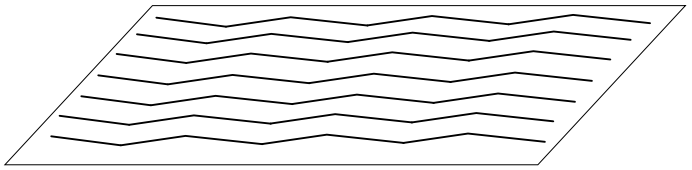

Fig. 2 Polymeric brush which is parallel to a surface

3 Surface Energy of a Beam-Lattice-Type Coating

Here we convert the discrete model discussed above into a continual one. To this end let as consider an elastic solid body which occupies volume v with the boundary ∂v. In what follows we consider infinitesimal deformations, so it is no need to distinguish reference and current placements. On the part S of the boundary a polymeric coating is perfectly attached. It consists of almost aligned elastic beams, see Fig. 3. Each beam is perfectly connected to the surface. As beams are assumed to be very thin we neglect their torsional energy during deformations. On the other hand we consider their stretching/shrinking and bending together with the deformation of the material in the bulk. Following [5, 8], for each beam we introduce directors $\mathbf{d}_k^{(i)}$, $k = 1, 2, 3$, in such way that $\mathbf{d}_3^{(i)}$ coincides with the tangent vector $\boldsymbol{\tau}$ to the curve associated with the ith beam, $\mathbf{d}_1^{(i)} = \mathbf{n}$, where $\mathbf{n}$ is the unit normal to S, and $\mathbf{d}_2^{(i)} = \mathbf{d}_3^{(i)} \times \mathbf{d}_1^{(i)}$, "$\times$" stands for the cross product. We also introduce the surface orthogonal coordinates s_1 and s_2 on S such that s_1 is the arc-length parameter, and it is directed along beams. So $\mathbf{d}_3^{(i)}$ and $\mathbf{d}_2^{(i)}$ are the tangent vector to s_1- and s_2-curves, respectively.

Let us introduce the surface displacement field as a vector-function of the surface coordinate

$$\mathbf{u} = \mathbf{u}(s_1, s_2). \tag{1}$$

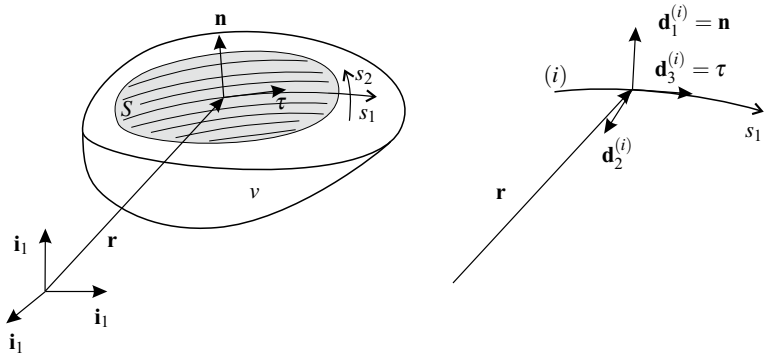

Fig. 3 Polymeric brush which is parallel to a surface

We represent $\mathbf{u}$ in the natural basis $\{\mathbf{d}_k\}$ as follows

$$\mathbf{u} = u_1\mathbf{d}_1 + u_2\mathbf{d}_2 + u_3\mathbf{d}_3. \tag{2}$$

Hereinafter for simplicity we omit the superscript "(i)". With Euler–Bernoulli kinematics we can represent the strain energy density of a beam as a quadratic form

$$\mathscr{U}_b = \frac{1}{2}\mathbb{K}_s u_{3,1}^2 + \frac{1}{2}\mathbb{K}_{b\parallel} u_{2,11}^2 + \frac{1}{2}\mathbb{K}_{b\perp} u_{1,11}^2, \tag{3}$$

where $\mathbb{K}_s$ is the tangent stiffness, $\mathbb{K}_{b\parallel}$ and $\mathbb{K}_{b\perp}$ are bending stiffness parameters of the beam. For brevity we used the following notations for derivatives

$$(\ldots)_{,1} = \frac{\partial}{\partial s_1}(\ldots), \quad (\ldots)_{,2} = \frac{\partial}{\partial s_2}(\ldots), \quad (\ldots)_{,11} = \frac{\partial^2}{\partial s_1^2}(\ldots), \quad \text{etc.}$$

Let us note that (3) is the simplest example of the quadratic strain energy used in the beam theory.

Having in mind that polymeric chains interact to each other, we also introduce the interaction energy again as a quadratic function

$$\mathscr{U}_i = \frac{1}{2}\mathbb{K}_t u_{2,2}^2 + \frac{1}{2}\mathbb{K}_r \left[u_{2,12}^2 + u_{1,12}^2\right], \tag{4}$$

with stiffness parameters $\mathbb{K}_t$ and $\mathbb{K}_r$ which are responsible for resistance with respect to changes of mean distance between chains in s_2-directions and to relative rotations of chains, respectively.

As a result, we introduce the surface strain energy density expressed in surface coordinates

$$\mathscr{U} = \frac{1}{2}\mathbb{K}_s u_{3,1}^2 + \frac{1}{2}\mathbb{K}_{b\parallel} u_{2,11}^2 + \frac{1}{2}\mathbb{K}_{b\perp} u_{1,11}^2 + \frac{1}{2}\mathbb{K}_t u_{2,2}^2 + \frac{1}{2}\mathbb{K}_r \left[u_{2,12}^2 + u_{1,12}^2\right]. \tag{5}$$

Note that all introduced stiffness parameters are assumed to be positive, so the surface energy is positive too. Nevertheless, it is obvious that $\mathscr{U}$ is highly non-symmetric with respect to its arguments. In the other words $\mathscr{U}$ does not contain the complete of the displacements derivatives. So by analogy with other models, see [16], we can call it reduced or degenerated surface energy. As $\mathscr{U}$ contains second derivatives as in the Steigmann–Ogden model, we can also call this model *the reduced surface strain gradient elasticity*. The further mathematical analysis of the model can be performed as in [3, 4, 17, 18, 20].

4 Equilibrium Conditions

In order to get the equilibrium conditions we apply the variational approach. We derive the latter and the static boundary conditions as a result of the variational equation

$$\delta \mathscr{L} = 0, \tag{6}$$

where the Lagrange functional is defined as

$$\mathscr{L} = \int_v \mathscr{W}\, \mathrm{d}v + \int_S \mathscr{U}\, \mathrm{d}a, \tag{7}$$

and $\mathscr{W}$ is the strain energy in the bulk. It is given by

$$\mathscr{W} = \mathscr{W}(\mathbf{e}), \quad \mathbf{e} = \mathbf{e}(\mathbf{u}) = \frac{1}{2}(\nabla \mathbf{u} + \nabla \mathbf{u}^T), \tag{8}$$

where ∇ is the 3D nabla-operator. Note that here for simplicity we omitted an external loading. We define the stress tensor by the formula

$$\boldsymbol{\sigma} = \frac{\partial \mathscr{W}}{\partial \mathbf{e}}.$$

Following standard technique of the calculus of variations from (6) we get the equilibrium equation in v

$$\nabla \cdot \boldsymbol{\sigma} = \mathbf{0}. \tag{9}$$

For the derivation of the natural boundary conditions from (6) more efforts are required. Let us for simplicity neglect of a curvature of S. In the other words we assume that S is a part of a plane. In this case s_1 and s_2 are usual Cartesian coordinates and $\mathbf{d}_k$ are constants. In particular, $\mathbf{n} = \mathbf{d}_1$ and the stress vector $\mathbf{n} \cdot \boldsymbol{\sigma}$ has the form

$$\mathbf{n} \cdot \boldsymbol{\sigma} = \sigma_{11}\mathbf{d}_1 + \sigma_{12}\mathbf{d}_2 + \sigma_{13}\mathbf{d}_3.$$

Omitting derivation details after integration by parts we get

$$\sigma_{11} = -\mathbb{K}_{b\perp} u_{1,1111} - \mathbb{K}_r u_{1,1212}, \tag{10}$$

$$\sigma_{12} = \mathbb{K}_t u_{2,22} - \mathbb{K}_{b\parallel} u_{2,1111} + \mathbb{K}_r u_{2,1212}, \tag{11}$$

$$\sigma_{13} = \mathbb{K}_s u_{3,11}. \tag{12}$$

Boundary conditions (10)–(12) present various types of an elastic support. In particular, (12) corresponds to Ventcel-type of boundary conditions, whereas (10) and (11) are more general. Let us underline that here the differential order of the boundary conditions essentially depends on the preferred direction. In the considered case it is $\mathbf{d}_3$-direction, that is along chains.

5 Conclusions

Motivating by the structure of polymeric brushes we proposed the new model elasticity under small deformations. Within the model we introduced the surface strain energy as a function of a certain set of first and second derivatives of the surface displacements. Considering it as model of 2D material we have to conclude that the corresponding material is highly anisotropic. It constitutes an intermediate class between classic elasticity and strain gradient elasticity. Here we are restricted ourselves by a plane surface with coating. The analysis of the curved surface will be presented in forthcoming papers as well as natural conditions at edges ∂S and at corner points with the use of the technique presented by Abali et al. [1], dell'Isola and Seppecher [10], Eremeyev [13–15], Eremeyev et al. [20], Zemlyanova and Mogilevskaya [46].

Acknowledgements The author acknowledges financial support from the Russian Science Foundation under the grant "*Methods of microstructural nonlinear analysis, wave dynamics and mechanics of composites for research and design of modern metamaterials and elements of structures made on its base*" (No. 15-19-10008-P).

References

1. Abali, B.E., Müller, W.H., dell'Isola, F.: Theory and computation of higher gradient elasticity theories based on action principles. Arch. Appl. Mech. **87**(9), 1495–1510 (2017)
2. Aifantis, E.C.: Gradient deformation models at nano, micro, and macro scales. J. Eng. Mater. Technol. **121**(2), 189–202 (1999)
3. Altenbach, H., Eremeyev, V.A., Lebedev, L.P.: On the existence of solution in the linear elasticity with surface stresses. ZAMM **90**(3), 231–240 (2010)
4. Altenbach, H., Eremeyev, V.A., Lebedev, L.P.: On the spectrum and stiffness of an elastic body with surface stresses. ZAMM **91**(9), 699–710 (2011)
5. Altenbach, H., Bîrsan, M., Eremeyev, V.A.: Cosserat-type rods. In: Altenbach H, Eremeyev VA (eds) Generalized Continua from the Theory to Engineering Applications, CISM International Centre for Mechanical Sciences (Courses and Lectures), vol. 541, Springer, Vienna, pp 179–248 (2013). https://doi.org/10.1007/978-3-7091-1371-4_4
6. Azzaroni, O.: Polymer brushes here, there, and everywhere: recent advances in their practical applications and emerging opportunities in multiple research fields. J. Polym. Sci. Part A: Polym. Chem. **50**(16), 3225–3258 (2012)
7. Azzaroni, O., Szleifer, I. (eds.).: Polymer and Biopolymer Brushes: for Materials Science and Biotechnology. Wiley, Hoboken (2018)
8. Bîrsan, M., Altenbach, H., Sadowski, T., Eremeyev, V.A., Pietras, D.: Deformation analysis of functionally graded beams by the direct approach. Compos. Part B: Eng. **43**(3), 1315–1328 (2012)
9. Brittain, W.J., Minko, S.: A structural definition of polymer brushes. J. Polym. Sci. Part A: Polym. Chem. **45**(16), 3505–3512 (2007)
10. dell'Isola, F., Seppecher, P.: Edge contact forces and quasi-balanced power. Meccanica **32**(1), 33–52 (1997)
11. Duan, H.L., Wang, J., Karihaloo, B.L.: Theory of elasticity at the nanoscale. In: Advances in Applied Mechanics, vol 42, pp. 1–68. Elsevier (2008)

12. Eremeyev, V.A.: On effective properties of materials at the nano-and microscales considering surface effects. Acta Mech. **227**(1), 29–42 (2016a)
13. Eremeyev, V.A.: On equilibrium of a second-gradient fluid near edges and corner points. In: Naumenko, K., Aßmus, M. (eds.) Advanced Methods of Continuum Mechanics for Materials and Structures, Advanced Structured Materials, vol. 60, pp. 547–556. Springer, Singapore (2016b)
14. Eremeyev, V.A.: On the effective properties of elastic materials and structures at the micro- and nano-scale considering various models of surface elasticity. In: Trovalusci, P. (ed.) Materials with Internal Structure: Multiscale and Multifield Modeling and Simulation, pp. 29–41. Springer, Cham (2016c). https://doi.org/10.1007/978-3-319-21494-8_3
15. Eremeyev, V.A.: On dynamic boundary conditions within the linear Steigmann–Ogden model of surface elasticity and strain gradient elasticity. In: Altenbach, H., Belyaev, A., Eremeyev, V.A., Krivtsov, A., Porubov, A.V. (eds.) Dynamical Processes in Generalized Continua and Structures, Advanced Structured Materials, vol. 103, pp 195–207. Springer, Cham (2019). https://doi.org/10.1007/978-3-030-11665-1_10
16. Eremeyev, V.A., dell'Isola, F.: A note on reduced strain gradient elasticity. In: Altenbach, H., Pouget, J., Rousseau, M., Collet, B., Michelitsch, T. (eds.) Generalized Models and Non-classical Approaches in Complex Materials 1, pp. 301–310. Springer International Publishing, Cham (2018)
17. Eremeyev, V.A., Lebedev, L.P.: Existence of weak solutions in elasticity. Math. Mech. Solids **18**(2), 204–217 (2013)
18. Eremeyev, V.A., Lebedev, L.P.: Mathematical study of boundary-value problems within the framework of Steigmann-Ogden model of surface elasticity. Continuum Mech. Thermodyn. **28**(1–2), 407–422 (2016)
19. Eremeyev, V.A., Cloud, M.J., Lebedev, L.P.: Applications of Tensor Analysis in Continuum Mechanics. World Scientific, New Jersey (2018a)
20. Eremeyev, V.A., dell'Isola, F., Boutin, C., Steigmann, D.: Linear pantographic sheets: existence and uniqueness of weak solutions. J. Elast. **132**, 175–196 (2018b). https://doi.org/10.1007/s10659-017-9660-3
21. Feng, C., Huang, X.: Polymer brushes: efficient synthesis and applications. Acc. Chem. Res. **51**(9), 2314–2323 (2018). https://doi.org/10.1021/acs.accounts.8b00307, pMID: 30137964
22. Forest, S., Cordero, N.M., Busso, E.P.: First vs. second gradient of strain theory for capillarity effects in an elastic fluid at small length scales. Comput. Mater. Sci. **50**(4), 1299–1304 (2011)
23. Gerasimov, R.A., Eremeyev, V.A., Petrova, T.O., Egorov, V.I., Maksimova, O.G., Maksimov, A.V.: Computer simulation of the mechanical properties of metamaterials. J. Phys. Conf. Ser. **738**(1), 012100 (2016)
24. Gerasimov, R.A., Eremeyev, V.A., Petrova, T.O., Egorov, V.I., Maksimova, O.G., Maksimov, A.V.: Study of mechanical properties of ferroelectrics metamaterials using computer simulation. Ferroelectrics **508**(1), 151–160 (2017a)
25. Gerasimov, R.A., Maksimova, O.G., Petrova, T.O., Eremeyev, V.A., Maksimov, A.V.: Analytical and computer methods to evaluate mechanical properties of the metamaterials based on various models of polymeric chains. In: Wave Dynamics and Composite Mechanics for Microstructured Materials and Metamaterials, pp. 35–69. Springer (2017b)
26. Gurtin, M.E., Murdoch, A.I.: A continuum theory of elastic material surfaces. Arch. Ration Mech. An **57**(4), 291–323 (1975)
27. Gurtin, M.E., Murdoch, A.I.: Surface stress in solids. Int. J. Sol. Struct. **14**(6), 431–440 (1978)
28. Han, Z., Mogilevskaya, S.G., Schillinger, D.: Local fields and overall transverse properties of unidirectional composite materials with multiple nanofibers and Steigmann-Ogden interfaces. Int. J. Solids Struct. **147**, 166–182 (2018)
29. Hencky, H.: Über die angenäherte Lösung von Stabilitätsproblemen im Raum mittels der elastischen Gelenkkette. der Esienbau **11**, 437–452 (1920)
30. Javili, A., dell'Isola, F., Steinmann, P.: Geometrically nonlinear higher-gradient elasticity with energetic boundaries. J. Mech. Phys. Solids **61**(12), 2381–2401 (2013a)

31. Javili, A., McBride, A., Steinmann, P.: Thermomechanics of solids with lower-dimensional energetics: on the importance of surface, interface, and curve structures at the nanoscale. a unifying review. Appl. Mech. Rev. **65**(1), 010802 (2013b)
32. Lebedev, L.P., Cloud, M.J., Eremeyev, V.A.: Tensor Analysis with Applications in Mechanics. World Scientific, New Jersey (2010)
33. Liebold, C., Müller, W.H.: Are microcontinuum field theories of elasticity amenable to experiments? A review of some recent results. In: Differential Geometry and Continuum Mechanics, pp. 255–278. Springer (2015)
34. Lurie, A.I.: Nonlinear Theory of Elasticity. North-Holland, Amsterdam (1990)
35. Nazarenko, L., Stolarski, H., Altenbach, H.: Effective properties of short-fiber composites with gurtin-murdoch model of interphase. Int. J. Solids Struct. **97**, 75–88 (2016)
36. Petrova, T., Maksimova, O., Gerasimov, R., Maksimov, A.: Application of analytical and numerical methods to simulation of systems with orientation interactions. Phys. Solid State **54**(5), 937–939 (2012)
37. Steigmann, D.J., Ogden, R.W.: Plane deformations of elastic solids with intrinsic boundary elasticity. Proc. R. Soc. A **453**(1959), 853–877 (1997)
38. Steigmann, D.J., Ogden, R.W.: Elastic surface-substrate interactions. Proc. R. Soc. A **455**(1982), 437–474 (1999)
39. Stockmayer, W.H.: Theory of molecular size distribution and gel formation in branched-chain polymers. J. Chem. Phys. **11**(2), 45–55 (1943)
40. Turco, E.: Discrete is it enough? The revival of Piola-Hencky keynotes to analyze three-dimensional Elastica. Continuum Mech. Thermodyn. **30**(5), 1039–1057 (2018)
41. Turco, E., dell'Isola, F., Cazzani, A., Rizzi, N.L.: Hencky-type discrete model for pantographic structures: numerical comparison with second gradient continuum models. Z. für angew. Math. und Phys. **67**(4), 85 (2016)
42. Turco, E., Golaszewski, M., Giorgio, I., Placidi, L.: Can a hencky-type model predict the mechanical behaviour of pantographic lattices? In: Mathematical Modelling in Solid Mechanics, pp. 285–311. Springer (2017)
43. Turco, E., Misra, A., Pawlikowski, M., dell'Isola, F., Hild, F.: Enhanced Piola–Hencky discrete models for pantographic sheets with pivots without deformation energy: numerics and experiments. Int. J. Solids Struct. (2018)
44. Wang, C.M., Zhang, H., Gao, R.P., Duan, W.H., Challamel, N.: Hencky bar-chain model for buckling and vibration of beams with elastic end restraints. Int. J. Struct. Stab. Dyn. **15**(07), 1540,007 (2015)
45. Wang, J., Huang, Z., Duan, H., Yu, S., Feng, X., Wang, G., Zhang, W., Wang, T.: Surface stress effect in mechanics of nanostructured materials. Acta Mech. Solida Sin. **24**, 52–82 (2011)
46. Zemlyanova, A.Y., Mogilevskaya, S.G.: Circular inhomogeneity with Steigmann-Ogden interface: Local fields, neutrality, and Maxwell's type approximation formula. Int. J. Solids Struct. **135**, 85–98 (2018)
47. Zhang, H., Wang, C., Ruocco, E., Challamel, N.: Hencky bar-chain model for buckling and vibration analyses of non-uniform beams on variable elastic foundation. Eng. Struct. **126**, 252–263 (2016)

Finite Element Study of Ceramic Matrix Piezocomposites with Mechanical Interface Properties by the Effective Moduli Method with Different Types of Boundary Conditions

G. Iovane and A. V. Nasedkin

Abstract The paper deals with the problem of finding the effective moduli of a ceramic matrix composite with surface stresses on the interphase boundaries. The composite consists of a PZT ceramic matrix, elastic inclusions and interface boundaries. It is assumed that the interface stresses depend on the surface strains according to the Gurtin–Murdoch model. This model describes the size effects and contributes to the total stress-strain state only for nanodimensional inclusions. The homogenization problem was set and solved with the help of the effective moduli method for piezoelectric composites with interface boundaries and finite-element technologies used for simulating the representative volumes and solving the resulting boundary-value electroelastic problems. Here in the effective moduli method, different combinations of linear first-kind boundary conditions and constant second-kind boundary conditions for mechanical and electric fields were considered. The representative volume consisted of cubic finite elements with the material properties of the matrix or inclusions and also included the surface elements on the interfaces. Bulk elements were supplied with the material properties of the matrix or inclusions, using a simple random method. In the numerical example, the influence of the fraction of inclusions, the interface stresses and boundary conditions on the effective electroelastic modules were analysed.

G. Iovane
Department of Computer Science, University of Salerno, 84084 Fisciano, SA, Italy
e-mail: giovane@unisa.it

A. V. Nasedkin (✉)
Institute of Mathematics, Mechanics and Computer Science, Southern Federal University, Milchakova Street 8a, Rostov-on-Don 344090, Russia
e-mail: nasedkin@math.sfedu.ru

M. A. Sumbatyan (ed.), *Wave Dynamics, Mechanics and Physics of Microstructured Metamaterials*, Advanced Structured Materials 109,
https://doi.org/10.1007/978-3-030-17470-5_12

1 Introduction

Composite materials on the base of PZT ceramics are widely used for the production of practically feasible devices for hydroacoustics, medical diagnostics and ultrasound, level and flow measurement, aerospace and automotive industries. From the analysis of piezoelectric materials it is known that their physical properties remain to be the essential limiting factor in the development of the most effective new piezoelectric transducers. A lot of nanostructured PZT composite materials, which were developed recently, demonstrate a range of significant advanced features, such as the possibilities of controllable modification of the functional characteristics, the ultra-low Q-factor, and other.

Furthermore, it is important to note that the simulation of micro- and nanosructured composite materials has some specific features. As it is known, the nanomaterials have unconventional physical properties that significantly differ from the characteristics of the bodies with usual sizes. For example, the known experimental fact is that the stiffness increases with the reduction of the nanoobject sizes. The surface effect may be one of the factors explaining this behavior. Numerous studies conducted in the recent years have shown that the surface stresses are important for micro- and nanoscale bodies. In connection to this, an interesting problem to consider is to extend this approach to the nanostructured piezoelectric composite materials [4, 10, 16, 29, 30, 33–35, 37], etc. For piezoelectric nanobodies it is possible to consider not only surface mechanical stresses, but also surface electric fields [9, 22]. Piezoelectric and magnetoelectric nanosized materials with surface or imperfect interface effects were investigated in [4, 9, 11, 13–15, 29], etc. Thus, in [36], using the self-consistent method, an effective shear modulus for a fiber reinforced piezocomposite was found. Theoretical studies of the homogenization problems for nanoscale piezoelectric composites were carried out in [3, 12, 21, 22, 35], etc.

In this paper, we use the homogenization models for two-phase piezoelectric composites, which were previously developed in the framework of the effective moduli method for piezoelectric composites of usual sizes [1, 27, 28]. We use these models to build more complicated models for nanoscale PZT composites, which additionally take into account interface mechanical boundary conditions.

We consider four static piezoelectric problems in a representative volume element (RVE) that allow us to determine the full set of the effective moduli. These problems differ from each other by the boundary conditions, which are set on external surfaces of RVE as follows: (i) mechanical displacements and electric potential ($u\varphi$-problem), (ii) mechanical stress vector and electric potential ($p\varphi$-problem), (iii) mechanical displacements and normal component of electric displacement vector (uD-problem), and (iv) mechanical stress vector and normal component of electric displacement vector (uD-problem). For each type of these boundary-value problems we provide the respective formulae for the effective moduli calculation for transversely isotropic piezoelectric composites.

We use an integrated approach to the determination of the effective moduli of nanostructured piezoelectric ceramic matrix composites with stochastic distribution

of inclusions. In order to take into account nanoscale level at the borders between material and inclusions, we use the Gurtin–Murdoch model of surface or interface stresses. To simulate the RVE and to calculate the effective moduli, we use ANSYS finite element package. This approach is based on the theory of effective moduli for composite mechanics, the simulation of the RVE and the finite element method. We adopt that the contact boundaries between material and inclusions are covered by the membrane elements in order to take the interface stresses into account.

As an example, we give and analyse the results of numerical computations for a ceramic matrix composite with various values of interface moduli and percentage of inclusions, and different types of boundary conditions.

2 Formulation of Homogenization Problems

Let V be a representative volume element (RVE) of the ceramic matrix material, which we will consider as a two-phase composite. We will assume that the first phase is a piezoceramic material, and the second phase consists of a set of elastic inclusions. We denote the regions occupied by the phases with the numbers $j = 1, 2$ as $V^{(j)}$. Let $S = \partial V$ be the outer boundary of the RVE, $S^i = \partial V^{(1)} \cap \partial V^{(2)}$ is the set of contact boundaries between materials with different phases, i.e. the interface boundaries; x_m are the Cartesian coordinates, $m = 1, 2, 3$; n_m are the components of the vector of unit normal, external or relative to the volume of V (on S), or external to the volume of the material of the primary phase $V^{(1)}$ (on S^i).

In the volume V we will consider the static problem of electroelasticity with respect to the components $u_k = u_k(x_m)$ of the displacement vector and the electric potential $\varphi = \varphi(x_m)$. In contrast to an ordinary electroelastic problem, here we suppose that at the interface boundary there are the interface (surface) stresses that depend only on the interface (surface) strains according to the Gurtin–Murdoch model. Thus, in the volume V we assume that the equations of the electroelasticity theory are satisfied

$$\sigma_{km,m} = 0, \quad D_{k,k} = 0, \quad \mathbf{x} \in V\,, \tag{1}$$

$$T_\alpha = c^E_{\alpha\zeta} S_\zeta - e_{m\alpha} E_m, \quad D_k = e_{k\zeta} S_\zeta + \varepsilon^S_{km} E_m\,, \tag{2}$$

$$\varepsilon_{km} = (\partial_m u_k + \partial_k u_m)/2, \quad E_k = -\varphi_k\,, \tag{3}$$

where, hereinafter, the Latin indices k and m can vary from 1 to 3, and the Greek indices α and ζ can vary from 1 to 6; the summation over repeated indices is assumed; $T_1 = \sigma_{11}, T_2 = \sigma_{22}, T_3 = \sigma_{33}, T_4 = \sigma_{23}, T_5 = \sigma_{13}, T_6 = \sigma_{12}$; σ_{km} are the components of the stress tensor; $S_1 = \varepsilon_{11}, S_2 = \varepsilon_{22}, S_3 = \varepsilon_{33}, S_4 = 2\varepsilon_{23}, S_5 = 2\varepsilon_{13}, S_6 = 2\varepsilon_{12}$, ε_{km} are the components of the strain tensor; D_k are the components of the electric displacement or electric flux density vector; E_m are the components of the electric field intensity vector; $c^E_{\alpha\zeta}$ are the elastic stiffness moduli at constant electric field;

$e_{m\alpha}$ are the piezomoduli (stress coefficients; ε^S_{km} are the dielectric constants or the dielectric permittivity moduli at constant mechanical strain. The superscripts E and S indicate the corresponding moduli measured at constant electric field intensity and at constant mechanical strain, respectively.

Note that the Voigt notation is used in the constitutive equations (2), but in their tensor form, so that instead of the matrices $c^E_{\alpha\zeta}$, $e_{k\zeta}$ and ε^S_{km} of the size 6×6, 3×6 and 3×3, the tensors of the fourth, third and second ranks are used, respectively. Therefore, if it is necessary to transfer to another coordinate system, the material moduli will change according to the laws of changing the tensors of the corresponding ranks.

In accordance with the Gurtin–Murdoch model for surface stresses and strains we add to the system of equations (1)–(3) the following interface relations on the boundary S^i

$$n_m[\sigma_{km}] = \partial^i_m \sigma^i_{km}, \quad T^i_\alpha = c^{Ei}_{\alpha\zeta} S^i_\zeta, \quad \mathbf{x} \in S^i\,, \tag{4}$$

$$\varepsilon^i_{km} = (\partial^i_k u^i_m + \partial^i_m u^i_k)/2, \quad u^i_m = A_{ml} u_l, \quad A_{ml} = \delta_{ml} - n_m n_l\,. \tag{5}$$

Here, $[\sigma_{km}] = \sigma^{(1)}_{km} - \sigma^{(2)}_{km}$ is the jump stresses on the interface boundary; $\partial^i_m = \partial_m - n_m(n_l \partial_l)$ are the components of the interface (surface) gradient operator; $T^i_1 = \sigma^i_{11}, T^i_2 = \sigma^i_{22}, T^i_3 = \sigma^i_{33}, T^i_4 = \sigma^i_{23}, T^i_5 = \sigma^i_{13}, T^i_6 = \sigma^i_{12}, \sigma^i_{km}$ are the components of the interface (surface) stress tensor; $S^i_1 = \varepsilon^i_{11}, S^i_2 = \varepsilon^i_{22}, S^i_3 = \varepsilon^i_{33}, S^i_4 = 2\varepsilon^i_{23}, S^i_5 = 2\varepsilon^i_{13}, S^i_6 = 2\varepsilon^i_{12}$, ε^i_{km} are the components of the interface (surface) strain tensor; $c^{Ei}_{\alpha\zeta}$ are the interface (surface) elastic stiffness moduli. The superscript i refers to "interface", and does not have integer values.

We assume that the first phase of the composite is a piezoceramic material, polarized in the direction of the x_3 axis. Then, as is known, the matrices of its material moduli $c^E_{\alpha\zeta} = c^{E(1)}_{\alpha\zeta}$, $e_{k\zeta} = e^{(1)}_{k\zeta}$ and $\varepsilon^S_{km} = \varepsilon^{S(1)}_{km}$ have the following structure

$$\mathbf{c}^E = \begin{bmatrix} c^E_{11} & c^E_{12} & c^E_{13} & 0 & 0 & 0 \\ c^E_{12} & c^E_{11} & c^E_{13} & 0 & 0 & 0 \\ c^E_{13} & c^E_{13} & c^E_{33} & 0 & 0 & 0 \\ 0 & 0 & 0 & c^E_{44} & 0 & 0 \\ 0 & 0 & 0 & 0 & c^E_{44} & 0 \\ 0 & 0 & 0 & 0 & 0 & c^E_{66} \end{bmatrix}, \quad \mathbf{e}^* = \begin{bmatrix} 0 & 0 & e_{31} \\ 0 & 0 & e_{31} \\ 0 & 0 & e_{33} \\ 0 & e_{15} & 0 \\ e_{15} & 0 & 0 \\ 0 & 0 & 0 \end{bmatrix}, \quad \boldsymbol{\varepsilon}^S = \begin{bmatrix} \varepsilon^S_{11} & 0 & 0 \\ 0 & \varepsilon^S_{11} & 0 \\ 0 & 0 & \varepsilon^S_{33} \end{bmatrix}, \tag{6}$$

where $c^E_{66} = (c^E_{11} - c^E_{12})/2$.

The material of elastic inclusions is considered to be isotropic. The moduli of such material can also be represented as (6) with $c^E_{\alpha\zeta} = c^{E(2)}_{\alpha\zeta}$, $e_{k\zeta} = e^{(2)}_{k\zeta}$ and $\varepsilon^S_{km} = \varepsilon^{S(2)}_{km}$, subject to additional conditions $c^{E(2)}_{11} = c^{E(2)}_{33}$, $c^{E(2)}_{12} = c^{E(2)}_{13}$, $c^{E(2)}_{44} = c^{E(2)}_{66}$, $\varepsilon^{S(2)}_{11} = \varepsilon^{S(2)}_{33}$, $e^{(2)}_{k\zeta} = 0$.

Thus, both materials can be considered as transversely isotropic or materials of 6 mm anisotropy class. Then it is logical to suppose that the mixed composite formed of these materials will have the same class of anisotropy.

We will assume that the set S^i is the class union of the plane sections S^{ir} with normals parallel to one of the axes x_l, $r = 1, 2, \ldots, n^i$. For each of these sections S^{ir}, we introduce the local rectangular coordinate systems with the axes $\tilde{x}_1^{ir}, \tilde{x}_2^{ir}, \tilde{x}_3^{ir}$, where the axes $\tilde{x}_1^{ir}, \tilde{x}_2^{ir}$ lie in the plane of the segment S^{ir}, and the axis $\tilde{x}_3^{ir}$ is perpendicular to the plane of this segment. For such sections, only the two-dimensional components of the interface stress tensors $\tilde{T}_1^{ir} = \tilde{\sigma}_{11}^{ir}, \tilde{T}_2^{ir} = \tilde{\sigma}_{22}^{ir}, \tilde{T}_3^{ir} = \tilde{\sigma}_{12}^{ir}$, and the two-dimensional components of the interface strain tensors $\tilde{S}_1^{ir} = \tilde{\varepsilon}_{11}^{ir}, \tilde{S}_2^{ir} = \tilde{\varepsilon}_{22}^{ir}, \tilde{S}_3^{ir} = 2\tilde{\varepsilon}_{12}^{ir}$ can be considered. For these components, we can write the two-dimensional Hooke's interface law and present the relations (4), (5) in the form

$$[\tilde{\sigma}_{33}^{r}] = 0, \quad [\tilde{\sigma}_{3q}^{r}] = \tilde{\partial}_p^{ir} \tilde{\sigma}_{pq}^{ir}, \quad \tilde{T}_k^{ir} = \tilde{c}_{km}^{Eir} \tilde{S}_m^{ir}, \quad \tilde{\mathbf{x}} \in S^{ir}, \tag{7}$$

$$\tilde{\varepsilon}_{pq}^{ir} = (\tilde{\partial}_q^{ir} \tilde{u}_p^{ir} + \tilde{\partial}_p^{ir} \tilde{u}_q^{ir})/2, \tag{8}$$

where $p, q = 1, 2$; $k, m = 1, 2, 3$; the superscript r and the symbol $(\tilde{\ldots})$ denote the value calculated in the local coordinate system $O\tilde{x}_1^{ir}\tilde{x}_2^{ir}\tilde{x}_3^{ir}$.

We assume that in the case of ceramic matrix PZT composite with nanostructured inclusions the interface stiffness moduli can be calculated using the data of the moduli of PZT ceramics and the moduli of inclusions by the formula $c_{\alpha\zeta}^{Ei} = l_d |c_{\alpha\zeta}^{E(1)} - c_{\alpha\zeta}^{E(2)}|$, where $l_d = 10^{-10}$ (m).

In addition, we will suppose that the matrices of the interface moduli inherit the anisotropy type of the surrounding materials, i.e. materials of 6 mm class. Therefore, for plane sections S^{ir} with normals parallel to the x_3 axis, for the matrix of stiffness moduli in the local coordinate system we can assume that $\tilde{c}_{km}^{Eir} = \tilde{c}_{km}^{Ei(12)}$, and for sections S^{ir} with normals perpendicular to the axis x_3, we can suppose that $\tilde{c}_{km}^{Eir} = \tilde{c}_{km}^{Ei(13)}$, where

$$\tilde{\mathbf{c}}^{Ei(12)} = \begin{bmatrix} c_{11}^{Ei} & c_{12}^{Ei} & 0 \\ c_{12}^{Ei} & c_{11}^{Ei} & 0 \\ 0 & 0 & c_{66}^{Ei} \end{bmatrix}, \quad \tilde{\mathbf{c}}^{Ei(13)} = \begin{bmatrix} c_{11}^{Ei} & c_{13}^{Ei} & 0 \\ c_{13}^{Ei} & c_{33}^{Ei} & 0 \\ 0 & 0 & c_{44}^{Ei} \end{bmatrix}. \tag{9}$$

In the considered case, we can assume that a homogeneous material will have the same anisotropy class 6 mm. Then, the homogenization problems will consist in determining ten effective moduli ($c_{11}^{E\,\mathrm{eff}}, c_{12}^{E\,\mathrm{eff}}, c_{13}^{E\,\mathrm{eff}}, c_{33}^{E\,\mathrm{eff}}, c_{44}^{E\,\mathrm{eff}}, e_{31}^{\mathrm{eff}}, e_{33}^{\mathrm{eff}}, e_{15}^{\mathrm{eff}}, \varepsilon_{11}^{S\,\mathrm{eff}}, \varepsilon_{33}^{S\,\mathrm{eff}}$).

Following [22], these moduli can be determined by solving the electroelastic problems (1)–(3) in the volume V with (4), (5) or (7), (8) with the linear by x_m boundary conditions ($u\varphi$-problems)

$$u_j = x_k \varepsilon_{0kj}, \quad \varphi = -x_k E_{0k}, \qquad \mathbf{x} \in S, \tag{10}$$

where ε_{0kj} and E_{0k} are some constant values independent from x_k.

By using (10), we can select such boundary conditions that enable us to obtain explicit expressions for the full set of the effective moduli.

Indeed, these moduli can be found from the solutions of the following five problems (1)–(3), (4), (5) or (7), (8), and (10):
– $u\varphi$-problems I-II, $l = 1, 3$, $m = 1, 2, 3$,

$$\varepsilon_{0kj} = e_0\delta_{lk}\delta_{lj}, \quad E_{0k} = 0 \;\Rightarrow\; c_{lm}^{E\,\mathrm{eff}} = \langle\sigma_{mm}\rangle_{VS}/e_0, \quad e_{3l}^{\mathrm{eff}} = \langle D_3\rangle_V/e_0\,, \tag{11}$$

– $u\varphi$-problem III

$$\varepsilon_{0kj} = e_0(\delta_{2k}\delta_{3j} + \delta_{3k}\delta_{2j})/2,\; E_{0k} = 0 \;\Rightarrow\; c_{44}^{E\,\mathrm{eff}} = \langle\sigma_{23}\rangle_{VS}/e_0,\; e_{15}^{\mathrm{eff}} = \langle D_2\rangle_V/e_0\,, \tag{12}$$

– $u\varphi$-problem IV

$$\varepsilon_{0kj} = 0, \quad E_{0k} = E_0\delta_{1k} \;\Rightarrow\; e_{15}^{\mathrm{eff}} = -\langle\sigma_{13}\rangle_{VS}/E_0, \quad \varepsilon_{11}^{S\,\mathrm{eff}} = \langle D_1\rangle_V/E_0\,, \tag{13}$$

– $u\varphi$-problem V, $m = 1, 2, 3$,

$$\varepsilon_{0kj} = 0, \quad E_{0k} = E_0\delta_{3k} \;\Rightarrow\; e_{3m}^{\mathrm{eff}} = -\langle\sigma_{mm}\rangle_{VS}/E_0, \quad \varepsilon_{33}^{S\,\mathrm{eff}} = \langle D_3\rangle_V/E_0\,, \tag{14}$$

where δ_{jk} is the Kronecker symbol; hereinafter the angle brackets $\langle(\bullet)\rangle_{VS}$ denote the averaged integral volume and interface values, and the angle brackets $\langle(\bullet)\rangle_V$ denote the averaged only integral volume values

$$\langle(\bullet)\rangle_{VS} = \frac{1}{|V|}\Big(\int_V (\bullet)\,dV + \int_{S^i} (\bullet)^i\,dS\Big), \quad \langle(\bullet)\rangle_V = \frac{1}{|V|}\Big(\int_V (\bullet)\,dV\Big). \tag{15}$$

The justification for the use of averaging (15) with volume and surface integrals for composites with surface or interface stresses (4), (5) can be found, for example, in [2, 17] and can be transferred to the homogenization problems (1)–(3), (4), (5) or (7), (8), and (10) for piezoelectric composites.

The expressions (10) are linear essential boundary conditions, which for a homogeneous piezoelectric comparison medium provide the constant components of the stresses, strains, electric fluxes, and electric intensity fields. Besides, we can use different boundary conditions for the homogenization problems, which also provide the constant stresses, strains, electric fluxes, and electric intensity fields for a homogeneous piezoelectric comparison medium [27, 28].

Thus, instead of expressions (10), we can adopt natural boundary condition for the stress with known constant values and essential electric boundary condition with the known linear be x_m electric potential ($p\varphi$-problems)

$$n_k\sigma_{kj} = p_{0j}, \quad p_{0j} = n_k\sigma_{0kj}, \quad \varphi = -x_kE_{0k}, \qquad \mathbf{x} \in S\,, \tag{16}$$

where σ_{0kj} and E_{0k} are the fixed values.

Using this approach, in order to determine the other full set of effective moduli for a ceramic matrix piezocomposite ($s_{11}^{E\,\mathrm{eff}}$, $s_{12}^{E\,\mathrm{eff}}$, $s_{13}^{E\,\mathrm{eff}}$, $s_{33}^{E\,\mathrm{eff}}$, $s_{44}^{E\,\mathrm{eff}}$, d_{31}^{eff}, d_{33}^{eff}, d_{15}^{eff}, $\varepsilon_{11}^{T\,\mathrm{eff}}$, $\varepsilon_{33}^{T\,\mathrm{eff}}$), we must solve five boundary-value problems (1)–(3), (4), (5) or (7), (8),

and (16) with various values of σ_{0kj} and E_{0k}, having set only one or two components σ_{0kj}, E_{0k} not equal to zero:
– $p\varphi$-problems I-II, $l = 1, 3$, $m = 1, 2, 3$,

$$\sigma_{0kj} = s_0\delta_{lk}\delta_{lj}, \quad E_{0k} = 0 \;\Rightarrow\; s_{lm}^{E\,\mathrm{eff}} = \langle\varepsilon_{mm}\rangle_V/s_0, \quad d_{3l}^{\mathrm{eff}} = \langle D_3\rangle_V/s_0\,, \tag{17}$$

– $p\varphi$-problem III

$$\sigma_{0kj} = s_0(\delta_{2k}\delta_{3j} + \delta_{3k}\delta_{2j})/2,\; E_{0k} = 0 \;\Rightarrow\; s_{44}^{E\,\mathrm{eff}} = \langle\varepsilon_{23}\rangle_V/s_0,\; d_{15}^{\mathrm{eff}} = \langle D_2\rangle_V/s_0\,, \tag{18}$$

– $p\varphi$-problem IV

$$\sigma_{0kj} = 0, \quad E_{0k} = E_0\delta_{1k} \;\Rightarrow\; d_{15}^{\mathrm{eff}} = \langle\varepsilon_{13}\rangle_V/E_0, \quad \varepsilon_{11}^{T\,\mathrm{eff}} = \langle D_1\rangle_V/E_0\,, \tag{19}$$

– $p\varphi$-problem V, $m = 1, 2, 3$,

$$\sigma_{0kj} = 0, \quad E_{0k} = E_0\delta_{3k} \;\Rightarrow\; d_{3m}^{\mathrm{eff}} = \langle\varepsilon_{mm}\rangle_V/E_0, \quad \varepsilon_{33}^{T\,\mathrm{eff}} = \langle D_3\rangle_V/E_0\,. \tag{20}$$

After solving these five $p\varphi$-problems and finding from (17) to (20) the elastic compliance moduli $s_{\alpha\zeta}^{E\,\mathrm{eff}}$ at constant electric field, the piezomoduli (charge coefficients) $d_{m\alpha}^{\mathrm{eff}}$, and dielectric permittivity moduli $\varepsilon_{km}^{T\,\mathrm{eff}}$ at constant mechanical stress, we can calculate the basic moduli by using the formulae

$$\mathbf{c}^{E\,\mathrm{eff}} = (\mathbf{s}^{E\,\mathrm{eff}})^{-1}, \quad e_{m\alpha}^{\mathrm{eff}} = d_{m\zeta}^{\mathrm{eff}}c_{\alpha\zeta}^{E\,\mathrm{eff}}, \quad \varepsilon_{km}^{S\,\mathrm{eff}} = \varepsilon_{km}^{T\,\mathrm{eff}} - d_{k\zeta}^{\mathrm{eff}}e_{m\zeta}^{\mathrm{eff}}\,. \tag{21}$$

It is clear that the moduli $c_{\alpha\zeta}^{E\,\mathrm{eff}}$, $e_{m\alpha}^{\mathrm{eff}}$, $\varepsilon_{km}^{S\,\mathrm{eff}}$ found from the solutions of the $p\varphi$-problems (1)–(3), (4), (5) or (7), (8), and (15)–(21), generally speaking, may differ from the moduli found from the solution of the $u\varphi$-problems (1)–(3), (4), (5) or (7), (8), and (10)–(15).

With a different alternative approach, we can adopt essential mechanical boundary conditions with known linear components of the displacement vector and natural electric boundary conditions with known constant normal component of the electric flux density vector (uD-problems)

$$u_j = x_k\varepsilon_{0kj}, \quad n_kD_k = n_kD_{0k}, \qquad \mathbf{x} \in S\,. \tag{22}$$

Then we solve five electroelastic problems (1)–(3), (4), (5) or (7), (8), and (22) with various values ε_{0kj} and D_{0k}, having set in (22) only one or two non-zero components from ε_{0kj}, D_{0k}, and in the result we can find the effective moduli $c_{11}^{D\,\mathrm{eff}}$, $c_{12}^{D\,\mathrm{eff}}$, $c_{13}^{D\,\mathrm{eff}}$, $c_{33}^{D\,\mathrm{eff}}$, $c_{44}^{D\,\mathrm{eff}}$, h_{31}^{eff}, h_{33}^{eff}, h_{15}^{eff}, $\beta_{11}^{S\,\mathrm{eff}}$, $\beta_{33}^{S\,\mathrm{eff}}$:
– uD-problems I-II, $l = 1, 3$, $m = 1, 2, 3$,

$$\varepsilon_{0kj} = e_0\delta_{lk}\delta_{lj}, \quad D_{0k} = 0 \;\Rightarrow\; c_{lm}^{D\,\mathrm{eff}} = \langle\sigma_{mm}\rangle_{VS}/e_0, \quad h_{3l}^{\mathrm{eff}} = -\langle E_3\rangle_V/e_0\,, \tag{23}$$

– uD-problem III

$$\varepsilon_{0kj} = e_0(\delta_{2k}\delta_{3j} + \delta_{3k}\delta_{2j})/2,\ D_{0k} = 0 \ \Rightarrow\ c_{44}^{D\,\mathrm{eff}} = \langle\sigma_{23}\rangle_{VS}/e_0,\ h_{15}^{\mathrm{eff}} = -\langle E_2\rangle_V/e_0\,, \tag{24}$$

– uD-problem IV

$$\varepsilon_{0kj} = 0,\quad D_{0k} = D_0\delta_{1k}\ \Rightarrow\ h_{15}^{\mathrm{eff}} = -\langle\sigma_{13}\rangle_{VS}/D_0,\quad \beta_{11}^{S\,\mathrm{eff}} = \langle E_1\rangle_V/D_0\,, \tag{25}$$

– uD-problem V, $m = 1, 2, 3$,

$$\varepsilon_{0kj} = 0,\quad D_{0k} = D_0\delta_{3k}\ \Rightarrow\ h_{3m}^{\mathrm{eff}} = -\langle\sigma_{mm}\rangle_{VS}/D_0,\quad \beta_{33}^{S\,\mathrm{eff}} = \langle E_3\rangle_V/D_0\,. \tag{26}$$

By using obtained from (23)–(26) the elastic stiffness moduli $c_{\alpha\zeta}^{D\,\mathrm{eff}}$ at constant electric displacement, the piezomoduli (strain coefficients) $h_{m\alpha}^{\mathrm{eff}}$, and the dielectric impermittivity moduli $\beta_{km}^{S\,\mathrm{eff}}$ at constant strain, we can determine the basic moduli by the formulae

$$\boldsymbol{\varepsilon}^{S\,\mathrm{eff}} = (\boldsymbol{\beta}^{S\,\mathrm{eff}})^{-1},\quad e_{m\alpha}^{\mathrm{eff}} = \varepsilon_{mk}^{S\,\mathrm{eff}}h_{k\alpha}^{\mathrm{eff}},\quad c_{\alpha\zeta}^{E\,\mathrm{eff}} = c_{\alpha\zeta}^{D\,\mathrm{eff}} - e_{k\alpha}^{\mathrm{eff}}h_{k\zeta}^{\mathrm{eff}}\,. \tag{27}$$

Again, it can be noted that the moduli $c_{\alpha\zeta}^{E\,\mathrm{eff}}$, $e_{m\alpha}^{\mathrm{eff}}$, $\varepsilon_{km}^{S\,\mathrm{eff}}$ obtained from the solutions of uD-problems (1)–(3), (4), (5) or (7), (8), and (22)–(28) may differ from the moduli with the same notations, obtained from the solutions of $u\varphi$- and $p\varphi$-problems.

Finally, we can assume natural mechanical and electric boundary conditions with known constant components of the stress vector and normal component of the electric flux density vector (pD-problems)

$$n_k\sigma_{kj} = p_{0j},\quad p_{0j} = n_k\sigma_{0kj},\quad n_kD_k = n_kD_{0k},\qquad \mathbf{x}\in S\,, \tag{28}$$

In this case, we solve five electroelastic problems (1)–(3), (4), (5) or (7), (8), and (28) with various values of σ_{0kj} and D_{0k}, having set in (28) only one or two non-zero components σ_{0kj} and D_{0k}, which enables us to find the effective moduli $s_{11}^{D\,\mathrm{eff}}$, $s_{12}^{D\,\mathrm{eff}}$, $s_{13}^{D\,\mathrm{eff}}$, $s_{33}^{D\,\mathrm{eff}}$, $s_{44}^{D\,\mathrm{eff}}$, g_{31}^{eff}, g_{33}^{eff}, g_{15}^{eff}, $\beta_{11}^{T\,\mathrm{eff}}$, $\beta_{33}^{T\,\mathrm{eff}}$:
– pD-problems I-II, $l = 1, 3$, $m = 1, 2, 3$,

$$\sigma_{0kj} = s_0\delta_{lk}\delta_{lj},\quad D_{0k} = 0\ \Rightarrow\ s_{lm}^{D\,\mathrm{eff}} = \langle\varepsilon_{mm}\rangle_V/s_0,\quad g_{3l}^{\mathrm{eff}} = -\langle E_3\rangle_V/s_0\,, \tag{29}$$

– pD-problem III

$$\sigma_{0kj} = s_0(\delta_{2k}\delta_{3j} + \delta_{3k}\delta_{2j})/2,\ D_{0k} = 0\ \Rightarrow\ s_{44}^{D\,\mathrm{eff}} = \langle\varepsilon_{23}\rangle_V/s_0,\ g_{15}^{\mathrm{eff}} = -\langle E_2\rangle_V/s_0\,, \tag{30}$$

– pD-problem IV

$$\sigma_{0kj} = 0,\quad D_{0k} = D_0\delta_{1k}\ \Rightarrow\ g_{15}^{\mathrm{eff}} = \langle\varepsilon_{13}\rangle_V/D_0,\quad \beta_{11}^{T\,\mathrm{eff}} = \langle E_1\rangle_V/D_0\,, \tag{31}$$

– pD-problem V, $m = 1, 2, 3$,

$$\sigma_{0kj} = 0, \quad D_{0k} = D_0\delta_{3k} \;\Rightarrow\; g_{3m}^{\text{eff}} = \langle \varepsilon_{mm} \rangle_V / D_0, \quad \beta_{33}^{T\,\text{eff}} = \langle E_3 \rangle_V / D_0 \,. \tag{32}$$

From (29) to (32) we determine the elastic compliance moduli $s_{\alpha\zeta}^{D\,\text{eff}}$ at constant electric displacement, the piezomoduli (voltage coefficients) $g_{m\alpha}^{\text{eff}}$, and the dielectric impermittivity moduli $\beta_{km}^{S\,\text{eff}}$ at constant stress. Using this set, we at first determine the moduli $c_{\alpha\zeta}^{D\,\text{eff}}$, $h_{m\alpha}^{\text{eff}}$, $\beta_{km}^{T\,\text{eff}}$ by the formulae

$$\mathbf{c}^{D\,\text{eff}} = (\mathbf{s}^{D\,\text{eff}})^{-1}, \quad h_{m\alpha}^{\text{eff}} = g_{m\zeta}^{\text{eff}} c_{\zeta\alpha}^{D\,\text{eff}}, \quad \beta_{km}^{S\,\text{eff}} = \beta_{km}^{T\,\text{eff}} + g_{k\zeta}^{\text{eff}} h_{m\zeta}^{\text{eff}}, \tag{33}$$

and after that by (27) we can obtain the basic effective moduli.

In this variant of homogenization problems the moduli $c_{\alpha\zeta}^{E\,\text{eff}}$, $e_{m\alpha}^{\text{eff}}$, $\varepsilon_{km}^{S\,\text{eff}}$ found from the solutions of pD-problems (1)–(3), (4), (5) or (7), (8), and (28)–(33), (27) are not required to be equal to the moduli obtained from the solutions of other problems.

In order to solve all four types of boundary value electroelastic problems, we will use the finite element method, having previously simulated the representative volume of the composite material.

3 Representative Volumes and Finite Element Models

All homogenization problems described in the previous section were solved in the ANSYS finite element package. In order to implement different solution stages automatically, we have developed special programs written in the APDL ANSYS language.

The representative volume elements (RVE) consisted of bulk and interface finite elements. First, we have created an array of volume elements that included geometrically identical cubes with sides a. On each axis of the Cartesian coordinate system, n cubic elements were located. Thus, the RVE had n^3 cubic elements, and the size of RVE on each axis was $L = na$.

Each cubic finite element was provided with either material properties of piezoceramic ceramics polarized in the direction of the x_3 axis (phase 1), or material properties of elastic inclusions (phase 2). Among all bulk finite elements, the elements of the second phase were selected by a random algorithm in accordance with a given percentage of inclusions p. All bulk elements were eight-node SOLID5 hexahedrons with piezoelectric properties for one of the phases.

Next, the interface elements were automatically created. For this, at the intermediate stage, the edges of the elements of inclusions that did not reach the outer boundary of the RVE were covered with quadrilateral elements TARGE170 with four nodes, needed only for selecting the interface boundaries. At the next stage, these elements were replaced with the four-node shell elements SHELL181 with the membrane stress option.

As it has been observed, in ANSYS we can simulate the interface effects using such finite elements. Note that for ANSYS shell element with the membrane stress option, it is necessary to specify the stiffness modulus $c^s_{\alpha\zeta}$ and thickness h^s. At that, the shell element ANSYS with the option of membrane stresses can be used as an interface element, when taking into account the conditions (4), (5) or (7), (8), if we assume $c^{Ei}_{\alpha\zeta} = h^s c^s_{\alpha\zeta}$ [24, 25]. Thus, for the calculation in ANSYS, the values of the shell element stiffness modulus and the element thickness are not important separately, but their product is. In contrast to [24, 25], here we consider the RVE in a dimensionless form, with the side of a separate finite element equal to 1. Thus, the spatial dimensionless parameter is equal to the minimum size a of the element of the second phase. As noted in the previous section, we set the surface modulus of stiffness by the formula $c^{Ei}_{\alpha\zeta} = l_d |c^{E(1)}_{\alpha\zeta} - c^{E(2)}_{\alpha\zeta}|$, where $l_d = 10^{-10}$ (m). We also assume that $h^s = a$, $c^s_{\alpha\zeta} = (k^s/l_d) c^{Ei}_{\alpha\zeta}$, where k^s is a dimensionless coefficient. Then, $a = l_d/k^s$, and therefore the coefficient k^s is inversely proportional to the minimum inclusion size a. In further numerical experiments, the interface moduli $c^{Ei}_{\alpha\zeta}$ were assumed to be constant, and the coefficient k^s and the percentage of inclusions p varied. It can be seen that an increase in the coefficient k^s leads to a decrease in the minimum size of the inclusion a, and when $k^s > 1$ the value a becomes less than $l_d = 10^{-10}$ (m).

For shell elements SHELL181, it is necessary to ensure the type of anisotropy consistent with the anisotropy of bulk finite elements. Since the volume elements are cubes, the faces of which are parallel to the coordinate axes of the main Cartesian coordinate system, the shell elements can be located only in planes parallel to the planes Ox_1x_2, Ox_1x_3, and Ox_2x_3. At the same time, for transversely isotropic material its properties in the planes Ox_1x_3 and Ox_2x_3 are the same. It turns out that for the shell elements it is necessary to provide the specification of material properties in the element coordinate systems corresponding to the local coordinate systems $O\tilde{x}^{ir}_1\tilde{x}^{ir}_2\tilde{x}^{ir}_3$ described in the previous section. More specifically, for the shell elements located in planes parallel to the plane Ox_1x_2, the material properties must be set in accordance with the first formula (9), and for the elements located in planes perpendicular to the plane Ox_1x_2, the material properties must be set in accordance with the second formula (9). This procedure was automated for the developed programs in the APDL language.

For clarity, an example of a representative volume consisting of a small number of elements $n = 10$ and with the percentage of inclusions $p = 2\%$ is given in Fig. 1. In this figure we can see the entire volume on the left; the elements of the second phase in the center; and the interface shell elements on the right. In this case, the shell elements located perpendicular to the plane Ox_1x_2 are shown in yellow-brown, and the elements parallel to the plane Ox_1x_2 are shown in blue.

At the next stage, for the generated RVE, we solved static piezoelectric $u\varphi$-, $p\varphi$-, uD- or uD-problems, and after that in ANSYS postprocessor we calculated the averaged characteristics (stresses, strains, electric fluxes and electric intensity fields) by (9) according to (11)–(14), (17)–(20), (23)–(26), or (29)–(32). As a result, we have obtained the full sets of the effective material moduli of ceramic matrix piezocomposite.

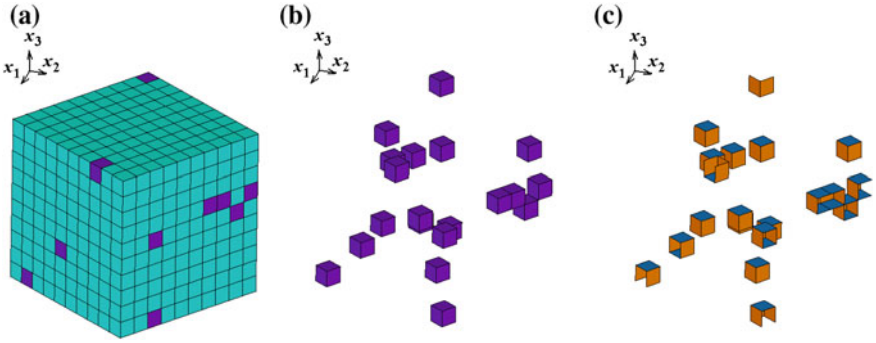

Fig. 1 Example of RVE: full volume (**a**), inclusions (**b**), interface elements (**c**)

4 Numerical Results

To provide an example, we have considered the PZT-5/α-Al_2O_3 ceramic matrix composite. For solid piezoelectric ceramics PZT-5, the following material parameters were taken: $c_{11}^{E(1)} = 12.1 \times 10^{10}$; $c_{12}^{E(1)} = 7.54 \times 10^{10}$; $c_{13}^{E(1)} = 7.52 \times 10^{10}$; $c_{33}^{E(1)} = 11.1 \times 10^{10}$; $c_{44}^{E(1)} = 2.11 \times 10^{10}$ (N/m^2); $e_{31}^{(1)} = -5.4$; $e_{33}^{(1)} = 15.8$; $e_{15}^{(1)} = 12.3$ (C/m^2); $\varepsilon_{11}^{S(1)} = 916\varepsilon_0$; $\varepsilon_{33}^{S(1)} = 830\varepsilon_0$, where $\varepsilon_0 = 8.85 \times 10^{-12}$ (F/m) is the dielectric permittivity of the vacuum.

For the corundum, we have preliminarily averaged its moduli as polycrystalline inclusions to the isotropic phase. As a result, the following moduli of corundum were obtained: $c_{11}^{E(2)} = 46.88 \times 10^{10}$; $c_{12}^{E(2)} = 14.22 \times 10^{10}$ (N/m^2); $\varepsilon_{11}^{S(2)} = 10\varepsilon_0$.

In all further calculations, the RVE included 20 elements along one of the axes. We varied the percentage of inclusions p from 0 to 100 %, the multiplier value for surface stresses $k^s = 1 \times 10^{-5}$ and $k^s = 1$, and the type of the problem. We have found that a change in the electric boundary conditions had a significantly smaller effect on effective moduli compared to a change in the mechanical boundary conditions. For this reason, below we present the results only for $u\varphi$- and $p\varphi$-problems.

The results of the calculations are presented in Figs. 2, 3, 4 and 5. Here $r(...)$ denotes the relative value of the effective modulus, with respect to the value of the corresponding modulus for PZT ceramics without inclusions. Thus, $r(c_{11}^E) = c_{11}^{E\text{eff}}/c_{11}^E$, where $c_{11}^{E\text{eff}}$ is the effective elastic modulus for the ceramic matrix piezocomposite with or without interface stresses, c_{11}^E is the value of the corresponding elastic modulus for an ordinary PZT ceramic material, and so on. The curves 1 correspond to the case of $u\varphi$-problem without interface stresses, when $k^s = 0$; the curves 2 correspond to the case of $p\varphi$-problem also without interface stresses, when $k^s = 0$; the curves 3 correspond to the case of $u\varphi$-problem with large interface stresses, when $k^s = 1$, whereas the curves 4 correspond to the case of $p\varphi$-problem also with large interface stresses, when $k^s = 1$. Note that the dependencies of the relative moduli $r(c_{12}^E)$ and $r(c_{12}^E)$ are almost identical, as well as the dependencies of the relative moduli $r(\varepsilon_{11}^S)$

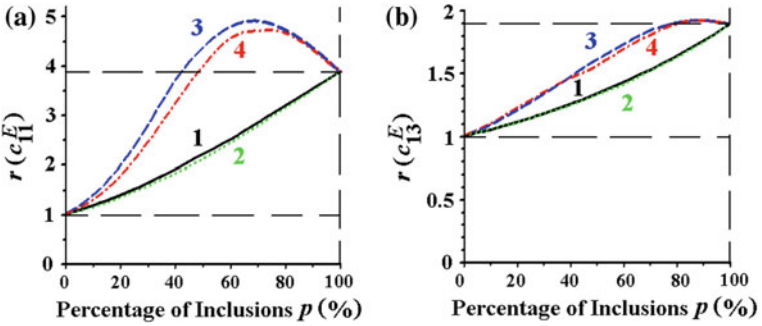

Fig. 2 Dependencies of the relative effective moduli $c_{11}^{E\text{eff}}$ (**a**) and $c_{13}^{E\text{eff}}$ (**b**) on the percentage of inclusions

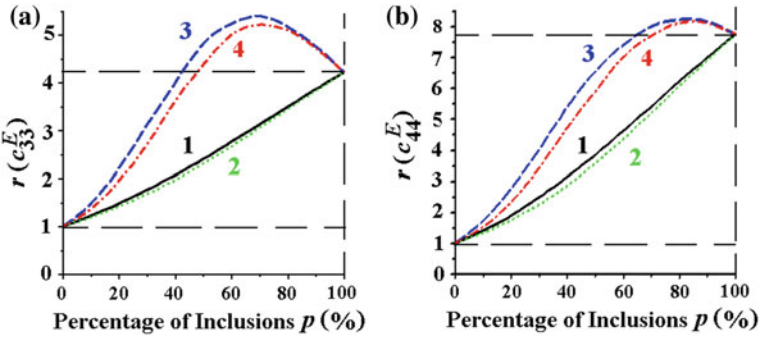

Fig. 3 Dependencies of the relative effective moduli $c_{33}^{E\text{eff}}$ (**a**) and $c_{44}^{E\text{eff}}$ (**b**) on the percentage of inclusions

and $r(\varepsilon_{33}^S)$, which are also almost the same. Thus, Figs. 2, 3, 4 and 5 actually show the dependencies of all ten effective moduli.

As can be seen from the comparison of Figs. 2, 3, 4 and 5, the curves 1–4 differ most significantly among themselves for the elastic stiffness moduli (Figs. 2 and 3). The presence of large interface stresses significantly increases the effective stiffness moduli.

Besides, there are cases when the ceramic matrix composite with interface stresses have greater effective stiffness moduli than the more hard material in the composite. These situations take place when the curves 3 and 4 are located higher that the upper dashed lines, which refers to the ratio of the elastic modulus of more hard inclusion to the corresponding elastic modulus of the PZT ceramic material.

Note that the percentage of hard inclusions and the presence of interface stresses have the same influence on the effective elastic moduli: an increase in the percentage of hard inclusions leads to the growth of the elastic moduli, while the interface stresses also increase the elastic moduli. Therefore, these effects lead to an increase in the total harshness of the ceramic matrix composite. However, for very small and for very large inclusion contents, the surface area of the interface becomes small,

and therefore the effective elastic moduli become close to the corresponding elastic moduli of the individual phases.

From Figs. 2 and 3 we can also conclude that the solutions of the $u\varphi$-problems give slightly larger values of elastic moduli as compared to the solutions of the $p\varphi$-problems. This can be explained by the fact that the $u\varphi$-model with given displacements turns out to be somewhat more rigid than the $p\varphi$-model with given stresses. The difference between the solutions of the two problems becomes more evident in the presence of interface stresses (the difference between curves 3 and 4 is significantly larger compared to the difference between curves 1 and 2).

Since we used the model of interface stresses, which depended only on the strains, and not on the electric fields, the effect of such stresses on the piezoelectric moduli and the dielectric constants turned out to be weaker (Figs. 4 and 5). Interface stresses have the greatest effect on the relative values of the transverse piezomodulus $r(e_{31}^{\text{eff}})$, increasing it for small percentages of inclusions and decreasing it for large proportions of inclusions. Moreover, in the $p\varphi$-problem, the piezomoduli have larger values than in the $u\varphi$-problem. This behaviour of the piezomoduli differs significantly from the behaviour of the stiffness moduli.

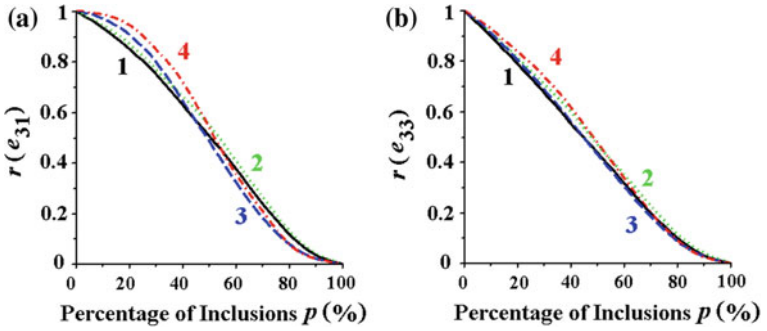

Fig. 4 Dependencies of the relative effective moduli e_{31}^{eff} (**a**) and e_{33}^{eff} (**b**) on the percentage of inclusions

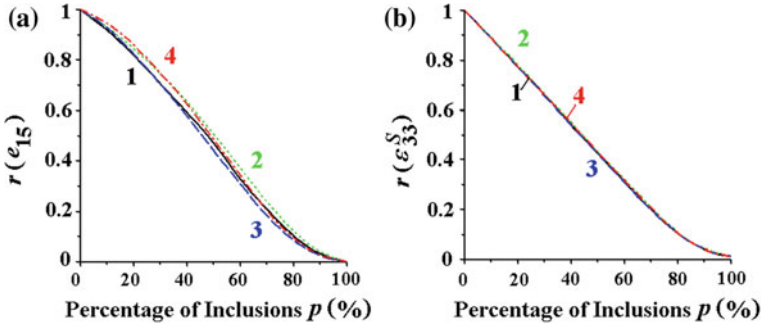

Fig. 5 Dependencies of the relative effective moduli e_{15}^{eff} (**a**) and $\varepsilon_{33}^{S\text{eff}}$ (**b**) on the percentage of inclusions

The dielectric constants (Fig. 5b) are least dependent on both the interface stresses and the type of homogenization problem.

Thus, we can assume that the effective piezoelectric moduli and the dielectric constants will more noticeably depend on nanoscale effects, if instead of the models of uncoupled interface stresses we use more general electromechanically coupled models [9, 23].

5 Concluding Remarks

Thus, in the present investigation in accordance with [27, 28] we have applied the effective moduli method and the finite element technique in order to solve the homogenization problems for ceramic matrix PZT composites with uncoupled mechanical interface effects. This interface model gives valid results only for nanostructured composites with nanoinclusions. We have formulated four types of the static piezoelectric homogenization problems for a representative volume element. These problems are characterized by the boundary conditions which provide the constant values of mechanical stresses, strains, electric fields intensity, and electric displacements for homogeneous piezoelectric material. For each type of boundary conditions, we have presented the sets of five boundary-value problems, which allowed us to define a complete set of the effective moduli for transversely isotropic ceramic matrix composite.

The solutions of the homogenization piezoelectric problems were obtained numerically in the ANSYS finite element package. We used the regular cubic representative volumes with hexahedral eight-node piezoelectric finite elements and random distribution of inclusions. In order to take into account the mechanical interface effects, we added shell four-node finite elements with membrane option on the interphase facets of volume elements. We also specified anisotropic material properties for the shell elements, in accordance with the location of the element coordinate systems and the anisotropy type of the volume elements in these coordinate systems.

To provide an example, we have considered the composite material consisting of a PZT ceramic matrix and α-corundum crystallites Al_2O_3 as inclusions. The material moduli of inclusions were assumed to be isotropic. We have presented the numerical results of the effective moduli calculation for different types of boundary conditions, different percentage of inclusions, and different interface effects values. We have found that due to the interface effect, there were cases when the effective moduli of the composite were superior to the moduli of its individual phases. Such phenomena are known for nanoporous elastic materials [5–8, 18, 24, 25]. At the same time, other types of boundary conditions can lesser the extent to which the values of the effective moduli are affected.

More accurate results can be obtained by using the models of the representative volumes with different connectivities [1, 19, 20, 26–28], the electromechanically coupled interface effects [9, 23], by taking into account the inhomogeneities of the polarization field near the inclusions, and by introducing porosity between the matrix and inclusions [31, 32].

Acknowledgements This work for second author was supported by the Russian Science Foundation (grant number 15-19-10008-P).

References

1. Bobrov, S.V., Nasedkin, A.V., Rybjanets, A.N.: Finite element modeling of effective moduli of porous and polycrystalline composite piezoceramics. In: Topping, B.H.V., Montero, G., Montenegro, R. (eds.) Proceedings VIII International Conference on Computational Structures Technology, Civil-Comp Press, Stirlingshire, UK, Paper 107 (2006)
2. Chatzigeorgiou, G., Javili, A., Steinmann, P.: Multiscale modelling for composites with energetic interfaces at the micro-or nanoscale. Math. Mech. Solids. **20**, 1130–1145 (2015)
3. Chen, T.: Exact size-dependent connections between effective moduli of fibrous piezoelectric nanocomposites with interface effects. Acta Mech. **196**, 205–217 (2008)
4. Dai, Sh., Gharbi, M., Sharma, P., Park, H.S.: Surface piezoelectricity: size effects in nanostructures and the emergence of piezoelectricity in non-piezoelectric materials. J. Appl. Phys. **110**, 104305-1–104305-7 (2011)
5. Duan, H.L., Wang, J., Karihaloo, B.L.: Theory of elasticity at the nanoscale. In: Advances in Applied Mechanics, vol. 42, pp. 1–68. Elsevier (2008)
6. Duan, H.L., Wang, J., Karihaloo, B.L., Huang, Z.P.: Nanoporous materials can be made stiffer than non-porous counterparts by surface modification. Acta Mater. **54**, 2983–2990 (2006)
7. Eremeyev, V.A.: On effective properties of materials at the nano- and microscales considering surface effects. Acta Mech. **227**, 29–42 (2016)
8. Eremeyev, V., Morozov, N.: The effective stiffness of a nanoporous rod. Dokl. Phys. **55**(6), 279–282 (2010)
9. Eremeyev, V.A., Nasedkin, A.V.: Mathematical models and finite element approaches for nanosized piezoelectric bodies with uncoupled and coupled surface effects. In: Sumbatyan, M.A. (ed.) Wave Dynamics and Composite Mechanics for Microstructured Materials and Metamaterials. Ser. Advanced Structured Materials, vol. 59, pp. 1–18. Springer, Singapore (2017)
10. Fang, X.-Q., Zhu, C.-S., Liu, J.-X., Liu, X.-L.: Surface energy effect on free vibration of nano-sized piezoelectric double-shell structures. Phys. B: Condens. Matter. **529**, 41–56 (2018)
11. Gu, S.-T., He, Q.-C.: Interfacial discontinuity relations for coupled multifield phenomena and their application to the modeling of thin interphases as imperfect interfaces. J. Mech. Phys. Solids. **59**, 1413–1426 (2011)
12. Gu, S.-T., He, Q.-C., Pensee, V.: Homogenization of fibrous piezoelectric composites with general imperfect interfaces under anti-plane mechanical and in-plane electrical loadings. Mech. Mater. **88**, 12–29 (2015)
13. Gu, S.-T., Liu, J.-T., He. Q.-C.: Piezoelectric composites: Imperfect interface models, weak formulations and benchmark problems. Comp. Mater. Sci. **94**, 182–190 (2014)
14. Gu, S.-T., Liu, J.-T., He. Q.-C.: The strong and weak forms of a general imperfect interface model for linear coupled multifield phenomena. Int. J. Eng. Sci. **85**, 31–46 (2014)
15. Gu, S.-T., Qin, L.: Variational principles and size-dependent bounds for piezoelectric inhomogeneous materials with piezoelectric coherent imperfect interfaces. Int. J. Eng. Sci. **78**, 89–102 (2014)

16. Huang, G.Y., Yu, S.W.: Effect of surface piezoelectricity on the electromechanical behaviour of a piezoelectric ring. Phys. Status Solidi B. **243**(4), R22–R24 (2006)
17. Javili, A., McBride, A., Mergheima, J., Steinmann, P., Schmidt, U.: Micro-to-macro transitions for continua with surface structure at the microscale. Int. J. Solids Struct. **50**, 2561–2572 (2013)
18. Jeong, J., Cho, M., Choi, J.: Effective mechanical properties of micro/nano-scale porous materials considering surface effects. Interact. Multiscale Mech. **4**(2), 107–122 (2011)
19. Kudimova, A.B., Nadolin, D.K., Nasedkin, A.V., Nasedkina, A.A., Oganesyan, P.A., Soloviev, A.N.: Models of porous piezocomposites with 3–3 connectivity type in ACELAN finite element package. Mater. Phys. Mech. **37**(1), 16–24 (2018)
20. Kudimova, A.B., Nadolin, D.K., Nasedkin, A.V., Oganesyan, P.A., Soloviev, A.N.: Finite element homogenization models of bulk mixed piezocomposites with granular elastic inclusions in ACELAN package. Mater. Phys. Mech. **37**(1), 25–33 (2018)
21. Malakooti, M.H., Sodano, H.A.: Multi-inclusion modeling of multiphase piezoelectric composites. Compos.: Part B. **47**, 181–189 (2013)
22. Nasedkin, A.V.: Some homogenization models of nanosized piezoelectric composite materials of types ceramics-pores and ceramics-ceramics with surface effects. In: Guemes, A., Benjeddou, A., Rodellar, J., Leng, J. (eds.) VIII ECCOMAS Thematic Conference on Smart Structures and Materials, VI Int. Conf. on Smart Materials and Nanotechnology in Engineering-SMART 2017, 5–8 June 2017, Madrid, Spain, pp. 1137–1147. CIMNE, Barcelona, Spain (2017)
23. Nasedkin, A.V., Eremeyev, V.A.: Harmonic vibrations of nanosized piezoelectric bodies with surface effects. ZAMM **94**(10), 878–892 (2014)
24. Nasedkin, A.V., Kornievsky, A.S.: Finite element modeling and computer design of anisotropic elastic porous composites with surface stresses. In: Sumbatyan, M.A. (ed.) Wave Dynamics and Composite Mechanics for Microstructured Materials and Metamaterials. Series Advanced Structured Materials, vol. 59, pp. 107–122. Springer, Singapore (2017)
25. Nasedkin, A.V., Kornievsky, A.S.: Finite element modeling of effective properties of elastic materials with random nanosized porosities. ycisl. meh. splos. sred – Comput. Continuum Mech. **10**(4), 375–387 (2017)
26. Nasedkin, A.V., Nasedkina, A.A., Remizov, V.V.: Finite element modeling of porous thermoelastic composites with account for their microstructure. Vycisl. meh. splos. sred – Comput. Continuum Mech. **7**(1), 100–109 (2014)
27. Nasedkin, A.V., Shevtsova, M.S.: Improved finite element approaches for modeling of porous piezocomposite materials with different connectivity. In: Parinov, I.A. (ed.) Ferroelectrics and Superconductors: Properties and Applications, pp. 231–254. Nova Science Publication, NY (2011)
28. Nasedkin, A.V., Shevtsova, M.S.: Multiscale computer simulation of piezoelectric devices with elements from porous piezoceramics In: Parinov, I.A., Chang, S.-H. (eds.) Physics and Mechanics of New Materials and Their Applications, pp. 185–202. Nova Science Publ., NY (2013)
29. Pan, X.H., Yu, S.W., Feng, X.Q.: A continuum theory of surface piezoelectricity for nanodielectrics. Sci. China: Phys. Mech. Astron. **54**(4), 564–573 (2011)
30. Park, H.S., Devel, M., Wang, Z.: A new multiscale formulation for the electromechanical behavior of nanomaterials. Comput. Methods Appl. Mech. Eng. **200**, 2447–2457 (2011)
31. Rybyanets, A.N., Konstantinov, G.M., Naumenko, A.A., Shvetsova, N.A., Makarev, D.I., Lugovaya, M.A.: Elastic, dielectric, and piezoelectric properties of ceramic lead zirconate titanate/α-Al_2O_3 composites. Phys. Solid State. **57**(3), 527–530 (2015)
32. Rybyanets, A.N., Naumenko, A.A., Konstantinov, G.M., Shvetsova, N.A., Lugovaya, M.A.: Elastic loss and dispersion in ceramic-matrix piezocomposites. Phys. Solid State. **57**(3), 558–562 (2015)
33. Wang, K.F., Wang, B.L., Kitamura, T.: A review on the application of modified continuum models in modeling and simulation of nanostructures. Acta Mech. Sin. **32**(1), 83–100 (2016)
34. Wang, W., Li, P., Jin, F., Wang, J.: Vibration analysis of piezoelectric ceramic circular nanoplates considering surface and nonlocal effects. Compos. Struct. **140**, 758–775 (2016)

35. Wang, Z., Zhu, J., Jin, X.Y., Chen, W.Q., Zhang, Ch.: Effective moduli of ellipsoidal particle reinforced piezoelectric composites with imperfect interfaces. J. Mech. Phys. Solids. **65**, 138–156 (2014)
36. Xiao, J.H., Xu, Y.L., Zhang, F.C.: Size-dependent effective electroelastic moduli of piezoelectric nanocomposites with interface effect. Acta Mech. **222**, 59–67 (2011)
37. Zhao, D., Liu, J.L., Wang, L.: Nonlinear free vibration of a cantilever nanobeam with surface effects: semi-analytical solutions. Int. J. Mech. Sci. **113**, 184–195 (2016)

A Far-Field Asymptotic Analysis in the High-Frequency Diffraction by Cracks

M. Y. Remizov

Abstract On the basis of recently obtained asymptotic solutions of integral equations by the Wiener-Hopf method for diffraction by a straight finite-length crack in a linear elastic medium, we study the properties of the far-zone scattered field at high frequencies for (1) - anti-plane problem in a homogeneous medium, (2) - anti-plane problem for an interface crack, and (3) - in-plane problem in a homogeneous medium.The method proposed is founded on a high-frequency solution of the basic integral equation of the scattering problem. Then we develop an explicit analytical representation for the leading asymptotic term, by estimating the far-field behavior of the relevant integrals with high oscillations by the method of stationary phase. This allows us to obtain the final form of the scattered field in an explicit analytical form as some quadratures.

1 Introduction

The high-frequency regime in diffraction processes is a case when standard numerical methods encounter significant obstacles since these require too huge discrete grids. Various asymptotic approaches have been proposed to overcome this difficulty [1–5]. In [6] a new method allied to the classical "Edge Waves" method [1] is proposed. Typically, this requires a certain factorization of a symbolic function [7]. In the case of scalar anti-plane (SH-) wave diffraction by cracks located in a linear isotropic homogeneous elastic medium the factorization of such a function is attained in a simple way. The in-plane diffraction by cracks involves the Rayleigh function as a more complex form and in [6] an efficient approximate factorization of such a function uniformly valid all over the real axis was proposed. For the scalar SH-diffraction by the finite-length linear interface crack between two different elastic

M. Y. Remizov (✉)
Institute of Mathematics, Mechanics and Computer Science, Southern Federal University, Milchakova Street 8a, Rostov-on-Don 344090, Russia
e-mail: remizov72@mail.ru

M. A. Sumbatyan (ed.), *Wave Dynamics, Mechanics and Physics of Microstructured Metamaterials*, Advanced Structured Materials 109,
https://doi.org/10.1007/978-3-030-17470-5_13

half-planes a new efficient factorization to the arising symbolic function is applied in [8], where a closed-form solution has been constructed.

The present work continues to study the properties of the far-field scattering in the problems listed above as 1–3, on high-frequency diffraction by cracks of finite length. The discussion is restricted to the 2d elastic case for isotropic unbounded media, where the integrals with high oscillations, forming a displacement field, have been estimated by the method of stationary phase.

It should be noted that some fundamental aspects of new methods for hypersingular integral equations arising in diffraction by cracks, are discussed, among many other publications, in [9–15].

2 Anti-plane Diffraction Problem

Let us consider the SH- (anti-plane) problem on diffraction of a plane incident wave by a straight finite-length crack $x \in [-a, a],\ y = 0$ located in the linear elastic isotropic space. The plane incident transverse wave forms angle θ with respect to vertical axis $y : w^{inc}(x, y) = \exp[-ik_s(x \sin\theta + y \cos\theta)]$, where k_s is the transverse wave number and the time-dependent factor $\exp(-i\omega t)$ is hidden. Note that in the anti-plane problem the displacement vector is $\bar{u}(x, y, z) = \{0, 0, w(x, y)\}$, where function w satisfies the Helmholtz equation:

$$\frac{\partial^2 w}{\partial x^2} + \frac{\partial^2 w}{\partial y^2} + k_s^2 w = 0. \tag{2.1}$$

The boundary conditions correspond to stress-free faces of the crack:

$$\begin{gathered} y = 0; \quad |x| \le a: \ \tau_{xz}^{(1,2)} = -\tau_{xz}^{inc}, \quad \tau_{yz}^{(1,2)} = -\tau_{yz}^{inc}; \\ y = 0; \quad |x| > a: \ \tau_{xz}^{(1)} = \tau_{xz}^{(2)}, \quad \tau_{yz}^{(1)} = \tau_{yz}^{(2)}, \quad w^{(1)} = w^{(2)}, \end{gathered} \tag{2.2}$$

where all relations are written for the scattered component of the wave field. The superscripts (1, 2) are related to the upper $y \le 0$ and lower $y \ge 0$ half-planes, respectively. By introducing the unknown function of the crack opening

$$\left(w^{(2)} - w^{(1)}\right)(x, 0) = \begin{cases} 0, & |x| > a, \\ q_z(x), & |x| \le a. \end{cases} \tag{2.3}$$

and applying the Fourier transform, this classical problem can be reduced to the integral equation which holds over the length of the crack [1]:

$$\begin{gathered} \int_{-a}^{a} q_z(\xi) K_z(x - \xi)\, d\xi = -2ik_s \cos\theta e^{-ik_s x \sin\theta}, \\ K_z(x) = \frac{1}{2\pi} \int_{-\infty}^{\infty} L_z(s) e^{-ixs}\, ds, \quad L_z(s) = \sqrt{s^2 - k_s^2}, \quad |x| \le a. \end{gathered} \tag{2.4}$$

The scattered field at any point in the plane is presented in the following form:

$$w^{sc}(x,y) = \frac{1}{2\pi}\int_{-\infty}^{\infty} F_z(s)e^{-\sqrt{s^2-k_s^2}|y|}e^{-ixs}ds,$$
$$F_z(s) = \text{sign}(y)\int_{-a}^{a} q_z(\xi)e^{i\xi s}d\xi. \tag{2.5}$$

The leading asymptotic term of the high-frequency solution to integral equation (2.4) is constructed by using the Wiener-Hopf method [5, 6]:

$$q_z(x) = q_1(a+x) + q_2(a-x) - q_0(x),$$
$$q_{1,2}(a \pm x) = \frac{B_{1,2}e^{\mp ixk_s\sin\theta}e^{-\pi i/2}\,\text{Erf}\left[e^{-\pi i/4}\sqrt{(k_s \pm k_s\sin\theta)(a\pm x)}\right]}{\sqrt{k_s \pm k_s\sin\theta}},$$
$$q_0(x) = 2\,e^{-ixk_s\sin\theta},\quad B_{1,2} = \frac{2k_s\cos(\theta)e^{\pm iak_s\sin\theta}}{\sqrt{\pm k_s\sin\theta - k_s}}. \tag{2.6}$$

After that the far-field representation, (with $R \to \infty$), is [7]:

$$w^{sc}(x,y) \approx sign(y)\sqrt{\frac{k_s}{2\pi R}}\sin\varphi e^{i(k_sR-\pi/4)}\int_{-a}^{a} q_z(\xi)d\xi e^{-i\xi k_s\cos\varphi}. \tag{2.7}$$

3 Anti-plane Diffraction Problem for Interface Crack

Let us consider the SH- (anti-plane) problem on diffraction of a plane incident transverse wave by a straight finite-length crack $x \in (-a, a)$, $y = 0$ located on the interface boundary between two different linear elastic isotropic half-planes. Let all quantities related to the upper medium $y \geq 0$ be designated by subscript 1, and related to the lower medium $y \leq 0$ – by subscript 2. The incident wave arrives from infinity in medium 1, forming angle θ with respect to vertical axis y: $w^{inc}(x,y) = \exp[-ik_1(x\sin\theta + y\cos\theta)]$, where k_1 is the transverse wave number for the upper half-space, and time-dependent factor $\exp(-i\omega t)$ is hidden. Then the transverse displacements w_j satisfy the Helmholtz equations in the upper ($j = 1$) and lower ($j = 2$) half-spaces, respectively [6]:

$$\frac{\partial^2 w_j}{\partial x^2} + \frac{\partial^2 w_j}{\partial y^2} + k_j^2 w = 0,\quad k_j = \frac{\omega}{c_j},\quad c_j^2 = \frac{\mu_j}{\rho_j},\quad j = 1, 2, \tag{3.1}$$

where μ_j and ρ_j designate elastic shear modulus and mass density for respective medium. The boundary conditions are stress-free faces of the crack and the continuity of the displacement and the stress on the interface outside the crack ($y = 0$):

$$\frac{\partial w_1}{\partial y} = \frac{\partial w_2}{\partial y} = 0, \quad |x| \le a; \qquad w_1 = w_2, \ \mu_1 \frac{\partial w_1}{\partial y} = \mu_2 \frac{\partial w_2}{\partial y}, \ |x| > a\,. \tag{3.2}$$

Let us represent the wave field in the upper medium as the sum of the incident and the scattered ones: $w_1 = e^{-ik_1(x\sin\theta + y\cos\theta)} + w_1^{sc}$. By applying the Fourier transform along x-axis: $w_1(x, y) \Longrightarrow W_1(s, y)$, $w_2(x, y) \Longrightarrow W_2(s, y)$, one easily obtains from (3.1):

$$\begin{aligned} W_1 =& A_1(s)e^{-\gamma_1 y} + 2\pi\delta(s - k_1\sin\theta)e^{-ik_1 y\cos\theta}, \\ W_2 =& A_2(s)e^{\gamma_2 y}, \quad \gamma_j = \sqrt{s^2 - k_j^2}, \ j = 1, 2, \end{aligned} \tag{3.3}$$

where the following obvious relation (δ is Dirac's delta-function):

$$\int_{-\infty}^{\infty} e^{-ik_1 x\sin\theta}\, e^{ixs}\, dx = 2\pi\delta(s - k_1\sin\theta) \tag{3.4}$$

has been used, and A_1, A_2 are two arbitrary functions of Fourier parameter s. It should be noted that expressions (3.3) automatically satisfy the radiation condition at infinity.

It follows from (3.2) that $\mu_1 \partial w_1/\partial y = \mu_2 \partial w_2/\partial y$, $y = 0$ for all $|x| < \infty$. This implies:

$$-\mu_1[\gamma_1 A_1 + 2\pi i k_1 \cos\theta\ \delta(s - k_1\sin\theta)] = \gamma_2\mu_2 A_2. \tag{3.5}$$

In order to obtain a second relation between two quantities A_1 and A_2, let us introduce the new unknown function $q_z(x) : q_z(x) = w_1(x, +0) - w_2(x, -0)$, $|x| \le a$. Therefore, if $q_z(x) \Longrightarrow Q(s)$, then

$$\begin{aligned} Q(s) &= W_1(s, 0) - W_2(s, 0) = A_1 + 2\pi\delta(s - k_1\sin\theta) - A_2 \\ &= 2\pi\left(1 - \frac{ik_1}{\gamma_1}\cos\theta\right)\delta(s - k_1\sin\theta) - \left(1 + \frac{\mu_2\gamma_2}{\mu_1\gamma_1}\right)A_2, \end{aligned} \tag{3.6}$$

where the value of A_1 in terms of A_2 has been used, see Eq. (3.5). Now, Eqs. (3.3) and (3.6) imply:

$$
\begin{aligned}
W_1(s,y) &= (-2\pi \frac{\mu_2\gamma_2 + \mu_1 ik_1\cos\theta}{\mu_1\gamma_1 + \mu_2\gamma_2}\,\delta(s-k_1\sin\theta) \\
&\quad + \frac{\gamma_2\mu_2 Q(s)}{\mu_1\gamma_1+\mu_2\gamma_2})e^{-\gamma_1 y} + 2\pi\delta(s-k_1\sin\theta)e^{-ik_1 y\cos\theta} \\
W_2(s,y) &= \mu_1(2\pi \frac{\gamma_1 - ik_1\cos\theta}{\mu_1\gamma_1+\mu_2\gamma_2}\,\delta(s-k_1\sin\theta)) \\
&\quad - \frac{\gamma_1 Q(s)}{\mu_1\gamma_1+\mu_2\gamma_2})e^{\gamma_2 y}.
\end{aligned}
\tag{3.7}
$$

Then the remaining unused boundary condition in (3.2), $\partial w_2(x,0)/\partial y = 0$, $|x| \le a$, by applying the inverse Fourier transform to (3.7), results to the basic integral equation for function $q_z(x)$, ($\mathrm{Re}\sqrt{s^2-1} \ge 0$, $\mathrm{Re}\sqrt{s^2-k^2} \ge 0$):

$$
\int_{-ak_1}^{ak_1} q_z(\xi)K(x-\xi)d\xi = f(x),\ |x| \le ak_1;\quad K(x) = \frac{1}{\pi}\int_0^\infty L(s)\cos(xs)ds,
$$

$$
L(s) = \frac{\sqrt{s^2-1}\,\sqrt{s^2-k^2}}{\mu\sqrt{s^2-1}+\sqrt{s^2-k^2}},\quad \mu = \frac{\mu_1}{\mu_2},\ k^2 = \frac{k_2^2}{k_1^2} = \frac{\mu_1\rho_2}{\mu_2\rho_1},
$$

$$
f(x) = \left[\frac{(\sqrt{s^2-1}-i\cos\theta)\sqrt{s^2-k^2}}{\mu\sqrt{s^2-1}+\sqrt{s^2-k^2}}e^{-ixs}\right]_{s=\sin\theta} = Ae^{-ix\sin\theta},
$$

$$
A = \frac{-2i\cos\theta\sqrt{\sin^2\theta-k^2}}{\sqrt{\sin^2\theta-k^2}-i\mu\cos\theta},
\tag{3.8}
$$

written in a dimensionless form.

It can easily be proved that the denominator of the fraction in function $L(s)$ does not vanish. It can also be estimated that $K(x) = O(1/x^2)$, $x \to 0$. Some stable numerical algorithms for such hyper-singular integral equations are described in [7, 8].

In the high-frequency regime numerical treatment of Eq. (3.8) becomes inefficient, since this leads to a huge size of the discrete mesh. For this reason, let us construct an asymptotic solution of the integral equation, as $ak_1 \to \infty$. The method we use is allied to the classical "Edge Waves" technique [1]. Let us represent the solution as a combination of three functions:

$$
q_z(x) = q_1(ak_1 + x) + q_2(ak_1 - x) - q_0(x),
\tag{3.9}
$$

satisfying, respectively, the following three equations:

$$\int\limits_{-ak_1}^{\infty} q_1(ak_1+\xi)K(x-\xi)d\xi = f(x)+\int\limits_{-\infty}^{-ak_1}[q_2(ak_1-\xi)-q_0(\xi)]K(x-\xi)d\xi,$$

$$-ak_1 < x < \infty$$

$$\int\limits_{-\infty}^{ak_1} q_2(ak_1-\xi)K(x-\xi)\,d\xi = f(x)+\int\limits_{ak_1}^{\infty}[q_1(ak_1+\xi)-q_0(\xi)]K(x-\xi)\,d\xi,$$

$$-\infty < x < ak_1,$$

$$\int\limits_{-\infty}^{\infty} q_0(\xi)\,K(x-\xi)\,d\xi = f(x), \quad -\infty < x < \infty. \tag{3.10}$$

The leading asymptotic term of the solution can be constructed by rejecting the residual integrals in the right-hand sides of the first and the second lines of (3.10). Then these two equations become the standard Wiener-Hopf equations on semi-infinite intervals. As soon as they are solved, the correctness of the hypothesis, that the rejected right-hand-side tails are asymptotically small, can be checked by substituting the found solutions into those tail integrals. Physically, this means that the reciprocal wave influence of the edges to each other is asymptotically small in the first approximation.

The third equation of (3.10) is a simple convolution integral equation on the infinite axis and its solution is easily obtained by the Fourier transform ($f(x) \Longrightarrow F(s)$):

$$q_0(x) = A\int\limits_{-\infty}^{\infty}\frac{\delta(s-\sin\theta)}{L(s)}e^{-ixs}ds = \frac{Ae^{-ix\sin\theta}}{L(\sin\theta)} = 2\,e^{-ix\sin\theta}. \tag{3.11}$$

It is very interesting to notice that $q_0(x)$ is the same as it could be predicted by Kirchhoff's physical diffraction theory [1].

The Wiener-Hopf equations discussed above, after evident change of variables $x' = ak_1 \pm x$, $\xi' = ak_1 \pm \xi$, can be rewritten in a more standard form, holding over interval $(0, \infty)$ for $0 \le x' < \infty$:

$$\int\limits_{0}^{\infty} q_{1,2}(\xi')K(x'-\xi')\,d\xi' = f_{1,2}(x'), \quad f_{1,2}(x') = f[\pm(x'-ak_1)]. \tag{3.12}$$

Further steps of the Wiener-Hopf method are rather standard [5]. The solution to Eq. (3.12) is obtained in the following form ($q_{1,2}(x') \Longrightarrow Q^{+}_{1,2}(s)$):

$$Q^{+}_{1,2}(s) = \frac{Ae^{\pm iak_1 \sin\theta}}{iL^{-}(\pm\sin\theta)(\pm\sin\theta - s)L^{+}(s)}, \qquad L(s) = L^{+}(s)L^{-}(s), \tag{3.13}$$

which after application of the inverse Fourier transform gives the solution to Eq. (3.7). Note that superscripts "+" and "−" designate functions analytical in the upper (Im $s \geq 0$) and the lower (Im $s \leq 0$) half-planes of complex-valued variable s. It should also be noted that $L = L^{+}L^{-}$ is the factorization of function $L(s)$. As proposed in [6], the denominator of expression (3.3b) is approximated as follows:

$$\mu\sqrt{s^2-1} + \sqrt{s^2-k^2} \approx \frac{\mu+1}{(B+1)^2}\left(B\sqrt{s+1} + \sqrt{s+k}\right)_{+} \cdot \left(B\sqrt{s-1} + \sqrt{s-k}\right)_{-}.$$

With this approximation the efficient factorization of function $L(s)$ is easily constructed as follows:

$$L(s) = \left[\frac{(B+1)\sqrt{s+1}\,\sqrt{s+k}}{\sqrt{\mu+1}\,(B\sqrt{s+1} + \sqrt{s+k})}\right]_{+}\left[\frac{(B+1)\sqrt{s-1}\,\sqrt{s-k}}{\sqrt{\mu+1}\,(B\sqrt{s-1} + \sqrt{s-k})}\right]_{-} \tag{3.14}$$

The introduced parameter $B = B(\mu, k) > 0$ may be chosen, for given values of physical parameters μ and k, to provide better approximation uniformly over all finite real-valued values of variable $s \in (-\infty, \infty)$. In the case when $\mu_1/\mu_2 = \rho_1/\rho_2$ parameter $k = 1$, hence the approximation is absolutely precise with $B = 0$. By calculating the maximum relative error ε, between exact and approximating complex-valued functions, for $s \in (-\infty, \infty)$, one should take only physically true cases when both μ_1/μ_2 and ρ_1/ρ_2 relations are simultaneously less or greater than the unit value. Then the numerical investigation shows that the maximum relative error ε is always less than 1–2%. Then Eq. (3.14) takes the form:

$$Q^{+}_{1,2}(s) = \frac{De^{\pm iak_1 \sin\theta}}{(\pm\sin\theta - s)}\left(\frac{1}{\sqrt{1 \mp \sin\theta}} + \frac{B}{\sqrt{k \mp \sin\theta}}\right)\left(\frac{1}{\sqrt{s+1}} + \frac{B}{\sqrt{s+k}}\right),$$
$$D = \frac{A(\mu+1)}{(B+1)^2}. \tag{3.15}$$

The Fourier inversion of this function may be performed by passing to inverse Laplace transform with the change $is = -p$, $s = ip$, where p is the Laplace parameter. Expression (3.15) contains elementary functions with tabulated Laplace inversions [9]:

$$\frac{1}{(\alpha - s)\sqrt{s+\beta}} = \frac{e^{\pi i/4}}{(p + i\alpha)\sqrt{p - i\beta}}, \iff \frac{ie^{-i\alpha x'}}{\sqrt{\alpha+\beta}}\,\mathrm{Erf}\left[e^{-\pi i/4}\sqrt{(\alpha+\beta)x'}\right],$$

where $\mathrm{Erf}(z)$ is the probability integral. Since $x' = ak_1 \pm x$, the inversion of (3.15) gives

$$q^{+}_{1,2}(ak_1 \pm x) = Di\left(\frac{1}{\sqrt{1 \mp \sin\theta}} + \frac{B}{\sqrt{k \mp \sin\theta}}\right) e^{\mp ix\sin\theta}$$
$$\times \left\{\frac{\mathrm{Erf}\left[e^{-\pi i/4}\sqrt{(1 \pm \sin\theta)(ak_1 \pm x)}\right]}{\sqrt{1 \pm \sin\theta}} + \frac{B\,\mathrm{Erf}\left[e^{-\pi i/4}\sqrt{(k \pm \sin\theta)(ak_1 \pm x)}\right]}{\sqrt{k \pm \sin\theta}}\right\}.$$

On the basis of this explicit asymptotic representation it can be proved that the right-hand-side "tails" in Eq. (3.10) tend to zero, as $ak_1 \to \infty$, that is to be proved to justify the basic hypothesis permitting rejection of the tails.

By applying the inverse Fourier transform to Eq. (3.7), one comes to the displacement functions, corresponding to the scattered field for each half-plane ($\mu = \mu_1/\mu_2$):

$$w^{sc}_1(x,y) = -\frac{1}{2\pi}\int\limits_{-a}^{a} q_z(\xi)d\xi \int\limits_{-\infty}^{\infty} \frac{\gamma_2(s)}{\mu\gamma_1(s) + \gamma_2(s)} e^{-\gamma_1(s)y - is(x-\xi)}ds, \quad y > 0,$$
$$w^{sc}_2(x,y) = \frac{1}{2\pi}\int\limits_{-a}^{a} q_z(\xi)d\xi \int\limits_{-\infty}^{\infty} \frac{\mu\gamma_1(s)}{\mu\gamma_1(s) + \gamma_2(s)} e^{\gamma_2(s)y - is(x-\xi)}ds, \quad y < 0. \tag{3.16}$$

Let $x - \xi = R\cos\varphi - \xi = r\cos\psi$, $y = R\sin\varphi = r\sin\psi$, $(R, r) \to \infty$. Then functions (3.16) can be rewritten in the following form:

$$w^{sc}_j(x,y) = \frac{1}{2\pi}\int\limits_{-a}^{a} q_z(\xi)d\xi \int\limits_{-\infty}^{\infty} F_j(s) e^{ir\left(\sqrt{k_j^2 - s^2}\sin\varphi + s\cos\varphi\right)}ds, \quad j = 1, 2,$$
$$F_1(s) = -\frac{\gamma_2(s)}{\mu\gamma_1(s) + \gamma_2(s)}, \qquad F_2(s) = \frac{\mu\gamma_1(s)}{\mu\gamma_1(s) + \gamma_2(s)}. \tag{3.17}$$

Further treatment is based upon the classical far field approximation for the quantity r in the argument of the exponential functions in (3.17):

$$r = \sqrt{x^2 + y^2 - 2x\xi + \xi^2} \approx R - \xi\cos\varphi + O(1/R), \quad R = \sqrt{x^2 + y^2} \to \infty.$$

Thus, the asymptotic estimate takes the following form, as $R \to \infty$, $j = 1, 2$, [7]:

$$w^{sc}_j(x,y) \approx \sqrt{\frac{k_j}{2\pi R}}\sin\varphi e^{i(k_j R - \pi/4)} F_j(k_j\cos\varphi) \int\limits_{-a}^{a} q_z(\xi)d\xi e^{-i\xi k_j\cos\varphi} \tag{3.18}$$

and the problem is then reduced to the calculation of the arisen integral.

As in the scalar problem of diffraction by a linear scatterer, the developed method allows one to obtain the far field scattering pattern of the interface linear crack of finite length for middle and high frequencies.

4 In-Plane Diffraction Problem

In this section we consider the (2d) in-plane problem of the same geometry ($|x| \le 1$, $y = 0$). The in-plane longitudinal wave is incident on the crack at the angle θ relatively axis y with the wave potentials:

$$\varphi^{inc}(x, y) = e^{-ik_p(x\sin\theta + y\cos\theta)}; \quad \psi^{inc}(x, y) = 0. \tag{4.1}$$

Noting the potentials for the upper half-plane $y \ge 0$ by subindex (1), for the lower $y \le 0$ by (2), the total wave field can be represented as a sum of incident and scattered ones, $j = 1, 2$:

$$\varphi_j(x, y) = \varphi_j^{inc}(x, y) + \varphi_j^{sc}(x, y); \quad \psi_j(x, y) = \psi_j^{sc}(x, y), \quad \psi_j^{inc} \equiv 0. \tag{4.2}$$

The scattered components of the solution in terms of the Fourier transform, in accordance with Zommerfeld's radiation condition, take the forms:

$$\Phi_{1,2}(s, y) = A_{1,2}(s)e^{-\gamma(s)|y|}, \quad \gamma(s) = \sqrt{s^2 - k_p^2}; \tag{4.3}$$

$$\Psi_{1,2}(s, y) = B_{1,2}(s)e^{-\beta(s)|y|}, \quad \beta(s) = \sqrt{s^2 - k_s^2}. \tag{4.4}$$

The unknown quantities A_j, B_j can be found using the following boundary conditions:

$$y = 0, \quad |x| \le 1: \ \tau_{xy}^{(1,2)} = -\tau_{xy}^{inc}; \quad \tau_{yy}^{(1,2)} = -\tau_{yy}^{inc}; \tag{4.5}$$

$$\begin{aligned} &y = 0, \quad |x| > 1: \ \tau_{xy}^{(1)} = \tau_{xy}^{(2)}; \quad \tau_{yy}^{(1)} = \tau_{yy}^{(2)}; \\ &U_x^{(1)} = U_x^{(2)}; \quad U_y^{(1)} = U_y^{(2)}. \end{aligned} \tag{4.6}$$

Let us introduce the normal opening of the crack $g_y(x)$ and the tangential one $q_x(x)$, which are the relative displacements of the opposite crack faces ($y = 0$):

$$U_x^{(1)} - U_x^{(2)} = \begin{cases} 0, & |x| > 1; \\ q_x(x), & |x| \le 1; \end{cases} \quad U_y^{(1)} - U_y^{(2)} = \begin{cases} 0, & |x| > 1; \\ q_y(x), & |x| \le 1. \end{cases} \tag{4.7}$$

Then, the same technique like applied above in the anti-plane problems, leads to the system of integral equations with respect to functions $q_x(x)$, $q_y(x)$, $|x| \le 1$:

$$\int_{-1}^{1} q_x(\xi)K_x(x - \xi)\, d\xi = -k_p^2 k_s^2 \sin 2\theta e^{-ik_p x\sin\theta}, \tag{4.8}$$

$$c^2 \int_{-1}^{1} q_y(\xi) K_y(x-\xi)\, d\xi = 2k_p^2 k_s^2 (2c^2 \sin^2\theta - 1) e^{-ik_p x \sin\theta}, \tag{4.9}$$

where

$$K_x(x) = \frac{1}{2\pi} \int_{-\infty}^{\infty} L_x(s) e^{-isx}\, ds; \quad L_x(s) = \frac{\Delta(s)}{\beta(s)},$$

$$K_y(x) = \frac{1}{2\pi} \int_{-\infty}^{\infty} L_y(s) e^{-isx}\, ds; \quad L_y(s) = \frac{\Delta(s)}{\gamma(s)},$$

$|x| \le 1, y = 0, c^2 = k_p^2/k_s^2, \Delta(s) = (2s^2 - k_s^2)^2 - 4s^2\gamma(s)\beta(s)$ – the Rayleigh function. It can directly be shown that the kernels in Eqs. (4.8), (4.9) possess hypersingular behavior as $\xi \to x$, like in the anti-plane problem.

By analogy to the above consideration, the high-frequency solution for the integral equations (4.8), (4.9) can be obtained by the same Wiener-Hopf method [5, 6]:

$$q(x) = q_1(a+x) + q_2(a-x) - q_0(x), \quad q(x) = q_{x,y}(x). \tag{4.10}$$

By applying the inverse Fourier transform to (4.3), (4.4), one comes to the potentials, corresponding to the scattered field for the lower half-plane ($y < 0$):

$$\begin{aligned}
\varphi_2^{sc}(x,y) &= \frac{1}{2\pi} \int_{-a}^{a} q_x(\xi) d\xi \int_{-\infty}^{\infty} \frac{is}{k_s^2} e^{\gamma(s)y - is(x-\xi)} ds \\
&\quad - \frac{1}{2\pi} \int_{-a}^{a} q_y(\xi) d\xi \int_{-\infty}^{\infty} \frac{2s^2 - k_s^2}{2\gamma(s)k_s^2} e^{\gamma(s)y - is(x-\xi)} ds, \\
\psi_2^{sc}(x,y) &= -\frac{1}{2\pi} \int_{-a}^{a} q_y(\xi) d\xi \int_{-\infty}^{\infty} \frac{is}{k_s^2} e^{\beta(s)y - is(x-\xi)} ds \\
&\quad - \frac{1}{2\pi} \int_{-a}^{a} q_x(\xi) d\xi \int_{-\infty}^{\infty} \frac{2s^2 - k_s^2}{2\beta(s)k_s^2} e^{\beta(s)y - is(x-\xi)} ds,
\end{aligned} \tag{4.11}$$

Thus, the asymptotic estimate of the infinite integrals in (4.11) take the following form in the far zone ($R \to \infty$), [5]:

$$\begin{aligned}
\varphi_2^{sc}(x,y) \approx \sqrt{\frac{k_p}{2\pi R}} e^{i(k_p R - \pi/4)} \Big(&\int_{-a}^{a} q_x(\xi) \frac{ik_p \sin 2\varphi}{2k_s^2} e^{-i\xi k_p \cos\varphi} d\xi \\
&+ \int_{-a}^{a} q_y(\xi) \frac{2k_p^2 \cos^2\varphi - k_s^2}{2ik_p k_s^2} e^{-i\xi k_p \cos\varphi} d\xi \Big)
\end{aligned} \tag{4.12}$$

$$\psi_2^{sc}(x,y) \approx \sqrt{\frac{k_s}{2\pi R}} e^{i(k_s R - \pi/4)} \Big(\int_{-a}^{a} q_x(\xi) \frac{\cos 2\varphi}{2ik_s} e^{-i\xi k_s \cos\varphi} d\xi$$

$$- \int_{-a}^{a} q_y(\xi) \frac{i \sin 2\varphi}{2k_s} e^{-i\xi k_s \cos\varphi} d\xi \Big) \tag{4.13}$$

and the problem is again reduced to the calculation of the arisen integrals. The far zone scattered fields for $y > 0$ can be obtained by analogy, being omitted for the sake of brevity.

5 Results and Conclusions

5.1 *Anti-plane Problem in Homogeneous Medium*

Some examples of the numerical calculations are presented in Figs. 1 and 2. If the angle of incidence θ, frequency parameter ak_s and radius R are fixed, then the behavior of the amplitude of the scattered field $|w_z^{sc}(x,y)|$ versus angle of observation φ illustrates the property that the symmetric leaves of the diagrams in both the upper and the lower half-planes become shorter with increasing of θ (see Fig. 1). If one defines here the mirror mode, when the direction of the reflected wave is dominant at high frequencies in the direction of the incident wave, then the angles of observation φ and incidence θ are related by the ratio $\varphi = \pi/2 - \theta$. It is obvious from Fig. 2 that in the mirror mode the scattering diagram for higher ak_s has longer leaves than the ones for lower frequencies. Within this observation, one can also state that the highest value of the scattering amplitude takes place for normal incidence.

5.2 *Anti-plane Problem for Interface Crack*

The next examples are presented in Figs. 3, 4 and 5 for a pair of different elastic materials, with $k_1 = k_2$. All the Figures demonstrate behavior of the high-frequency scattering diagram $|w_j^{sc}(x,y)|$, in the upper ($j = 1$) and the lower ($j = 2$) medium versus angle of observation φ (Figs. 3 and 4) and angle of incidence θ, in the mirror mode (Fig. 5). Different lines in these figures are related to different values of θ, (Fig. 3), and to the scattering diagrams in the mirror mode with replacing materials between the upper and the lower half-planes, Fig. 5.

If angle θ, frequency parameter ak_1 and radius R are fixed, then the behavior of functions $|w_j^{sc}(x,y)|$ versus φ indicates that the the longest leaves of the diagram in each half-plane become shorter with the increasing of θ, see Fig. 3. Here the mass densities are related as $\rho_1 = 2\rho_2$. The highest value of the scattering diagram takes

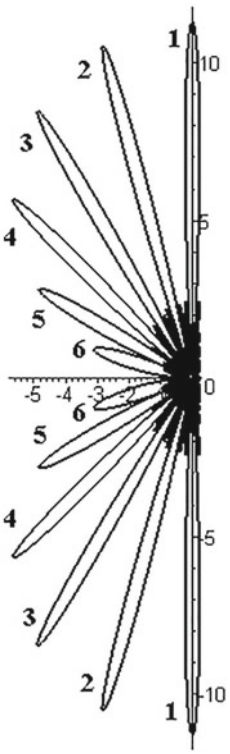

Fig. 1 Scattering diagram versus polar angle φ of the observation: $ak_s = 50$. Line $1 - \theta = 0°$, line $2 - \theta = 15°$, line $3 - \theta = 30°$, line $4 - \theta = 45°$, line $5 - \theta = 60°$, line $6 - \theta = 75°$

place for the normal incidence ($\theta = 0$) that is natural from the physical point of view. For fixed θ, the scattered amplitude in the upper medium is weaker than in the lower one. The same property takes place when the materials of the upper and the lower half-planes are replaced: $\rho_1 = \rho_2/2$ (Fig. 4). Such a physical regime provides in two times longer lengths of leaves, compared to respective diagrams in Fig. 1. When replacing the materials of the upper and the lower half-planes, one can observe that weaker scattering takes place if mass density of the first medium is higher than of the second one. The greatest magnitude of the mirror mode diagrams take place when $\theta = 0$, which is a normal direction with respect to the line of the crack (Fig. 5).

5.3 In-Plane Problem

Some results for the in-plane problem are presented in Figs. 6 and 7. For fixed θ, frequency parameters ak_s, ak_p, $(k_s/k_p = 1.8)$ and radius R, the behavior of the principal amplitude $|\varphi_j^{sc}(x, y)|$ versus φ also demonstrates decreasing of almost equal and symmetric leaves in the upper $(j = 1)$ and lower $(j = 2)$ half-plane, with the increasing of θ (see Fig. 6). For the transverse potential $|\psi_j^{sc}(x, y)|$ with increasing

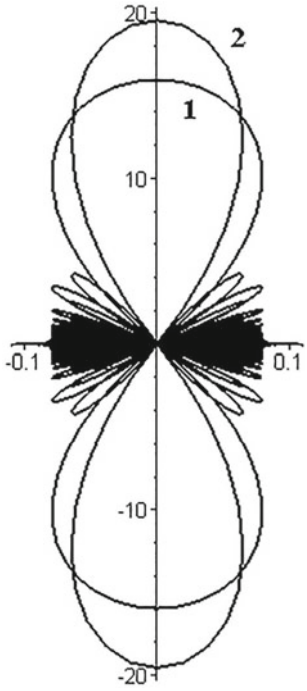

Fig. 2 Scattering diagram versus angle of incidence θ in the echo-regime: line $1 - ak_s = 100$, line $2 - ak_s = 150$

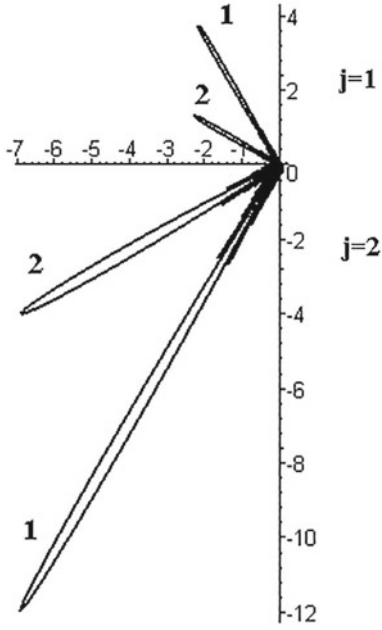

Fig. 3 Scattering diagram versus polar angle φ of the observation: $\rho_1/\rho_2 = 2,\ \mu_1/\mu_2 = 2,\ ak_1 = ak_2 = 100$. Line $1 - \theta = 30°$, line $2 - \theta = 60°$

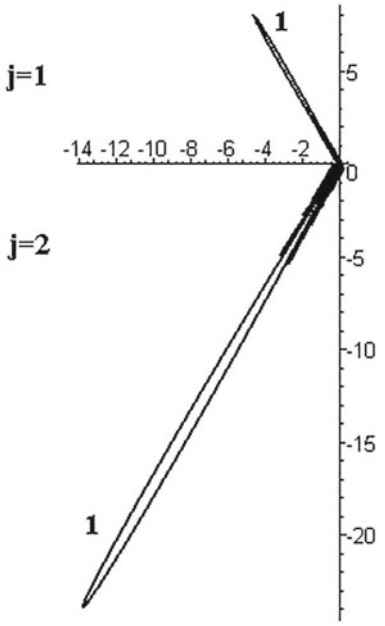

Fig. 4 Scattering diagram versus polar angle φ of the observation: $\rho_1/\rho_2 = 0.5,\ \mu_1/\mu_2 = 0.5,\ ak_1 = ak_2 = 100$. Line 1 – $\theta = 30°$

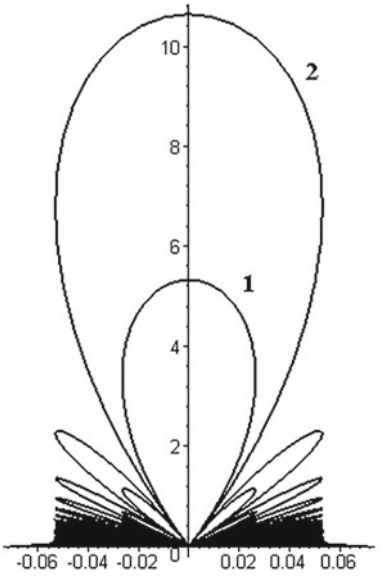

Fig. 5 Scattering diagram versus angle of incidence θ in the mirror-regime: $ak_1 = ak_2 = 100$. Line 1 – $\rho_1/\rho_2 = 2$, $\mu_1/\mu_2 = 2$, line 2 – $\rho_1/\rho_2 = 0.5$, $\mu_1/\mu_2 = 0.5$

of the incident angle one can observe the scattered leaves of different length in the upper and lower half-plane. It can be noted that the longitudinal potential is quantitatively dominant compared to the transverse one.

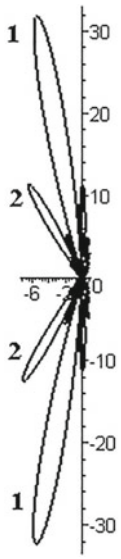

Fig. 6 Scattering diagram $|\varphi_j^{sc}|$ versus angle φ of the observation: $ak_s = 50$. Line $1 - \theta = 10°$, line $2 - \theta = 30°$

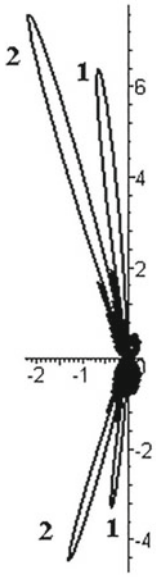

Fig. 7 Scattering diagram $|\psi_j^{sc}|$ versus angle φ of observation: $ak_s = 50$. Line $1 - \theta = 10°$, line $2 - \theta = 30°$

In the analysis for different frequencies it is obvious from Figs. 8 and 9 that with increasing of the ak_s, ak_p the magnitude of the scattering diagram for the potential grows, keeping dominance in the direction of incident wave. In the mirror mode, the scattering diagrams $|\varphi_j^{sc}|$, with fixed frequency parameter, like in the previous problems, have the dominance compared to respective $|\psi_j^{sc}|$. It should be noted that the longest scattering leaves correspond to the incidence with $\theta = 0$.

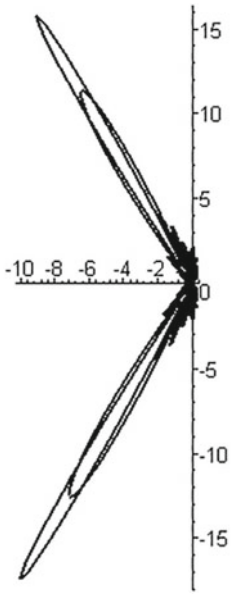

Fig. 8 Scattering diagram $|\varphi_j^{sc}|$ versus angle φ of observation: $\theta = 30°$. Short leaves – $ak_s = 50$, long leaves – $ak_s = 100$

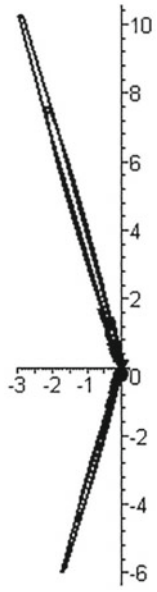

Fig. 9 Scattering diagram $|\psi_j^{sc}|$ versus angle φ of observation: $\theta = 30°$. Short leaves – $ak_s = 50$, long leaves – $ak_s = 100$

5.4 General Conclusions

The leading asymptotic terms for the solutions in problems 1–3 allow one to describe the properties of the far field scattering diagrams for the crack of finite length for any high frequency. The scattered field is completely determined by the direction of the incident wave. The highest values of the far-field amplitudes for the reflected wave take place in direction of the incident wave. With frequency increasing, the longest leaves of the scattered field keep their directions. The maximum levels of the mirror mode diagrams take place in the normal direction regarding the line of the crack.

When comparing the three studied problems with each other, it should be noted that in the anti-plane cases the increase of the angle of incidence leads to a gradual decrease of the lengths of the leaves in the scattering diagram, for the both half-planes. In the in-plane problem, with the same variation of the incident angle, the main leaves decrease much faster.

Acknowledgements The author expresses his gratitude to Professor M. A. Sumbatyan, Southern Federal University, Russia, for valuable comments. He would also like to notice that this work has been performed in frames of the project 9.5794.2017/8.9 under support of the Russian Ministry for Education and Science.

References

1. Ufimtsev, P.Y.: Fundamentals of the Physical Theory of Diffraction. Wiley, Hoboken, New Jercey (2007)
2. Colton, D., Kress, R.: Integral Equation Methods in Scattering Theory. SIAM, New York (1983)
3. Babich, V.M., Buldyrev, V.S.: Short-Wavelength Diffraction Theory. Springer, Heidelberg, Berlin (1989)
4. Shenderov, E.L.: Sound penetration through a rigid screen of finite thickness with apertures. Soviet Phys. Acoust. **16**(2) (1970)
5. Sumbatyan, M.A., Scalia, A.: Equations of Mathematical Diffraction Theory. CRC Press, Boca Raton, Florida (2005)
6. Remizov, M.Y., Sumbatyan, M.A.: A semi-analytical method of solving problems of the high-frequency diffraction of elastic waves by cracks. J. Appl. Math. Mech. **77**, 452–456 (2013)
7. Mittra, R., Lee, S.W.: Analytical Techniques in the Theory of Guided Waves. Macmillan, New York (1971)
8. Sumbatyan, M.A., Remizov, M.Y.: Asimotitic analysis in the anti-plane high-frequency diffraction by interface cracks. Appl. Math. Lett. **34**, 72–75 (2014)
9. Achenbach, J.D.: Wave Propagation in Elastic Solids. North-Holland, Amsterdam (1973)
10. Iovane, G., Lifanov, I.K., Sumbatyan, M.A.: On direct numerical treatment of hypersingular integral equations arising in mechanics and acoustics. Acta Mech. **162**, 99–110 (2003)
11. Chen, Z., Zhou, Y.F.: A new method for solving hypersingular integral equations of the first kind. Appl. Math. Lett. **24**, 636–641 (2011)
12. Fradkin, LJu, Stacey, R.: The high-frequency description of scatter of a plane compressional wave by an elliptic crack. Ultrasonics **50**, 529–538 (2010)
13. Rogoff, Z.M., Kiselev, A.P.: Diffraction at jump of curvature on an impedance boundary. J Wave Motion **33**, 183–208 (2001)

14. Gridin, D.: High-frequency asymptotic description of head waves and boundary layers surrounding the critical rays in an elastic half-space. J. Acoust. Soc. Am. **104**, 1188–1197 (1998)
15. Pal, S.C., Ghosh, M.L.: High frequency scattering of anti-plane shear waves by an interface crack Indian. J. Pure. Appl. Math. **21**, 1107–1124 (1990)

3d Propagation of Ultrasonic Waves Through a System of Defects in an Elastic Material, with Arbitrary Reflections and Transformations

Nikolay V. Boyev, Mezhlum A. Sumbatyan and Vittorio Zampoli

Abstract In frames of the three-dimensional problem, we study a short wavelength diffraction of elastic waves by a system of voids in the elastic medium. The defects are bounded by arbitrary smooth surfaces. The problem is reduced to a classical diffraction problem for high-frequency waves irradiated from a point source in the elastic medium by the system of voids located in this medium. We consider multiple reflections with various possible transformations of elastic waves. To study the problem, a special method is proposed, which is based on the asymptotic estimate of the diffraction integrals by the multidimensional stationary phase method. On the basis of the developed method, we obtain in explicit form the leading asymptotic term of the displacements in the diffracted field, for arbitrary cases of multiple reflections (longitudinal wave to longitudinal one and transverse wave to transverse one) and transformations (longitudinal wave to transverse one and transverse wave to longitudinal one), at the points of mirror reflections. The obtained explicit expressions for the displacements agree with the Geometrical Diffraction Theory (GDT) for elastic waves.

1 Introduction

The problems of the short wavelength diffraction by surfaces of the obstacles in acoustic and elastic media have broad application in the engineering practice. Impulses filled of short waves are used when investigating metamaterials produced as an inclusion of arrays of obstacles, as a rule—of a periodic structure, to a matrix of an elastic material. In evaluation of location and shape of the obstacles in the acoustic and elastic media, there are used sensors working in the ultrasonic range.

N. V. Boyev · M. A. Sumbatyan (✉)
Southern Federal University, 105/42 Bolshaya Sadovaya Str,
Rostov-on-Don 344006, Russian Federation
e-mail: sumbat@math.rsu.ru

V. Zampoli
University of Salerno, Via Giovanni Paolo II, 132, 84084 Fisciano (Salerno), Italy

M. A. Sumbatyan (ed.), *Wave Dynamics, Mechanics and Physics of Microstructured Metamaterials*, Advanced Structured Materials 109,
https://doi.org/10.1007/978-3-030-17470-5_14

The short-wave diffraction of the acoustic waves by curvilinear contours have bee studied by various methods [1, 2]. The single reflection of the elastic wave in the two-dimensional case is studied in [2, 3]. In frames of the three-dimensional problem in [4, 5] the authors develop an approximation of the geometrical optics in explicit form, for acoustic waves with single and multiple [5] reflections from arbitrary smooth surfaces. In [6] there are studied single and double reflections of the elastic waves with arbitrary transformations. In [7] the authors study a propagation of the plane longitudinal wave through a metamaterial which is a triple-periodic system of rigid spheres embedded in an elastic matrix. In the present work, in frames of the three-dimensional local problem, we propose a method, to study multiple reflections of the longitudinal wave to the longitudinal one, multiple periodic transformation of the elastic wave (with the period "longitudinal-transverse-longitudinal") and the sequence of arbitrary multiple reflections and transformations, based upon an estimate of the Kirchhoff diffraction integral by the multidimensional stationary phase method.

2 Formulation of the Three-Dimensional Local Problem

Let a spherical monochromatic high-frequency wave irradiated from point x_0 fall to a boundary surface (Fig. 1). The spherical wave is generated by the force $\mathbf{Q}e^{-i\omega t}$ located at point x_0, where ω is the frequency of the oscillations. The displacements at the point y of elastic medium, caused by this wave, are defined by the Kupradze matrix [8]:

$$
\begin{aligned}
&U_j^{(k)}(y, x_0) = U_{jp}^{(k)}(y, x_0) + U_{js}^{(k)}(y, x_0),\\
&U_{jp}^{(k)}(y, x_0) = -\frac{1}{4\pi\rho\omega^2}\frac{\partial^2}{\partial y_k \partial y_j}\left(\frac{e^{ik_p R_0}}{R_0}\right), \quad k, j = 1, 2, 3,\\
&U_{js}^{(k)}(y, x_0) = \frac{1}{4\pi\rho\omega^2}\left[k_s^2\delta_{kj}\left(\frac{e^{ik_s R_0}}{R_0}\right) + \frac{\partial^2}{\partial y_k \partial y_j}\left(\frac{e^{ik_s R_0}}{R_0}\right)\right], R_0 = |x_0 - y|. \quad (1)
\end{aligned}
$$

Here λ, μ are the Lamé coefficients, ρ is the mass density of the elastic material, $k_p = \omega/c_p$, $k_s = \omega/c_s$, are the wave numbers, and c_p, c_S are the speeds of the longitudinal and transverse waves, respectively, δ_{kj} is the Kronecker delta.

The aim of the present work is to study the amplitude characteristics of the wave diffracted by the array of void obstacles in the elastic material.

3 Method of Solution

The dependence on time of all physical quantities is assumed harmonic. For example, for the displacements in the elastic medium this reads: $\mathbf{u}(x_1, x_2, x_3, t) =$

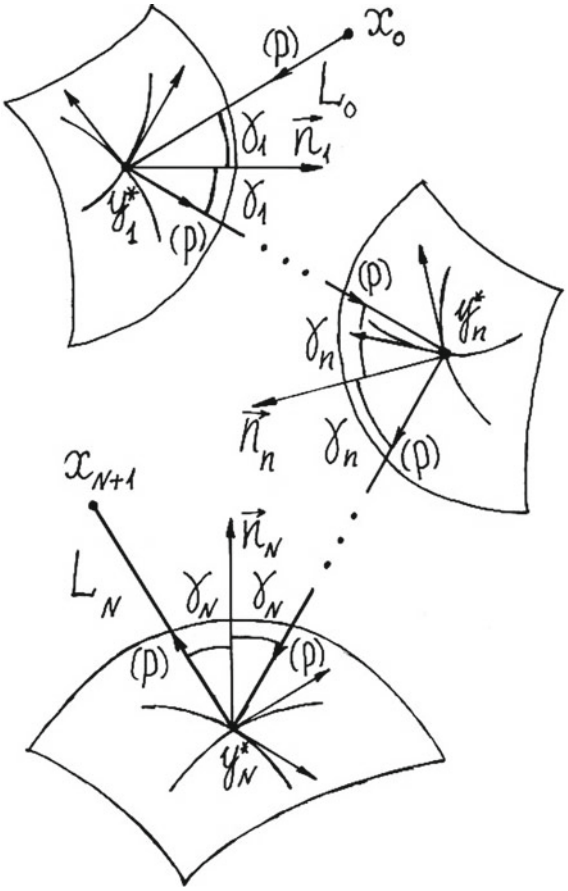

Fig. 1 N-fold $p-p-p-\cdots-p-p-p$ re-reflection of the high-frequency longitudinal wave along the ray $x_0 - y_1^* - y_2^* - \cdots - y_{N-1}^* - y_N^* - x_{N+1}$ on the free boundary surfaces of a system of N voids located in the elastic medium

$\mathrm{Re}\big[\mathbf{u}\,(x_1, x_2, x_3)\exp(-i\,\omega\,t)\big]$, where $\mathbf{u}(x_1, x_2, x_3)$ is the amplitude of the oscillations.

The Kupradze matrix defines at the point точке y to the radial direction $\mathbf{q} = (\mathbf{x}_0\mathbf{y})\cdot|\mathbf{x}_0\mathbf{y}|^{-1}$ nontrivial some displacements in the longitudinal (p-wave) and transverse (s-wave) waves. The explicit form of these displacements in the incident wave is written out in [6]. In the high-frequency regime, as $k_p \to \infty$ and $k_s \to \infty$ in directions $\mathbf{q}$ and $\mathbf{q}_1$ one obtains the following asymptotic representation in the incident wave

$$\mathbf{u}_{\mathbf{q}}^{(p)}(y) = Q_{\mathbf{q}}\mathbf{q}\frac{k_p^2}{4\pi\,\rho\,\omega^2}\frac{e^{ik_pR_0}}{R_0}\left[1 + \mathrm{O}\left(\frac{1}{k_pR_0}\right)\right], \quad Q_{\mathbf{q}} = (\mathrm{Q}, \mathrm{q}), \tag{2}$$

$$\mathbf{u}_{\mathbf{q}_1}^{(s)}(y) = Q_{\mathbf{q}_1}\mathbf{q}_1\frac{k_s^2}{4\pi\,\rho\,\omega^2}\frac{e^{ik_sR_0}}{R_0}\left[1 + \mathrm{O}\left(\frac{1}{k_s\,R_0}\right)\right], \quad Q_{\mathbf{q}_1} = \big(\mathrm{Q}, \mathrm{q}_1\big). \tag{3}$$

The direction $\mathbf{q}_1$ is perpendicular to $\mathbf{q}$. $Q_{\mathbf{q}}$, and $Q_{\mathbf{q}_1}$ is the projection of the force $\mathbf{Q}$ in directions $\mathbf{q}$ and $\mathbf{q}_1$, respectively.

The Cartesian components of the displacement vector in the wave reflected from the free boundary surface at point x of the elastic medium can be written out as the Somilyana representation [9]

$$u_k(x) = \iint\limits_S \mathbf{T}_y[\mathbf{U}^{(k)}(y,x)] \cdot \mathbf{u}(y) dS_y, \quad k = 1,2,3, \tag{4}$$

$$\mathbf{T}_y\big[\mathbf{U}^{(k)}(y,x)\big] = 2\mu \frac{\partial \mathbf{U}^{(k)}}{\partial n} + \lambda\, \mathbf{n}\, \mathrm{div}\big(\mathbf{U}^{(k)}\big) + \mu\big(\mathbf{n} \times \mathrm{rot}\big(\mathbf{U}^{(k)}\big)\big),\ y \in S, \tag{5}$$

Here the Kupradze matrix $\mathbf{U}^{(k)}(y,x)$ is obtained from the matrix $\mathbf{U}^{(k)}(y,x_0)$ (1) by the change of point x_0 to point x and he distance R_0 to the distance $R = |y - x|$, $\mathbf{T}_y$ is the force vector at point y, $\mathbf{u}(y)$ is the vector of full displacement field over the boundary surface of the void, $\mathbf{n}$ is the unit normal to surface S.

Let us extract, from the vectors of full displacement on the boundary surface and the force vector $\mathbf{T}_y$ at point y, the term which is defined by the longitudinal (p) and transverse (s) waves:

$$u_k(x) = \iint\limits_S \left\{\mathbf{T}_y[\mathbf{U}_p^{(k)}(y,x)] + \mathbf{T}_y[\mathbf{U}_s^{(k)}(y,x)]\right\} \cdot [\mathbf{u}(y;\, p) + \mathbf{u}(y;\, s)] dS_y,$$

$$u_k(x) = u_k(x;\, p{-}p) + u_k(x;\, p{-}s) + u_k(x;\, s{-}p) + u_k(x;\, s{-}s)$$

$$u_k(x;\, p{-}p) = \iint\limits_S \mathbf{T}_y[\mathbf{U}_p^{(k)}(y,x)] \cdot \mathbf{u}(y;\, p) dS_y, \tag{6}$$

$$u_k(x;\, p{-}s) = \iint\limits_S \mathbf{T}_y[\mathbf{U}_s^{(k)}(y,x)] \cdot \mathbf{u}(y;\, p) dS_y, \tag{7}$$

$$u_k(x;\, s{-}p) = \iint\limits_S \mathbf{T}_y[\mathbf{U}_p^{(k)}(y,x)] \cdot \mathbf{u}(y;\, s) dS_y, \tag{8}$$

$$u_k(x;\, s{-}s) = \iint\limits_S \mathbf{T}_y[\mathbf{U}_s^{(k)}(y,x)] \cdot \mathbf{u}(y;\, s) dS_y \tag{9}$$

Here $\mathbf{u}(y;\ p)$ ($\mathbf{u}(y;\, s)$) is the vector of full displacement on the boundary surface S, formed by the incidence of longitudinal (transverse) wave.

The first (6) and the fourth (9) terms describe the $p{-}p$ and $s{-}s$ reflections, but the second (7) and the third (8) ones the $p{-}s$ and $s{-}p$ transformations.

In the classical GDT, developed for scalar acoustics [10] and dynamic theory of elasticity [11], there is a difference between the high-frequency asymptotics in local and global sense. In the global formulation the problem is to calculate full field at point x. In our case, on the basis of representation (6)–(9) the full wave field at point x of the elastic medium is a sum of the four indicated integral terms (6)–(9) and

the incident spherical wave. In the local formulation the problem is to determine the leading asymptotic term of the diffracted amplitude in a small vicinity of any ray irradiated from point x_0, reflected from the boundary surface at point y^* and arriving at the receiving point x.

4 Multiple Re-reflections of the Longitudinal Wave

The diffraction of the high-frequency wave may be studied both in frames of the classical GDT [1] and on the basis of the integral representation of the Kirchhoff physical diffraction theory [12]. The foundation of the integral representation in N times re-reflected longitudinal wave gives a modification of the Kirchhoff integral representation Кирхгофа [13], realized in the case of double reflection [6].

Let a high-frequency spherical wave (2) propagate from point x_0 of the elastic medium. Let us assume that a longitudinal wave propagates along the ray $x_0 - y_1^* - y_2^* - \cdots - y_N^* - x_{N+1}$, where the points of specular reflection y_1^*, y_2^*, …, y_{N-1}^*, y_N^*, may belong to both a surface of the same void and boundary surfaces of N different voids (Fig. 1). Besides, we admit the cases of sequential location of several points on the same surfaces, while there the only point on some other surfaces. The wave is recorded at point x_{N+1} of the elastic medium. Hereinafter we consider the local formulation of the problem, where in the high-frequency regime of the time-harmonic process the displacements at the receiving point is defined by a reflection of the wave from small neighborhoods $S_1^*, S_2^*, \ldots, S_N^*$ of the boundary surfaces at the specular reflection points y_1^*, y_2^*, y_3^*, …, y_N^*.

Let us pass to integral representations of the Cartesian components of the displacement $u_k^{(p)}(x_{N+1})$ in the reflected wave at the receiving point x_{N+1}. The displacements in N times reflected wave at point x_{N+1} can be determined by integration over a small vicinity S_N^* of the last point of mirror reflection y_N^* of the rays formed at single reflection from a vicinity S_{N-1}^* of the previous point of mirror reflection y_{N-1}^*. The components of the displacement at the receiving point $u_k^{(p)}(x_{N+1})$ in the Cartesian coordinate system, at the last point of mirror reflection y_N^* is thus given by the following formula:

$$u_k^{(p)}(x_{N+1}) = \iint\limits_{S_N^*} \mathbf{T}_{y_N}[\mathbf{U}_p^{(k)}(y_N, x_{N+1})] \cdot \mathbf{u}(y_N; p) dS_N. \tag{10}$$

Here $\mathbf{u}(y_N; p)$ is the displacement at the incident wave at point $y_N \in S_N^*$ окрестности y_N^*, which is defined after reflection on the vicinity S_{N-1}^* of point $y_N^* \mathbf{n}_N$ is the unit normal to surface S_N^* at point y_N, in direction to the elastic medium.

At the same time, the displacement $\mathbf{u}(y_N; p)$ itself is expressed as an integral representation in terms of the incident wave to the vicinity S_N^*, which is incoming after the reflection on the vicinity S_{N-1}^*

$$u_k(y_N;\, p) = \iint\limits_{S^*_{N-1}} \mathbf{T}_{y_{N-1}}[\mathbf{U}^{(k)}_p(y_{N-1}, y_N)] \cdot \mathbf{u}(y_{N-1};\, p) dS_{N-1}. \tag{11}$$

Such an approach cam be extended also to the forming of the reflected wave at any vicinity S^*_N along the considered ray. In frames of such a modification the components of the displacement at the points of the vicinity $y_n \in S^*_n (n = 2, 3, \ldots, N)$ are expressed by the formula:

$$u_k(y_n;\, p) = \iint\limits_{S^*_{n-1}} \mathbf{T}_{y_{n-1}}[\mathbf{U}^{(k)}_p(y_{n-1}, y_n)] \cdot \mathbf{u}(y_{n-1};\, p) dS_{n-1}, \tag{12}$$

where $\mathbf{u}(y_n;\, p)$ is the displacement at point $y_n \in S^*_n$, $\mathbf{u}(y_{n-1};\, p)$ is the displacement at the incident wave at point $y_{n-1} \in S^*_{n-1}$ of the vicinity of point y^*_{n-1}, which is defined after reflection of the wave on the vicinity S^*_{n-2} of point y^*_{n-2}, $\mathbf{n}_{n-1}$ is the unit normal to the surface S^*_{n-1} at point y_{n-1}, directed to the elastic medium.

Moving along the re-reflected ray in the inverse direction, i.e. along the ray луча $x_{N+1} - y^*_N - \cdots - y^*_2 - y^*_1 - x_0$, we come to the forming of the incident waveon the vicinity S^*_2.

At the point y_2 of the vicinity S^*_2 of the second point of mirror reflection y^*_2 the integral representation for $u_k\,(y_2;\, p)$ takes the form:

$$u_k(y_2;\, p) = \iint\limits_{S^*_1} \mathbf{T}_{y_1}[\mathbf{U}^{(k)}_p(y_1, y_2)] \cdot \mathbf{u}^{inc}(y_1;\, p) dS_1, \tag{13}$$

where $\mathbf{u}^{inc}(y_1;\, p)$ defines the incident field of the displacements (4), corresponding to the point source x_0 (2).

Substituting subsequent integral representations to previous expressions (10)–(13), one obtains for $u^{(p)}_k(x_{N+1})$ the following 2N-fold integral

$$u^{(p)}_k(x_{N+1}) = \iint\limits_{S^*_N} \iint\limits_{S^*_{N-1}} \cdots \iint\limits_{S^*_2} \iint\limits_{S^*_1} \mathbf{T}_{y_N} \mathbf{T}_{y_{N-1}} \ldots \mathbf{T}_{y_2} \mathbf{T}_{y_1} \cdot \mathbf{u}^{inc}(y_1;\, p) dS_1 dS_2 \ldots dS_{N-1} dS_N. \tag{14}$$

The asymptotic solution developed below has a local character and gives the leading asymptotic term for the amplitude of the diffracted field in a small vicinity of any ray emitted from x_0, reflected from the surfaces of the voids, sequentially at points y^*_1, y^*_2, y^*_3, …, y^*_N and arrived at point x_{N+1}. Obviously, such rays exist only in the case when all reflection point y^*_1, y^*_2, y^*_3, …, y^*_N, and the receiving point x_{N+1} are located in the "light" zone.

In order to construct the leading asymptotic term of the integral (14), let us apply the asymptotic representation [6] for the force vector (7).

It should be noted that the incident $y_{n-1}^* - y_n^*$ and the reflected $y_n^* - y_{n+1}^*$ rays belong to the same plane with the normal $\mathbf{n}_n$ at point y_n^*.

Let us denote the distances $\left|x_0 - y_1^*\right| = L_0$, $\left|y_n^* - y_{n+1}^*\right| = L_n$, $\left|y_N^* - y_{N+1}^*\right| = L_N$, $n = 1, 2, \ldots, N-1$. After taking in the asymptotic representations (7) all slowly varying function out of (14), the amplitude of the radial displacement of N times reflected ray at point x_{N+1}, in the local spherical coordinate system r, θ, ψ at point of mirror reflection y_N^* of the boundary surface, is expressed as the following integral

$$u_r^{(p)}(x_{N+1}) = i^N \frac{Q_{\mathbf{q}}}{4\pi\mu} \frac{k_p^2}{k_s^2} \left(\frac{k_p}{2\pi}\right)^N \left(\frac{k_p^2}{2k_s^2}\right)^N L_0^{-1} \prod_{n=1}^{N} L_n^{-1} \cos\gamma_n V_{pp}\left(y_n^*\right) \times \iint\limits_{S_N^*} \iint\limits_{S_{N-1}^*} \cdots \iint\limits_{S_2^*} \iint\limits_{S_1^*} e^{ik_p\phi} dS_1 dS_2 \ldots dS_{N-1} dS_N, \tag{15}$$

$$u_\theta^{(p)}(x_{N+1}) = 0, \quad u_\psi^{(p)}(x_{N+1}) = 0,$$
$$\phi_p = |x_0 - y_1| + |y_1 - y_2| + \cdots + |y_{N-1} - y_N| + |y_N - x_{N+1}|$$
$$L_0 = \left|x_0 - y_1^*\right|, L_{n-1} = \left|y_{n-1}^* - y_n^*\right|, \quad n = 2, \ldots, N; \quad L_N = \left|y_N^* - x_{N+1}\right|, \tag{16}$$

where L_0 is the distance between the emitter x_0 and the first point of mirror reflection y_1^*, L_N is the distance between the receiver x_{N+1} and the last point of mirror reflection y_N^*, $L_{n-1}(n = 2, 3, \ldots, N)$ is the distance between the points of mirror reflection y_{n-1}^* and y_n^*, $V_{pp}\left(y_n^*\right)$ is the reflection coefficient of the longitudinal wave to longitudinal one [14, 15] at point y_n^*.

In the factors in front of the integral the values of $\cos\gamma_n$ for the incident ray are taken at the point of mirror reflection y_n^*.

The neighborhoods $S_1^*, S_2^*, \ldots, S_N^*$ a related to the right Cartesian coordinate systems, defined by the normals $\mathbf{n}_1, \mathbf{n}_2, \ldots\ldots, \mathbf{n}_N$ to the surfaces at points $y_1^*, y_2^*, \ldots, y_N^*$, directed to the elastic medium and tangential to the curvature lines. Let us denote as $O_n X_1^{(n)} X_2^{(n)} X_3^{(n)}, n = 1, 2, \ldots, N$ the Cartesian coordinate system with the origin at point y_n^*.

To determine the coordinates of the current point $y_n \in S_n^*, n = 1, 2, 3, \ldots, N$, at any vicinity S_N^* let us count the lengths of the arcs $\Delta s_1^{(n)}, \Delta s_2^{(n)}$ from point y_n^* along the curvature lines. Then the current point y_n of the convex surface S_n in the local coordinate system $O_n X_1^{(n)} X_2^{(n)} X_3^{(n)}$ has the following coordinates:

$$y_n = \left(\Delta s_1^{(n)}, \Delta s_2^{(n)}, -0.5\left(k_1^{(n)}\left(\Delta s_1^{(n)}\right)^2 + k_2^{(n)}\left(\Delta s_2^{(n)}\right)^2\right)\right),$$

where $k_1^{(n)}, k_2^{(n)}$ are the principal curvatures, and $\left(k_1^{(n)}\left(\Delta s_1^{(n)}\right)^2 + k_2^{(n)}\left(\Delta s_2^{(n)}\right)^2\right)$ is the second quadratic form of the surface S_n^* at point y_n^*. Up to small quantities of

the second order $\left(\Delta s_1^{(1)}\right)^2, \Delta s_1^{(1)}\Delta s_2^{(1)}, \left(\Delta s_2^{(1)}\right)^2, \left(\Delta s_1^{(N)}\right)^2, \Delta s_1^{(N)}\Delta s_2^{(N)}, \left(\Delta s_2^{(N)}\right)^2$ the asymptotic representations for the distances $|x_0 - y_1|$ и $|y_N - x_{N+1}|$ have the following form:

$$\begin{aligned}|x_0 - y_1| = L_0 &- \Delta s_1^{(1)}\cos\alpha_1 - \Delta s_2^{(1)}\cos\beta_1 \\ &+ 0.5\left(L_0^{-1}\sin^2\alpha_1 + k_1^{(1)}\cos\gamma_1\right)\left(\Delta s_1^{(1)}\right)^2 \\ &- L_0^{-1}\cos\alpha_1\cos\beta_1\Delta s_1^{(1)}\Delta s_2^{(1)} \\ &+ 0.5\left(L_0^{-1}\sin^2\beta_1 + k_2^{(1)}\cos\gamma_1\right)\left(\Delta s_1^{(1)}\right)^2, \end{aligned} \tag{17}$$

$$\begin{aligned}|y_N - x_{N+1}| = L_N &+ \Delta s_1^{(N)}\cos\alpha_N + \Delta s_2^{(N)}\cos\beta_N \\ &+ 0.5\left(L_N^{-1}\sin^2\alpha_N + k_1^{(N)}\cos\gamma_N\right)\left(\Delta s_1^{(N)}\right)^2 \\ &- L_N^{-1}\cos\alpha_N\cos\beta_N\Delta s_1^{(N)}\Delta s_2^{(N)} \\ &+ 0.5\left(L_N^{-1}\sin^2\beta_N + k_2^{(N)}\cos\gamma_N\right)\left(\Delta s_1^{(N)}\right)^2. \end{aligned} \tag{18}$$

In the presented formulas above and hereinafter in this section $\{-\cos\alpha_n, -\cos\beta_n, -\cos\gamma_n\}$ is the direction of the incident ray and $\{-\cos\alpha_n, -\cos\beta_n, \cos\gamma_n\}$ is the direction of the reflected ray at point y_n in the vicinity S_n^*, related to the local coordinate system.

Each of the distances $|y_{n-1} - y_n| = |\mathbf{y}_n\mathbf{y}_{n-1}|, n = 2, 3, \ldots, N$ in the phase φ (16) is considered in the Cartesian coordinate system $O_nX_1^{(n)}X_2^{(n)}X_3^{(n)}$ at point y_n^*. For the vector $\mathbf{y}_n\mathbf{y}_{n-1}$ let us use the representation:

$$\begin{aligned}\mathbf{y}_n\mathbf{y}_{n-1} &= \mathbf{y}_n^*\mathbf{y}_{n-1}^* + \mathbf{A}_n^{n-1}\mathbf{y}_{n-1}^*\mathbf{y}_{n-1} - \mathbf{y}_n^*\mathbf{y}_n; \\ \mathbf{y}_n^*\mathbf{y}_n &= \left\{\Delta s_1^{(n)}, \Delta s_2^{(n)}, -0.5\left(k_1^{(n)}\left(\Delta s_1^{(n)}\right)^2 + k_2^{(n)}\left(\Delta s_2^{(n)}\right)^2\right)\right\}. \end{aligned} \tag{19}$$

Here the coordinates of vector $\mathbf{y}_i^*\mathbf{y}_i$ $(i = n-1, n)$ are written out in the local Cartesian coordinates of points y_{n-1}^* and y_n^*.

The matrix $\mathbf{A}_n^{n-1} = \left(a_{i,j}^n\right)$, $i, j = 1, 2, 3$ is the orthogonal matrix of the passage from the Cartesian basis $O_nX_1^{(n)}X_2^{(n)}X_3^{(n)}$ at point y_n^* to the Cartesian basis $O_{n-1}X_1^{(n-1)}X_2^{(n-1)}X_3^{(n-1)}$ at point y_{n-1}^*.

By taking into account the orthogonality of matrix $\mathbf{A}_n^{n-1}$, each term $|y_{n-1} - y_n|, n = 2, 3, \ldots, N$ in the phase φ (16) is reduced to the form:

$$\begin{aligned}|y_{n-1} - y_n| = L_{n-1} &\\ &+ \cos\alpha_{n-1}\Delta s_1^{(n-1)} + \cos\beta_{n-1}\Delta s_2^{(n-1)}\end{aligned}$$

$$
\begin{aligned}
&+ 0.5\cos\gamma_{n-1}\left[k_1^{(n-1)}\left(\Delta s_1^{(n-1)}\right)^2 + k_2^{(n-1)}\left(\Delta s_2^{(n-1)}\right)^2\right]\\
&- \cos\alpha_n\Delta s_1^{(n)} - \cos\beta_n\Delta s_2^{(n)}\\
&- 0.5\cos\gamma_n\left[k_1^{(n)}\left(\Delta s_1^{(n)}\right)^2 + k_2^{(n)}\left(\Delta s_2^{(n)}\right)^2\right]\\
&+ L_{n-1}^{-1}\left[0.5\sin^2\alpha_{n-1}\left(\Delta s_1^{(n-1)}\right)^2 + 0.5\sin^2\beta_{n-1}\left(\Delta s_2^{(n-1)}\right)^2\right.\\
&- \cos\alpha_{n-1}\cos\beta_{n-1}\Delta s_1^{(n-1)}\Delta s_2^{(n-1)}\\
&+ 0.5\sin^2\alpha_n\left(\Delta s_1^{(n)}\right)^2 + 0.5\sin^2\beta_n\left(\Delta s_2^{(n)}\right)^2\\
&- \cos\alpha_n\cos\beta_n\Delta s_1^{(n)}\Delta s_2^{(n)}\\
&+ \left(\cos\alpha_{n-1}\cos\alpha_n - a_{11}^n\right)\Delta s_1^{(n-1)}\Delta s_1^{(n)}\\
&+ \left(\cos\beta_{n-1}\cos\beta_n - a_{12}^n\right)\Delta s_2^{(n-1)}\Delta s_1^{(n)}\\
&+ \left(\cos\alpha_{n-1}\cos\alpha_n - a_{21}^n\right)\Delta s_1^{(n-1)}\Delta s_2^{(n)}\\
&\left.+\left(\cos\beta_{n-1}\cos\beta_n - a_{22}^n\right)\Delta s_2^{(n-1)}\Delta s_2^{(n)}\right]\\
&n = 2, 3, \ldots, N.
\end{aligned}
\tag{20}
$$

In the general case of N-fold re-reflection, in the phase φ (16) there is no linear term $\Delta s_j^{(n)}(j = 1, 2; n = 1, 2, \ldots, N)$. This means that the points $y_n^* \in S_n^*$ of the direct ray reflection correspond to the stationary value of the phase φ.

By applying the estimate as $k_p \to \infty$ 2N for the multiple Somilyana integral (15) the multidimensional (2N-fold) stationary phase method [16], we obtain the amplitude of the radial displacement in N times re-reflected p-wave:

$$
u_r^{(p)}(x_{N+1}) = \frac{Q_{\mathbf{q}}}{4\pi\mu}\frac{k_p^2}{k_s^2}\prod_{n=1}^{N}\cos\gamma_n V_{pp}\left(y_n^*\right)\frac{\exp\left\{i\left[k_p\sum\limits_{n=0}^{N}L_n + \frac{\pi}{4}\left(\delta_{2N}^{(p)} + 2N\right)\right]\right\}}{\prod\limits_{n=0}^{N}L_n\sqrt{\left|\det\left(D_{2N}^{(p)}\right)\right|}},
\tag{21}
$$

where $\delta_{2N}^{(p)} = signD_{2N}^{(p)}$ is the sign of the hessian matrix $D_{2N}^{(p)} = (d_{i\,j}),\quad i, j = 1, 2, 3, \ldots, 2N$, which is band-like (with the width of the band equal to seven) and symmetric $d_{i\,j} = d_{j\,i}$ with the following non trivial elements $d_{ij}, i \le j$.

Diagonal elements:

$$
\begin{Bmatrix} d_{2n-1,2} \\ d_{2n,2n} \end{Bmatrix} = \left(L_{n-1}^{-1} + L_n^{-1}\right)\begin{Bmatrix} \sin^2\alpha_n \\ \sin^2\beta_n \end{Bmatrix} + 2\begin{Bmatrix} k_1^{(n)} \\ k_2^{(n)} \end{Bmatrix}\cos\gamma_n, n = \overline{1, N}
\tag{22}
$$

Out-of-diagonal elements:

$$
\begin{aligned}
d_{2n-1,2n} &= -\left(L_{n-1}^{-1} + L_n^{-1}\right)\cos\alpha_n \cos\beta_n,\ n = \overline{1, N},\\
d_{2n-1,2n+1} &= L_n^{-1}(\cos\alpha_n \cos\alpha_{n+1} - a_{11}^n),\ n = \overline{1, N-1},\\
d_{2n-1,2n+2} &= L_n^{-1}(\cos\alpha_n \cos\beta_{n+1} - a_{21}^n),\ n = \overline{1, N-1},\\
d_{2n,2n+1} &= L_n^{-1}(\cos\beta_n \cos\alpha_{n+1} - a_{12}^n),\ n = \overline{1, N-1},\\
d_{2n,2n+2} &= L_n^{-1}(\cos\beta_n \cos\beta_{n+1} - a_{22}^n),\ n = \overline{1, N-1}.
\end{aligned} \tag{23}
$$

Let us note that the estimate of the multidimensional diffraction integral (15) is not reduced to a sequential asymptotic estimate of the double integrals, since the structure of the phase function represents itself a complex combination depending on all points of vicinities $S_1^*, S_2^*, \ldots, S_N^*$, participating in the ray reflections.

The elements of this matrix coincide with the elements of matrix D_{2N} from [4] in the case of N–fold re-reflection of the acoustic wave. But one should take into account that in the elements of matrix $D_{2N}^{(p)}$: $\{-\cos\alpha_n, -\cos\beta_n, -\cos\gamma_n\}$ is the direction of the incident p-wave regarding the coordinate system at point y_n^*, and $\{-\cos\alpha_{n+1}, -\cos\beta_{n+1}, -\cos\gamma_{n+1}\}$ is the direction of the reflected p-wave at point y_n^* regarding the coordinate system at point y_{n+1}^*, $k_1^{(n)}, k_2^{(n)} (n = 1, 2, \ldots, N)$ are the principal curvatures of the surface at point y_n^*.

Therefore, in the present section we have obtained the leading asymptotic term for the displacements in the longitudinal wave re-reflected arbitrary finite number of times, from the surfaces of a system of voids located in the elastic medium. Formula (12) for the amplitude of N times re-reflected p-wave differs from the amplitude for pressure in N times re-reflected acoustic wave [4], by a certain inessential factor in (21) and a product of the reflection coefficients $V_{pp}\left(y_n^*\right)$ of p-wave [14, 15] at the point $y_n^*, n = 1, 2, \ldots, N$ of mirror reflection.

5 Multiple Reflections with Periodic Transformation of Elastic Waves

Let us consider this topic on a concrete example. If the location and the shape of the surfaces are such that the trajectory of the ray $x_0 - y_1^* - y_2^* - \cdots - y_{2N-1}^* - y_{2N}^* - x_{2N+1}$ leads to $p-s-p-s-\ldots-p-s-p$ reflection (this can be realized only for even number of mirror reflections, Fig. 2), then the amplitude of the radial displacement in the 2N times reflected ray at point x_{2N+1} relatively the local spherical coordinate system r, θ, ψ at the last point of mirror reflection y_{2N}^* is represented by the integral

$$
\begin{aligned}
u_r^{(p)}(x_{2N+1}) = \frac{Q_{\mathbf{q}}}{4\pi\mu}\left(\frac{k_p}{k_s}\right)^2\left(\frac{k_p k_s}{4\pi^2}\right)^N L_0^{-1}\\
\prod_{n=1}^{N} L_{2n-1}^{-1} L_{2n}^{-1} \cos\gamma_{2n-1}^{(s)} \cos\gamma_{2n}^{(p)} V_{ps}\left(y_{2n-1}^*\right) V_{sp}\left(y_{2n}^*\right)
\end{aligned}
$$

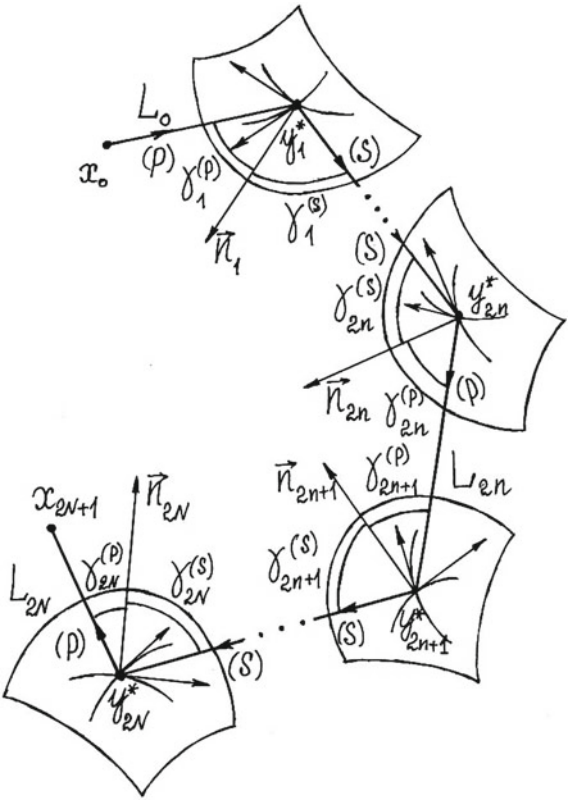

Fig. 2 2N-fold $p-s-p-\cdots-p-s-p$ re-reflection of the high-frequency longitudinal wave along the ray $x_0 - y_1^* - y_2^* - \cdots - y_{2N-1}^* - y_{2N}^* - x_{2N+1}$ from a system of 2N voids

$$\times \iint\limits_{S_{2N}} \iint\limits_{S_{2N-1}} \cdots \iint\limits_{S_2} \iint\limits_{S_1} e^{ik_p\phi} dS_1 dS_2 \ldots dS_{2N-1} dS_{2N},$$

$$u_\theta^{(p)}(x_{2N+1}) = 0, u_\psi^{(p)}(x_{2N+1}) = 0, \tag{24}$$

$$\phi = |x_0 - y_1| + k_s\, k_p^{-1} \sum_{n=1}^{N} |y_{2n-1} - y_{2n}| + \sum_{n=1}^{N-1} |y_{2n} - y_{2n+1}| + |y_{2N} - x_{2N+1}|,$$

$$L_0 = \left|x_0 - y_1^*\right|, L_n = \left|y_n^* - y_{n+1}^*\right|, n = 1, 2, \ldots, 2N-1\,; L_{2N} = \left|y_{2N}^* - x_{2N+1}\right|, \tag{25}$$

where L_0 is the distance between the emitter x_0 and the first point of mirror reflection y_1^*, L_{2N}—between the receiver x_{2N+1} and the last point of mirror reflection y_{2N}^*, $L_n (n = 1, 2, 3, \ldots, 2N-1)$ is the distance between the points of mirror reflection y_n^* and y_{n+1}^*.

The first $|x_0 - y_1|$ and the last $|y_{2N} - x_{2N+1}|$ terms in the phase ϕ (25) have the same structure like in (17) and (18), and the others are analogous to (20).

The asymptotic expansions for the distances $|y_{2n-1} - y_{2n}| = |\mathbf{y}_{2n-1}\mathbf{y}_{2n}|$ and $|y_{2n} - y_{2n+1}| = |\mathbf{y}_{2n}\mathbf{y}_{2n+1}|$ are obtained on the basis of the following vector representations

$$\mathbf{y}_{2n}\mathbf{y}_{2n-1} = \mathbf{y}^*_{2n}\mathbf{y}^*_{2n-1} + \mathbf{A}^{2n-1}_{2n}\mathbf{y}^*_{2n-1}\mathbf{y}_{2n-1} - \mathbf{y}^*_{2n}\mathbf{y}_{2n}. \tag{26}$$

$$\mathbf{y}_{2n+1}\mathbf{y}_{2n} = \mathbf{y}^*_{2n+1}\mathbf{y}^*_{2n} + \mathbf{A}^{2n}_{2n+1}\mathbf{y}^*_{2n}\mathbf{y}_{2n} - \mathbf{y}^*_{2n+1}\mathbf{y}_{2n+1}. \tag{27}$$

Here $\mathrm{A}^{2n-1}_{2n} = \left(a_{ij}\right)^{2n-1}_{2n}$ and $\mathrm{A}^{2n}_{2n+1} = \left(a_{ij}\right)^{2n}_{2n+1}$, $i, j = 1, 2, 3$; $n = 1, 2, \ldots, N-1$ are the transition matrices from the Cartesian coordinate system at point y^*_{2n} (and respectively, y^*_{2n+1}) to the Cartesian coordinate system at point y^*_{2n-1} (and respectively, y^*_{2n}).

By applying for the asymptotic estimate, as $k_p \to \infty$, the 4N-fold Kirchhoff integral (20) the 4N-forl stationary phase method, we obtain the amplitude of the radial displacement in the 2N times re-reflected p-wave:

$$u^{(p)}_r(x_{2N+1}) = B_1 \times \frac{\exp\left\{i\left[k_p L_0 + \sum\limits_{n=1}^{N}\left(k_s L_{2n-1} + k_p L_{2n}\right) + \frac{\pi}{4}(\delta_{4N} + 4N)\right]\right\}}{\prod\limits_{n=0}^{2N} L_n\sqrt{|\det(D_{4N})|}},$$

$$B_1 = \frac{Q_{\mathbf{q}}}{4\pi\mu}\left(\frac{k_s}{k_p}\right)^{N-2}\prod_{n=1}^{N} V_{ps}\left(y^*_{2n-1}\right)V_{sp}\left(y^*_{2n}\right)\cos\gamma^{(s)}_{2n-1}\cos\gamma^{(p)}_{2n}, \tag{28}$$

where $\delta_{4N} = sign\, D_{4N}$ is the sign of the Hessian matrix $D_{4N} = (d_{mk})$, $m, k = 1, 2, 3, \ldots, 4N$, which is band-like (with the width of the band equal to seven) and symmetric $d_{mk} = d_{mk}$, with the following nontrivial elements $d_{mk}, m \le k$, $m, k \le 4N$,

$$\begin{Bmatrix} d_{4n-3,4n-3} \\ d_{4n-2,4n-2} \end{Bmatrix} = \frac{1}{L_{2n-2}}\begin{Bmatrix} \sin^2\alpha^{(p)}_{2n-1} \\ \sin^2\beta^{(p)}_{2n-1} \end{Bmatrix} + \frac{k_s}{k_p L_{2n-1}}\begin{Bmatrix} \sin^2\alpha^{(s)}_{2n-1} \\ \sin^2\beta^{(s)}_{2n-1} \end{Bmatrix}$$
$$+ \begin{Bmatrix} k_1^{(2n-1)} \\ k_2^{(2n-1)} \end{Bmatrix}\left(\cos\gamma^{(p)}_{2n-1} + \frac{k_s}{k_p}\cos\gamma^{(s)}_{2n-1}\right), n = \overline{1, N}$$

$$\begin{Bmatrix} d_{4n-1,4n-1} \\ d_{4n,4n} \end{Bmatrix} = \frac{k_s}{k_p L_{2n-1}}\begin{Bmatrix} \sin^2\alpha^{(s)}_{2n} \\ \sin^2\beta^{(s)}_{2n} \end{Bmatrix} + \frac{1}{L_{2n}}\begin{Bmatrix} \sin^2\alpha^{(p)}_{2n} \\ \sin^2\beta^{(p)}_{2n} \end{Bmatrix}$$
$$+ \begin{Bmatrix} k_1^{(2n)} \\ k_2^{(2n)} \end{Bmatrix}\left(\frac{k_s}{k_p}\cos\gamma^{(s)}_{2n} + \cos\,\gamma^{(p)}_{2n}\right), n = \overline{1, N},$$

$$d_{4n-3,4n-2} = -\frac{1}{L_{2n-2}}\cos\alpha^{(p)}_{2n-1}\cos\beta^{(p)}_{2n-1}$$
$$- \frac{k_s}{k_p L_{2n-1}}\cos\alpha^{(s)}_{2n-1}\cos\beta^{(s)}_{2n-1}, n = \overline{1, N},$$

$$d_{4n-1,4n} = -\frac{k_s}{k_p L_{2n-1}} \cos\alpha_{2n}^{(s)} \cos\beta_{2n}^{(s)} - \frac{1}{L_{2n}} \cos\alpha_{2n}^{(p)} \cos\beta_{2n}^{(p)}, n = \overline{1, N},$$

$$d_{4n-3,4n-1} = \frac{k_s}{k_p L_{2n-1}} \left(\cos\alpha_{2n-1}^{(s)} \cos\alpha_{2n}^{(s)} - (a_{11})_{2n}^{2n-1} \right), n = \overline{1, N-1},$$

$$d_{4n-3,4n} = \frac{k_s}{k_p L_{2n-1}} \left(\cos\alpha_{2n-1}^{(s)} \cos\beta_{2n}^{(s)} - (a_{21})_{2n}^{2n-1} \right), n = \overline{1, N-1},$$

$$d_{4n-2,4n-1} = \frac{k_s}{k_p L_{2n-1}} \left(\cos\beta_{2n-1}^{(s)} \cos\alpha_{2n}^{(s)} - (a_{12})_{2n}^{2n-1} \right), n = \overline{1, N-1},$$

$$d_{4n-2,4n} = \frac{k_s}{k_p L_{2n-1}} \left(\cos\beta_{2n-1}^{(s)} \cos\beta_{2n}^{(s)} - (a_{22})_{2n}^{2n-1} \right), n = \overline{1, N-1},$$

$$d_{4n-1,4n+1} = \frac{1}{L_{2n}} \left(\cos\alpha_{2n}^{(p)} \cos\alpha_{2n+1}^{(p)} - (a_{11})_{2n+1}^{2n} \right), n = \overline{1, N-1},$$

$$d_{4n-1,4n+2} = \frac{1}{L_{2n}} \left(\cos\alpha_{2n}^{(p)} \cos\beta_{2n+1}^{(p)} - (a_{21})_{2n+1}^{2n} \right), n = \overline{1, N-1},$$

$$d_{4n,4n+1} = \frac{1}{L_{2n}} \left(\cos\beta_{2n}^{(p)} \cos\alpha_{2n+1}^{(p)} - (a_{12})_{2n+1}^{2n} \right), n = \overline{1, N-1},$$

$$d_{4n,4n+2} = \frac{1}{L_{2n}} \left(\cos\beta_{2n}^{(p)} \cos\beta_{2n+1}^{(p)} - (a_{22})_{2n+1}^{2n} \right); n = \overline{1, N-1}.$$

Here $\left\{ -\cos\alpha_{2n-1}^{(p)}, -\cos\beta_{2n-1}^{(p)}, -\cos\gamma_{2n-1}^{(p)} \right\}$ is the direction of incidence of p-wave, and $\left\{ -\cos\alpha_{2n-1}^{(s)}, -\cos\beta_{2n-1}^{(s)}, \cos\gamma_{2n-1}^{(s)} \right\}$—the direction of the reflection of s-wave, in the coordinate system at point y_{2n-1}^*; $\left\{ -\cos\alpha_{2n}^{(s)}, -\cos\beta_{2n}^{(s)}, -\cos\gamma_{2n}^{(s)} \right\}$—the direction of incidence of s-wave, and $\left\{ -\cos\alpha_{2n}^{(p)}, -\cos\beta_{2n}^{(p)}, \cos\gamma_{2n}^{(p)} \right\}$—the direction of reflection of p-wave in the coordinate system at point y_{2n}^*.

6 Multiple Reflections with All Possible Transformations of Elastic Waves

The geometry of the boundary surfaces of the voids in the elastic medium and their location may form such trajectories of rays $x_0 - y_1^* - y_2^* - \cdots - y_N^* - x_{N+1}$, which lead to any possibility of sequential reflections and transformations at the points of mirror reflection. Generally, the trajectory of the wave is a three-dimensional polyline with vertices at the points of mirror reflection.

Let for N times reflected ray at any possible sequence at the point of mirror reflection y_1^*, y_2^*, …, y_{N-1}^*, y_N^* there is realized the $p-p$ and $s-s$ reflections N_1 and N_3 times, respectively, but $p-s$ and $s-p$ transformations—N_2 and N_4 times, respectively. At the receiving point x_{N+1} there can be

received both longitudinal $u(x_{N+1}) = u_r^{(p)}(x_{N+1})$ and transverse $u(x_{N+1}) = \left(u_\theta^{(S)}(x_{N+1})\cos\alpha + u_\psi^{(S)}(x_{N+1})\cos\beta\right)\sin^{-1}\gamma$ wave, where $\{\cos\alpha, \cos\beta, \cos\gamma\}$ is the direction of the reflected wave in the local Cartesian coordinate system at the receiving point x_{N+1}.

When so doing, the amplitude of the radial and tangential displacement in N times reflected ray at point x_{N+1} regarding the local spherical coordinate system r, θ, ψ at point y_N of the boundary surface of the obstacle, is represented by a multiple Kirchhoff integral, which is formed by the same rules like the diffraction integrals (15) and (24), taking in account concrete reflections and transformations of the propagating ray at the point of mirror reflection:

$$u(x_{N+1}) = i^N B\left(\frac{k_p}{2\pi}\right)^{N_1+N_2}\left(\frac{k_s}{2\pi}\right)^{N_3+N_4} L_0^{-1}\prod_{n=1}^{N} L_n^{-1}\cos\gamma_n^{(2)} V(y_n^*) \times \iint\limits_{S_N^*}\iint\limits_{S_{N-1}^*}\cdots\iint\limits_{S_2^*}\iint\limits_{S_1^*} e^{ik_p\varphi} dS_1 dS_2 \ldots dS_{N-1} dS_N, \tag{29}$$

$$\varphi = k_p^{-1}\left(k_1|x_0 - y_1| + \sum_{n=1}^{N-1} k_n|y_n - y_{n+1}| + k_N|y_N - x_{N+1}|\right),$$

$$L_0 = |x_0 - y_1^*|,\ L_n = |y_n^* - y_{n+1}^*|,\ L_N = |y_N^* - x_{N+1}|,\ n = 1, 2, \ldots, N-1. \tag{30}$$

Here $B = \frac{Q_q}{4\pi\mu}\left(\frac{k_p}{k_s}\right)^{2N_1+N_4}$.

In the expressions (29)–(32) $\mathbf{q}_n^{(1)} = \left\{\cos\alpha_n^{(1)}, \cos\beta_n^{(1)}, \cos\gamma_n^{(1)}\right\}$ and $\mathbf{q}_n^{(2)} = \left\{\cos\alpha_n^{(2)}, \cos\beta_n^{(2)}, \cos\gamma_n^{(2)}\right\}$ are, respectively, the direction of the incidence and reflection of the wave at the points of mirror reflection y_n^*.

Let us mention the four combinations of the pairs of directions $\mathbf{q}_n^{(1)}, \mathbf{q}_n^{(2)}$:

1. $\mathbf{q}_n^{(1)} = \mathbf{q}_n^{(p)}, \mathbf{q}_n^{(2)} = \mathbf{q}_n^{(p)}, V(y_n^*) = V_{pp}(y_n^*), (p{-}p)$;
2. $\mathbf{q}_n^{(1)} = \mathbf{q}_n^{(p)}, \mathbf{q}_n^{(2)} = \mathbf{q}_n^{(s)}, V(y_n^*) = V_{ps}(y_n^*), (p{-}s)$;
3. $\mathbf{q}_n^{(1)} = \mathbf{q}_n^{(s)}, \mathbf{q}_n^{(2)} = \mathbf{q}_n^{(s)}, V(y_n^*) = V_{ss}(y_n^*), (s{-}s)$;
4. $\mathbf{q}_n^{(1)} = \mathbf{q}_n^{(s)}, \mathbf{q}_n^{(2)} = \mathbf{q}_n^{(p)}, V(y_n^*) = V_{sp}(y_n^*), (s{-}p)$.

If at the point y_n^* there is realized a respective reflection or transformation indicated in the brackets. $V(y_n^*)$ is the coefficient of the reflection or transmission [14, 15] at the point y_n^* of the respective wave. In the phase φ (30) the parameter $k_n = k_p$ $(p{-}p, p{-}s)$ and $k_n = k_s(s{-}s, s{-}p)$, if the reflections or transformations indicated in the brackets are realized at point y_n^*. By applying for the asymptotic estimate of the diffraction integral (29) the $2N$-fold stationary phase method [14] we obtain the geometrical-optics approximation for the displacements in the passed elastic wave

$$u(x_{N+1}) = B_2 \frac{\exp\left\{i\left[\sum\limits_{n=0}^{N} k_n L_n + \frac{\pi}{4}(\delta_{2N} + 2N)\right]\right\}}{\prod\limits_{n=0}^{N} L_n \sqrt{|\det(D_{2N})|}}$$

$$B_2 = B \prod_{n=1}^{N} \cos\gamma_n^{(2)} V\left(y_n^*\right) \tag{31}$$

where $\delta_{2N} = sign D_{2N}$, and $D_{2N} = (d_{nm}), n, m = 1, 2, 3, \ldots, 2N$ is the Hessian matrix, which is band-like and symmetric $d_{n\,m} = d_{m\,n}$, with the following nontrivial elements $d_{n\,m}, n < m$:

$$\begin{aligned}
d_{2n-1,2n-1} &= \frac{k_{1n}}{k_p L_{n-1}} \cos\alpha_n^{(1)} \\
&\quad + \frac{k_{2n}}{k_p L_n} \cos\alpha_n^{(2)} + k_1^n \left(\frac{k_{1n}}{k_p} \cos\gamma_n^{(1)} + \frac{k_{2n}}{k_p} \cos\gamma_n^{(2)}\right), n = \overline{1, N} \qquad (32) \\
d_{2n,2n} &= \frac{k_{1n}}{k_p L_{n-1}} \cos\beta_n^{(1)} + \frac{k_{2n}}{k_p L_n} \cos\beta_n^{(2)} \\
&\quad + k_2^n \left(\frac{k_{1n}}{k_p} \cos\gamma_n^{(1)} + \frac{k_{2n}}{k_p} \cos\gamma_n^{(2)}\right), n = \overline{1, N}, \\
d_{2n-1,2n} &= -\left(\frac{k_{1n}}{k_p L_{n-1}} \cos\alpha_n^{(1)} \cos\beta_n^{(1)} + \frac{k_{2n}}{k_p L_n} \cos\alpha_n^{(2)} \cos\beta_n^{(2)}\right), n = \overline{1, N}, \\
d_{2n-1,2n+1} &= \frac{1}{L_n}\left(\cos\alpha_n^{(1)} \cos\alpha_{n+1}^{(1)} - a_{11}^n\right), n = \overline{1, N-1} \\
d_{2n-1,2n+2} &= \frac{1}{L_n}\left(\cos\alpha_n^{(1)} \cos\beta_{n+1}^{(1)} - a_{21}^n\right), n = \overline{1, N-1}, \\
d_{2n,2n+1} &= \frac{1}{L_n}\left(\cos\beta_n^{(1)} \cos\alpha_{n+1}^{(1)} - a_{12}^n\right), n = \overline{1, N-1}, \\
d_{2n,2n+2} &= \frac{1}{L_n}\left(\cos\beta_n^{(1)} \cos\alpha_{n+1}^{(1)} - a_{22}^n\right), n = \overline{1, N-1}
\end{aligned}$$

Here $\left\{\cos\alpha_n^{(1)}, \cos\beta_n^{(1)}, \cos\gamma_n^{(1)}\right\}$ are the direction of the incidence of the wave, and $\left\{\cos\alpha_n^{(2)}, \cos\beta_n^{(2)}, \cos\gamma_n^{(2)}\right\}$ is the direction of the wave reflection at point y_n^*, $k_1^{(n)}, k_2^{(n)}$—the principal curvatures of the boundary surface at the point y_n^*.

In the diagonal elements of the Hessian matrix for parameters k_{1n} and k_{2n} there are possible the four pair of the values:

1. $k_{1n} = k_p, k_{2n} = k_p$ $(p-p)$;
2. $k_{1n} = k_p, k_{2n} = k_s$ $(p-s)$;
3. $k_{1n} = k_s, k_{2n} = k_s$ $(s-s)$;
4. $k_{1n} = k_s, k_{2n} = k_p$ $(s-p)$.

Depending on which type of the reflection or transformation is realized at point y_n^*

7 Conclusion

In the present work we give the leading asymptotic term (31) of the amplitude of the displacement $u(x_{N+1})$ of the reflected along the ray $x_0 - y_1^* - y_2^* - \cdots - y_N^* - x_{N+1}$ high-frequency longitudinal or transverse wave with the arbitrary sequence of reflections and transformations from N obstacles located in the elastic medium in the tree-dimensional case. The trajectory of the wave is a three-dimensional polyline with the vertices at the points of mirror reflections. The amplitude of the displacement in the multiply reflected elastic wave (31), (32) is defined by the distances from the source to the first reflection point y_1^*, parameter L_0, from the last mirror reflection point y_N^* to the receiving point, parameter L_N, the distances L_n, $n = 1, 2, \ldots, N-1$ between points y_n^* and y_{n+1}^*. Points $y_1^*, y_2^*, \ldots, y_{N-1}^*, y_N^*$ may belong to both boundary surfaces $S_1, S_2 \ldots, S_{N-1}, S_N$ of N different voids, and the surface S of a single void of a complex non-convex shape. There are also possible the cases when boundary surfaces of some voids each contain one reflection point, and some other obstacles contain several reflection points. The leading asymptotic term of the displacement also contains in explicit form the principal curvatures of the surfaces $k_1^{(n)}, k_2^{(n)} (n = 1, 2, \ldots, N)$ at points $y_1^*, y_2^*, \ldots, y_{N-1}^*, y_N^*$, along the direction $\mathbf{q}_n^{(1)} = \left\{\cos\,\alpha_n^{(1)}, \cos\,\beta_n^{(1)}, \cos\,\gamma_n^{(1)}\right\}$ and $\mathbf{q}_n^{(2)} = \left\{\cos\,\alpha_n^{(2)}, \cos\,\beta_n^{(2)}, \cos\,\gamma_n^{(2)}\right\}$ of the incident and reflected wave, respectively, at the point of mirror reflection, as well as the reflection and transformation coefficients $V\left(y_n^*\right)$. The phase of the reflected wave $u(x_{N+1})$ (31) is defined by the distances $L_0, L_1, L_2, \ldots, L_{N-1}, L_N$, by the wave numbers k_p and k_s, by the sign δ_{2N} of the Hessian matrix D_{2N}, as well as by the number of points of mirror reflection.

Acknowledgements The present work is performed within the framework of the Project no. 15-19-10008-P of the Russian Science Foundation (RSCF).

References

1. Babich, V.M., Buldyrev, V.S. Asymptotic Methods in Short-Wavelength Diffraction Theory. Alpha Science International, London (2009)
2. Sumbatyan, M.A., Boyev, N.V.: High-frequency diffraction by nonconvex obstacles. J. Acoust. Soc. Am. **95**(5)(Part 1), 2347–2353 (1994)
3. Bojarski, N.N.: A survey of the physical optics inverse scattering identity. IEEE Trans. Anten. Prop. **AP 30**(5), 980–988 (1982)
4. Boyev, N.V., Sumbatyan, M.A.: A short-wave diffraction by bodies, bounded by arbitrary smooth surface. Russ. Dokl. **392**(5) (2003)
5. McNamara, D.A., Pistotius, C.W.I.: Introduction to the Uniform Geometrical Theory of Diffraction. Artech House Microwave Library (1990)

6. Boyev, N.V.: Short-wave diffraction of elastic waves by voids in an elastic medium with double reflections and transformations. In: Wave Dynamics and Composite Mechanics for Microstructured Materials and Metamaterials. Springer Series: Advanced Structured Materials, vol. 59, pp. 91–106 (2017)
7. Boyev, N.V., Sumbatyan, M.A.: Ray tracing method for a high-frequency propagation of the ultrasonic wave through a triple-periodic array of spheres. In: Wave Dynamics and Composite Mechanics for Microstructured Materials and Metamaterials. Springer Series: Advanced Structured Materials, vol. 59, pp. 173–187 (2017)
8. Kupradze, V.D.: Potential Methods in the Theory of Elasticity. Israel Program for Scientific Translations (1965)
9. Novatsky, V.: Theory of Elasticity. Mir., Moscow (1975) (in Russian)
10. Borovikov, V.A., Borovikov, V.A., Kinber, B.Y., Kinber, B.E.: Geometrical Theory of Diffraction. The Institution of Electrical Engineers, London (1994)
11. Achenbach, J.D., Gautesen, A.K., McMaken, H.: Ray Methods for Waves in Elastic Solids: With Applications to Scattering by Cracks. Pittman, New York (1982)
12. Hoenl, H., Maue A., Westpfahl, K.: Diffraction Theory. Mir., Moscow (1964) (in Russian)
13. Shenderov, E.L.: Wave Problems of Hydroacoustics. Sudostroenie, Leningrad (1972) (in Russian)
14. Brekhovskikh, L.: Waves in Layered Media. Academic Press, New York (2012)
15. Grinchenko, V.T., Meleshko, V.V.: Harmonic Oscillations and Waves in Elastic Bodies. Naukova Dumka, Kiev (1981) (in Russian)
16. Fedorjuk, M.V.: Saddle Point Method. Nauka, Moscow (1977) (in Russian)

Numerical Investigation of Effective Moduli of Porous Elastic Material with Surface Stresses for Various Structures of Porous Cells

A. V. Nasedkin and A. S. Kornievsky

Abstract The chapter deals with the model problem of finding the effective moduli of a nanoporous elastic material, in which the surface stresses are defined on the pore surface to reflect the size effect using the Gurtin–Murdoch model. One cell of a porous material in the form of a cube with one pore located in the center is considered. The objective of the study is to assess the influence of the pore shape and the magnitude of the scale factors on the effective moduli of the composite material. The homogenization problem is formulated within the framework of the effective moduli method, and to find its solution, the finite element method and the ANSYS software package are used. In the finite element model, the surface stresses are taken into account by membrane elements covering the pore surfaces and conformable with the finite element mesh of bulk elements. Numerical experiments carried out for pores of cubic and spherical shapes show the cumulative significant effect of pore geometry and scale factors on the effective elastic moduli.

1 Introduction

The problems of nanomechanics remain extremely relevant for the last few years. Numerous studies have revealed a scale effect, which consists in changing the effective stiffness and other material moduli for nanoscale bodies in comparison with the corresponding values for bodies of usual macro-dimensions. A number of theories have been developed to explain the scale factor. One of these widely used theories is the model of surface elasticity. There are a number of reviews [10, 16, 35, 36] devoted to research on the surface theory of elasticity and its applications. In turn, among the theories of surface elasticity, the most popular is the Gurtin–Murdoch

A. V. Nasedkin (✉) · A. S. Kornievsky
Institute of Mathematics, Mechanics and Computer Science, Southern Federal University, Milchakova Street 8a, Rostov-on-Don 344090, Russia
e-mail: nasedkin@math.sfedu.ru

A. S. Kornievsky
e-mail: alexandr5koren@gmail.com

M. A. Sumbatyan (ed.), *Wave Dynamics, Mechanics and Physics of Microstructured Metamaterials*, Advanced Structured Materials 109,
https://doi.org/10.1007/978-3-030-17470-5_15

model [15]. The use of this model actually leads to the fact that the boundaries of the nano-sized body are covered with elastic membranes, the internal forces in which are determined by surface stresses. Elastic membranes can be placed at the interphase boundaries inside the body with nanoscale inclusions, which makes it possible to simulate imperfect interface boundaries with stress jumps [3–5, 7, 8, 14, 24].

The Gurtin–Murdoch model was repeatedly used to describe elastic nanostructured composites. Thus, in [1, 2, 6–9, 11, 22, 23, 31] and others, within the framework of the theory of elasticity with surface stresses, the mechanical properties of composites with spherical nanoinclusions (nanopores), as well as fibrous and other nanocomposites, were investigated. Techniques of finite element approximation for elastic materials with surface effects and examples of calculations are presented in [12, 13, 17–21, 26–28, 32, 34] and others.

In this paper, we study the effective stiffness properties of a nanoporous isotropic elastic material for various forms of pores. Porous material is considered as a limiting case of a two-phase mixed composite, when the material of inclusions has negligibly small stiffness moduli. The nano-dimensionality at the boundaries of the material with pores was taken into account using the Gurtin–Murdoch surface stress model. This paper is a continuation of research [26–30]. In the development of the above-mentioned paper, the scale factor is associated with the pore size and the effect of pore shape on the effective composite properties is studied.

2 Mathematical Problem Statement

Let Ω be a unit cubic cell of elastic porous material with one pore of cubic or spherical form; a is the cubic cell side; $\Omega = \Omega^{(1)} \cup \Omega^{(2)}$; $\Omega^{(1)}$ is the part of Ω with main elastic material; $\Omega^{(2)}$ is the pore; $\Gamma = \partial\Omega$ is the external boundary of the cell; $\Gamma^s = \partial\Omega^{(2)}$ is the boundary of the pore; n_k are the components of the unit normal vector external with respect to the volume of the main elastic material $\Omega^{(1)}$.

The unit cell Ω is linked to the Cartesian coordinate system $Ox_1x_2x_3$ so that it occupies the region $|x_k| \le a/2$. Then, in the case of a cubic pore with side b ($b < a$), the domain $\Omega^{(2)}$ will be defined by the inequalities $|x_k| \le b/2$, and in the case of a spherical pore with radius R, the domain $\Omega^{(2)}$ is given by the inequality $r \le R$, $r = \sqrt{x_1^2 + x_2^2 + x_3^2}$.

We will assume that in the volume Ω the system of equations of the static theory of elasticity is satisfied with respect to the components $u_k = u_k(\mathbf{x})$ of the displacement vector

$$\partial\sigma_{ij}/\partial x_j = 0, \quad \sigma_{ij} = \lambda\varepsilon_{kk}\delta_{ij} + 2\mu\varepsilon_{ij}, \quad \varepsilon_{ij} = (\partial u_i/\partial x_j + \partial u_j/\partial x_i)/2, \qquad (1)$$

where σ_{ij} and ε_{ij} are the components of the stress and strain tensors, respectively; λ, μ are the Lame's coefficients; δ_{ij} is the Kronecker symbol.

Here we consider the pore as an elastic material with negligible Lame's coefficients. Thus, the system of equations (1) is satisfied in Ω, with $\lambda = \lambda^{(m)}$, $\mu = \mu^{(m)}$ for $\mathbf{x} \in \Omega^{(m)}$; $\lambda^{(2)} \ll \lambda^{(1)}$, $\mu^{(2)} \ll \mu^{(1)}$.

We will accept that the pore $\Omega^{(2)}$ is nanosized and in accordance with the Gurtin–Murdoch model, at its boundary Γ^s the surface stresses σ_{ij}^s exist, and the following equations hold

$$n_j[\sigma_{ij}] = \partial^s \sigma_{ij}^s / \partial x_j, \qquad \mathbf{x} \in \Gamma^s, \tag{2}$$

$$\sigma_{ij}^s = \lambda^s \varepsilon_{kk}^s \delta_{ij} + 2\mu^s \varepsilon_{ij}^s, \quad \varepsilon_{ij}^s = (\partial^s u_i^s / \partial x_j + \partial^s u_j^s / \partial x_i)/2, \tag{3}$$

$$\partial^s / \partial x_j = \partial / \partial x_j - n_j (n_k \partial / \partial x_k), \quad u_i^s = (\delta_{ik} - n_i n_k) u_k, \tag{4}$$

where $[\sigma_{ij}] = \sigma_{ij}^{(1)} - \sigma_{ij}^{(2)}$ is the stress jump over the boundary Γ^s between the volumes with different materials; $\partial^s / \partial x_j$ are the components of the surface nabla-operator; λ^s, μ^s are the surface Lame's coefficients; ε_{ij}^s are the surface strains; u_i^s are the surface displacements.

In the rectangular local coordinate system, attached with tangent orts $\tilde{\mathbf{e}}_1 = \boldsymbol{\tau}_1$, $\tilde{\mathbf{e}}_2 = \boldsymbol{\tau}_2$ and normal $\tilde{\mathbf{e}}_3 = \mathbf{n}$, the sets of the values $\tilde{u}_i^s$, $\tilde{\varepsilon}_{ij}^s$, $\tilde{\sigma}_{ij}^s$ are pertaining to surface, i.e. $\tilde{u}_3^s = 0$, $\tilde{\varepsilon}_{13}^s = \tilde{\varepsilon}_{23}^s = \tilde{\varepsilon}_{33}^s = 0$, $\tilde{\sigma}_{13}^s = \tilde{\sigma}_{23}^s = \tilde{\sigma}_{33}^s = 0$.

Note that as we can see from Eq. (1) the surface stresses σ_{ij}^s have the dimensionality (N/m) different from the dimensionality (N/m^2) of usual bulk stresses σ_{ij}. Also the surface Lame's coefficients λ^s, μ^s have the dimensionality (N/m) different from the dimensionality (N/m^2) of usual bulk Lame's coefficients λ, μ.

When calculating the effective moduli of a porous elastic material with surface stresses, we will find the basic moduli that are important for practical applications. As is well known, for elastic isotropic materials such moduli are the stiffness moduli c_{11}, c_{12}, the Young's modulus E, the Poisson's ratio ν, the shear modulus $G = \mu = c_{44}$, and the bulk modulus K. These moduli can be expressed through the Lame's coefficients by the following formulae

$$c_{11} = \lambda + 2\mu, \quad c_{12} = \lambda, \quad E = \frac{\mu(3\lambda + 2\mu)}{\lambda + \mu}, \quad \nu = \frac{\lambda}{2(\lambda + \mu)}, \quad K = \lambda + \frac{2}{3}\mu, \tag{5}$$

or through the Young's modulus and the Poisson's ratio

$$\lambda = \frac{\nu E}{(1 + \nu)(1 - 2\nu)}, \quad \mu = \frac{E}{2(1 + \nu)}, \quad K = \frac{E}{3(1 - 2\nu)}. \tag{6}$$

Similarly, instead of the surface Lame's coefficients λ^s and μ^s we can use other surface moduli. For example, we can introduce the surface Young's modulus E^s and the surface Poisson's ratio ν^s having expressed from the first formula (3) the surface strains ε_{ij}^s through the surface stresses σ_{ij}^s in a form similar to the standard Hooks's law for the three-dimensional theory of elasticity

$$\varepsilon_{ij}^s = -\frac{\nu^s}{E^s}\sigma_{kk}^s\delta_{ij} + \frac{(1+\nu^s)}{E^s}\sigma_{ij}^s. \tag{7}$$

Since in (3) and in (7) the surface quantities are related, the expressions for the surface moduli will differ from (5), (6) [19]

$$c_{11}^s = \lambda^s + 2\mu^s,\ c_{12}^s = \lambda^s,\ E^s = \frac{4\mu^s(\lambda^s+\mu^s)}{\lambda^s+2\mu^s},\ \nu^s = \frac{\lambda^s}{\lambda^s+2\mu^s},\ K^s = \lambda^s + \mu^s, \tag{8}$$

$$\lambda^s = \frac{\nu^s E^s}{1-(\nu^s)^2},\quad \mu^s = \frac{E^s}{2(1+\nu^s)},\quad K^s = \frac{E^s}{2(1-\nu^s)}. \tag{9}$$

Here, in (8), (9) we define the surface compression modulus K^s in the form corresponding to [1, 19, 24] and differ from [6–8] and others.

Thus, a nanoporous composite with surface stresses on the pore boundaries is characterized by four elastic moduli, for example, $E^{(1)}$, $\nu^{(1)}$, E^s and ν^s ($E^{(2)} \approx 0$). We will assume that the "equivalent" homogeneous material will be isotropic and will be characterizes by two independent moduli, for example, by c_{11}^{eff} and c_{12}^{eff}. In order to find these effective moduli, it is enough to solve the problem (1)–(4) in the unit cell Ω with the boundary conditions

$$u_1 = \varepsilon_0 x_1,\quad u_2 = u_3 = 0,\qquad \mathbf{x} \in \Gamma, \tag{10}$$

where $\varepsilon_0 = \text{const}$.

After solving the problem (1)–(4), (10) similar to [26–29], we can calculate the effective stiffness moduli by using the formulae

$$c_{11}^{\text{eff}} = \langle\sigma_{11}\rangle/\varepsilon_0,\quad c_{12}^{\text{eff}} = \langle\sigma_{22}\rangle/\varepsilon_0, \tag{11}$$

where the angle brackets $\langle(\bullet)\rangle$ denote the averaged integral volume and interface values [3, 4, 18, 19]

$$\langle(\bullet)\rangle = \frac{1}{|\Omega|}\Big(\int_\Omega (\bullet)\,d\,\Omega + \int_{\Gamma^s} (\bullet)^s\,d\,\Gamma\Big). \tag{12}$$

We can check that the homogenized material will be isotropic, if for the solution of the problem (1)–(4), (10) we verify that $c_{12}^{\text{eff}} \approx \langle\sigma_{33}\rangle/\varepsilon_0$; $\langle\sigma_{jk}\rangle \approx 0$, $j \neq k$. For additional control we can solve the shear problem (1)–(4) with boundary conditions: $u_1 = 0$, $u_2 = \varepsilon_0 x_3/2$, $u_3 = \varepsilon_0 x_2/2$, $\mathbf{x} \in \Gamma$. From the solution of this problem we can anew calculate the shear modulus $c_{44}^{\text{eff}} = \langle\sigma_{23}\rangle/\varepsilon_0$, and this modulus should be approximately equal to $c_{44}^{\text{eff}} \approx (c_{11}^{\text{eff}} - c_{12}^{\text{eff}})/2$, where the stiffness moduli c_{11}^{eff} and c_{12}^{eff} are found from the solution of the problem (1)–(4), (10).

In conclusion of this section, we note that the model of the pore as an elastic material gives some error, but since $\lambda^{(2)} \approx 0$, $\mu^{(2)} \approx 0$, we should expect that the stress components in the pore region will also be small $\sigma_{ij}^{(2)} \approx 0$.

3 Finite Element Results and Discussion

The boundary problems (1)–(4), (10) were solved numerically in the ANSYS finite element package.

By virtue of the problem symmetry and for the convenience of analyzing the fields inside the volume, a quarter of the cell $\{-a \le x_1 \le a, 0 \le x_2 \le a, 0 \le x_3 \le a\}$ was considered with symmetry conditions on the faces $x_2 = 0$, $x_3 = 0$. Inside the cell, as a pore either a quarter cube $\{-b \le x_1 \le b, 0 \le x_2 \le b, 0 \le x_3 \le b\}$ (case 1), or a quarter ball $\{r \le R, 0 \le x_2, 0 \le x_3\}$ (case 2) were set. The 10-node tetrahedral structural SOLID92 elements were used as volumetric elements. The presence of surface stresses was modelled with 8-node SHELL281 elements with the option of membrane stresses and with degenerate triangular 6-node shapes. The shell elements were covered the inner boundary of the pore and were located on the triangular faces of the corresponding bulk tetrahedral elements, which ensured the conformality of the finite element mesh consisting of bulk and shell elements.

The grid of bulk finite elements was created in ANSYS with a limit on the maximum size of elements equal to $\hat{a}/10$, where $\hat{a}$ is the dimensionless cell size. Bulk elements inherit the material properties of the main elastic material and pore associated with a quarter of the volumes $\Omega^{(1)}$ and $\Omega^{(2)}$. Then, shell finite elements were created automatically on the elements faces located on the inner surface of the pore. Variants of the constructed finite element meshes without elements with the material properties of pores are shown in Fig. 1 for the case of cubic pores (a) and spherical pores (b). Shell elements in Fig. 1 highlighted in a darker, and porosity p is the same and equal to 40%.

We considered steel as the main material with the following elastic moduli: $E^{(1)} = 2 \cdot 10^{11}$ (N/m^2), $\nu^{(1)} = 0.3$. In the pore volume, we set negligible stiffness moduli using the formulae: $E^{(2)} = \kappa E^{(1)}$, $\kappa = 10^{-10}$, $\nu^{(2)} = \nu^{(1)}$.

For surface moduli we accept the following formulae: $E^s = d^s E^{(1)}$, $\nu^s = \nu^{(1)}$, $d^s = 10^{-10}$ (m). Note that, unfortunately, so far there are very few data on surface moduli, and they are quite contradictory. Therefore, in a large number of theoretical papers, the same values of surface moduli from [25, 33] are used, which greatly differ in different crystallographic planes and some are negative. In this regard, here we use the model values of the surface moduli.

Analogously to [26, 27], we model in ANSYS the surface effects by using shall finite elements with the membrane stress option. For these elements we specify the Young's modulus E^m, the Poisson's ratio ν^m and thickness h^m. In order for the membrane element can be used as a surface element, we must accept: $E^s = h^m E^m$, $\nu^s = \nu^m$ [26, 27]. We also assume that $h^m = b, E^m = k^s E$, where k^s is a dimensionless coefficient. Then, $b = d^s/k^s$, and therefore the coefficient k^s is inversely proportional to the size b of cubic pore.

In the calculations, we determined the pore size as dimensionless, with the side of cubic pore $\hat{b}$ being equal to 1. We set the dimensionless radius $\hat{R} = (3\pi/4)^{1/3}$ so that the volume of the spherical pore is equal to the volume of the cubic pore. The

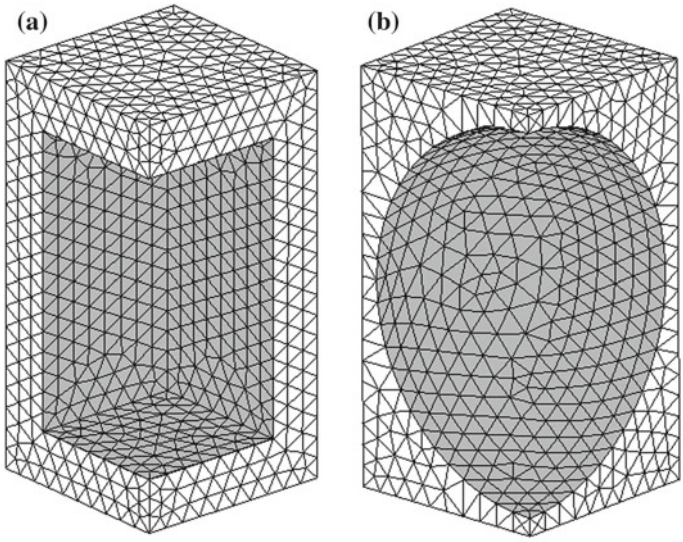

Fig. 1 Finite element mesh for two cases of quarter unit cell without pore elements

dimensionless cell size $\hat{a}$ for both cases was determined depending on the specified percentage of porosity p: $\hat{a} = (p/100)^{-1/3}\hat{b} = (p/100)^{-1/3}$.

We analysed the influence of the pore forms, the percentage of porosity and the surface stresses on the effective moduli. We varied the percentage of porosity p from 0 to 50%, the multiplier value for surface stresses k^s, and the pore form (cube or sphere).

The results of the calculations are presented in Figs. 2, 3, 4, 5, 6 and 7. Here $r(\ldots)$ designates the relative value of the effective modulus, with respect to the value of the corresponding modulus for main elastic material without pore. Thus, $r(c_{11}) = c_{11}^{\text{eff}}/c_{11}^{(1)}$, where c_{11}^{eff} is the effective stiffness modulus for the porous material with or without interface stresses, $c_{11}^{(1)}$ is the value of the corresponding stiffness modulus for the dense main material, and so on. The curves 1 correspond to the case of porous material without surface stresses, when $k^s = 0$; the curves 2 correspond to the case of porous material with small surface stresses, when $k^s = 0.1$; the curves 3 correspond to the case of porous material with large enough surface stresses, when $k^s = 0.5$, and the curves 4 correspond to the case of porous material with very large surface stresses, when $k^s = 1$. Figures 2, 3, 4, 5, 6 and 7 on the left (a) show graphs for the case of a cubic pore, and on the right (b) show similar curves for the case of a spherical pore.

Figures 2, 3, 4, 5, 6 and 7 demonstrate an essential dependence of the effective moduli, both on the pore shape and on the coefficient of surface stresses k^s. These dependencies also differ by module type. So, for moduli characterizing uniaxial tension, shear and transversal deformations, these dependences are different.

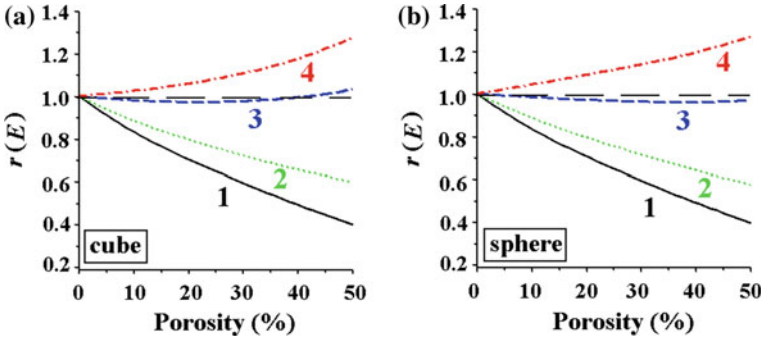

Fig. 2 Dependencies of the relative effective Young's modulus E versus porosity

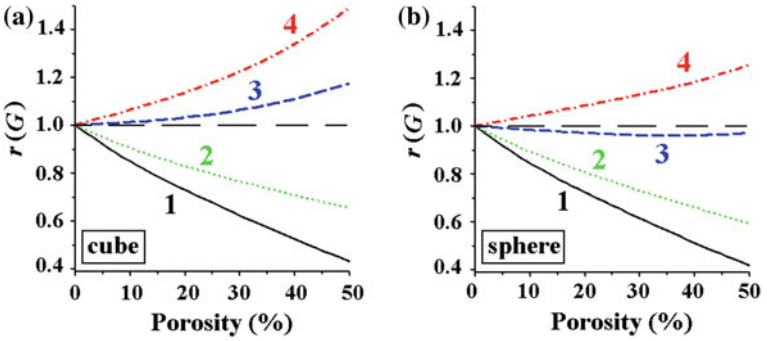

Fig. 3 Dependencies of the relative effective shear modulus G versus porosity

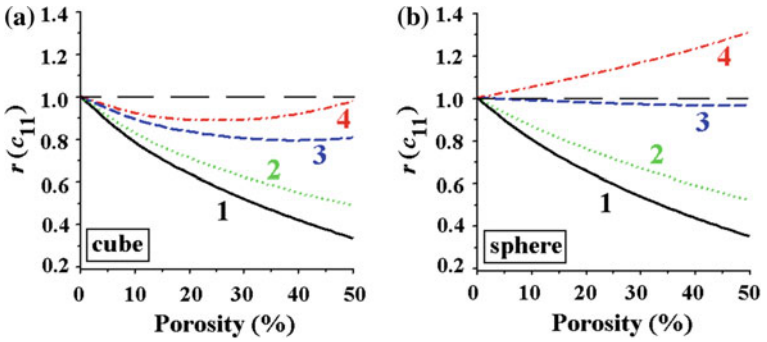

Fig. 4 Dependencies of the relative effective stiffness modulus c_{11} versus porosity

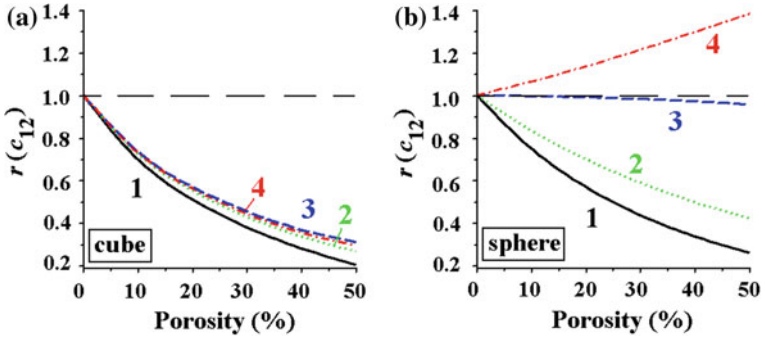

Fig. 5 Dependencies of the relative effective stiffness modulus c_{12} versus porosity

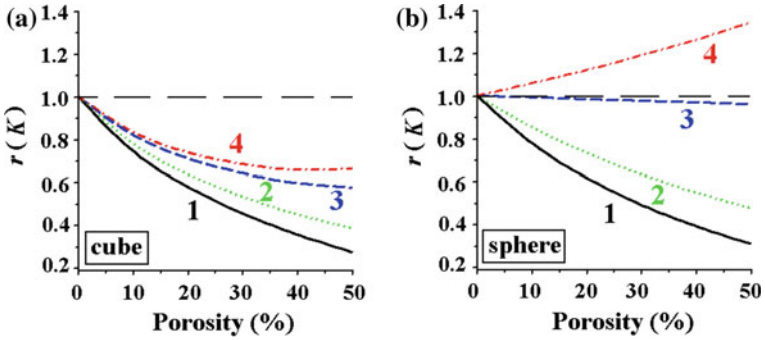

Fig. 6 Dependencies of the relative effective bulk modulus K versus porosity

In the absence of surface stresses (curves 1), all moduli decrease with increasing porosity, and the shapes of the pores have a certain effect, though it is not so extensive. The presence of surface stresses radically changes the pattern of dependencies. All moduli can be subdivided into two groups, in which the dependencies of the moduli on porosity and on the shape of the pores are most similar to each other. The first group includes the moduli characterizing uniaxial tension: the Young's modulus E, the shear modulus G, and the stiffness modulus c_{11} (Figs. 2, 3 and 4). The second group includes the moduli characterizing transverse deformations and uniform compression: the stiffness modulus c_{12}, the bulk modulus K, and the Poisson's ratio ν (Figs. 5, 6 and 7).

For very large coefficients k^s for a cubic pore, as the porosity increases, the Young's modulus E and shear modulus G grow faster than in the case of a spherical pore. On the contrary, the stiffness modulus c_{11} for large k^s grows faster for a spherical pore.

Meanwhile, for the stiffness modulus c_{12}, the bulk modulus K, and the Poisson's ratio ν, these behaviours differ significantly from porosity. For all used coefficients k^s, these moduli decrease with increasing porosity for a cubic pore. However, for a spherical pore, these moduli increase for large k^s (curves 4). In this case, the most

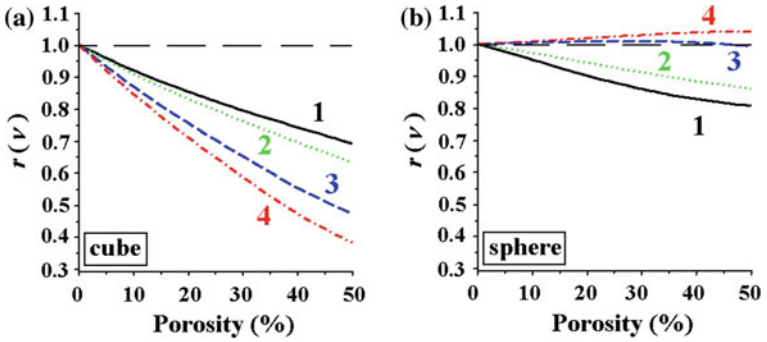

Fig. 7 Dependencies of the relative effective Poisson's ratio ν versus porosity

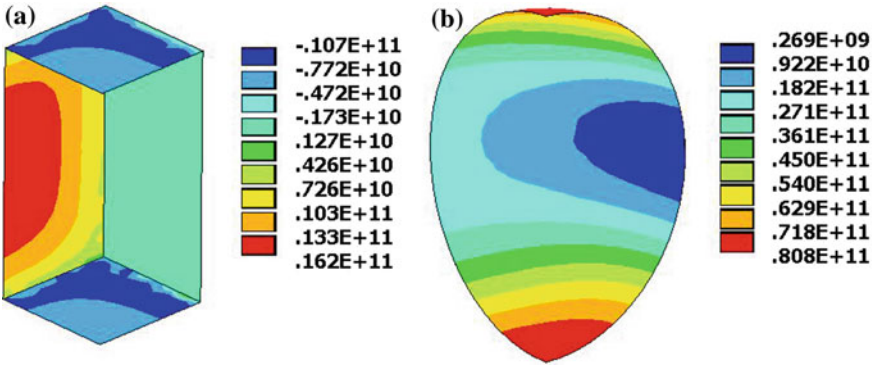

Fig. 8 Stresses σ_{22} in membrane elements for cubic pore (**a**) and for spherical pore (**b**)

interesting is the behaviour of the Poisson coefficient ν, which for a cubic pore not only decreases with increasing porosity, but this decrease becomes stronger with increasing k^s, which differs from the corresponding behavior of the stiffness modulus c_{12} and the bulk modulus K.

Such differences can be explained by the fact that for a cubic pore under extension along the x_1 axis, the stresses σ_{22} (and similarly for σ_{33}) in membrane elements change sign, and on edges perpendicular to the axis x_2 do not occur. In the case of a spherical pore, membrane elements are located on curved surfaces. Therefore, with uniaxial tension in membrane elements, the various stress components arise, and the main stresses σ_{11} on a curved surface significantly affect to the stresses σ_{22} and σ_{33}. As can be seen from Fig. 8, the stresses σ_{22} in membrane elements on the sphere surface do not change sign, and their maximum values are almost five times larger than for a cubic pore. Since the stiffness modulus c_{12} according to (11), (12) is calculated by integrating the stresses σ_{22} both by volume elements and surface elements, then it is clear that the surface stresses for a spherical pore increase the modulus c_{12} significantly more than for a cubic pore.

Similar reasoning is true for the bulk modulus K, and it is obvious that the sphere-shaped pore reinforced over the surface gives a more rigid structure for a full compression in the composite than the cubic pore reinforced over the surface.

Thus, summarizing the above, we can conclude that the shape of the pores has a significant influence on the effective moduli of the porous material, especially when taking into account surface stresses for nanoscale pores.

Finally, we can note the well-known fact that for a nanoporous material its effective moduli may be larger than for a solid material. As can be seen in Figs. 2, 3, 4, 5, 6 and 7, these situations occur when the values of the relative effective moduli are greater than 1 (i.e. the curves 3 or 4 turn out to be above the dashed line $r(\ldots) = 1$). An explanation of this can be found in many papers [9–11, 26, 27] and therefore is not repeated here.

Further studies can be aimed at solving the problems with periodic boundary conditions, with representative volumes with a large number of pores of different shapes and with the definition of surface moduli by using different formulae that was accepted in this paper.

Acknowledgements This work was supported by the Russian Science Foundation (grant number 15–19-10008-P).

References

1. Brisard, S., Dormieux, L., Kondo, D.: Hashin-Shtrikman bounds on the bulk modulus of a nanocomposite with spherical inclusions and interface effects. Comp. Mater. Sci. **48**, 589–596 (2010)
2. Brisard, S., Dormieux, L., Kondo, D.: Hashin-Shtrikman bounds on the shear modulus of a nanocomposite with spherical inclusions and interface effects. Comp. Mater. Sci. **50**, 403–410 (2010)
3. Chatzigeorgiou, G., Javili, A., Steinmann, P.: Multiscale modelling for composites with energetic interfaces at the micro-or nanoscale. Math. Mech. Solids. **20**, 1130–1145 (2015)
4. Chatzigeorgiou, G., Meraghni, F., Javili, A.: Generalized interfacial energy and size effects in composites. J. Mech. Phys. Solids. **106**, 257–282 (2017)
5. Chen, T., Dvorak, G.J., Yu, C.C.: Solids containing spherical nano-inclusions with interface stresses: effective properties and thermal-mechanical connections. Int. J. Solids Struct. **44**, 941–955 (2007)
6. Duan, H.L., Wang, J., Huang, Z.P., Karihaloo, B.L.: Eshelby formalism for nano-inhomogeneities. Proc. R. Soc. A. **461**, 3335–3353 (2005)
7. Duan, H.L., Wang, J., Huang, Z.P., Karihaloo, B.L.: Size-dependent effective elastic constants of solids containing nano-inhomogeneities with interface stress. J. Mech. Phys. Solids. **53**, 1574–1596 (2005)
8. Duan, H.L., Wang, J., Huang, Z.P., Luo, Z.Y.: Stress concentration tensors of inhomogeneities with interface effects. Mech. Mater. **37**, 723–736 (2005)
9. Duan, H.L., Wang, J., Karihaloo, B.L., Huang, Z.P.: Nanoporous materials can be made stiffer than non-porous counterparts by surface modification. Acta Materialia. **54**, 2983–2990 (2006)
10. Eremeyev, V.A.: On effective properties of materials at the nano- and microscales considering surface effects. Acta Mech. **227**, 29–42 (2016)
11. Eremeyev, V., Morozov, N.: The effective stiffness of a nanoporous rod. Dokl. Physics. **55**(6), 279–282 (2010)

12. Gad, A.I., Mahmoud. F.F., Alshorbagy. A.E., Ali-Eldin. S.S.: Finite element modeling for elastic nano-indentation problems incorporating surface energy effect. Int. J. Mech. Sciences. **84**, 158–170 (2014)
13. Gao, W., Yu, S.W., Huang, G.Y.: Finite element characterization of the size-dependent mechanical behaviour in nanosystem. Nanotechnology **17**, 1118–1122 (2006)
14. Gu, S.-T., Liu, J.-T., He, Q.-C.: Size-dependent effective elastic moduli of particulate composites with interfacial displacement and traction discontinuities. Int. J. Solids Struct. **51**, 2283–2296 (2014)
15. Gurtin, M.E., Murdoch, A.I.: A continuum theory of elastic material surfaces. Arch. Rat. Mech. Analysis. **57**(4), 291–323 (1975)
16. Hamilton, J.C., Wolfer, W.G.: Theories of surface elasticity for nanoscale objects. Surface Sci. **603**, 1284–1291 (2009)
17. Javili, A., Chatzigeorgiou, G., McBride, A.T., Steinmann, P., Linder, C.: Computational homogenization of nano-materials accounting for size effects via surface elasticity. GAMM-Mitteilungen **38**(2), 285–312 (2015)
18. Javili, A., McBride, A., Mergheima, J., Steinmann, P., Schmidt, U.: Micro-to-macro transitions for continua with surface structure at the microscale. Int. J. Solids Struct. **50**, 2561–2572 (2013)
19. Javili, A., McBride, A., Steinmann, P.: Thermomechanics of solids with lower-dimensional energetics: on the importance of surface, interface, and curve structures at the nanoscale. A unifying review. Appl. Mech. Rev. **65**, 010802-1–31 (2013)
20. Javili, A., Steinmann, P.: A finite element framework for continua with boundary energies. Part I: the two-dimensional case. Comput. Methods Appl. Mech. Engrg. **198**, 2198–2208 (2009)
21. Javili, A., Steinmann, P.: A finite element framework for continua with boundary energies. Part II: The three-dimensional case. Comput. Methods Appl. Mech. Engrg. **199**, 755–765 (2010)
22. Jeong, J., Cho, M., Choi, J.: Effective mechanical properties of micro/nano-scale porous materials considering surface effects. Interact. Multiscale Mech. **4**(2), 107–122 (2011)
23. Kushch, V.I., Mogilevskaya, S.G., Stolarski, H.K., Crouch, S.L.: Elastic fields and effective moduli of particulate nanocomposites with the Gurtin-Murdoch model of interfaces. Int. J. Solids Struct. **50**, 1141–1153 (2013)
24. Le Quang, H., He, Q.-C.: Variational principles and bounds for elastic inhomogeneous materials with coherent imperfect interfaces. Mech. Mater. **40**, 865–884 (2008)
25. Miller, R.E., Shenoy, V.B.: Size-dependent elastic properties of nanosized structural elements. Nanotechnology. **11**, 139–147 (2000)
26. Nasedkin, A.V., Kornievsky, A.S.: Finite element modeling and computer design of anisotropic elastic porous composites with surface stresses. In: M.A. Sumbatyan (Ed.) Wave Dynamics and Composite Mechanics for Microstructured Materials and Metamaterials. Ser. Advanced Structured Materials, vol. 59, pp. 107–122. Springer, Singapore (2017)
27. Nasedkin, A.V., Kornievsky, A.S.: Finite element modeling of effective properties of elastic materials with random nanosized porosities. ycisl. meh. splos. sred – Computational Continuum Mechanics. **10**(4), 375–387 (2017)
28. Nasedkin, A.V., Kornievsky, A.S.: Finite element homogenization of elastic materials with open porosity at different scale levels. AIP Conf. Proc. **2046**, 020064 (2018)
29. Nasedkin, A.V., Nasedkina, A.A., Kornievsky, A.S.: Modeling of nanostructured porous thermoelastic composites with surface effects. AIP Conf. Proc. **1798**, 020110 (2017)
30. Nasedkin, A.V., Nasedkina, A.A., Kornievsky, A.S.: Finite element modeling of effective properties of nanoporous thermoelastic composites with surface effects. In: Greece. M. Papadrakakis, E. Onate, B.A. Schrefler (eds.) Coupled Problems 2017 - Proceeding VII International Conference on Coupled Problems in Science and Engineering, 12–14 June 2017, pp. 1140–1151. Rhodes Island, CIMNE, Barcelona, Spain (2017)
31. Nazarenko, L., Bargmann, S., Stolarski, H.: Energy-equivalent inhomogeneity approach to analysis of effective properties of nanomaterials with stochastic structure. Int. J. Solids Struct. **59**, 183–197 (2015)
32. Riaz, U., Ashraf, S.M.: Application of Finite Element Method for the Design of Nanocomposites. In: Musa, S.M. (ed.), Computational Finite Element Methods in Nanotechnology, pp. 241–290. CRC Press (2012)

33. Sharma, P., Ganti, S., Bhate, N.: Effect of surfaces on the size-dependent elastic state of nano-inhomogeneities. Appl. Phys. Lett. **82**, 535–537 (2003)
34. Tian, L., Rajapakse, R.K.N.D.: Finite element modelling of nanoscale inhomogeneities in an elastic matrix. Comp. Mater. Sci. **41**, 44–53 (2007)
35. Wang, J., Huang, Z., Duan, H., Yu, S., Feng, X., Wang, G., Zhang, W., Wang, T.: Surface stress effect in mechanics of nanostructured materials. Acta Mechanica Solida Sinica. **24**(1), 52–82 (2011)
36. Wang, K.F., Wang, B.L., Kitamura, T.: A review on the application of modified continuum models in modeling and simulation of nanostructures. Acta Mech. Sin. **32**(1), 83–100 (2016)

Electro-Magneto-Elastic Coupled Waves in Piezoactive Periodic Structures

Karen B. Ghazaryan, Davit G. Piliposyan and Gayane T. Piliposian

Abstract Based on the complete set of Maxwell' electrodynamics equations and the theory of elasticity the two-dimensional equations have obtained describing the coupled wave process in piezoactive electro-magneto-elastic (MEE) structure and allowing solution of a new class of problems, in particular, the problems of propagation and internal resonance of electro-magneto-elastic waves in periodic MEE structures. For longitudinal lattice vibrations of oppositely polarized MEE periodic superlattice the effect of phonon–photon polariton is investigated with a full three-phase coupling between elastic, electromagnetic fields. The results show that the new coupled phonon–photon polariton exhibits properties different from piezoelectric or piezomagneticpolaritons.

1 Introduction

Materials made of piezoelectric and piezomagnetic phases have the ability of converting energy from one form to the other (among magnetic, electric, and mechanical energies). Furthermore, composites made of piezoelectric and piezomagnetic materials exhibit a magnetoelectric piezo effect that is not present in the single-phase piezoelectric or piezomagnetic material [1, 2]. This is achieved by artificially combining electro-elastic (piezoelectric) and magneto-elastic (piezomagnetic) particles within an elastic matrix [3]. Propagation of electro-magneto-elastic waves in periodic composites where the constituent materials possess coupled response effects (e.g. piezoelectric and piezomagnetic effects), have already found a wide range of application in smart materials. A combination of these two effects in a single composite provides new properties such as the magneto-electro-elastic effect, which recently

K. B. Ghazaryan (✉) · D. G. Piliposyan
Institute of Mechanics, National Academy of Sciences, Yerevan, Armenia
e-mail: ghkarren@gmail.com

G. T. Piliposian
Department of Mathematical Sciences, The University of Liverpool, M&O Building, Liverpool L69 7ZL, UK

M. A. Sumbatyan (ed.), *Wave Dynamics, Mechanics and Physics of Microstructured Metamaterials*, Advanced Structured Materials 109,
https://doi.org/10.1007/978-3-030-17470-5_16

attracted much attention due to a growing interest in the application of the magneto-electric composites, for example, in medical ultrasonic imaging, electronic packaging [4]. A number of papers have been published investigating the existence and propagation of different kinds of waves in MEE materials, for example [5–8]. In most of these studies, the quasi-static approximation is adopted for the electromagnetic field. Under this assumption, both the optical effect and the effect from the rotational part of the electric field are neglected. Although it is believed that the optical effect is not significant it might be useful in some applications to accurately predict the piezoelectricity induced electromagnetic radiation. Such applications can for example include optical detection or nondestructive evaluation [9]. The problems of electro -acoustic waves in a piezoelectric non-periodic medium in a dynamic setting (none quasi-static) were considered in [10, 11]. In periodic structures the dynamic setting of Maxwell's equations is necessary to consider when investigating frequency forbidden band gaps, polariton effects and the coupling internal resonance of elastic and electromagnetic waves [12, 13]. In the long-wavelength approximation this setting has been used to investigate a new type of polariton coupling in peizoelectric and piezomagnetic crystals [14–17]. In this paper based on results of [18] we present studies defining the phonon–photon polariton coupling effects in a new type of MEE periodic superlattice with a full three-phase coupling between mechanical, electric and magnetic fields.

2 General Relations and Equations of MEE Media

We consider a piezoactive magneto-electro-elastic (MEE) media in the framework of linear theory elasticity and full dynamic setting of the Maxwell's electrodynamic equations, which gives an opportunity to study the wave process in both acoustic and optic wave frequency regions.

Interaction between elastic waves and electrodynamic waves in MEE media can be described by the following equations

$$\operatorname{div}\boldsymbol{\sigma} = \rho\frac{\partial^2 \boldsymbol{U}}{\partial t^2}, \operatorname{rot}\mathbf{E} = -\frac{\partial \mathbf{B}}{\partial t}, \operatorname{rot}\mathbf{H} = \frac{\partial \mathbf{D}}{\partial t} \tag{1}$$

and basic constitutive relations

$$\boldsymbol{\sigma} = \mathbf{c} : \boldsymbol{S} - \boldsymbol{e} \cdot \mathbf{E} - \mathbf{d} \cdot \mathbf{H}, \tag{2}$$

$$\mathbf{D} = \mathbf{e} : \boldsymbol{S} + \boldsymbol{\varepsilon} \cdot \mathbf{E} + \mathbf{g} \cdot \mathbf{H}, \tag{3}$$

$$\mathbf{B} = \mathbf{d} : \mathrm{S} + \mathbf{g} \cdot \mathbf{E} + \boldsymbol{\mu} \cdot \mathbf{H}, \tag{4}$$

Here $\boldsymbol{\sigma}$, $\boldsymbol{S}$, $\boldsymbol{\varepsilon}$, $\boldsymbol{\mu}$ and g are the stress, strain, dielectric permittivity, magnetic permeability and magneto-electric tensors, **e**, **d**, **c** are the piezoelectric, piezomagnetic, elastic stiffness tensors tensor, **D**, **E**, **B**, **H** are electric displacement, electric field, magnetic induction and magnetic field vectors and $\boldsymbol{U}$ is the displacement vector, dot corresponds to the tensor convolution operation, double dot corresponds to the tensor double convolution operation.

We consider two dimensional wave propagation in an electro-magneto-elastic medium of 6 mm class hexagonal symmetry, when the plane of symmetry coincides with plane (x, y) and the crystallographic polling axis coincides with the direction of z axis. For this media the 2D constitutive relations can be cast as $(\partial_z = 0)$

$$\begin{aligned}
&B_x = d_{15}\partial_x U_z + g_{11}E_x + \mu_{11}H_x, && D_x = e_{15}\partial_x U_z + \varepsilon_{11}E_x + g_{11}H_x,\\
&B_y = d_{15}\partial_y U_z + g_{11}E_y + \mu_{11}H_y, && D_y = e_{15}\partial_y U_z + \varepsilon_{11}E_y + g_{11}H_y,\\
&B_z = d_{31}(\partial_x U_x + \partial_y U_y) + g_{33}E_z + \mu_{33}H_z, && D_z = e_{31}(\partial_x U_x + \partial_y U_y) + \varepsilon_{33}E_z + g_{33}H_z,\\
&\sigma_{yz} = c_{44}\partial_y U_z - e_{15}E_y - d_{15}H_y, && \sigma_{xx} = c_{11}\partial_x U_x + c_{12}\partial_y U_y - e_{31}E_z - d_{31}H_z,\\
&\sigma_{xz} = c_{44}\partial_x U_z) - e_{15}E_x - d_{15}H_x, && \sigma_{yy} = c_{12}\partial_x U_x + c_{11}\partial_y U_y - e_{31}E_z - d_{31}H_z.\\
&\sigma_{xy} = c_{66}(\partial_y U_x + \partial_x U_y), &&
\end{aligned} \tag{5}$$

(6)

Substituting (4) into we obtain the following coupled set equations with respect to eight functions $H_z(x, y)$, $H_x(x, y)$, $U_z(x, y)$, $U_x(x, y)$, $U_y(x, y)$, $E_z(x, y)$, $E_x(x, y)$, $E_y(x, y)$

$$\begin{aligned}
\frac{\partial E_x}{\partial t} &= -\frac{1}{j_1}\left(\chi\,\frac{\partial^2 U_z}{\partial x \partial t} - \frac{\partial}{\partial y}(g_{11}E_z + \mu_{11}H_z)\right),\\
\frac{\partial H_x}{\partial t} &= -\frac{1}{j_1}\left(\delta\,\frac{\partial^2 U_z}{\partial x \partial t} + \frac{\partial}{\partial y}(g_{11}H_z + \varepsilon_{11}E_z)\right),\\
\frac{\partial E_y}{\partial t} &= -\frac{1}{j_1}\left(\chi\,\frac{\partial^2 U_z}{\partial y \partial t} + \frac{\partial}{\partial x}(g_{11}E_z + \mu_{11}H_z)\right),\\
\frac{\partial H_y}{\partial t} &= -\frac{1}{j_1}\left(\delta\,\frac{\partial^2 U_z}{\partial y \partial t} - \frac{\partial}{\partial x}(g_{11}H_z + \varepsilon_{11}E_z)\right),
\end{aligned} \tag{7}$$

$$j_1\frac{\partial^2}{\partial t^2}\left(g_{33}E_z + \mu_{33}H_z + d_{31}\left(\frac{\partial U_x}{\partial x} + \frac{\partial U_y}{\partial y}\right)\right) - \Delta(g_{11}E_z + \mu_{11}H_z) = 0,$$

$$j_1\frac{\partial^2}{\partial t^2}\left(\varepsilon_{33}E_z + g_{33}H_z + e_{31}\left(\frac{\partial U_x}{\partial x} + \frac{\partial U_y}{\partial y}\right)\right) - \Delta(\varepsilon_{11}E_z + g_{11}H_z) = 0, \tag{8}$$

$$c_{11}\frac{\partial^2 U_y}{\partial y^2} + c_{66}\frac{\partial^2 U_y}{\partial x^2} + (c_{66} + c_{12})\frac{\partial^2 U_x}{\partial x \partial y} - \rho\frac{\partial^2 U_y}{\partial t^2} - \frac{\partial}{\partial y}(e_{31}E_z + d_{31}H_z) = 0,$$

$$c_{11}\frac{\partial^2 U_x}{\partial x^2} + c_{66}\frac{\partial^2 U_x}{\partial y^2} + (c_{66} + c_{12})\frac{\partial^2 U_y}{\partial x \partial y} - \rho\frac{\partial^2 U_x}{\partial t^2} - \frac{\partial}{\partial x}(e_{31}E_z + d_{31}H_z) = 0, \tag{9}$$

where

$$\partial_x = \partial \big/ \partial x, \partial_y = \partial \big/ \partial y, \Delta = \frac{\partial^2}{\partial x^2} + \frac{\partial^2}{\partial y^2},$$

$$j_1 = \varepsilon_{11}\mu_{11} - g_{11}^2, \delta = (d_{15}\varepsilon_{11} - e_{15}g_{11}), \chi = (e_{15}\mu_{11} - d_{15}g_{11}),$$

From the analysis of these equations it follows that in contrary to the piezoelectric case [12], for the MEE media of 6 mm class hexagonal symmetry the interconnected elastic and electric excitations do not decouple into plane and anti-plane states.

Let us consider the several special cases of Eqs. (7–9):

In the cases of pure piezoelectric media ($d_{15} = d_{31} = 0, g_{11} = g_{33} = 0$) or pure piezomagnetic media the anti-plane and in-plane states are now decoupled

1. Piezoelectric media

Anti-plane state $\left(U_z, H_z, E_y, E_x\right)$

$$\left(\frac{e_{15}^2}{\varepsilon_{11}} + c_{44}\right)\Delta U_z - \rho\frac{\partial^2 U_z}{\partial t^2} = 0, \Delta H_z - \varepsilon_{11}\mu_{33}\frac{\partial^2 H_z}{\partial t^2} = 0, \tag{10}$$

$$\varepsilon_{11}\frac{\partial E_x}{\partial t} + e_{15}\frac{\partial^2 U_z}{\partial x \partial t} = \frac{\partial H_z}{\partial y}, \varepsilon_{11}\frac{\partial E_y}{\partial t} + e_{15}\frac{\partial^2 U_z}{\partial y \partial t} = -\frac{\partial H_z}{\partial x}. \tag{11}$$

In-plane state $\left(U_{yx}, U_y, E_z, H_x, H_y\right)$

$$c_{11}\frac{\partial^2 U_y}{\partial y^2} + c_{66}\frac{\partial^2 U_y}{\partial x^2} + (c_{66} + c_{12})\frac{\partial^2 U_x}{\partial x \partial y} - \rho\frac{\partial^2 U_y}{\partial t^2} = e_{31}\frac{\partial E_z}{\partial y}, \tag{12}$$

$$c_{11}\frac{\partial^2 U_x}{\partial x^2} + c_{66}\frac{\partial^2 U_x}{\partial y^2} + (c_{66} + c_{12})\frac{\partial^2 U_y}{\partial x \partial y} - \rho\frac{\partial^2 U_x}{\partial t^2} = e_{31}\frac{\partial E_z}{\partial x}, \tag{13}$$

$$\mu_{11}\frac{\partial^2}{\partial t^2}\left(\varepsilon_{33}E_z + e_{31}\left(\frac{\partial U_x}{\partial x} + \frac{\partial U_y}{\partial y}\right)\right) - \Delta E_z = 0, \tag{14}$$

$$\mu_{11}\frac{\partial H_x}{\partial t} = -\frac{\partial E_z}{\partial y}, \mu_{11}\frac{\partial H_y}{\partial t} = \frac{\partial E_z}{\partial x}. \tag{15}$$

2. Piezo-magnetic media

Anti-plane state $\left(U_x, U_y, H_z, E_y, E_x\right)$

$$\left(\frac{d_{15}^2}{\mu_{11}} + c_{44}\right)\Delta U_z - \rho\frac{\partial^2 U_z}{\partial t^2} = 0, \Delta E_z - \varepsilon_{33}\mu_{11}\frac{\partial^2 E_z}{\partial t^2} = 0, \tag{16}$$

$$\mu_{11}\frac{\partial H_x}{\partial t} + d_{15}\frac{\partial^2 U_z}{\partial x \partial t} = -\frac{\partial E_z}{\partial y}, \mu_{11}\frac{\partial H_y}{\partial t} + d_{15}\frac{\partial^2 U_z}{\partial y \partial t} = -\frac{\partial E_z}{\partial x}. \tag{17}$$

In-plane state $\left(U_x, U_y, H_z, E_y, E_x\right)$

$$c_{11}\frac{\partial^2 U_y}{\partial y^2} + c_{66}\frac{\partial^2 U_y}{\partial x^2} + (c_{66} + c_{12})\frac{\partial^2 U_x}{\partial x \partial y} - \rho\frac{\partial^2 U_y}{\partial t^2} = d_{31}\frac{\partial H_z}{\partial y}, \tag{18}$$

$$c_{11}\frac{\partial^2 U_x}{\partial x^2}+c_{66}\frac{\partial^2 U_x}{\partial y^2}+(c_{66}+c_{12})\frac{\partial^2 U_y}{\partial x\partial y}-\rho\frac{\partial^2 U_y}{\partial t^2}=d_{31}\frac{\partial H_z}{\partial x}, \tag{19}$$

$$\mu_{11}\frac{\partial^2}{\partial t^2}\left(\varepsilon_{33}H_z+d_{31}\left(\frac{\partial U_x}{\partial x}+\frac{\partial U_y}{\partial y}\right)\right)-\Delta H_z=0, \tag{20}$$

$$\varepsilon_{11}\frac{\partial E_x}{\partial t}=\frac{\partial H_z}{\partial y},\qquad \varepsilon_{11}\frac{\partial E_y}{\partial t}=-\frac{\partial H_z}{\partial x}. \tag{21}$$

Let now consider the wave propagation along the axis x perpendicular to the poling direction z of MEE structure. For a plane wave propagating along the x axis there are two types of waves: transverse uncoupled waves describing by equations (U_z, H_x, E_x), $\left(U_y\right)$

$$\frac{\partial E_x}{\partial t}=-\frac{\chi}{j_1}\frac{\partial^2 U_z}{\partial x\partial t},\ \frac{\partial H_x}{\partial t}=-\frac{\delta}{j_1}\frac{\partial^2 U_z}{\partial x\partial t},\ (d_{15}\delta+e_{15}\chi+j_1c_{44})\Delta U_z-j_1\rho\frac{\partial^2 U_z}{\partial t^2}=0, \tag{22}$$

$$c_{66}\frac{\partial^2 U_y}{\partial x^2}-\rho\frac{\partial^2 U_y}{\partial t^2}=0, \tag{23}$$

and coupled (hybrid) longitudinal and electromagnetic waves $\left(U_x, H_z, E_y, E_z, H_y\right)$ describing by equations

$$c_{11}\frac{\partial^2 U_x}{\partial x^2}-\rho\frac{\partial^2 U_x}{\partial t^2}-\frac{\partial}{\partial x}(e_{31}E_z+d_{31}H_z)=0, \tag{24}$$

$$\frac{\partial E_y}{\partial t}=-\frac{1}{j_1}\frac{\partial}{\partial x}(g_{11}E_z+\mu_{11}H_z),\ \frac{\partial H_y}{\partial t}=\frac{1}{j_1}\frac{\partial}{\partial x}(g_{11}H_z+\varepsilon_{11}E_z), \tag{25}$$

$$j_1\frac{\partial^2}{\partial t^2}\left(g_{33}E_z+\mu_{33}H_z+d_{31}\frac{\partial U_x}{\partial x}\right)-\frac{\partial^2}{\partial x^2}(g_{11}E_z+\mu_{11}H_z)=0, \tag{26}$$

$$j_1\frac{\partial^2}{\partial t^2}\left(\varepsilon_{33}E_z+g_{33}H_z+e_{31}\frac{\partial U_x}{\partial x}\right)-\frac{\partial^2}{\partial x^2}(\varepsilon_{11}E_z+g_{11}H_z)=0, \tag{27}$$

Seeking in Eqs. (24–27) the elastic displacement U_x and the normal components H_z, E_z of electromagnetic field vector in the form of the plane harmonic waves travelling along the x axis (k is the wave vector, ω is the wave frequency)

$$E_z=E_{z0}\exp[i(kx-\omega t)],\ H_z=H_{z0}\exp[i(kx-\omega t)], \tag{28}$$

$$E_y=E_{y0}\exp[i(kx-\omega t)],\ H_y=H_{y0}\exp[i(kx-\omega t)], \tag{29}$$

$$U_x=U_{x0}\exp[i(kx-\omega t)], \tag{30}$$

we get the following dispersion equation $\left(\eta=\omega/k\right)$

$$d_{31}e_{31}\eta^2\left(-2g_1+2g_{33}j_1\eta^2\right)+d_{31}^2\eta^2\left(\varepsilon_{11}-j_1\eta^2\varepsilon_{33}\right)$$

$$+ e_{31}^2\eta^2\left(\mu_{11} - j_1\eta^2\mu_{33}\right) = \left(c_{11} - \eta^2\rho\right)\left(1 - 2j_{13}\eta^2 + j_1 j_3\eta^4\right), \quad (31)$$

$$j_1 = \varepsilon_{11}\mu_{11} - g_{11}^2;\ j_3 = \varepsilon_{33}\mu_{33} - g_{33}^2;\ j_{13} = \frac{(\varepsilon_{33}\mu_{11} + \varepsilon_{11}\mu_{33} - 2g_{11}g_{33})}{2}, \quad (32)$$

For an MEE structures the dispersion Eq. (31) defines the three hybrid waves couple with each other making an electro-magneto-elastic waves defined by $\left(u_x, H_y, E_z, H_z, E_y\right)$ indicating that a longitudinal acoustic wave will be excited by and coupled to the y and z polarized electromagnetic waves. The acoustic wave in its turn can also emit two orthogonally polarized electromagnetic waves.

In the absence of the MEE piezo effect ($d_{31} = 0, e_{31} = 0, g_{11} = 0, g_{33} = 0$) this equation uncouples into three equations determining three separate independent waves, a pure elastic longitudinal wave with phase velocity $\eta_a = \sqrt{c_{11}/\rho}$, and two pure electromagnetic waves $T_e\left(E_y, H_z\right)$ and $T_m\left(E_z, H_y\right)$ with different phase velocities $\eta_e = (\varepsilon_{11}\mu_{33})^{-1/2}$, $\eta_m = (\varepsilon_{33}\mu_{11})^{-1/2}$.

In the cases of pure piezoelectric media or pure piezomagnetic media dispersion equation defining weak interaction [20] of hybrid quasi electromagnetic, quasi acoustic waves and pure electromagnetic waves of T_e or T_m modes can be found as

$$\left(-e_{31}^2\eta^2\mu_{11} + \left(1 - \varepsilon_{33}\mu_{11}\eta^2\right)\left(c_{11} - \eta^2\rho\right)\right)\left(1 - \varepsilon_{11}\mu_{33}\eta^2\right) = 0, \quad (34)$$

$$\left(-d_{31}^2\eta^2\varepsilon_{11} + \left(1 - \varepsilon_{11}\mu_{331}\eta^2\right)\left(c_{11} - \eta^2\rho\right)\right)\left(1 - \varepsilon_{33}\mu_{11}\eta^2\right) = 0, \quad (35)$$

For bi-anisotropic electromagnetic media [19] $d_{31} = 0, e_{31} = 0$ we have the dispersion equation

$$\left(1 - 2j_{13}\eta^2 + j_1 j_3\eta^4\right) = 0, \quad (36)$$

determining two separate independent electromagnetic waves with different velocities

$$\eta_{1,2} = \sqrt{\frac{j_{13} \pm \sqrt{j_{13}^2 - j_1 j_3}}{j_1 j_3}}, \qquad (j_{13} > 0,\ j_1 > 0,\ j_3 > 0). \quad (37)$$

3 Magneto-Electro–Elastic Polariton Coupling in a Periodic Structure

We consider now the case of coupled electro-magnetic and longitudinal elastic waves propagation in periodic MEE superlattice structure (Fig. 1) having positive and negative domains of equal thickness aligned periodically of period β along the x axis and spontaneous polarization in the $\pm z$ direction. The viscous damping properties of

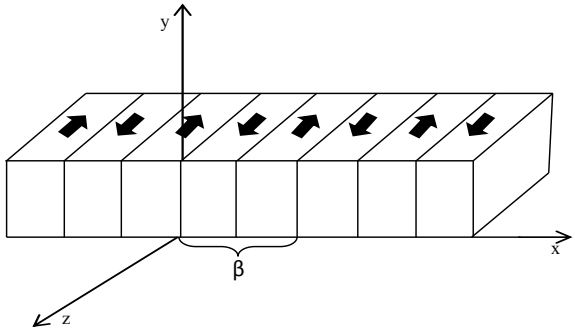

Fig. 1 Periodic oppositely polarized MEE superlattice structure

a MEE superlattice structure defining by damping coefficient η_{11} will be also taking into account [20]

The piezoelectric and piezomagnetic coefficients $e_{31}(x), d_{31}(x)$ are assumed to be periodic functions of period β with

$$e_{31}(x) = e_0 f(x), d_{31}(x) = d_0 f(x),$$
$$f(x) = 1, x \in \left(0, \beta/2\right), \qquad f(x) = -1, x \in \left(\beta/2, \beta\right). \tag{38}$$

The equation of motion can be rewritten written as

$$\left(c_{11} + \eta_{11}\frac{\partial}{\partial t}\right)\frac{\partial^2 U_x}{\partial x^2} - \rho\frac{\partial^2 U_x}{\partial t^2} = \frac{\partial}{\partial x}\left[f(x)(e_0 E_z + d_0 H_z)\right] \tag{39}$$

Using the Fourier transformation of $f(x)$, $f(x) = \sum_m f_m \exp(i K_m x)$

$$f_m = i(1 - \cos(\pi m))(\pi m)^{-1}, K_m = 2\pi m \beta^{-1}, \tag{40}$$

in the long-wavelength approximation (the electromagnetic wave wavelength is much larger than the period of piezo active lattice) the solution of Eq. (39) can be found as [15]

$$U_x(x) = -\sum_m \frac{i K_m f_m}{(c_{11} - i\eta_{11}\omega)\mathrm{K}_m^2 - \rho\omega^2}(e_0 \mathrm{E}_z + d_0 \mathrm{H}_z)\exp(i K_m x), \quad m = 1, 3, 5 \ldots. \tag{41}$$

Here and henceforth harmonic time dependence $\exp(-i\omega t)$ for all physical variables is assumed.

Using the Eq. (41) we can find that

$$d_{31}\frac{\partial U_x}{\partial x} = \tilde{\mu}_{33}(x, \omega) H_z + \tilde{g}_{33}(x, \omega) E_z, \tag{42}$$

$$e_{31}\frac{\partial U_x}{\partial x} = \tilde{\varepsilon}_{33}(x, \omega) E_z + \tilde{g}_{33}(x, \omega) H_z, \tag{43}$$

$$\tilde{g}_{33} = e_0 d_0 \tilde{f}(x,\omega),\ \tilde{\varepsilon}_{33} = e_0^2 \tilde{f}(x,\omega),\ \tilde{\mu}_{33} = d_0^2 \tilde{f}(x,\omega), \tag{44}$$

$$\tilde{f}(x,\omega) = f(x) \sum_m \frac{f_m K_m^2 \exp(i K_m x)}{(c_{11} - i\eta_{11}\omega) K_m^2 - \rho\omega^2}, \tag{45}$$

In the long wave approximation model the periodic MEE can be taken to be homogeneous in space [15, 16] so that the following space average values $F(\omega) = \frac{1}{\beta} \int_0^\beta F(x,\omega)dx$ for $\tilde{\varepsilon}_{33}(x,\omega)$, $\tilde{g}_{33}(x,\omega)$ and $\tilde{\mu}_{33}(x,\omega)$ are applicable.

With this homogenization Eq. (42) can be written as

$$\tilde{\varepsilon}_{33}(\omega) = e_0^2 \sum_m R_m(\omega),\ \tilde{g}_{33}(\omega) = e_0 d_0 \sum_m R_m(\omega),\ R_m(\omega) = \frac{4\omega_m^2}{c_{11}\left(\omega_m^2 - \omega^2 - i\gamma_m\omega\right)}, \tag{46}$$

where $\omega_m = K_m c_a$ are the resonance frequencies of the MEE superlattice,$c_a = \sqrt{c_{11}/\rho}$ the acoustic wave velocity, and $\gamma_m = \eta_{11}\omega_m^2/c_{11}$ the damping coefficient. For wave frequencies very close to one of the resonance frequencies the contribution of other high-order reciprocal vectors can be neglected, giving the following equations for the frequency dependence of the dielectric, magnetic permeability and magneto-electric functions:

$$\tilde{\varepsilon}_{33}(\omega) = e_0^2 R_m(\omega),\ \tilde{\mu}_{33}(\omega) = d_0^2 R_m(\omega),\ \tilde{g}_{33}(\omega) = e_0 d_0 R_m(\omega). \tag{47}$$

Using (22) we can rewrite the Eq. (44) as

$$\varepsilon_{11}\frac{d^2E_z}{dx^2} + g_{11}\frac{d^2H_z}{dx^2} + j_1\omega^2\left[\varepsilon_{33}(\omega)E_z + g_{33}(\omega)H_z\right] = 0, \tag{48}$$

$$\mu_{11}\frac{d^2H_z}{dx^2} + g_{11}\frac{d^2E_z}{dx^2} + j_1\omega^2\left[g_{33}(\omega)E_z + \mu_{33}(\omega)H_z\right] = 0, \tag{49}$$

Here $\varepsilon_{33}(\omega) = \varepsilon_{33} + \tilde{\varepsilon}_{33}(\omega)$; $g_{33}(\omega) = g_{33} + \tilde{g}_{33}(\omega)$, $\mu_{33}(\omega) = \mu_{33} + \tilde{\mu}_{33}(\omega)$.

Assuming a dependence $\exp(ikx)$ for all the physical variables in (48), (49), from Eqs. (26, 27) the following dispersion relation follows:

$$\begin{aligned} &k^4 + k^2\omega^2(2g_{11}g_{33}(\omega) - \mu_{11}\varepsilon_{33}(\omega) - \varepsilon_{11}\mu_{33}(\omega)) \\ &\quad + \omega^4\left(\varepsilon_{11}\mu_{11} - g_{11}^2\right)\left(\varepsilon_{33}(\omega)\mu_{33}(\omega) - g_{33}^2(\omega)\right) = 0, \end{aligned} \tag{50}$$

In the case of a piezoelectric (PE) superlattice the dispersion Eq. (50) uncouples into two equations, $c_d^2k^2 - \omega^2 = 0$ for a pure EM (electromagnetic) wave $T_m\left(E_z, H_y\right)$ and $\left(c_e k/\omega\right)^2 = \varepsilon_{33}(\omega)$ for a coupled transverse EM and longitudinal elastic wave $\left(u_x, E_y, H_z\right)$. In this case polariton interaction without viscous damping is studied in [15–17]. For a piezomagnetic (PM) superlattice the dispersion Eq. (50) uncouples into equations $c_e^2k^2 - \omega^2 = 0$ for a pure EM wave $T_e\left(E_y, H_z\right)$ and $\left(c_d k/\omega\right)^2 = \mu_{33}(\omega)$ for a coupled EM and a longitudinal elastic wave $\left(u_x, E_z, H_y\right)$.

4 Numerical Analysis and Results

For an MEE crystal all the waves couple with each other making a hybrid electro-magneto-elastic waves defined by $(u_x, H_y, E_z, H_z, E_y)$ specifying that a longitudinal acoustic wave will be excited by and coupled to the y and z polarized original EM waves. The acoustic wave in its turn can also emit two orthogonally polarized EM waves.

For numerical calculations the material parameters of the MEE crystal $BaTiO_3$–$CoFe_2O_4$ are taken from [21] and the damping constant taken $\gamma_1 = 0.03\eta_{11}\omega^2/c_{11}$.

To show the MEE effect in polariton excitation in the MEE superlattice we first discuss the dispersion equation $(c_e k/\omega)^2 = \varepsilon_{33}(\omega)$ for a PE superlattice. The dependence of the real and imaginary parts of the dimensionless roots $\tilde{k}_{1,2} = (k_{1,2}\beta)/\pi$ of the dispersion equation for the first-order polariton and the dimensionless dielectric function $\widehat{\varepsilon}_{33}(\omega) = \varepsilon_{33}(\omega)/\varepsilon_{33}$ on the normalized frequency are shown in Fig. 2. The T_m wave decouples and the T_e EM wave couples with the longitudinal elastic wave-making a polariton band gap at the resonance frequency. The two dotted oblique lines are T_m and T_e modes without piezoelectric and piezomagnetic effects. In the long wave region where the wave number of the longitudinal acoustic wave is sufficiently small so that it can be approximated by the wave number of the electromagnetic T_e wave there is a narrow frequency gap around the resonance frequency where the real part of the dispersion curve experiences a discontinuity and the imaginary part reaches its maximum suggesting full absorption. The values of the imaginary parts are comparable with those of the real parts near the frequency gap where the propagation of the related mode is not supported.

In the case of a PM superlattice the dispersion equation $(c_d k/\omega)^2 = \mu_{33}(\omega)$ shows two propagating modes, a T_e wave decoupled from the lattice vibrations and the wave coupled with the longitudinal elastic wave (Fig. 3). A PM polariton excitation occurs at resonance when the frequency of the longitudinal lattice vibrations coincides with the frequency of the T_m mode wave. This leads to a PM polariton with a narrow frequency region where the large value of the imaginary part of the wave number suggests that the wave propagation here is forbidden.

With the three phase PE, PM and ME effects involved in the MEE superlattice, as results from Eqs. (48–50), there is a coupling between the EM wave (E_z, H_y) (Fig. 4). Due to the MEE effect the ab section of the dispersion curve of the PM superlattice (Fig. 3) exchanges from a T_e mode to a part of the upper branch of the root $\tilde{k}_2$ of the MEE dispersion Eq. (50) and away from the resonance point converges to a T_m mode (Fig. 3).

The cb section of the upper branch of the $\tilde{k}_2$ root of the PM dispersion curve (Fig. 2) becomes the upper branch of the root $\tilde{k}_1$ of the MEE dispersion equation and converges to a T_e mode (Fig. 3). As a result, as it can be seen from large imaginary values of lower branch of the root $\tilde{k}_2$ and upper branch of $\tilde{k}_1$, a polariton gap occurs between these dispersion curves. There is however always a wave propagating within this gap. It can be seen from the imaginary curves (Fig. 3) that this is the wave

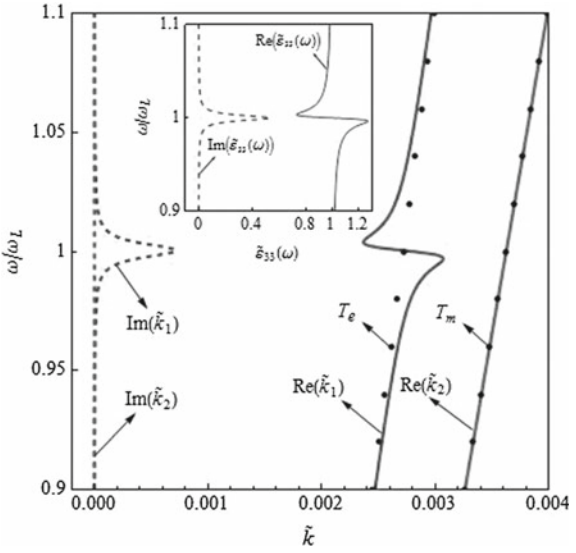

Fig. 2 The dispersion curve of the PE superlattice

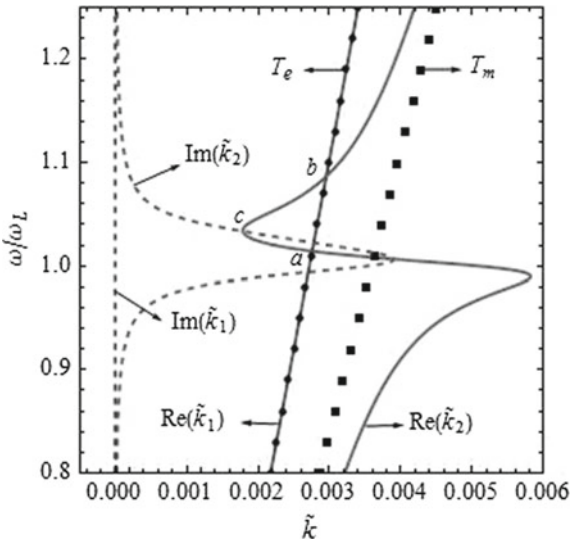

Fig. 3 The dispersion curve of the PM superlattice

described by the low part of the dispersion curve $\tilde{k}_1$ propagating as a T_e mode and at the point a converting into the upper branch of the root $\tilde{k}_2$ later converging into the T_m mode.

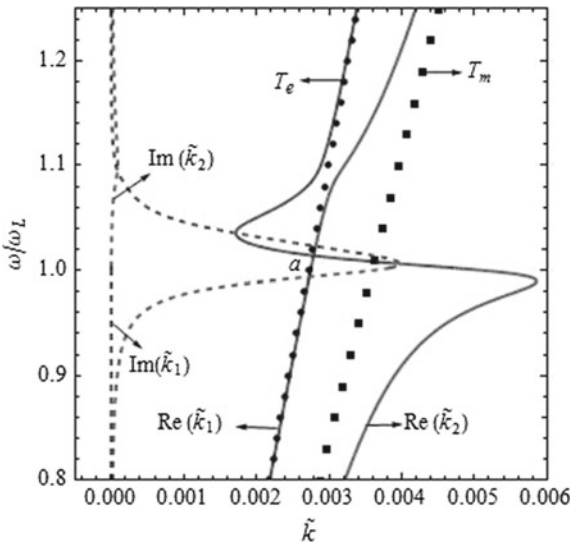

Fig. 4 The dispersion curve of the MEE superlattice

5 Conclusion

In the framework of the Maxwell' electrodynamics equations and the theory of elasticity the two-dimensional coupled equations have obtained defining elastic and electromagnetic fields interaction in MEE media. Based on this equations we have investigated phonon–photon polariton interaction in three-phase coupling between mechanical, electric and magnetic fields. We have demonstrated that due to the MEE effect a strong coupling occurs between longitudinal elastic wave and two modes of the electromagnetic waves resulting in a coupling of a new type polariton. It is shown that two orthogonally polarized electromagnetic waves couple with each other through the longitudinal elastic vibrations and transform the propagation mode around the internal resonance frequencies. The results show that the new three-phase coupled phonon–polariton exhibits properties different from two-phase piezoelectric and piezomagnetic polaritons.

References

1. Eerenstein, W., Mathur, N.D., Scott, J.F.: Multiferroic and magnetoelectric materials. Nature. V **442**, 759–765 (2006)
2. Nan, C.-W., et al.: Multiferroic magnetoelectric composites: historical perspective, status, and future directions. J. Appl. Phys. **103**, 031101–33 (2008)
3. Pakam, N., Arockiarajan, A.: An analytical model for predicting the effective properties of magneto-electro-elastic (MEE) composites. Comput. Mater. Sci. **65**, 19–28 (2012)
4. Lee, J., Boyd, J.G., Lagoudas, D.C.: Effective properties of three-phase electro-magneto-elastic composites. Int. J. Eng. Sci. **43**(10), 790–825 (2005)

5. Du, J., Jin, X., Wang, J.: Love wave propagation in layered magneto-electro-elastic structures with initial stress. Acta Mech. **192**(1–4), 169–189 (2007)
6. Mai, Y.W., Niraula, O.P., Wang, B.L.: A horizontal shear surface wave in magnetoelectroelastic materials. Philos. Mag. Lett. **87**(1), 53–58 (2007)
7. Wei, W.-Y., Liu, J.-X., Fang, D.-N.: Existence of shear horizontal surface waves in a magneto-electro-elastic material. Chin. Phys. Lett. **26**(10), 104301 (2009)
8. Piliposyan, D.: Shear surface waves at the interface of two magneto-electro-elastic media. Multidiscip. Model. Mater. Struct. **8**(3), 417–426 (2012)
9. Yu, L., et al.: Piezoelectric wafer active sensors for in situ ultrasonic-guided wave SHM. Fatigue Fract. Eng. Mater. Struct. **31**(8), 611–628 (2008)
10. Li, S.: The electromagneto-acoustic surface wave in a piezoelectric medium: the bleustein-gulyaev mode. J. Appl. Phys. **80**(9), 5264–5269 (1996)
11. Belubekyan, M.V.: Screen surface shear wave in a piezo-active semi-space of hexagonal symmetry. 2008. In: Proceedings of the 6th International Conference Problems of Dynamics of Interaction of Deformable Media, Yerevan, pp. 125–130
12. Piliposian, G.T., Avetisyan, A.S., Ghazaryan, K.B.: Shear wave propagation in periodic phononic/photonic piezoelectric medium. Wave Motion **49**(1), 125–134 (2012)
13. Piliposyan, D.G., Ghazaryan, K.B., Piliposian, G.T.: Shear Bloch waves and coupled phonon–polariton in periodic piezoelectric waveguides. Ultrasonics **54**(2), 644–654 (2014)
14. Liu, H., et al.: Coupling of electromagnetic waves and superlattice vibrations in a piezomagnetic superlattice: Creation of a polariton through the piezomagnetic effect. Phys. Rev. B **71**(12), 125106 (2005)
15. Zhang, X.-J., et al.: Phonon-polariton dispersion and the polariton based photonic band gap in piezoelectric superlattices. Phys. Rev. B **69**(8), 085118 (2004)
16. Huang, C., Zhu, Y.: Piezoelectric-induced polariton coupling in a superlattice. Phys. Rev. Lett. **94**(11), 117401 (2005)
17. Zhu, Y., et al.: New type of polariton in a piezoelectric superlattice. Phys. Rev. Lett. **90**(5), 053903 (2003)
18. Piliposyan, D., Ghazaryan, K., Piliposian, G.: Magneto-electro-elastic polariton coupling in a periodic structure. J. Phys. D: Appl. Phys. **48**(17), 175501 (2015)
19. Yakhno, V.G, Yakhno, T.M.: Maxwell's equations for bi-anisotropic materials as a symmetric hyperbolic system: Theory and computer application. In: 2011 International Conference on 2011 Electromagnetics in Advanced Applications (ICEAA), pp. 50–53
20. Auld, B.A.: Acoustic Fields and Waves in Solids. Wiley, New York (1973)
21. Xue, C.X,E.: Pan, On the longitudinal wave along a functionally graded magneto-electro-elastic rod. Int. J. Eng. Sci. **62**, 48–55 (2013)

Non-linear Dynamics of Pantographic Fabrics: Modelling and Numerical Study

Marco Laudato and Emilio Barchiesi

Abstract In this work, the dynamical behavior of a pantographic sheet undergoing sinusoidal (in time) imposed displacement is numerically investigated. The used model has been largely exploited to analyse the quasi-static behavior of pantographic materials. Here we propose to use a non-linear generalization of such a model for the description of a pantographic material dynamical behavior.

1 Introduction

In the last years, mechanical metamaterial framework has experienced a remarkable growth. Apart the promising technological applications, the interest in mechanical metamaterials lies also in the formidable mathematical problems arising during the modelling phase. Indeed, their macroscopic behavior can be forecasted in terms of a continuous field theory that is usually deduced by means of homogenization of the discrete description of the metamaterial's microstructure [1–7]. It has been shown that, if the microstructure is complex enough, the resulting homogenized continuous model cannot be always framed in classic continuum mechanics [8–18]. In more formal terms, it may happen that the action functional which describes such continuous model might depend upon the second (or higher) derivative of the displacement field. We refer to such models as generalized continua [19–22]. Of particular interest in this family is the so-called pantographic material [23]. This

M. Laudato
Dipartimento di Ingegneria e Scienze dell'Informazione e Matematica,
Università degli Studi dell'Aquila, Via Vetoio (Coppito 1), 67100 L'Aquila, Coppito, Italy

E. Barchiesi
International Center M&MOCS Mathematics and Mechanics of Complex Systems,
DICEAA, Universitá degli Studi dell'Aquila, Via Giovanni Gronchi
18 - Zona industriale di Pile, 67100 L'Aquila, Italy

E. Barchiesi (✉)
Dipartimento di Ingegneria Strutturale e Geotecnica, Università degli Studi di Roma "La Sapienza" Rome, Rome, Italy
e-mail: barchiesiemilio@gmail.com

M. A. Sumbatyan (ed.), *Wave Dynamics, Mechanics and Physics of Microstructured Metamaterials*, Advanced Structured Materials 109,
https://doi.org/10.1007/978-3-030-17470-5_17

system is characterized by a microstructure which consists of two arrays of fibers, orthogonally disposed, that in the intersection points are connected by means of a set of cylinders called pivots. Such a system has been studied for long time, from both the experimental [24] and theoretical [25, 26] point of view. However, the large part of this investigation has been devoted to the quasi-static characterization of its behavior and several models have been proposed, in both linear and non-linear regimes, resulting from homogenization procedures. A remarkable example is the model proposed in [5, 27–29] which has been obtained by homogenization, in a non-linear fashion, of a 2D deformation model of a pantographic material. In that work, moreover, the kinetic energy has been introduced but its effect was not analyzed in details.

We will consider, in this paper, a non-linear generalization of the model introduced in [30] which coincides, in the linear limit, with the linear limit of the model proposed in [5]. In particular, as we will discuss in details in Sect. 2, we consider a non-linear extension of such a model in which the strain energy depends upon the Green-Saint Venant tensor and its first gradient. Motivated by the recent effort which has been put on the experimental observation of the dynamics of pantographic sheets (see [31]), we will consider also the kinetic energy and we will present numerical simulations of a pantographic material in some exemplary dynamical regime cases. As we will outline in Sect. 3, we will numerically compute the displacement vector field of a pantographic sheet with one short-side undergoing an imposed sinusoidal oscillation (in time) while the other short-side is clamped. This work has to be considered as a first step in the modelling and numerical investigation of the dynamical behavior of a 2D pantographic material. In a forthcoming paper the presented numerical results will be compared with experimental observations.

2 2-Dimensional Finite Deformations Strain Gradient Elasticity

In this section we introduce a mathematical model for a two-dimensional pantographic metamaterial. Let us consider a 2-dimensional body, whose body points can be put in a bijective correspondence with a closed subset $\mathscr{B}$ of the Euclidean space $\mathbb{R}^2$. The set $\mathscr{B}$ represents the shape of the body in the reference (undeformed) configuration. We then introduce a Cartesian coordinate system $\left(\mathscr{O}, \left(\hat{e}_1, \hat{e}_2\right)\right)$, with $X = (X_1, X_2)$ the coordinates of the generic point in the Euclidean space $\mathbb{R}^2$. Working in a Lagrangian framework, we define a placement function $\chi : \mathscr{B} \times \mathbb{R}^+ \to \mathbb{R}^2$ such that the image $x = \chi(X, t)$ of X through χ is the position of point X at time t. The displacement function $u : \mathscr{B} \times \mathbb{R}^+ \to \mathbb{R}^2$ is defined as $u(X, t) = \chi(X, t) - X$. The placement function is the independent kinematic descriptor of the system. Let $F = \nabla_X \chi$ be the gradient (with respect to the Lagrangian coordinate X) of the placement function χ. Clearly, F belongs to Lin^+, the group of second order tensors with positive determinant i.e. orientation preserving. We then define an objective strain

measure $G = \left[F^T F - I\right]/2$ (sometime called Green-Saint Venant strain tensor), which is a quantity G accounting for the local change of shape of the body. Henceforth, we shall omit the subscript X in ∇_X and each space derivative will be considered a material derivative. The potential energy U is defined as

$$U = \int_{\mathscr{B}} \hat{U}^{strain}(G, \nabla G) - U^{ext}, \tag{1}$$

with $\hat{U}^{strain}(G, \nabla G)$ the strain energy density depending upon the Green-Saint Venant tensor and its first derivative, and

$$U^{ext} = \int_{\mathscr{B}} \left(b^{ext} \cdot u + m^{ext} \cdot \nabla u\right) + \tag{2}$$

$$\int_{\partial\mathscr{B}} \left[t^{ext} \cdot u + \tau^{ext} \cdot (\nabla u)\,\hat{n}\right] + \tag{3}$$

$$\int_{[\partial\partial\mathscr{B}]} f^{ext} \cdot u \tag{4}$$

the work done by the external forces onto the system. In Eq. (3), $\hat{n}$ is the unit external normal and the dot "$\cdot$" indicates tensor contraction. The quantities b^{ext} and m^{ext} in (2) are the external bulk force and double force per unit area, respectively, while quantities t^{ext} and τ^{ext} in (3) are the external force and double force per unit length, respectively. The vector $\hat{n}$ is the outward unit normal. Finally, f^{ext} in (4) is the external concentrated force, that is applied on the singularity points $[\partial\partial\mathscr{B}]$ (vertices) of $\partial\mathscr{B}$. The boundary $\partial\mathscr{B}$ is the union of m regular parts Σ_c (with $c = 1, \ldots, m$) (their intersection has zero 2-dimensional and 1-dimensional Lebesgue measure) and $[\partial\partial\mathscr{B}]$ is the (disjoint) union of the corresponding m vertex-points $\mathscr{V}_c$ (with $c = 1, \ldots, m$) with coordinates X^c. Thus, the last integral is the sum of the external works done by the concentrated forces applied at the vertices so that, for a generic field $g(X)$, we have

$$\int_{\partial\mathscr{B}} g(X)ds = \sum_{c=1}^{m} \int_{\Sigma_c} g(X)ds, \quad \int_{[\partial\partial\mathscr{B}]} g(X) = \sum_{c=1}^{m} g(X^c). \tag{5}$$

The action functional $\mathscr{A}$ reads then as

$$\mathscr{A} = \frac{1}{2}\int_0^T \int_{\mathscr{B}} \rho \|\dot{u}\|^2 - \int_0^T \int_{\mathscr{B}} \hat{U}^{strain} + U^{ext} \tag{6}$$

When the strain energy density $\hat{U}^{strain}(G, \nabla G)$ is considered to be depending quadratically upon the deformation tensor G and its gradient ∇G, the following representation formula holds [19]

$$\hat{U}^{strain} = \frac{1}{2}\varepsilon^T C_{3\times3}\varepsilon + \frac{1}{2}\eta^T A_{6\times6}\eta, \tag{7}$$

with

$$\varepsilon = \left(G_{11}\ G_{22}\ \sqrt{2}G_{12}\right)^T \tag{8}$$

and

$$\eta = \left(G_{11,1}\ G_{22,1}\ \sqrt{2}G_{12,2}\ G_{22,2}\ G_{11,2}\ \sqrt{2}G_{12,1}\right)^T. \tag{9}$$

In order to account for anisotropy of the material, we must assume invariance of the strain energy density under the action, on the Cartesian coordinate system $\left(\mathscr{O}, \left(\hat{e}_1, \hat{e}_2\right)\right)$ labeling points of the reference configuration, of some symmetry group S of transformations, which could be any subgroup of *Orth*. For instance, if the material is isotropic then, for a certain deformed configuration, any rotation or mirror transformation of the reference configuration will yield the same strain energy. In a mathematical form, this means that, if S is a symmetry group, then

$$U(G_{ij}, G_{ij,k}) = U(Q_{in}Q_{jm}G_{nm}, Q_{in}Q_{jm}Q_{kr}G_{nm,r}). \tag{10}$$

When the symmetry group is the dihedral group D4 (orthotropic material, such as pantographic metamaterials) we have the following representations for the matrices $C_{3\times3}$ and $A_{6\times6}$

$$C^{D4}_{3\times3} = \begin{pmatrix} c_{11} & c_{12} & 0 \\ c_{12} & c_{22} & 0 \\ 0 & 0 & c_{33} \end{pmatrix} \tag{11}$$

$$A^{D4}_{6\times6} = \begin{pmatrix} A^{D4}_{3\times3} & 0 \\ 0 & A^{D4}_{3\times3} \end{pmatrix}, \tag{12}$$

with c_{11} and c_{12} in $C^{D4}_{3\times3}$ corresponding to the two Lamé coefficients λ and μ, respectively, and

$$A^{D4}_{3\times3} = \begin{pmatrix} a_{11} & a_{12} & a_{13} \\ a_{12} & a_{22} & a_{23} \\ a_{13} & a_{23} & a_{33} \end{pmatrix}. \tag{13}$$

Clearly, a restriction of thermodynamic nature can still be enforced on the strain energy density $\hat{U}^{strain}$. Indeed it is necessary to assume that $\hat{U}^{strain}$ is positive definite or semi-definite (in such a case the existence of so-called floppy modes is contemplated). This translates in the matrices $C_{3\times3}$ and $A_{6\times6}$ in formula (7) being positive definite (at least one of them) or semi-definite, respectively.

3 Weak Form Problem and Numerical Simulations

In this section we show some numerical simulations of the modeled introduced previously. In particular, we consider a sinusoidal (in time) displacement applied to one of the short side (70 mm) of the pantographic sheet modeled as a rectangular continuous domain. The other short side is clamped while the other sides (210 mm) have free boundary conditions. The actual dynamics of the system is obtained by invoking the least action principle, namely we look for those configuration of the system such that $\delta\mathscr{A} = 0$ for all admissible motions δu. In order to derive the weak form problem associated to the functional (6) one considers its Gâteaux derivative:

$$\begin{aligned} 0 = \langle \mathscr{A}'(u), v, \dot{v} \rangle = &- \rho \int_0^T \int_{\mathscr{B}} \dot{u}_i \dot{v}_i + \int_0^T \int_{\mathscr{B}} \Bigg[\frac{\partial \hat{U}^{strain}(G, \nabla G)}{\partial G_{ij}} \frac{\partial G_{ij}}{\partial u_{i,j}} v_{i,j} \\ &+ \frac{\partial \hat{U}^{strain}(G, \nabla G)}{\partial G_{ij,k}} \frac{\partial G_{ij,k}}{\partial u_{i,j}} v_{i,j} + \frac{\partial \hat{U}^{strain}(G, \nabla G)}{\partial G_{ij,k}} \frac{\partial G_{ij,k}}{\partial u_{i,jk}} v_{i,jk} \\ &- b_i^{ext} v_i - m_{ij}^{ext} v_{i,j} \Bigg] - \int_0^T \int_{\partial\mathscr{B}} \left[t_i^{ext} v_i + \tau_i^{ext} \hat{n}_j v_{i,j} \right] + \\ &\int_0^T \int_{[\partial\partial\mathscr{B}]} f_i^{ext} v_i. \end{aligned} \tag{14}$$

By means of subsequent integration by parts we get

$$\begin{aligned} 0 = \langle \mathscr{A}'(u), v \rangle = \rho \int_0^T \int_{\mathscr{B}} \ddot{u}_i v_i - \int_0^T \int_{\mathscr{B}} v_i \left\{ \left[F_{i\alpha} (S_{\alpha j} - T_{\alpha jh}) \right]_{,j} + b_i^{ext} - m_{ij,j}^{ext} \right\} + \\ \int_0^T \int_{\partial\mathscr{B}} \left[v_i \left(t_i - t_i^{ext} - m_{ij}^{ext} \hat{n}_j \right) + v_{i,j} \hat{n}_j \left(\tau_i - \tau_i^{ext} \right) \right] + \\ \int_0^T \int_{[\partial\partial\mathscr{B}]} v_i \left(f_i - f_i^{ext} \right), \end{aligned} \tag{15}$$

where the following quantities have been defined

$$t_i = F_{i\alpha}(S_{\alpha j} - T_{\alpha jh,h})\hat{n}_j - P_{ka}(F_{i\alpha} T_{\alpha jh} P_{aj} \hat{n}_h)_{,k} \tag{16}$$

$$\tau_i = F_{i\alpha} T_{\alpha jh} \hat{n}_j \hat{n}_h \tag{17}$$

$$f_i = F_{i\alpha} T_{\alpha jh} V_{jh}. \tag{18}$$

The second order tensor P in (16) is the tangential projector operator ($P_{aj} = \delta_{aj} - \hat{n}_a \hat{n}_j$), while the second order tensor V in (16) is the vertex operator

$$V_{jh} = \nu_j^l \hat{n}_h^l + \nu_j^r \hat{n}_h^r, \tag{19}$$

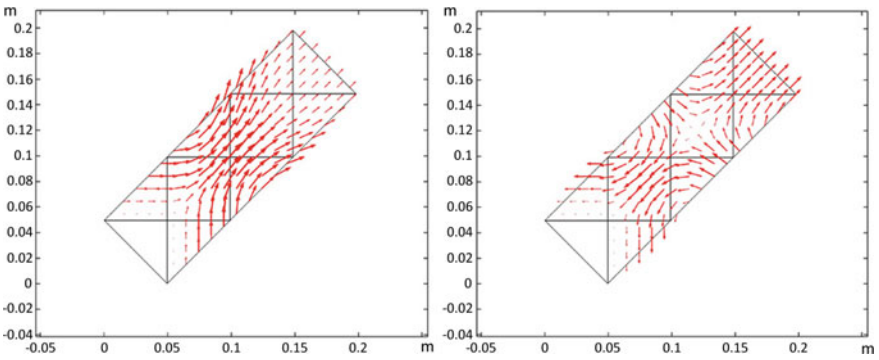

Fig. 1 Displacement vector field at maximum imposed displacement for a frequency of 100 Hz. Scales are in meters

where superscripts l and r refer to the two boundaries intersecting at a certain vertex-point $\mathscr{V}_c$ and ν is the outward unit tangent vector. The Lagrangian (first Piola-Kirchhoff) stress and hyper stress tensors are, respectively,

$$S_{\alpha j} = \frac{\partial \hat{U}^{strain}}{\partial G_{\alpha j}}, \qquad T_{\alpha jh} = \frac{\partial \hat{U}^{strain}}{\partial G_{\alpha j,h}}. \tag{20}$$

Three different frequencies, namely 100, 150, and 200 Hz, are considered. The maximum amplitude of the imposed displacement is 1 mm. Equation (15) has been solved by means of the software COMSOL Multiphysics. Figures 1, 2, and 3 show two snapshots of the displacement vector field at two different instant of time corresponding to configurations of maximum imposed displacement. The parameters of the model have been estimated in [30] and are reported in Table 1. The length of the arrows are proportional (scale factor 150) to the vectors' moduli. With respect to the figures, the imposed displacement acts on the upper-right short side of the rectangular domain, while the other short side has to be considered clamped.

In Fig. 4, snapshots at successive time instants of the (normalized) second gradient contribution to the deformation energy density field due to fibres' bending during perturbation propagation are shown. Frequency and (maximum) amplitude of the prescribed oscillation are 200 Hz and 1 mm, respectively. In Fig. 5, snapshots at successive time instants of the (normalized) first gradient contribution to the deformation energy density field due to macroscopic shear deformation of the 2D continuum, i.e. pivots' twist at micro-level, during perturbation propagation. Frequency and (maximum) amplitude of the prescribed oscillation are 200 Hz and 1 mm, respectively.

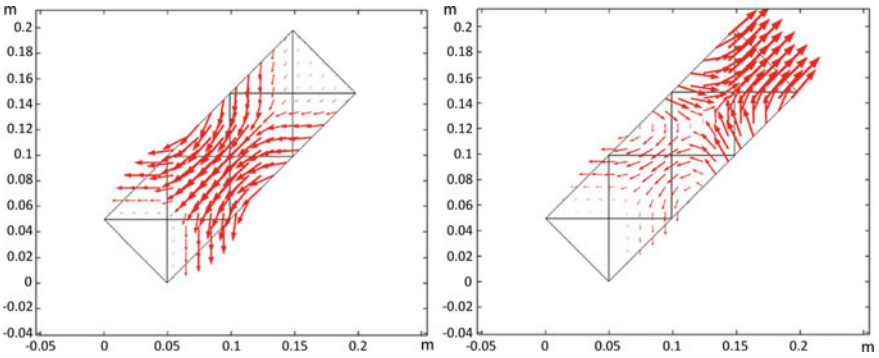

Fig. 2 Displacement vector field at maximum imposed displacement for a frequency of 150 Hz. Scales are in meters

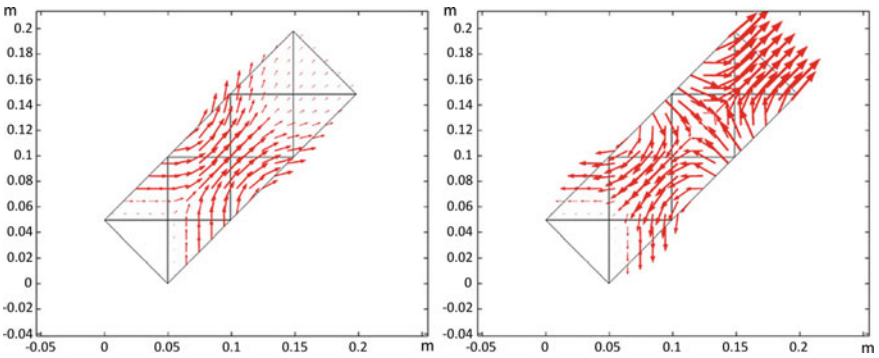

Fig. 3 Displacement vector field at maximum imposed displacement for a frequency of 200 Hz. Scales are in meters

Table 1 Values of the model's parameters

Parameter	Value
$c_{11} = c_{22}$	12310 N/m
c_{33}	141.76 N/m
$c_{12} = c_{21}$	0 N/m
$c_{13} = c_{31}$	0 N/m
$c_{23} = c_{32}$	0 N/m
a_{11}	0 J
$a_{12} = a_{21}$	0 J
$a_{13} = a_{31}$	0 J
a_{22}	0.00123 J
$a_{23} = a_{32}$	−0.00174 J
a_{33}	0.00246 J
ρ	0.00685 kg/m^2

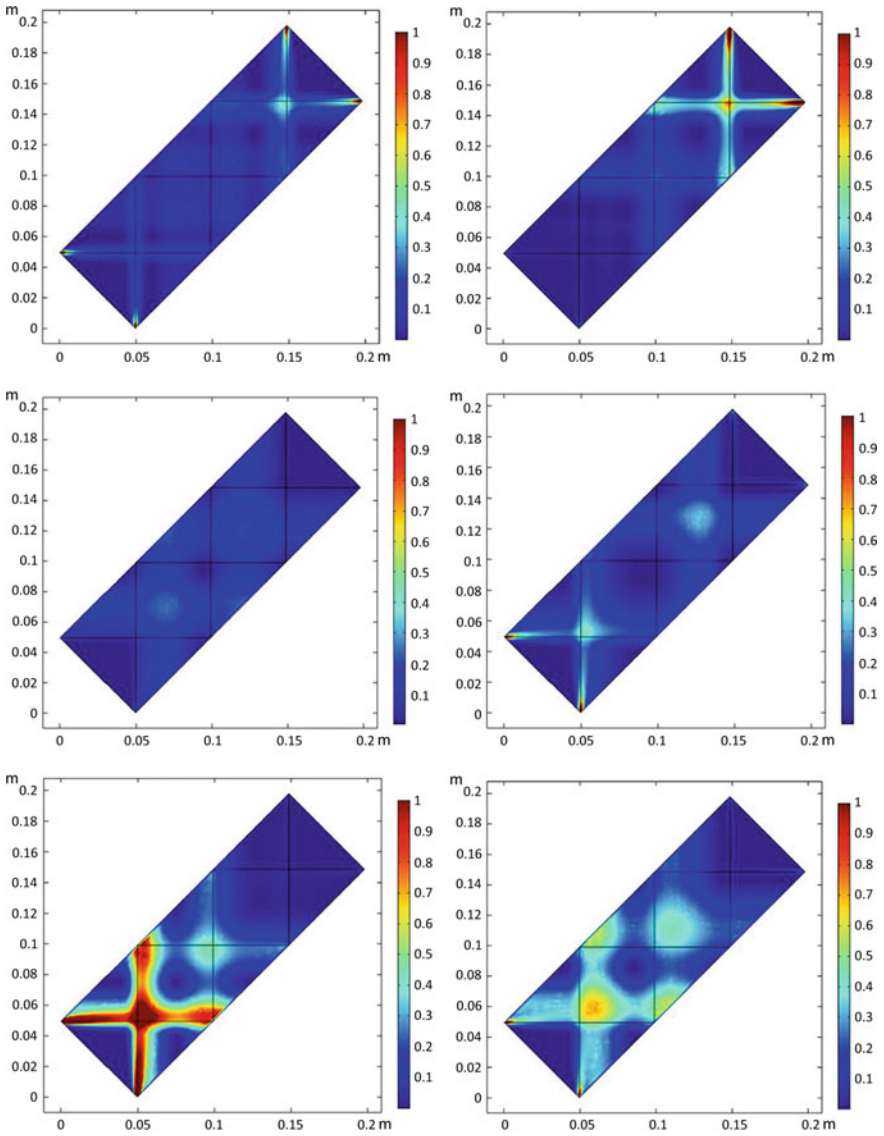

Fig. 4 Snapshots at successive time instants of the (normalized) second gradient contribution to the deformation energy density field due to fibres' bending during perturbation propagation. Frequency and (maximum) amplitude of the prescribed oscillation are 200 Hz and 1 mm, respectively. The images are ordered by successive time-steps from the top left corner to the bottom right corner

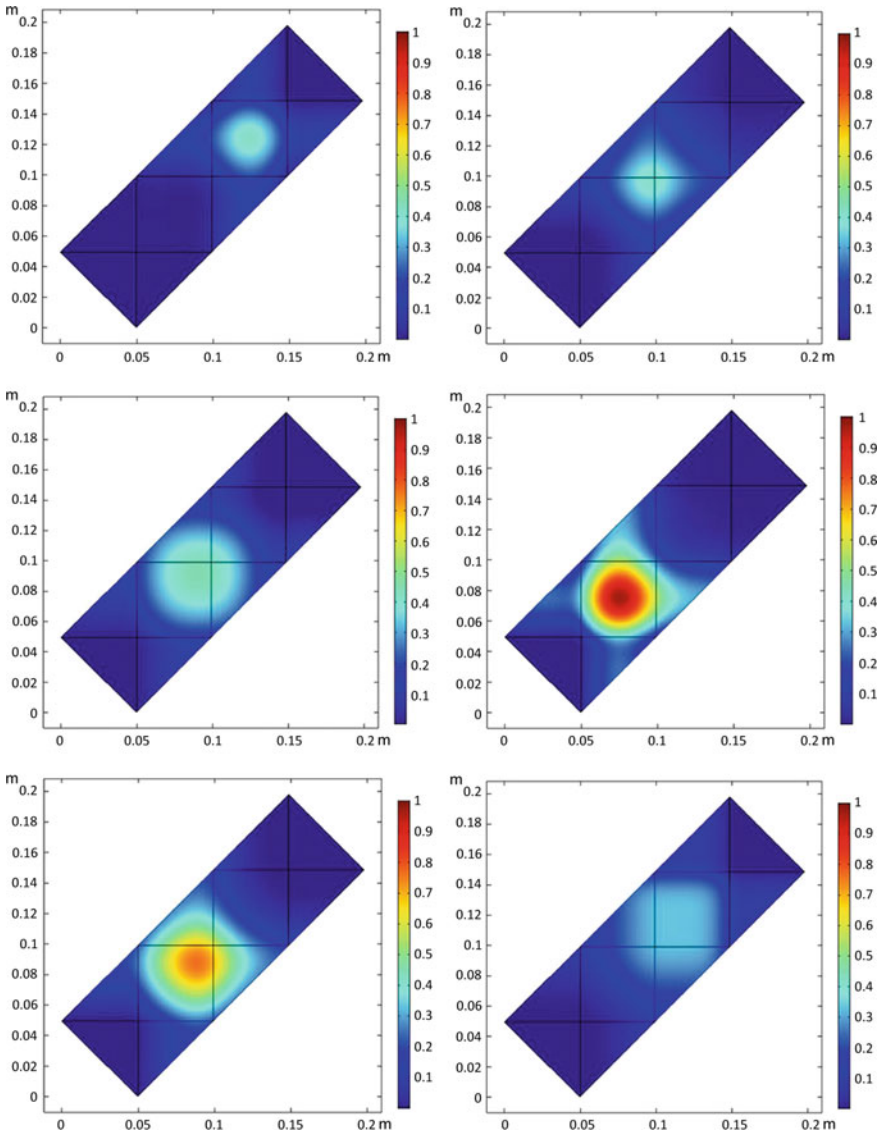

Fig. 5 Snapshots at successive time instants of the (normalized) first gradient contribution to the deformation energy density field due to macroscopic shear deformation of the 2D continuum, i.e. pivots' twist at micro-level, during perturbation propagation. Frequency and (maximum) amplitude of the prescribed oscillation are 200 Hz and 1 mm, respectively. The images are ordered by successive time-steps from the top left corner to the bottom right corner

4 Conclusions

In this work, by means of a non-linear generalization of the model presented in [30], we have numerically computed the displacement vector field of a pantographic sheet undergoing a sinusoidal (in time) imposed displacement. After the presentation of the model, in which the strain energy depends upon the Green-Saint Venant tensor and its first gradient, the weak form of the problem has been computed and solved by means of COMSOL Multiphysics. Relevant plots have been shown. This work represents the first step of a modelling campaign aimed at characterizing the dynamical behavior of pantographic materials. In particular, the generalization proposed here will be validate by experimental observations and we do expect that the feedback between numerical and experimental efforts will allow for a complete description of the dynamics of pantographic materials. Further applications can be conceived in the field of generalized thermoelasticity, as in [32, 33], or in the study of wave propagation in microstructured continua [34–36] and in plates and shells [37–40]. Useful results in the field of galloping phenomena can be, finally, found in [41–46]. The pantographic structures here studied in dynamics can be considered under different points of view. When taking into account the density of fibers, one can be obliged to introduce a different model to describe the network, as in [47]. This model can be studied in dynamics by using the results available in literature about dynamics of non-linear Euler-Bernoulli and Timoshenko beams (see for example [48–51]). Another possible generalization of the problem is represented by the study of the dynamics of pantographic structures embedded in soft matrices. Useful results in this framework can be found in [52–55] and in [56–58] for engineering-relevant composite materials. In perspective, the analysis here presented can be completed by the study of damage and damage evolution in pantographic structures. Preliminary results can be found in [59–65]. Numerical methods are nowadays of primary importance in the study of architectured materials. Some useful results in the field of isogeometric analysis can be found in [66–73], and in [74–77] for finite elements based continuum mechanics.

References

1. Alibert, J.J., Seppecher, P., dell'Isola, F.: Truss modular beams with deformation energy depending on higher displacement gradients. Math. Mech. Solids **8**(1), 51–73 (2003)
2. Barchiesi, E., Placidi, L.: A review on models for the 3D statics and 2D dynamics of pantographic fabrics. In: Wave Dynamics and Composite Mechanics for Microstructured Materials and Metamaterials. Springer, pp. 239–258 (2017)
3. Barchiesi, E., Spagnuolo, M., Placidi, L.: Mechanical metamaterials: a state of the art. Mathematics and Mechanics of Solids p. 1081286517735695 (2018)
4. di Cosmo, F., Laudato, M., Spagnuolo, M.: Acoustic metamaterials based on local resonances: Homogenization, optimization and applications. In: Generalized Models and Non-classical Approaches in Complex Materials 1, pp. 247–274. Springer (2018)
5. dell'Isola, F., Giorgio, I., Pawlikowski, M., Rizzi, N.L.: Large deformations of planar extensible beams and pantographic lattices: heuristic homogenization, experimental and numerical examples of equilibrium. Proc. .R Soc. A **472**(2185):20150,790 (2016)

6. dell'Isola, F., Seppecher, P., Alibert, J.J., Lekszycki, T., Grygoruk, R., Pawlikowski, M., Steigmann, D., Giorgio, I., Andreaus, U., Turco, E., et al.: Pantographic metamaterials: an example of mathematically driven design and of its technological challenges. Contin. Mech. Thermodyn. 1–34 (2018)
7. Placidi, L., Barchiesi, E., Turco, E., Rizzi, N.L.: A review on 2D models for the description of pantographic fabrics. Zeitschrift für angewandte Mathematik und Physik **67**(5), 121 (2016)
8. Abali, B.E.: Computational Reality: Solving Nonlinear and Coupled Problems in Continuum Mechanics, vol. 55. Springer (2016)
9. Abali, B.E., Müller, W.H., Eremeyev, V.A.: Strain gradient elasticity with geometric nonlinearities and its computational evaluation. Mech. Adv. Mater. Mod. Process. **1**(1), 4 (2015)
10. Abali, B.E., Müller, W.H., dell'Isola, F.: Theory and computation of higher gradient elasticity theories based on action principles. Arch. Appl. Mech. **87**(9), 1495–1510 (2017)
11. Abdoul-Anziz, H., Seppecher, P.: Strain gradient and generalized continua obtained by homogenizing frame lattices. Math. Mech. Complex Syst. **6**(3), 213–250 (2018)
12. De Masi, A., Merola, I., Presutti, E., Vignaud, Y.: Potts models in the continuum. uniqueness and exponential decay in the restricted ensembles. J. Stat. Phys. **133**(2):281–345 (2008)
13. De Masi, A., Merola, I., Presutti, E., Vignaud, Y.: Coexistence of ordered and disordered phases in potts models in the continuum. J. Stat. Phys. **134**(2), 243–306 (2009)
14. Misra, A., Chang, C.S.: Effective elastic moduli of heterogeneous granular solids. Int. J. Solids Struct. **30**(18), 2547–2566 (1993)
15. Pideri, C., Seppecher, P.: A second gradient material resulting from the homogenization of an heterogeneous linear elastic medium. Contin. Mech. Thermodyn. **9**(5), 241–257 (1997)
16. Pideri, C., Seppecher, P.: Asymptotics of a non-planar rod in non-linear elasticity. Asymptot. Anal. **48**(1,2):33–54 (2006)
17. Seppecher, P.: Second-gradient theory: application to Cahn-Hilliard fluids. In: Continuum thermomechanics, pp. 379–388. Springer (2000)
18. Yang, Y., Misra, A.: Higher-order stress-strain theory for damage modeling implemented in an element-free Galerkin formulation. CMES-Comput. Model. Eng. Sci. **64**(1), 1–36 (2010)
19. Auffray, N., Dirrenberger, J., Rosi, G.: A complete description of bi-dimensional anisotropic strain-gradient elasticity. Int. J. Solids Struct. **69**, 195–206 (2015)
20. Forest, S.: Mechanics of generalized continua: construction by homogenizaton. Le J. Phys. IV **8**(PR4):Pr4–39 (1998)
21. Forest, S., Sievert, R.: Elastoviscoplastic constitutive frameworks for generalized continua. Acta Mech. **160**(1–2), 71–111 (2003)
22. Rosi, G., Giorgio, I., Eremeyev, V.A.: Propagation of linear compression waves through plane interfacial layers and mass adsorption in second gradient fluids. ZAMM-J. Appl. Math. Mech./Zeitschrift für Angewandte Mathematik und Mechanik **93**(12), 914–927 (2013)
23. Scerrato, D., Giorgio, I., Rizzi, N.L.: Three-dimensional instabilities of pantographic sheets with parabolic lattices: numerical investigations. Zeitschrift für angewandte Mathematik und Physik **67**(3), 53 (2016)
24. Golaszewski, M., Grygoruk, R., Giorgio, I., Laudato, M., Di Cosmo, F.: Metamaterials with relative displacements in their microstructure: technological challenges in 3D printing, experiments and numerical predictions. Contin. Mech. Thermodyn. pp. 1–20 (2018)
25. Greco, L., Giorgio, I., Battista, A.: In plane shear and bending for first gradient inextensible pantographic sheets: numerical study of deformed shapes and global constraint reactions. Math. Mech. Solids **22**(10), 1950–1975 (2017)
26. Placidi, L., Barchiesi, E., Della Corte, A.: Identification of two-dimensional pantographic structures with a linear d4 orthotropic second gradient elastic model accounting for external bulk double forces. In: Mathematical Modelling in Solid Mechanics, pp. 211–232. Springer (2017)
27. Turco, E., dell'Isola, F., Cazzani, A., Rizzi, N.L.: Hencky-type discrete model for pantographic structures: numerical comparison with second gradient continuum models. Zeitschrift für angewandte Mathematik und Physik **67**(4):85 (2016a)

28. Turco, E., dell'Isola, F., Rizzi, N.L., Grygoruk, R., Müller, W.H., Liebold, C.: Fiber rupture in sheared planar pantographic sheets: numerical and experimental evidence. Mech. Res. Commun. **76**:86–90 (2016b)
29. Turco, E., Golaszewski, M., Cazzani, A., Rizzi, N.L.: Large deformations induced in planar pantographic sheets by loads applied on fibers: experimental validation of a discrete lagrangian model. Mech. Res. Commun. **76**:51–56 (2016c)
30. Boutin, C., Giorgio, I., Placidi, L., et al.: Linear pantographic sheets: asymptotic micro-macro models identification. Math. Mech. Complex Syst. **5**(2), 127–162 (2017)
31. Laudato, M., Manzari, L., Barchiesi, E., Di Cosmo, F., Göransson, P.: First experimental observation of the dynamical behavior of a pantographic metamaterial. Mech. Res. Commun. **94**, 125–127 (2018)
32. Abbas, I.A., Abdalla, A.E.N.N., Alzahrani, F.S., Spagnuolo, M.: Wave propagation in a generalized thermoelastic plate using eigenvalue approach. J. Therm. Stress. **39**(11), 1367–1377 (2016). https://doi.org/10.1080/01495739.2016.1218229
33. Abo-el-nour, N.A.A., Alshaikh, F., Vescovo, D.D., Spagnuolo, M.: Plane waves and eigenfrequency study in a transversely isotropic magneto-thermoelastic medium under the effect of a constant angular velocity. J. Therm. Stress. **40**(9), 1079–1092 (2017). https://doi.org/10.1080/01495739.2017.1334528
34. Altenbach, H., Eremeyev, V.A., Lebedev, L.P., Rendón, L.A.: Acceleration waves and ellipticity in thermoelastic micropolar media. Arch. Appl. Mech. **80**(3), 217–227 (2010)
35. Berezovski, A., Yildizdag, M.E., Scerrato, D.: On the wave dispersion in microstructured solids. Contin. Mech. Thermodyn. pp. 1–20 (2018)
36. Eremeyev, V.A., Lebedev, L.P., Cloud, M.J.: Acceleration waves in the nonlinear micromorphic continuum. Mech. Res. Commun. **93**, 70–74 (2018)
37. Altenbach, H., Eremeyev, V.A.: On the shell theory on the nanoscale with surface stresses. Int. J. Eng. Sci. **49**(12), 1294–1301 (2011)
38. Eremeyev, V., Zubov, L.: On constitutive inequalities in nonlinear theory of elastic shells. ZAMM **87**(2), 94–101 (2007)
39. Eremeyev, V.A., Altenbach, H., Morozov, N.F.: The influence of surface tension on the effective stiffness of nanosize plates. Dokl. Phys. **54**(2), 98–100 (2009)
40. Eremeyev, V.A., Lebedev, L.P., Altenbach, H.: Foundations of Micropolar Mechanics. Springer Science & Business Media (2012)
41. Di Egidio, A., Luongo, A., Paolone, A.: Linear and non-linear interactions between static and dynamic bifurcations of damped planar beams. Contin. Mech. Thermodyn. **42**(1), 88–98 (2007)
42. Luongo, A.: Mode localization in dynamics and buckling of linear imperfect continuous structures. In: Normal Modes and Localization in Nonlinear Systems, pp. 133–156. Springer (2001)
43. Luongo, A., Zulli, D., Piccardo, G.: Analytical and numerical approaches to nonlinear galloping of internally resonant suspended cables. J. Sound Vib. **315**(3), 375–393 (2008)
44. Pagnini, L., Freda, A., Piccardo, G.: Uncertainties in the evaluation of one degree-of-freedom galloping onset. Eur. J. Environ. Civ. Eng. **21**(7–8), 1043–1063 (2017)
45. Pagnini, L.C., Piccardo, G.: The three-hinged arch as an example of piezomechanic passive controlled structure. Contin. Mech. Thermodyn. **28**(5), 1247–1262 (2016)
46. Piccardo, G., Pagnini, L.C., Tubino, F.: Some research perspectives in galloping phenomena: critical conditions and post-critical behavior. Contin. Mech. Thermodyn. **27**(1–2), 261–285 (2015)
47. Andreaus, U., Spagnuolo, M., Lekszycki, T., Eugster, S.R.: A Ritz approach for the static analysis of planar pantographic structures modeled with nonlinear Euler–Bernoulli beams. Contin. Mech. Thermodyn. pp. 1–21 (2018)
48. Bîrsan, M., Altenbach, H., Sadowski, T., Eremeyev, V., Pietras, D.: Deformation analysis of functionally graded beams by the direct approach. Compos. Part B: Eng. **43**(3), 1315–1328 (2012)
49. Chróścielewski, J., Schmidt, R., Eremeyev, V.A.: Nonlinear finite element modeling of vibration control of plane rod-type structural members with integrated piezoelectric patches. Contin. Mech. Thermodyn. **31**(1), 147–188 (2019)

50. Eremeyev, V.A.: On characterization of an elastic network within the six-parameter shell theory. In: Shell Structures: Theory and Applications Volume 4: Proceedings of the 11th International Conference "Shell Structures: Theory and Applications" (SSTA 2017), October 11–13, 2017, pp. 81–84. Gdansk, Poland, CRC Press, Boca Raton (2018)
51. Spagnuolo, M., Andreaus, U.: A targeted review on large deformations of planar elastic beams: extensibility, distributed loads, buckling and post-buckling. Math. Mech. Solids **0**(0):1081286517737,000, https://doi.org/10.1177/1081286517737000 (2018)
52. Franciosi, P.: A decomposition method for obtaining global mean green operators of inclusions patterns. Application to parallel infinite beams in at least transversally isotropic media. Int. J. Solids Struct. (2018)
53. Franciosi, P., Lormand, G.: Using the radon transform to solve inclusion problems in elasticity. Int. J. Solids Struct. **41**(3–4), 585–606 (2004)
54. Franciosi, P., Brenner, R., El Omri, A.: Effective property estimates for heterogeneous materials with cocontinuous phases. J. Mech. Mater. Struct. **6**(5), 729–763 (2011)
55. Franciosi, P., Spagnuolo, M., Salman, O.U.: Mean Green operators of deformable fiber networks embedded in a compliant matrix and property estimates. Contin. Mech. Thermodyn. pp. 1–32 (2018)
56. Marmo, F., Rosati, L.: The fiber-free approach in the evaluation of the tangent stiffness matrix for elastoplastic uniaxial constitutive laws. Int. J. Numer. Methods Eng. **94**(9), 868–894 (2013)
57. Romano, G., Rosati, L., Ferro, G.: Shear deformability of thin-walled beams with arbitrary cross sections. Int. J. Numer. Methods Eng. **35**(2), 283–306 (1992)
58. Rosati, L., Marmo, F., Serpieri, R.: Enhanced solution strategies for the ultimate strength analysis of composite steel-concrete sections subject to axial force and biaxial bending. Comput. Methods Appl. Mech. Eng. **197**(9–12), 1033–1055 (2008)
59. Contrafatto, L., Cuomo, M.: A framework of elastic-plastic damaging model for concrete under multiaxial stress states. Int. J. Plast. **22**(12), 2272–2300 (2006)
60. Cuomo, M.: Continuum model of microstructure induced softening for strain gradient materials. Math. Mech. Solids p. 1081286518755845 (2018)
61. Placidi, L., Barchiesi, E., Misra, A.: A strain gradient variational approach to damage: a comparison with damage gradient models and numerical results. Math. Mech. Complex Syst. **6**(2):77–100 (2018a)
62. Placidi, L., Misra, A., Barchiesi, E.: Simulation results for damage with evolving microstructure and growing strain gradient moduli. Contin. Mech. Thermodyn. pp. 1–21 (2018b)
63. Placidi, L., Misra, A., Barchiesi, E.: Wo-dimensional strain gradient damage modeling: a variational approach. Zeitschrift für angewandte Mathematik und Physik **69**(3):56 (2018c)
64. Spagnuolo, M., Barcz, K., Pfaff, A., dell'Isola, F., Franciosi, P.: Qualitative pivot damage analysis in aluminum printed pantographic sheets: numerics and experiments. Mech. Res. Commun. **83**, 47–52 (2017)
65. Yang, Y., Misra, A.: Micromechanics based second gradient continuum theory for shear band modeling in cohesive granular materials following damage elasticity. Int. J. Solids Struct. **49**(18), 2500–2514 (2012)
66. Beirão Da Veiga, L., Hughes, T., Kiendl, J., Lovadina, C., Niiranen, J., Reali, A., Speleers, H.: A locking-free model for reissner-mindlin plates: analysis and isogeometric implementation via nurbs and triangular nurps. Math. Model. Methods Appl. Sci. **25**(08), 1519–1551 (2015)
67. Cazzani, A., Malagù, M., Turco, E.: Isogeometric analysis of plane-curved beams. Math. Mech. Solids **21**(5):562–577 (2016a)
68. Cazzani, A., Malagù, M., Turco, E., Stochino, F.: Constitutive models for strongly curved beams in the frame of isogeometric analysis. Math. Mech. Solids **21**(2):182–209 (2016b)
69. Greco, L., Cuomo, M.: B-spline interpolation of kirchhoff-love space rods. Comput. Methods Appl. Mech. Eng. **256**, 251–269 (2013)
70. Greco, L., Cuomo, M.: An implicit g1 multi patch b-spline interpolation for kirchhoff-love space rod. Comput. Methods Appl. Mech. Eng. **269**, 173–197 (2014)
71. Khakalo, S., Niiranen, J.: Isogeometric analysis of higher-order gradient elasticity by user elements of a commercial finite element software. Comput.-Aided Des. **82**, 154–169 (2017)

72. Niiranen, J., Kiendl, J., Niemi, A.H., Reali, A.: Isogeometric analysis for sixth-order boundary value problems of gradient-elastic kirchhoff plates. Comput. Methods Appl. Mech. Eng. **316**, 328–348 (2017)
73. Yildizdag, M.E., Demirtas, M., Ergin, A.: Multipatch discontinuous galerkin isogeometric analysis of composite laminates. Contin. Mech. Thermodyn. 1–14 (2018)
74. Cazzani, A., Atluri, S.: Four-noded mixed finite elements, using unsymmetric stresses, for linear analysis of membranes. Comput. Mech. **11**(4), 229–251 (1993)
75. Javili, A., McBride, A., Steinmann, P., Reddy, B.: A unified computational framework for bulk and surface elasticity theory: a curvilinear-coordinate-based finite element methodology. Comput. Mech. **54**(3), 745–762 (2014)
76. McBride, A., Mergheim, J., Javili, A., Steinmann, P., Bargmann, S.: Micro-to-macro transitions for heterogeneous material layers accounting for in-plane stretch. J. Mech. Phys. Solids **60**(6), 1221–1239 (2012)
77. Saeb, S., Steinmann, P., Javili, A.: Aspects of computational homogenization at finite deformations: a unifying review from reuss' to voigt's bound. Appl. Mech. Rev. **68**(5):050,801 (2016)